



MARMARA UNIVERSITY
INSTITUTE FOR GRADUATE STUDIES
IN PURE AND APPLIED SCIENCES



THE EFFECT OF VARIOUS PARAMETERS
ON THE PHOTOELECTROCHEMICAL
HYDROGEN PRODUCTION PERFORMANCE
OF PHOTOELECTRODES

ÖZLEM UĞUZ NELİ

Ph.D. THESIS
Department of Chemical Engineering

Thesis Supervisor
Prof. Dr. Atif KOCA

ISTANBUL, 2022



MARMARA UNIVERSITY
INSTITUTE FOR GRADUATE STUDIES
IN PURE AND APPLIED SCIENCES



THE EFFECT OF VARIOUS PARAMETERS
ON THE PHOTOELECTROCHEMICAL
HYDROGEN PRODUCTION PERFORMANCE
OF PHOTOELECTRODES

ÖZLEM UĞUZ NELİ
(724516003)

Ph.D. THESIS
Department of Chemical Engineering

Thesis Supervisor
Prof. Dr. Atıf KOCA

ISTANBUL, 2022

ACKNOWLEDGMENT

I would like to acknowledge my sincere gratitude to my supervisor Prof. Dr. Atif KOCA, who made this work possible. His guidance, motivation, enthusiasm and advice helped me through all the stages of writing my thesis.

A debt of gratitude is also owed to my colleague, a great friend, Research Assistant Özlem BUDAK for all her support and encouragement.

I thank Research Assistant Didem AYCAN, Assistant Professor Müge SENNAROĞLU BOSTAN, and Research Assistant Yaren ERDAĞ MADEN for their friendship and helps.

I would also like to give my thanks to The Scientific and Technological Research Council of Turkey (TUBITAK) Project Number: 219M328 and Marmara University BAPKO Project Number: FDK-2020-10022 for the financial grant.

Last but not the least, I would like to thank my beloved family, İbrahim UĞUZ, Emel UĞUZ, Özge UĞUZ, and Ozan NELİ for their endless love, understanding and being always by my side. Without you none of this would surely be possible.

March, 2022

Özlem UĞUZ NELİ

TABLE OF CONTENTS

ACKNOWLEDGEMENT

ABSTRACT

ÖZET

SYMBOLS

ABBREVIATIONS

LIST OF FIGURES

LIST OF TABLES

1. INTRODUCTION

1.1. Types of Energy and Energy Sources.....	2
1.2. Hydrogen Energy.....	3
1.2.1. Hydrogen production pathways.....	4
1.2.1.1. Hydrogen from fossil fuels.....	5
1.2.1.2. Hydrogen from renewable sources.....	8
1.3. Photoelectrochemical (PEC) Hydrogen Production Processes.....	14
1.3.1. Semiconductor Fundamentals.....	14
1.3.2. Photoelectrochemical (PEC) system Fundamentals.....	16
1.3.3. Parameters affecting the photoelectrochemical hydrogen production.....	21
1.3.4. Metal chalcogenides and graphene-based materials in PEC studies.....	24
1.3.5. Methods of thin film deposition.....	27
1.3.5.1. Physical vapor deposition.....	27
1.3.5.2. Chemical vapor deposition.....	28
1.3.5.3. Chemical bath deposition.....	29
1.3.5.4. Spin coating	30
1.3.5.5. Dip coating.....	31
1.3.5.6. Electrodeposition.....	31

1.3.6. Photoelectrochemical measurements.....	33
1.3.6.1. Open circuit potential.....	33
1.3.6.2. Linear sweep voltammetry (LSV).....	35
1.3.6.3. Chronoamperometry (CA).....	35
1.3.6.4. Electrochemical impedance spectroscopy (EIS).....	36
1.3.6.5. Mott-Schottky (M-S).....	37
1.3.7. Electrode characterization techniques.....	39
1.3.7.1. Scanning electron microscopy (SEM).....	39
1.3.7.2. Energy dispersive X-ray spectroscopy (EDS).....	40
1.3.7.3. X-ray diffraction (XRD).....	40
1.3.7.4. X-ray photoelectron spectroscopy (XPS).....	41
1.3.7.5. Raman spectroscopy (RS).....	41
1.3.7.6. UV-visible spectroscopy (UV-vis spectroscopy).....	42
1.4. Literature Survey on Photoelectrochemical Studies.....	43

2. EXPERIMENTAL STUDIES

2.1. Types of Energy and Energy Sources.....	49
2.2. Preparation of Graphene Oxide (GO) and Reduced Graphene Oxide (RGO).....	50
2.3. Preparation of Photoelectrodes by Solvothermal and Electrodeposition Method.....	51
2.4. Characterization Techniques.....	55
2.5. Photoelectrochemical Measurements.....	55

3. RESULTS AND DISCUSSION

3.1. Characterization and Photoelectrochemical Analyses of Solvothermally Prepared RGO-Cd _{0.60} Zn _{0.40} S-Pt Photoelectrodes.....	57
3.2. Characterization and Photoelectrochemical Analyses of Electrodeposited Photoelectrodes.....	63

3.2.1. Electrochemical Deposition, Characterization and Photoelectrochemical Performance of CdZnS and RGO-CdZnS Photoelectrodes.....	63
3.2.2. Electrochemical Deposition, Characterization and Photoelectrochemical Performance of CdZnSSe and RGO-CdZnSSe Photoelectrodes.....	81
3.2.3. Electrochemical Deposition, Characterization and Photoelectrochemical Performance of CdZnMSeS (M: Ni, Cu, Mo) and RGO- CdZnNiSeS Photoelectrodes.....	100

4. CONCLUSIONS

REFERENCES

CURRICULUM VITAE

ABSTRACT

THE EFFECT OF VARIOUS PARAMETERS ON THE PHOTOELECTROCHEMICAL HYDROGEN PRODUCTION PERFORMANCE OF PHOTOELECTRODES

The global population expansion and economic improvement have brought about problems such as increasing energy demand and diminishing fossil fuels. Moreover, harmful emissions due to the combustion of fossil fuels are released into the atmosphere having a negative impact on human health and environment. To overcome this handicap, the photoelectrochemical hydrogen generating process has a tremendous deal of potential. The key factor in photoelectrochemical studies is modifying the most effective photoelectrodes using the optimum parameters and the appropriate deposition methods. This study reports the one-step electrodeposition of CdZnS, CdZnSSe, CdZnNiSSe, CdZnCuSSe, CdZnMoSSe and the effect of reduced graphene oxide (RGO) decoration on the photoelectrochemical performance of fabricated photoelectrodes for the first time in the literature. Electrochemical deposition was carried out via repetitive cyclic voltammetry at room temperature. Photoelectrodes were annealed and their photoelectrochemical performances were investigated. To interpret their photoelectrochemical performance and efficiency, open circuit potential measurements, linear sweep voltammetry, chronoamperometry, UV-vis diffuse reflectance spectroscopy, electrochemical impedance spectroscopy, Mott-Schottky analyses were performed. The results demonstrated that optimizing the concentrations of the chalcogenides, annealing temperature, and RGO concentration decreased the rate of electron-hole recombination avoiding photocorrosion. Finally, the photocurrent density is increased from $25 \mu\text{A cm}^{-2}$ (ZnS) to 5.34 mA cm^{-2} (RGO(0.25)-Cd_{0.6}Zn_{0.2}Ni_{0.2}S_{0.2}Se_{0.8}) as a result of modifications. The maximum applied bias photon-to-current efficiency (ABPE) was estimated as 3.18% for RGO-Cd_{0.6}Zn_{0.2}Ni_{0.2}S_{0.2}Se_{0.8} photoelectrodes.

ÖZET

ÇEŞİTLİ PARAMETRELERİN FOTOELEKTROTLARA AİT FOTOELEKTROKİMYASAL HİDROJEN ÜRETİMİ PERFORMANSINA ETKİSİ

Küresel popülasyonun artması ve ekonomik kalkınmanın hızlanması, enerji üretim gerekliliğini ve enerji üretiminde yoğun olarak kullanılan fosil yakıt kaynaklarının miktarını azaltmıştır. Fosil yakıt yakımından kaynaklanan ve atmosfere salınan gazlar çevreye ve insan sağlığına büyük zarar vermektedir. Temiz bir alternatif olan hidrojen üretimi ve bu üretimi güneş ışığı varlığında fotoelektrokimyasal yolla yapmak çevresel kaygılara ve enerji ihtiyacına çözüm üretebilir. Fotoelektrokimyasal çalışmalarda, optimum parametreleri kullanarak en etkili fotoelektrotları geliştirmek önem taşımaktadır. Bu çalışmada CdZnS, CdZnSSe, CdZnNiSSe, CdZnCuSSe, CdZnMoSSe fotoelektrotlarının tek aşamalı elektrodepozisyonu ve indirgenmiş grafen oksit (RGO)'in hazırlanan bu fotoelektrotlar üzerindeki etkisi literatürde ilk kez incelenmiştir. Elektrokimyasal depozisyon ile fotoelektrot üretimi tekrarlı dönüşümlü voltametri yöntemi ile sağlanmıştır. Fotoelektrotların fotoelektrokimyasal özellikleri üç elektrotlu sistem ile incelenmiştir. Fotoelektrokimyasal performansı incelemek için açık devre potansiyeli, doğrusal taramalı voltametri, kronoamperometri, UV-vis difüz reflektans spektroskopisi, elektrokimyasal empedans spektroskopisi ve Mott-Schottky analizleri uygulanmıştır. Varılan sonuçlarla, kullanılan kalkojenlerin fotoelektrottaki kompozisyonlarının, tavlama sıcaklığının, RGO konsantrasyonunun optimize edilmesi elektron-hol rekombinasyonunun ve fotokorozyonun önlenmesini sağlayarak performansı artırmaktadır. Çalışmanın başında bulunan fotoakım yoğunluğu $25 \mu\text{A cm}^{-2}$ (ZnS) iken, yapılan modifikasyonlar sonucu bu değer 5.34 mA cm^{-2} 'a (RGO(0.25)-Cd_{0.6}Zn_{0.2}Ni_{0.2}S_{0.2}Se_{0.8}) yükselmiştir. Maksimum uygulanan bias ışıktan akım eldesi verimi RGO(0.25)-Cd_{0.6}Zn_{0.2}Ni_{0.2}S_{0.2}Se_{0.8} fotoelektrotu için %3.18 olarak tespit edilmiştir.

CLAIM FOR ORIGINALITY

THE EFFECT OF VARIOUS PARAMETERS ON THE PHOTOELECTROCHEMICAL HYDROGEN PRODUCTION PERFORMANCE OF PHOTOELECTRODES

In this thesis, a new electrochemical method was proposed to prepare new photoelectrodes bearing CdZnS, RGO-CdZnS, CdZnSSe, RGO-CdZnSSe, CdZnNiSSe, CdZnMoSSe, CdZnCuSSe, RGO- CdZnNiSSe composites and then these photoelectrodes were tested in the photoelectrochemical system to investigate the performance of photoelectrochemical hydrogen evolution reaction. According to our knowledge, there have been some reports on the simultaneous electrodeposition of CdZnS and CdZnSe. Yet, there is no any study investigating one-step simultaneous electrodeposition of RGO-CdZnS, RGO-CdZnSSe, CdZnNiSSe, CdZnMoSSe, CdZnCuSSe, RGO-CdZnNiSSe. All in all, the main idea of this thesis study emerges from using a facile, efficient, low cost technique to deposit thin films to perform as photoelectrodes. With this time efficient method, the deposition was achieved successfully and using reduced graphene oxide (RGO) prevented the aggregation of the particles avoiding the photocorrosion in photoelectrochemical processes.

SYMBOLS

C_{sc}	: Capacitance of space charge layer ($C\ g^{-1}$, $F\ g^{-1}$)
D	: Crystallite size (nm)
e	: Electronic charge (C)
E_c	: Energy of conduction band maximum
E_f	: Fermi level energy
$E_{f,m}$: Fermi level energy of metal
$E_{f,s}$: Fermi level energy of semiconductor
E_g	: Band gap energy (eV)
E_v	: Energy of valence band minimum
E_{vac}	: Vacuum energy
F	: Faraday's constant ($C\ mol^{-1}$)
J_{ph}	: Current density at the applied external potential ($mA\ cm^{-2}$)
k_B	: Boltzmann's constant (J/K)
n	: Number of electrons moving per mole of molecules
N_D	: Charge carrier density (cm^{-3})
$P_{incident}$: Power density of incident light ($mW\ cm^{-2}$)
R	: Reflectance (%)
R_{ct}	: Charge transfer resistance (ohm)
R_s	: Solution resistance (ohm)
T	: Temperature ($^{\circ}C$)
V_{app}	: Applied external potential (V)
V_{fb}	: Flat band potential ($KT\ e^{-1}$)
W	: Warburg element ($\Omega.s^{-1/2}$)
z	: Electrochemical equivalent of the substance
β	: Full-width at half maxima in radians (rad)
θ	: Diffraction angle ($^{\circ}$)
λ	: Wavelength of X-rays (nm)
ϵ_0	: Permittivity of free space ($F\ m^{-1}$)
ϵ_s	: Dielectric constant of deposited material ($F\ m^{-1}$)
Φ_m	: Metal work function (J)
Φ_s	: Semiconductor work function (J)
χ_s	: Electron affinity of semiconductor ($kJ\ mol^{-1}$)

ABBREVIATIONS

ABPE	: Applied bias photon-to-current efficiency
AM	: Air mass
CA	: Chronoamperometry
CE	: Counter electrode
CB	: Conduction band
CBD	: Chemical bath deposition
CPE	: Constant phase element
CV	: Cyclic voltammetry
CVD	: Chemical vapor deposition
DMSO	: Dimethyl sulfoxide
EDS	: Energy dispersive X-ray spectroscopy
EDTA	: Ethylene diamine tetra acetic acid
EIS	: Electrochemical impedance spectroscopy
FESEM	: Field emission scanning electron microscopy
FTO	: Fluorine tin oxide
GO	: Graphene oxide
HER	: Hydrogen evolution half reaction
ITO	: Indium tin oxide
M-S	: Mott-Schottky
LSV	: Linear sweep voltammetry
OER	: Oxygen evolution half reaction
OCP	: Open circuit potential
rCV	: Repetitive cyclic voltammetry
RE	: Reference electrode
RGO	: Reduced graphene oxide
SEM	: Scanning electron microscopy
SCE	: Saturated calomel electrode

SHE	: Standard hydrogen electrode
STH	: Solar-to-hydrogen
WE	: Working electrode
XPS	: X-ray photoelectron spectroscopy
XRD	: X-ray diffraction
PC	: Photocatalytic
PEC	: Photoelectrochemical
PVD	: Physical vapor deposition
RS	: Raman spectroscopy
TMCs	: Transition metal chalcogenides
VB	: Valence band

LIST OF FIGURES

Figure 1.1. Hydrogen production pathways	5
Figure 1.2. Scheme of H ₂ production by steam reforming, water-gas shift and H ₂ separation.....	7
Figure 1.3. The characteristics of basic technologies for water electrolysis	11
Figure 1.4. a) Schematic representation of main steps in photocatalytic water splitting process, b) Band structure diagram of a semiconductor.....	13
Figure 1.5. Illustration of a) n-type and b) p-type semiconductor.....	14
Figure 1.6. Energy band diagrams of n-type semiconductor and metal contacts.....	16
Figure 1.7. A scale to convert potentials between different reference electrodes.....	17
Figure 1.8. A schematical illustration of a photoelectrochemical cell.....	18
Figure 1.9. Examples of PEC configuration systems. a) open beaker with a Luggin capillary tube for the RE, b) three-port Teflon cell, c) three-port glass cell, d) robotic probe for combinatorial analysis.....	19
Figure 1.10. Three different configurations for PEC water splitting systems under illumination a) single photoanode (n-type semiconductor, b) single photocathode (p-type semiconductor), c) photoanode and photocathode tandem system.....	21
Figure 1.11. The bandgap and band edge values for the most common semiconductors with respect to the NHE and vacuum level.....	22
Figure 1.12. Schematics of the graphene, graphene oxide, reduced graphene oxide structure.....	26
Figure 1.13. A schematical illustration of physical vapor deposition technique.....	27
Figure 1.14. A schematical illustration of chemical vapor deposition technique.....	28
Figure 1.15. A schematical illustration of chemical bath deposition technique.....	30
Figure 1.16. A schematical illustration of spin coating technique.....	30
Figure 1.17. A general representation of dip coating technique.....	31
Figure 1.18. A general representation of electrodeposition technique.....	33
Figure 1.19. Potential vs. time curve of an n-type semiconductor under light switch on-	

off conditions.....	34
Figure 1.20. Voltage-time dependence in LSV.....	35
Figure 1.21. a) LSV and b) CA curves of an n-type photoelectrode under light switch on-off conditions.....	36
Figure 1.22. Nyquist (a) and Bode (b) plots.....	37
Figure 1.23. M-S curves of n-type photoelectrode samples.....	38
Figure 1.24. The components of a scanning electron microscope.....	39
Figure 1.25. Schematic representation of Bragg’s diffraction.....	41
Figure 1.26. Energy transitions in Raman spectroscopy.....	42
Figure 1.27. A schematical illustration of a UV-vis spectrophotometer.....	43
Figure 2.1. a) Solvothermal synthesis of GO, b) Resulting product (GO mixture) of solvothermal synthesis.....	50
Figure 2.2. Synthesis, photoelectrode preparation, and photocatalytic-photoelectrochemical measurements pathway.....	52
Figure 2.3. a) A photoelectrode ready-to-be tested (left) and b) a three-electrode set-up (right) for photoelectrochemical analyses.....	56
Figure 3.1. SEM images of RGO-Cd _{0.60} Zn _{0.40} S-Pt at a) 5000, b) 25000 and c) 50000 magnifications.....	57
Figure 3.2. a) XRD pattern of RGO-Cd _{0.60} Zn _{0.40} S-Pt, b) EDS spectrum of RGO-Cd _{0.60} Zn _{0.40} S-Pt.....	58
Figure 3.3. Raman spectra of ITO/RGO-Cd _{0.60} Zn _{0.40} S-Pt photoelectrode.....	59
Figure 3.4. a) UV-vis DRS and b) Tauc plots of RGO-Cd _{0.60} Zn _{0.40} S and RGO-Cd _{0.60} Zn _{0.40} S-Pt.....	60
Figure 3.5. a) Open circuit potential (OCP), b) Linear sweep voltammetry (LSV), c) Chronoamperometric (I-t), d) Mott-Schottky (M-S) curves of RGO-Cd _{0.60} Zn _{0.40} S-Pt photoelectrode.....	61
Figure 3.6. ABPE plot of RGO-Cd _{0.60} Zn _{0.40} S-Pt photoelectrode.....	63
Figure 3.7. rCV curves for the fabrication of a) CdS, b) ZnS, c) Cd _{0.8} Zn _{0.2} S thin films	

in the aqueous solution consisting of $\text{Cd}(\text{CH}_3\text{COO})_2 \cdot 2\text{H}_2\text{O}$, $\text{Zn}(\text{CH}_3\text{COO})_2 \cdot 2\text{H}_2\text{O}$ and $\text{Na}_2\text{S}_2\text{O}_3$ mixture at 100 mV s^{-1} scan rate.....	64
Figure 3.8. rCV responses of ITO electrode recorded during the fabrication of RGO(0.25)- $\text{Cd}_{0.8}\text{Zn}_{0.2}\text{S}$ thin film in the electrolyte consisting of RGO, $\text{Cd}(\text{CH}_3\text{COO})_2 \cdot 2\text{H}_2\text{O}$, $\text{Zn}(\text{CH}_3\text{COO})_2 \cdot 2\text{H}_2\text{O}$ and $\text{Na}_2\text{S}_2\text{O}_3$ mixture at 100 mVs^{-1} scan rate.....	66
Figure 3.9. Raman spectrum of GO.....	67
Figure 3.10. Raman spectra of a) as-synthesized $\text{Cd}_x\text{Zn}_{1-x}\text{S}$ ($x = 0.0, 0.2, 0.5, 0.8, 1.0$), b) annealed $\text{Cd}_{0.8}\text{Zn}_{0.2}\text{S}$ and c) RGO(0.25)- $\text{Cd}_{0.8}\text{Zn}_{0.2}\text{S}$ thin films.....	68
Figure 3.11. SEM images of RGO (0.25)- $\text{Cd}_{0.8}\text{Zn}_{0.2}\text{S}$ at a) low and b) high magnification. c) XRD pattern of RGO(0.25)- $\text{Cd}_{0.8}\text{Zn}_{0.2}\text{S}$ thin film. d) UV-vis DRS and T_{auc} plots of $\text{Cd}_{0.8}\text{Zn}_{0.2}\text{S}$ and RGO(0.25)- $\text{Cd}_{0.8}\text{Zn}_{0.2}\text{S}$ thin films annealed at 450°C	69
Figure 3.12. EDS spectrum of RGO(0.25)- $\text{Cd}_{0.8}\text{Zn}_{0.2}\text{S}$ thin film annealed at 450°C	70
Figure 3.13. Open circuit potential (OCP) curves of a) as-synthesized $\text{Cd}_x\text{Zn}_{1-x}\text{S}$ ($x=0.0, 0.2, 0.5, 0.8, 1.0$) photoelectrodes, b) $\text{Cd}_{0.8}\text{Zn}_{0.2}\text{S}$ photoelectrodes annealed at 350°C and 450°C , c) RGO(0.10, 0.25, 0.50)- $\text{Cd}_{0.8}\text{Zn}_{0.2}\text{S}$ photoelectrodes annealed at 450°C	72
Figure 3.14. Linear sweep voltammetry (LSV) curves of a) as-synthesized $\text{Cd}_x\text{Zn}_{1-x}\text{S}$ ($x=0.0, 0.2, 0.5, 0.8, 1.0$) photoelectrodes, b) $\text{Cd}_{0.8}\text{Zn}_{0.2}\text{S}$ photoelectrodes annealed at 350°C and 450°C , c) RGO(0.10, 0.25, 0.50)- $\text{Cd}_{0.8}\text{Zn}_{0.2}\text{S}$ photoelectrodes annealed at 450°C	74
Figure 3.15. Chronoamperometric I-t curves of a) as-synthesized $\text{Cd}_x\text{Zn}_{1-x}\text{S}$ ($x=0.0, 0.2, 0.5, 0.8, 1.0$) photoelectrodes, b) $\text{Cd}_{0.8}\text{Zn}_{0.2}\text{S}$ photoelectrodes annealed at 350°C and 450°C , c) RGO(0.10, 0.25, 0.50)- $\text{Cd}_{0.8}\text{Zn}_{0.2}\text{S}$ photoelectrodes annealed at 450°C . Applied bias is 0 V vs Ag/AgCl	75
Figure 3.16. a) Nyquist plots of $\text{Cd}_{0.8}\text{Zn}_{0.2}\text{S}$ and RGO(0.25)- $\text{Cd}_{0.8}\text{Zn}_{0.2}\text{S}$ photoelectrodes annealed at 450°C . (Frequency range: 10^{-2} - 10^5 Hz). b) Equivalent circuit model used for EIS data fitting.....	78

Figure 3.17. M-S plot of ITO/RGO(0.25)- Cd _{0.8} Zn _{0.2} S photoelectrode annealed at 450°C.....	80
Figure 3.18. Band diagram of ITO/RGO(0.25)-Cd _{0.8} Zn _{0.2} S electrode in PEC hydrogen evolution system.....	81
Figure 3.19. rCVs of a) Cd _{0.8} Zn _{0.2} S, b) Cd _{0.8} Zn _{0.2} S, c) Cd _{0.8} Zn _{0.2} S _{0.2} Se _{0.8} thin film construction.....	83
Figure 3.20. rCV curve for the fabrication of RGO-Cd _{0.8} Zn _{0.2} S _{0.2} Se _{0.8}	84
Figure 3.21. Raman spectra of a) Cd _{0.8} Zn _{0.2} S _{0.2} Se _{0.8} , b) RGO-Cd _{0.8} Zn _{0.2} S _{0.2} Se _{0.8} thin films.....	85
Figure 3.22. FESEM images of Cd _{0.8} Zn _{0.2} S _{0.2} Se _{0.8} and RGO-Cd _{0.8} Zn _{0.2} S _{0.2} Se _{0.8} thin films at a) low (x5000) and b) high (x50000) magnifications.....	86
Figure 3.23. EDS spectrum of RGO(0.25)-Cd _{0.8} Zn _{0.2} S _{0.2} Se _{0.8} photoelectrode.	86
Figure 3.24. X-ray photoelectron spectroscopy (XPS) spectra of Cd _{0.8} Zn _{0.2} S _{0.2} Se _{0.8} . a) Cd 3d, b) Zn 2p, c) S 2p, d) Se 3d, e) Survey.....	87
Figure 3.25. X-ray photoelectron spectroscopy (XPS) spectra of RGO-Cd _{0.8} Zn _{0.2} S _{0.2} Se _{0.8} . a) Cd 3d, b) Zn 2p, c) S 2p, d) Se 3d, e) C 1s, f) O 1s, g) Survey....	88
Figure 3.26. XRD patterns of Cd _{0.8} Zn _{0.2} Se, Cd _{0.8} Zn _{0.2} S _{0.2} Se _{0.8} , RGO- Cd _{0.8} Zn _{0.2} S _{0.2} Se _{0.8} thin films.....	89
Figure 3.27. UV-vis DRS (inset) and Tauc plots of Cd _{0.8} Zn _{0.2} S, Cd _{0.8} Zn _{0.2} Se, Cd _{0.8} Zn _{0.2} S _{0.2} Se _{0.8} and RGO- Cd _{0.8} Zn _{0.2} S _{0.2} Se _{0.8} thin films.....	90
Figure 3.28. LSV curves of a) Cd _{0.8} Zn _{0.2} S _x Se _{1-x} (x=0.0, 0.2, 0.5, 0.8, 1.0) and b) RGO(0.10, 0.25, 0.50)- Cd _{0.8} Zn _{0.2} S _{0.2} Se _{0.8} photoelectrodes.....	92
Figure 3.29. Chronoamperometric I-t curves of a) Cd _{0.8} Zn _{0.2} S _x Se _{1-x} (x=0.0, 0.2, 0.5, 0.8, 1.0) and b) RGO(0.10, 0.25, 0.50)-Cd _{0.8} Zn _{0.2} S _{0.2} Se _{0.8} photoelectrodes.....	93
Figure 3.30. Nyquist plots of a) Cd _{0.8} Zn _{0.2} S, Cd _{0.8} Zn _{0.2} Se, Cd _{0.8} Zn _{0.2} S _{0.2} Se _{0.8} , RGO(0.25)-Cd _{0.8} Zn _{0.2} S _{0.2} Se _{0.8} and b) Equivalent circuit model used for EIS data fitting.....	96
Figure 3.31. M-S plots of Cd _{0.8} Zn _{0.2} S, Cd _{0.8} Zn _{0.2} Se, Cd _{0.8} Zn _{0.2} S _{0.2} Se _{0.8} , and RGO-	

Cd _{0.8} Zn _{0.2} S _{0.2} Se _{0.8} photoelectrodes.....	98
Figure 3.32. ABPE values for Cd _{0.8} Zn _{0.2} S _{0.2} Se _{0.8} and RGO(0.25)-Cd _{0.8} Zn _{0.2} S _{0.2} Se _{0.8} photoelectrodes.....	98
Figure 3.33. Band diagram of RGO-Cd _{0.8} Zn _{0.2} S _{0.2} Se _{0.8} photoelectrode in PEC hydrogen production system.....	99
Figure 3.34. CV curves for the fabrication of CdS, CdSe, ZnS, ZnSe, CuS, CuSe, MoS, MoSe thin films.....	101
Figure 3.35. CV curves for the fabrication of a) Cd _{0.6} Zn _{0.2} Mo _{0.2} S _{0.2} Se _{0.8} , b) Cd _{0.6} Zn _{0.2} Cu _{0.2} S _{0.2} Se _{0.8} , c) Cd _{0.6} Zn _{0.2} Ni _{0.2} S _{0.2} Se _{0.8} and d) RGO-Cd _{0.6} Zn _{0.2} Ni _{0.2} S _{0.2} Se _{0.8} thin films.....	102
Figure 3.36. Raman spectra of Cd _{0.6} Zn _{0.2} Mo _{0.2} S _{0.2} Se _{0.8} , Cd _{0.6} Zn _{0.2} Cu _{0.2} S _{0.2} Se _{0.8} , Cd _{0.6} Zn _{0.2} Ni _{0.2} S _{0.2} Se _{0.8} and RGO-Cd _{0.6} Zn _{0.2} Ni _{0.2} S _{0.2} Se _{0.8} photoelectrodes.....	103
Figure 3.37. FESEM images of the fabricated photoelectrodes at magnification of 200000x. a) Cd _{0.6} Zn _{0.2} Ni _{0.2} S _{0.2} Se _{0.8} , b) RGO-Cd _{0.6} Zn _{0.2} Ni _{0.2} S _{0.2} Se _{0.8}	104
Figure 3.38. FESEM images of the prepared structures on ITO substrate at magnification of 5000x a) Cd _{0.6} Zn _{0.2} Mo _{0.2} S _{0.2} Se _{0.8} b) Cd _{0.6} Zn _{0.2} Cu _{0.2} S _{0.2} Se _{0.8} c) Cd _{0.6} Zn _{0.2} Ni _{0.2} S _{0.2} Se _{0.8} , d) RGO-Cd _{0.6} Zn _{0.2} Ni _{0.2} S _{0.2} Se _{0.8}	105
Figure 3.39. X-ray photoelectron spectroscopy (XPS) spectra of Cd _{0.6} Zn _{0.2} Ni _{0.2} S _{0.2} Se _{0.8} . a) Cd 3d, b) Zn 2p, c) Ni 2p, d) S 2p, e) Se 3d, f) Survey.....	106
Figure 3.40. X-ray photoelectron spectroscopy (XPS) spectra of RGO-Cd _{0.6} Zn _{0.2} Ni _{0.2} S _{0.2} Se _{0.8} . a) Cd 3d, b) Zn 2p, c) Ni 2p, d) S 2p, e) Se 3d, f) C 1s, g) O 1s, h) Survey.....	107
Figure 3.41. XRD patterns of Cd _{0.6} Zn _{0.2} Mo _{0.2} S _{0.2} Se _{0.8} , Cd _{0.6} Zn _{0.2} Cu _{0.2} S _{0.2} Se _{0.8} , Cd _{0.6} Zn _{0.2} Ni _{0.2} S _{0.2} Se _{0.8} and RGO-Cd _{0.6} Zn _{0.2} Ni _{0.2} S _{0.2} Se _{0.8} thin films.....	108
Figure 3.42. UV-vis DRS (inset) and Tauc plots of RGO-Cd _{0.6} Zn _{0.2} Ni _{0.2} S _{0.2} Se _{0.8} and Cd _{0.6} Zn _{0.2} Ni _{0.2} S _{0.2} Se _{0.8} thin films.....	109
Figure 3.43. LSV curves of Cd _{0.6} Zn _{0.2} Mo _{0.2} S _{0.2} Se _{0.8} , Cd _{0.6} Zn _{0.2} Cu _{0.2} S _{0.2} Se _{0.8} , Cd _{0.6} Zn _{0.2} Ni _{0.2} S _{0.2} Se _{0.8} and RGO-Cd _{0.6} Zn _{0.2} Ni _{0.2} S _{0.2} Se _{0.8} photoelectrodes.....	109

Figure 3.44. Chronoamperometric (CA) curves of $\text{Cd}_{0.6}\text{Zn}_{0.2}\text{Mo}_{0.2}\text{S}_{0.2}\text{Se}_{0.8}$, $\text{Cd}_{0.6}\text{Zn}_{0.2}\text{Cu}_{0.2}\text{S}_{0.2}\text{Se}_{0.8}$, $\text{Cd}_{0.6}\text{Zn}_{0.2}\text{Ni}_{0.2}\text{S}_{0.2}\text{Se}_{0.8}$ and RGO- $\text{Cd}_{0.6}\text{Zn}_{0.2}\text{Ni}_{0.2}\text{S}_{0.2}\text{Se}_{0.8}$ photoelectrodes.....	110
Figure 3.45. a) Nyquist plots and fitted curves of $\text{Cd}_{0.6}\text{Zn}_{0.2}\text{Mo}_{0.2}\text{S}_{0.2}\text{Se}_{0.8}$, $\text{Cd}_{0.6}\text{Zn}_{0.2}\text{Cu}_{0.2}\text{S}_{0.2}\text{Se}_{0.8}$, $\text{Cd}_{0.6}\text{Zn}_{0.2}\text{Ni}_{0.2}\text{S}_{0.2}\text{Se}_{0.8}$ and RGO- $\text{Cd}_{0.6}\text{Zn}_{0.2}\text{Ni}_{0.2}\text{S}_{0.2}\text{Se}_{0.8}$ photoelectrodes. b) Equivalent circuit model used for EIS data fitting.....	112
Figure 3.46. M-S plots for RGO- $\text{Cd}_{0.6}\text{Zn}_{0.2}\text{Ni}_{0.2}\text{S}_{0.2}\text{Se}_{0.8}$, $\text{Cd}_{0.6}\text{Zn}_{0.2}\text{Ni}_{0.2}\text{S}_{0.2}\text{Se}_{0.8}$, $\text{Cd}_{0.6}\text{Zn}_{0.2}\text{Cu}_{0.2}\text{S}_{0.2}\text{Se}_{0.8}$ and $\text{Cd}_{0.6}\text{Zn}_{0.2}\text{Mo}_{0.2}\text{S}_{0.2}\text{Se}_{0.8}$ photoelectrodes.....	113
Figure 3.47. Band diagram of RGO- $\text{Cd}_{0.6}\text{Zn}_{0.2}\text{Ni}_{0.2}\text{S}_{0.2}\text{Se}_{0.8}$ photoelectrode in PEC hydrogen production system.....	115
Figure 3.48. ABPE values for $\text{Cd}_{0.6}\text{Zn}_{0.2}\text{Ni}_{0.2}\text{S}_{0.2}\text{Se}_{0.8}$ and RGO- $\text{Cd}_{0.6}\text{Zn}_{0.2}\text{Ni}_{0.2}\text{S}_{0.2}\text{Se}_{0.8}$ photoelectrodes.....	115

LIST OF TABLES

Table 1.1. The roles of hydrogen during the energy transition to eliminate the impacts of global warming.....	4
Table 3.1. A representative summary of the performance of Cd, Zn, S, RGO bearing photoelectrodes stated in the literature.....	77
Table 3.2. Fitting results for EIS of $\text{Cd}_{0.8}\text{Zn}_{0.2}\text{S}$ and RGO(0.25)- $\text{Cd}_{0.8}\text{Zn}_{0.2}\text{S}$ photoelectrodes annealed at 450°C	79
Table 3.3. A representative summary of the performance of Cd, Zn, S, Se, RGO bearing photoelectrodes reported in literature.....	94
Table 3.4. Fitting results for EIS of RGO(0.25)- $\text{Cd}_{0.8}\text{Zn}_{0.2}\text{S}_{0.2}\text{Se}_{0.8}$, $\text{Cd}_{0.8}\text{Zn}_{0.2}\text{S}_{0.2}\text{Se}_{0.8}$, $\text{Cd}_{0.8}\text{Zn}_{0.2}\text{Se}$ and $\text{Cd}_{0.8}\text{Zn}_{0.2}\text{S}$ photoelectrodes.....	95
Table 3.5. M-S parameters for RGO(0.25)- $\text{Cd}_{0.8}\text{Zn}_{0.2}\text{S}_{0.2}\text{Se}_{0.8}$, $\text{Cd}_{0.8}\text{Zn}_{0.2}\text{S}_{0.2}\text{Se}_{0.8}$, $\text{Cd}_{0.8}\text{Zn}_{0.2}\text{Se}$ and $\text{Cd}_{0.8}\text{Zn}_{0.2}\text{S}$ photoelectrodes.....	97
Table 3.6. Literature survey on related photoelectrodes.....	111
Table 3.7. Fitting results for EIS of $\text{Cd}_{0.6}\text{Zn}_{0.2}\text{Mo}_{0.2}\text{S}_{0.2}\text{Se}_{0.8}$, $\text{Cd}_{0.6}\text{Zn}_{0.2}\text{Cu}_{0.2}\text{S}_{0.2}\text{Se}_{0.8}$, $\text{Cd}_{0.6}\text{Zn}_{0.2}\text{Ni}_{0.2}\text{S}_{0.2}\text{Se}_{0.8}$ and RGO- $\text{Cd}_{0.6}\text{Zn}_{0.2}\text{Ni}_{0.2}\text{S}_{0.2}\text{Se}_{0.8}$ photoelectrodes.....	113
Table 3.8. M-S parameters for RGO- $\text{Cd}_{0.6}\text{Zn}_{0.2}\text{Ni}_{0.2}\text{S}_{0.2}\text{Se}_{0.8}$, $\text{Cd}_{0.6}\text{Zn}_{0.2}\text{Ni}_{0.2}\text{S}_{0.2}\text{Se}_{0.8}$, $\text{Cd}_{0.6}\text{Zn}_{0.2}\text{Cu}_{0.2}\text{S}_{0.2}\text{Se}_{0.8}$ and $\text{Cd}_{0.6}\text{Zn}_{0.2}\text{Mo}_{0.2}\text{S}_{0.2}\text{Se}_{0.8}$ photoelectrodes.....	114

1. INTRODUCTION

The role of energy is undeniable for economic growth, social development, and improved life quality of humankind. The need to access cheap and abundant energy resources with least hazardous environmental impact has been rapidly increasing with the pronounced energy consumption at a rate of 1 percent and 5 percent each year in rich and emerging countries, respectively [1, 2]. Among all energy resources, the world is still heavily dependent on fossil fuels to keep its wheel of economy running [3]. However, energy generation utilizing fossil fuels has been addressed with various grave issues like air pollution and global warming. The consequences of these issues cause many health and ecological problems by affecting social life and economy as well [4]. Thus, in a world which is in necessity of huge amount of energy due to the acceleration of human activity, and facing the harsh conditions resulting from the backdrop of increasing energy consumption, it is extremely important to come up with alternative energy sources to grow the economy without causing any harm to the environment and health of living organisms. With the aim of this, developed countries are engaged in the investigations to find innovative ways to harness renewable energy sources like solar, geothermal, tidal, hydroelectric, and wind power [5]. Some of many advantages of renewable energy over fossil fuels are i) Energy from renewable sources are sustainable, since it is produced from non-biomass sources that emit little or no carbon dioxide gas to the atmosphere, ii) It provides opportunities to create jobs, especially in rural areas and contributes to the growth of economy as well as diversify energy sources, which in turn, increases a country's energy dependence and security [6]. Nevertheless, transitioning towards 100% renewable energy has some drawbacks because of the intermittent nature of these resources. To fully adapt this to existing plants, technical adaptation is required, specifically in relation to creating balance between varying demands and supplies for energy. The rise of the integrating renewable energy with the existing energy systems requires large-scale energy storage operation systems [7]. Even though renewable energy has some limitations on

practical applications, governments of numerous countries are ambitious to take actions to implement required technologies to benefit from the use of renewable energy. In this regard, an increasing number of states along with The United Nations Framework Convention on Climate Change (UNFCCC), have agreed on pursuing efforts to combat climate change by signing 2015 Paris Agreement. It's been agreed that by 2023, renewables will account for 12.4% of total energy consumption, with a 5-year growth rate of that proportion rising to 12.4 percent. In addition, about 30% of global power demand is anticipated to be met through renewables, and 70% of global growth in electricity generation is expected to be supplied by utilizing renewable energy, which is estimated to be the leading energy technology of the electricity field by 2023 [8, 9].

1.1. Types of Energy and Energy Sources

Types of energy fall into two broad categories: Kinetic energy (the energy that moving objects possess) and potential energy (the energy that is stored). Kinetic energy and potential energy are subdivided into five (mechanical, thermal, sound, electrical, radiant) and four (chemical, nuclear, gravitational, elastic) energy forms, respectively.

Energy sources can be classified into primary and secondary energy sources. The primary energy source is attainable from natural sources and available for direct use. Common examples of fossil fuel sources are coal and crude oil, nuclear fuels, biomass as well as renewable energy resources. Secondary source of energy –energy carrier- is generated through conversion of primary source in usable form and it is used to store, move and deliver energy. The conversion of primary source requires considerable amounts of scientific and technical inputs and enormous infrastructure. Some examples of secondary sources of energy can be given as electricity, natural gas, gasoline, hydrogen etc. [10, 11]. The names “renewable” and “non-renewable” energy take their names from the properties of their corresponding energy sources to

have the ability to naturally replenish on a human timescale or not. In this regard, the most popular renewable energy sources are wind, hydroelectric, solar, geothermal, ocean, biomass, and hydrogen, while non-renewable energy sources are associated with fossil fuels.

1.2. Hydrogen Energy

Exponential increase in population of the world and the desire of humankind to increase its life standards have resulted in a peak in energy demand since 1950. The worldwide consumption of energy is predicted to reach a climax in 2035, whereas the economy is envisioned to face tremendous depression starting from 2040. The problem of major reliance of economy on fossil fuels has been on the international agenda of countries because of their diminishing reserves and polluting characteristics. In the need of ascertaining security of energy supply, cutting down on hazardous emissions, enhancement of air quality, and creating of modern industrial and technology base, hydrogen comes out as a promising sustainable energy carrier due to the fact that hydrogen (H_2) is the most abundant (exceeding 90% of all atoms) and the lightest (molecular weight: 2.016 g/mol) element in the universe, and it is considered as potential cost-efficient clean fuel for the future economy [12]. Hydrogen has the maximum energy content (HHV:141.80 MJ/kg and LHV:119.96 MJ/kg) of conventional fuels per unit of weight. The basis of the hydrogen is the fusion from the Sun or stars, and the Sun is estimated to provide hydrogen by sustaining fusion reaction for another 5 billion years [13]. Even though there is abundance of hydrogen, development of infrastructure is necessary to be able to utilize it in the usable form. With this development, hydrogen has found various application areas in ammonia synthesis (~55%), refineries (~25%), methanol production (~10%), transport, buildings, and power generation (~10%) and the demand for hydrogen has been accelerated more than three folds since 1975 (18.2 Mt) [14, 15]. Nevertheless, there are numerous barriers for clean widespread use of hydrogen in today's world such as high cost of hydrogen production from low-carbon

energy, low availability of hydrogen infrastructure, and some regulations of governments. In contrary, the versatility of hydrogen and its high potential for decreasing emission levels are highly predicted to make hydrogen play an effective role in future of low carbon pathways through development of niche applications and cost reductions caused by improvement of renewable technology [16]. These roles of hydrogen during the energy transition to eliminate the impacts of global warming are given in Table 1.1. [17].

Table 1.1. The roles of hydrogen during the energy transition to eliminate the impacts of global warming [17].

Renewable energy integration	Decarbonization of energy systems
Flexible systems	Cleaner transportation
Amplified accessibility	Cleaner industrial processes
Enhanced resilience	Cleaner products for utilization
Multigenerational options	Renewable feedstock to all sectors
Decreased monopoly	Reduced environmental effect
Improved efficiency	Boosted sustainability

For future prospects, IEA estimates a rise exceeding 300 Gt (giga tonnes) of CO₂ emissions by 2050, which creates the need for energy system modification. The role and contribution of hydrogen is undeniable for this case. Moreover, the global hydrogen demand is projected to grow over 4% per year throughout the next five years mostly due to its increasing consumption for ammonia synthesis, crude oil refining, and methanol [13].

1.2.1. Hydrogen production pathways

As the most common element, hydrogen is present in the composition of many substances (fossil fuels, biomass, fresh and sea water etc.). To be able to generate hydrogen in an environmental friendly way, CO₂ emissions and other pollutants must go through some processes such as separation or sequestration when hydrogen is produced from fossil fuels [18]. Natural gas and coal, nuclear, biomass, and other renewable

sources can all be used to generate hydrogen [19]. Fossil fuels are currently the primary source of hydrogen generation. Figure 1.1 depicts the various methods in which hydrogen can be produced [20].

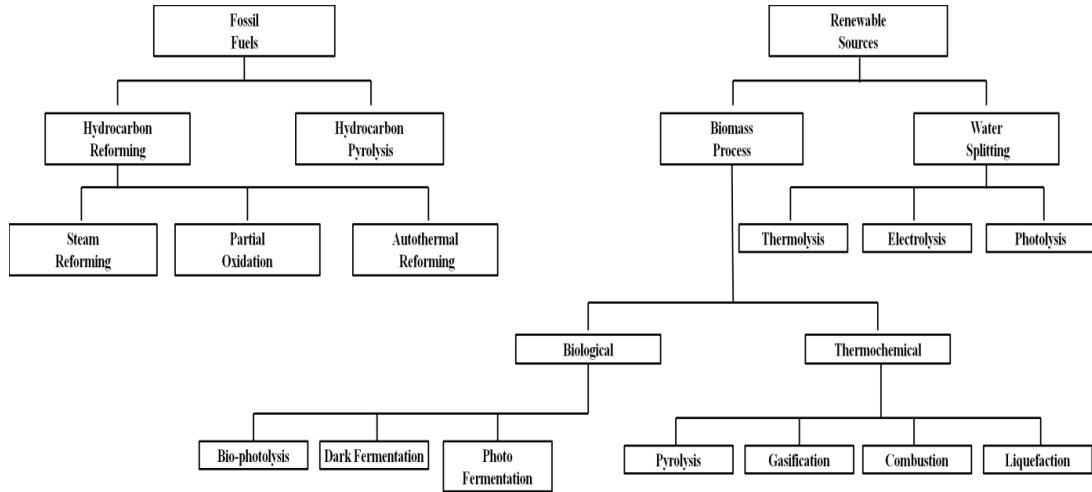


Figure 1.1. Hydrogen production pathways [20].

Figure 1.1. suggests that hydrogen production process is categorized into 2 main groups: Conventional technologies and renewable technologies. Conventional technologies group processes fossil fuels and it is subdivided into two main subgroups called pyrolysis hydrocarbon reforming. Hydrocarbon reforming includes three processes which are stream reforming, partial oxidation, and autothermal reforming. Hydrogen is generated through utilization of renewable sources such as biomass and water. Biomass based feedstocks are processed through biological (bio-photolysis, dark fermentation, photo fermentation) and thermochemical (pyrolysis, gasification, combustion, liquefaction) pathways. Water splitting establishes methods, namely, thermolysis, electrolysis, and photolysis for hydrogen production [20].

1.2.1.1. Hydrogen from fossil fuels

Fuel processing converts a material which consists of hydrogen, such as gasoline, ammonia, or methanol to a hydrogen rich stream [21]. Currently, hydrogen is mainly produced by using light hydrocarbons such as natural gas. Nevertheless, coal and petroleum coke could also be utilized for hydrogen production. It was reported that up

until now, methane, heavier hydrocarbons such as naphtha, and solid fuels such as coal had 48%, 30%, and 18% shares in the production of hydrogen, respectively [22]. The two general routes to generate hydrogen processing fossil fuels are hydrocarbon reforming and pyrolysis.

Hydrocarbon reforming

Hydrocarbon reforming, can be examined under three categories: Steam reforming, partial oxidation and autothermal reforming:

i) Steam Reforming: Today, steam reforming is the most widespread process for hydrogen production which involves a stage of syngas production from hydrocarbon fuels (1.1), water-gas shift reaction (1.2) and gas purification from impurities [23]:



Reaction 1.1 is highly endothermic, which means there is a necessity of high energy input to start the reaction. This initiation is achieved by combustion of additional amount of fuel.

The steam reforming reaction is reversible, and the output stream involves a mixture of CO and H₂. Since the output gas contains a high amount of CO, it is sent to water-gas shift reactor, where CO reacts with additional steam and is transformed into more hydrogen and CO₂ (Reaction 1.2) [24, 25].

Figure 1.2. displays a schematic representation of H₂ production by steam reforming, water-gas shift, and H₂ separation.

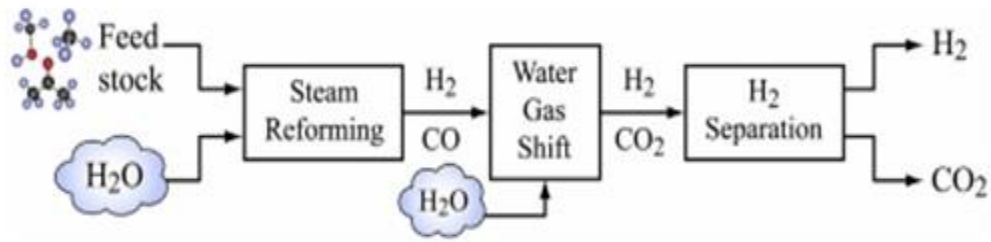
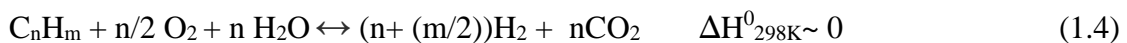


Figure 1.2. Scheme of H₂ production by steam reforming, water-gas shift and H₂ separation [25].

ii) Partial Oxidation: Partial oxidation is a type of chemical reaction in which the feedstock, such as methane or suitable hydrocarbonaceous fuel, reacts exothermically in the existence of a small amount of air. The resulting product is a mixture of gas containing mainly hydrogen and carbon monoxide because of the incomplete combustion as given in Reaction (1.3). The obvious advantage of partial oxidation is that the reaction is exothermic, but it has the least H₂ yield among fuel reforming processes [26]. Thus, partial oxidation is generally combined with steam reforming and more H₂ is produced at the end of the reaction [27].



iii) Autothermal Reforming: Combining exothermic and endothermic steam reforming, autothermal reforming achieves a nearly thermodynamic nature and increases the reaction's efficiency while also providing a high ratio of hydrogen to carbon [26]:



Hydrocarbon pyrolysis

Pyrolysis is a well-known way of hydrogen production, which expresses the decomposition of hydrogen-containing compounds such as hydrocarbons at elevated temperatures in an oxygen free atmosphere. Hydrogen solely yields as a product of the

following reaction:



The advantages of pyrolysis include the fact that toxic compounds are degraded by applying high temperatures in the reactor. However, it is an uneconomical technique and an air purification system is required to treat the exhaust gases [28].

1.2.1.2. Hydrogen from renewable sources

Hydrogen from biomass processes

The first step is providing economical and plentiful biomass feedstock such as plants, animal residuals, and urban wastes to be able to obtain hydrogen in a useful form from biomass processes [22]. Biomass processes can be investigated in two main categories, namely, biological processes and thermochemical processes.

i) Biological processes: Biohydrogen production has gained a lot of interest since 1980s. In former times, glucose was the only feedstock, yet today, starch, sucrose, cellulose and waste materials have important role in hydrogen production through biological processes. Among all biological processes, biophotolysis, dark fermentation and photo-fermentation are the most popular ones. Biophotolysis involves direct photolysis and indirect photolysis. In direct photolysis, solar energy is transformed into chemical energy with the aid of microalgae (green algae and Cyanobacteria). This photosynthetic reaction splits water molecules into hydrogen and oxygen ions followed by the conversion of hydrogen ions to hydrogen gas via the enzyme hydrogenase. Even though direct photolysis has a high theoretical efficiency (>80%), the genetic tendency of green algae to assemble in a large array of light absorbing chlorophyll antenna in their photosystems decreases its efficiency in practical usage.

Indirect biophotolysis is comprised of two steps: Photosynthesis (producing glucose from water and carbon dioxide) and conversion of glucose and water to H₂ and CO₂ by

light-induced process. The practical efficiency of this process quite low (1-2%). The disadvantages of this process is low efficiency and nonutilization of waste.

Dark fermentation is the fermentative conversion of organic substrates in the absence of light by anaerobic bacteria and some microalgae. This process yields mostly H₂ and CO₂ as well as trace amounts of CH₄ or H₂S, depending on the reaction process and substrate type. H₂ production will be at maximum rate when pH is kept at 5-6. The advantages of dark fermentation is no requirement for light and no dependence on weather conditions [29]. Dark fermentation has the highest hydrogen production rate, but it is complex because of various groups of bacteria used and series of reactions taking place.

Photo-fermentation is performed in existence of light and organic substrate is converted into H₂ and CO₂ by using photosynthetic bacteria [30]. Although this process has been studied for many years, overall low light conversion efficiencies, low volumetric rates of hydrogen production restrict its industrial application.

ii)Thermochemical processes: Thermochemical conversion processes of biomass holds some advantages over biological methods such as usability of wider range of feedstocks, giving higher overall efficiencies, and easier economical access. However, these processes have some drawbacks for commercialization. It involves four full paths, which are pyrolysis, gasification, combustion, and liquefaction. Pyrolysis is a mature technology for hydrogen production from biomass. It identifies the heat treatment (generally at around 200°C-760°C) of an organic or carbonaceous material to produce liquid-fuels, solid char and gaseous compounds. Pyrolysis types may differ in terms of the heating rate, operation temperature and residence time in a reactor. Another technology, gasification of biomass, is a well-established route to generate combustible gases (N₂, H₂, CO, CO₂, H₂O, CH₄) with a gasifying agent (air, pure oxygen, steam etc.). Gasification process takes place in four zones: Drying/preheating zone, pyrolysis/devolatilization zone, combustion zone, reduction/gasification zone. The operation temperature of gasification varies between 480°C-1600°C. Residual non-

volatile compounds are converted to syngas at high temperatures [31]. The third thermochemical process, combustion of biomass, simply states burning of biomass directly in the existence of excess air in a furnace/boiler. The efficiency from the process is low and this process is not preferential for H₂ formation because of high amounts of CO_x, NO_x, SO_x gases releasing into the atmosphere. Even though there are some advances in this technology, it has some limitations in the use, because fuel quality and consistency can vary significantly and it requires regular maintenance [32]. Liquefaction of biomass is explained in two processes, which are, hydrothermal liquefaction and direct liquefaction. In the presence of a catalyst, hydrothermal liquefaction converts biomass in an aqueous media at a temperature between 226°C and 362°C and a pressure between 5 and 20 MPa. To recover energy, hydrothermal liquefaction beats out pyrolysis since no prior treatment, like drying, is required. Hydrogen production is modest in this method. Temperature, pressure, catalyst loading, and biomass type are the most critical factors influencing hydrogen production [33].

Hydrogen from water splitting

Water is regarded as one of the planet's most abundant raw materials and H₂ production can be achieved via water-splitting processes such as thermolysis, electrolysis and photolysis. In thermolysis process, the temperature of water is increased (generally to 2500°C) so as water can decompose to H₂ and O₂. Utilization of solar, heat, or nuclear energy can be viable to provide high temperature. Apart from that, numerous thermochemical water splitting processes have been introduced to decrease the temperature and increase the overall efficiency. It is noteworthy that the parameters such as toxicity, cost, availability of chemicals, corrosion problems increases the economical concerns related to H₂ production [20].

In electrolysis process, when an direct electric current is passed through the system, the reactant, water, is dissociated to H₂ and O₂.



There are various electrolytes systems built for water electrolysis, which are alkaline water electrolysis (AWE), proton exchange membranes (PEMs), alkaline anion exchange membranes (AEMs), and solid oxide water electrolysis (SOE). In these systems, material selection and operation conditions are different, but the operating principles do not differ. Low temperature and high temperature can also be applied to different types of water electrolysis. Figure 1.3. summarizes the characteristics of basic technologies for water electrolysis [34].

	Low Temperature Electrolysis			High Temperature Electrolysis		
	Alkaline (OH ⁻) electrolysis	Proton Exchange (H ⁺) electrolysis		Oxygen ion(O ²⁻) electrolysis		
	Liquid	Polymer Electrolyte Membrane		Solid Oxide Electrolysis (SOE)		
	Conventional	Solid alkaline	H ⁺ - PEM	H ⁺ - SOE	O ²⁻ - SOE	Co-electrolysis
Operation principles						
Charge carrier	OH ⁻	OH ⁻	H ⁺	H ⁺	O ²⁻	O ²⁻
Temperature	20-80°C	20-200°C	20-200°C	500-1000°C	500-1000°C	750-900°C
Electrolyte	liquid	solid (polymeric)	solid (polymeric)	solid (ceramic)	solid (ceramic)	solid (ceramic)
Anodic Reaction (OER)	4OH ⁻ → 2H ₂ O + O ₂ + 4e ⁻	4OH ⁻ → 2H ₂ O + O ₂ + 4e ⁻	2H ₂ O → 4H ⁺ + O ₂ + 4e ⁻	2H ₂ O → 4H ⁺ + 4e ⁻ + O ₂	O ²⁻ → 1/2 O ₂ + 2e ⁻	O ²⁻ → 1/2 O ₂ + 2e ⁻
Anodes	Ni > Co > Fe (oxides) Perovskites: Ba _{0.5} Sr _{0.5} Co _{0.8} Fe _{0.2} O _{3-δ} , LaCoO ₃	Ni-based	IrO ₂ , RuO ₂ , Ir _x Ru _{1-x} O ₂ Supports: TiO ₂ , ITO, TiC	Perovskites with protonic-electronic conductivity	La ₂ Sr _{1-x} MnO ₃ + Y-Stabilized ZrO ₂ (LSM-YSZ)	La ₂ Sr _{1-x} MnO ₃ + Y-Stabilized ZrO ₂ (LSM-YSZ)
Cathodic Reaction (HER)	2H ₂ O + 4e ⁻ → 4OH ⁻ + 2H ₂	2H ₂ O + 4e ⁻ → 4OH ⁻ + 2H ₂	4H ⁺ + 4e ⁻ → 2H ₂	4H ⁺ + 4e ⁻ → 2H ₂	H ₂ O + 2e ⁻ → H ₂ + O ²⁻	H ₂ O + 2e ⁻ → H ₂ + O ²⁻ CO ₂ + 2e ⁻ → CO + O ²⁻
Cathodes	Ni alloys	Ni, Ni-Fe, NiFe ₂ O ₄	Pt/C MoS ₂	Ni-cermets	Ni-YSZ Subst. LaCrO ₃	Ni-YSZ perovskites
Efficiency	59-70%		65-82%	up to 100%	up to 100%	-
Applicability	commercial	laboratory scale	near-term commercialization	laboratory scale	demonstration	laboratory scale
Advantages	low capital cost, relatively stable, mature technology	combination of alkaline and H ⁺ -PEM electrolysis	compact design, fast response/start-up, high-purity H ₂	enhanced kinetics, thermodynamics: lower energy demands, low capital cost		+ direct production of syngas
Disadvantages	corrosive electrolyte, gas permeation, slow dynamics	low OH ⁻ conductivity in polymeric membranes	high cost polymeric membranes; acidic: noble metals	mechanically unstable electrodes (cracking), safety issues: improper sealing		
Challenges	Improve durability/reliability; and Oxygen Evolution	Improve electrolyte	Reduce noble-metal utilization	microstructural changes in the electrodes: delamination, blocking of TPBs, passivation		C deposition, microstructural change electrodes

Figure 1.3. The characteristics of basic technologies for water electrolysis [34].

Harnessing the power of the Sun to produce chemical energy such as hydrogen from water has been a captivating strategy in the last decades. Water splitting by photolysis enables the production of hydrogen by utilizing solar light and cleaving the bonds of water in the presence of a proper semiconductor by using two different pathways: Photocatalytic water splitting (PC) and photoelectrochemical water splitting (PEC).

In a general photocatalytic splitting process, photoreactor, photocatalyst, reactant, and light source are necessary to produce hydrogen gas. Here, the reactant can be water or an aqueous sacrificial reagent. The photocatalyst has to have the ability to work with UV or visible light. The efficiency of a photocatalyst mostly depends on its capability to harvest a significant portion of the sunlight. There are four major steps in photocatalytic water splitting processes:

- i) Harvesting solar light to provide energy to split water: Light with an energy level greater than or equal to the catalyst's band gap is used to irradiate the semiconductor. Typically, a semiconductor is a material which conducts current partly. A band gap energy (E_g) separates its valence band (VB) from its conduction band (CB).
- ii) Generation and separation of charge carriers: To get electrons to go from the VB to the CB of a semiconductor, you need to stimulate the photocatalyst. This process creates holes in the VB.
- iii) Transportation of electrons and holes (e^- - h^+) to the photocatalyst surface: Electron and hole pairs are transported to photocatalyst surface to perform redox reactions. Photoexcited holes are powerful oxidants capable of oxidizing many chemicals.
- iv) Redox reactions: Electrons and holes take place in reduction and oxidation reactions to produce hydrogen on the adsorbed species on the photocatalyst surface [35, 36]. Reactions (1.9), (1.10), (1.11), (1.12) show the reactions which take place during photocatalytic water splitting:



Equation (1.10) points out the existence of $\text{e}^{-}\text{-h}^{+}$ recombination due to the release of unproductive heat. This is a major problem in photocatalytic studies. Apart from that, back-oxidation reactions on noble metals and the rate limiting mass transfer events can be considered as some drawbacks for utilization of photocatalytic water splitting processes. However, many scientists have been working on and developing alternative strategies to increase the efficiency of photocatalysts in electrolytes and sacrificial reagents.

Figure 1.4.a. displays the schematic representation of major steps taking place in photocatalytic water splitting. The potentials at which redox reactions occur reside between CB and VB potentials. That means the lowest position of the CB has to be lower than the reduction position of $\text{H}_2\text{O}/\text{H}_2$, whereas the position of the VB should be higher than the potential of oxidation potential of $\text{H}_2\text{O}/\text{O}_2$ as shown in Figure 1.4.b.

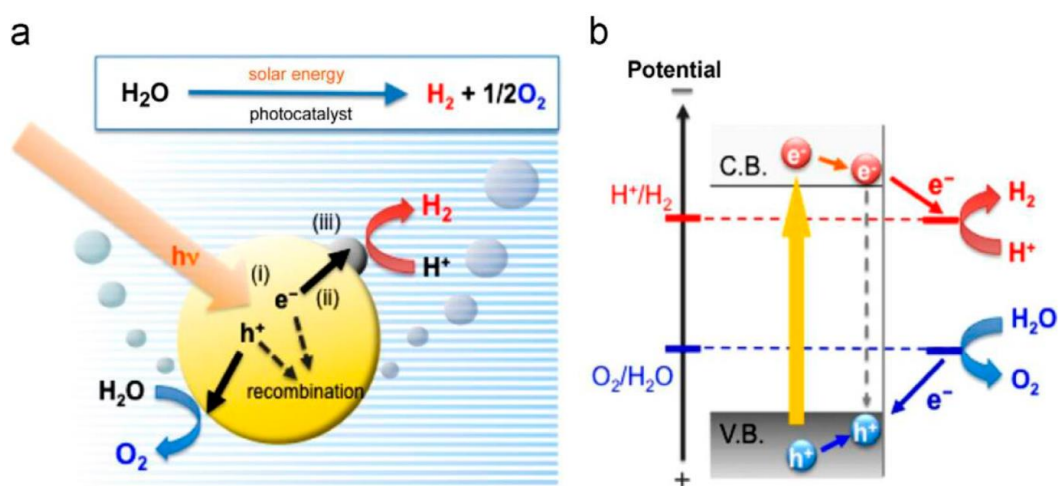


Figure 1.4. a) Schematic representation of main steps in photocatalytic water splitting process, b) Band structure diagram of a semiconductor [37].

1.3. Photoelectrochemical (PEC) Hydrogen Production Processes

The photoelectrochemistry process is characterized by the interaction between the electrochemical changes and applied light which causes electron excitation and charge transfer from a photoexcited material [38]. Before enlightening the mechanism of PEC processes, it is important to outline some terms briefly which are often included in PEC studies.

1.3.1. Semiconductor fundamentals

The atomic orbitals of solid state materials form broad energy bands unlike molecular systems, which are composed of discrete molecular orbitals. There are many permitted energy level bands, but of particular interest are the two uppermost bands which are separated by a forbidden energy gap, or band gap (E_g). These bands are named as the valence band (VB) and conduction band (CB). The VB is the highest range of energies in which electrons are filled at 0 K, while the CB is the lowest range of energies of empty states at 0 K. Fermi level, E_F , is yet another important term which is used in PEC studies. It is described as the energy at which the likelihood of finding an electron is 50% and generally lies at the center between VB and CB. There are different types of materials in terms of conductivity which are closely related to E_F and E_g . For metals, the position of the Fermi level is in the VB or the E_g overlaps. E_g values of semiconductors are between 1-3 eV, whereas these values are more than 4 eV for insulators.

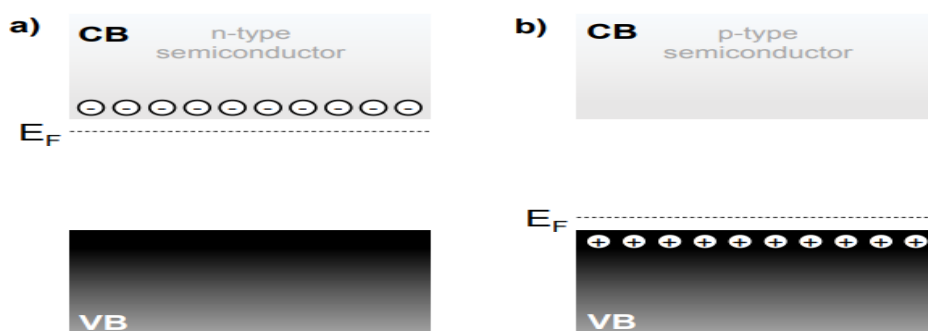


Figure 1.5. Illustration of **a)** n-type and **b)** p-type semiconductor [39].

It is possible to alter the Fermi level of a pristine (intrinsic) semiconductor by the adding impurities. On the other hand, in doped (extrinsic) semiconductors, chemical impurities introduce allowed energy states within the band gap. When the semiconductor is n-type, the energy states are located near the CB because of donor impurities. In a p-type semiconductor, acceptors create states near the VB [39].

Band bending: Mott and Schottky were first to propose the idea of band bending and analyze the rectifying effect when a metal is in contact with a semiconductor. Figure. 1.6. displays the ideal energy band diagrams of n-type semiconductor and metal contacts. In this situation, the difference in work functions between metal and semiconductor determines the flow direction of electrons. When the metal work function (Φ_m) is higher than the semiconductor work function (Φ_s), the direction of the electron transfer will be from the semiconductor to the metal. This flow will stop when the Fermi levels of metal ($E_{F,m}$) and semiconductor ($E_{F,s}$) are equalized. At the metal/semiconductor interface, where the metal is negatively charged and the semiconductor is positively charged near its surface, an equilibrium Helmholtz double layer forms. In this case, the low concentration of free charge carriers in the semiconductor avoids screening the electric field near its surface leading to depletion of free charge carrier concentration near the semiconductor surface in comparison with the bulk. This region is named the space charge region. In the n-type semiconductor, depletion of electrons occurs in the space charge region, which is called the depletion layer. The accumulation layer in the p-type semiconductor is named after the region in which electrons from the metal are transferred to the semiconductor and amassed in the space charge region.

The energy band edges of semiconductor can shift as a result of the electric field between the semiconductor and the metal because of charge transfer, which is called band bending. When $\Phi_m > \Phi_s$, the energy bands bend upward toward the interface, in contrary, when $\Phi_m < \Phi_s$ the edges bend downward toward the interface [40].

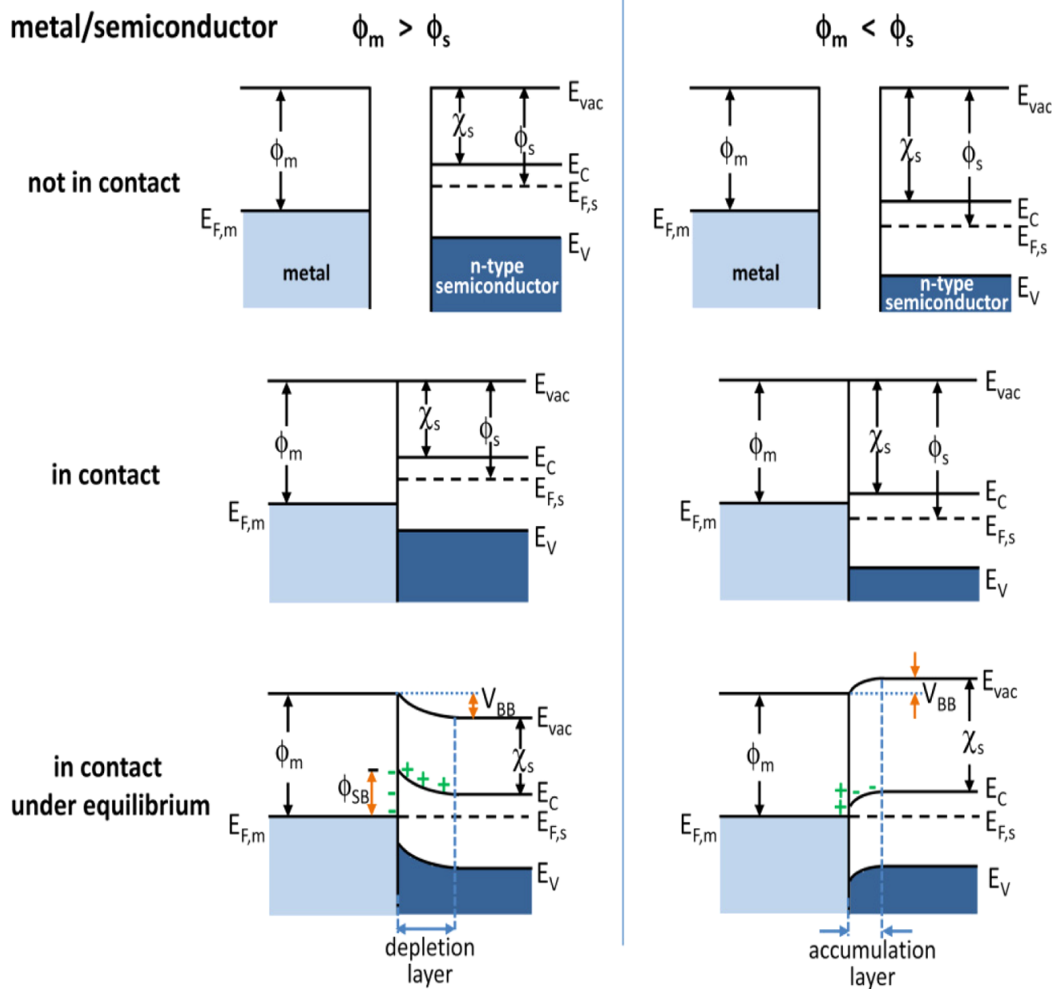


Figure 1.6. Energy band diagrams of n-type semiconductor and metal contacts. E_{vac} : vacuum energy; E_C : energy of conduction band minimum; E_V : energy of valence band maximum; Φ_m : metal work function; Φ_s : semiconductor work function; χ_s : electron affinity of semiconductor [40].

1.3.2. Photoelectrochemical (PEC) system fundamentals

Photoelectrochemical systems exhibit high potential in using a greater range of the solar spectrum considerably. In PEC processes, hydrogen is produced as a result of conversion of solar energy. For these reasons, this technique of hydrogen production is regarded as environmentally beneficial, renewable, and cost-effective. To set up a PEC cell to perform photoelectrochemical experiment, an n-type or p-type semiconductor-based photocatalyst is prepared on an electrode substrate (i.e. indium tin oxide (ITO)

glass, fluorine doped tin oxide (FTO) glass) to act as working electrode (WE) in the form of photoanode or photocathode. The other electrodes in a conventional three-electrode configuration system are counter electrode (CE) and reference electrode (RE). Working electrode is connected to the counter electrode through an external circuit to monitor the current between working and counter electrodes. The counter electrode is generally made of an inert material such as Pt, Au, glassy carbon, and graphite. The reference electrode has a constant and well-defined electrochemical potential and its potential remains stable during PEC studies. It is connected to the working electrode to serve as a steady potential supply to the working electrode. The standard hydrogen electrode (SHE) can be regarded as the basic reference element in PEC devices and it is composed of a 1.0 M $H^+(aq)$ solution involving platinum inside a tube. The value of standard electrode potential is zero. However, the practical usage of this reference electrode is rather hard due to the requirement of hydrogen gas [41]. The silver/silver chloride (Ag/AgCl), saturated calomel electrode (mercury/mercury(I) chloride)(SCE), copper/copper sulfate (Cu/CuSO₄), mercury/mercurous sulfate (Hg/Hg₂SO₄) reference electrodes are more often used in practical applications [42]. Figure 1.7. shows a simple scale to convert potentials between different reference electrodes. Another important element in a PEC process is the aqueous electrolyte in which the electrodes are immersed [43]. The photoelectrode material dictates the choice of electrolyte for PEC systems.

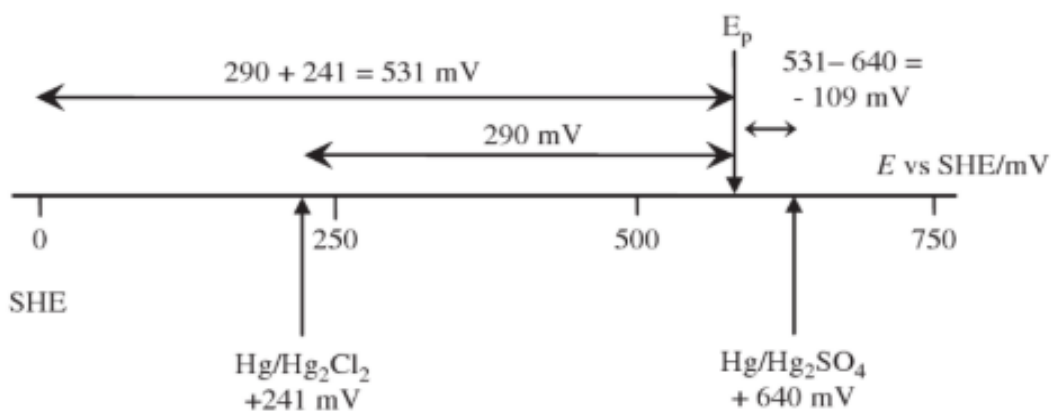


Figure 1.7. A scale to convert potentials between different reference electrodes [42].

Photoelectrochemical hydrogen production takes place in a photoelectrochemical cell which is schematically represented in Figure 1.8. Typically, at least one of the electrodes should be light sensitive. In a conventional photoelectrochemical cell, the working electrode is commonly an n or p type semiconductor, with a platinum (Pt) counter electrode. Under light irradiation, electron-hole pairs are generated on the working electrode (n type (photoanode) or p type (photocathode) semiconductor) when the light source supplies the light with an energy level that is equal or higher than the bandgap of the photoelectrode. Electrons are captured in the photoanode and transferred to the counter electrode when an n-type semiconductor is employed and finally they participate in the hydrogen evolution half reaction (HER). The photogenerated electrons reduce H^+ into H_2 at the counter electrode, and holes participate in oxidation of water into O_2 and H^+ at the photoanode surface, which states oxygen evolution half reaction (OER). When a p-type semiconductor is used as photocathode in PEC studies, photogenerated electrons are used to reduce H^+ into H_2 , whereas, water is oxidized into O_2 and H^+ in the counter electrode. Duration of charge transfer is determined by the equalization of redox potentials between the photoelectrode and electrolyte.

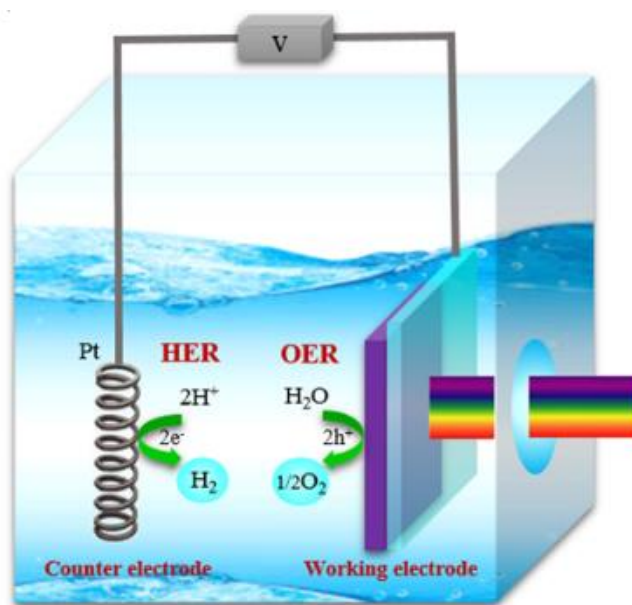


Figure 1.8. A schematical illustration of a photoelectrochemical cell. (In this example, an n-type semiconductor is given) [44].

There are many different approaches to perform two or three electrode configurations to perform PEC studies. Figure 1.9. shows some examples of photoelectrochemical setups which are compatible with reactor designs. In Figure 1.9a, the open cell configuration in which a film-covered WE is placed along the center of the container, close to the CE. A Luggin capillary is used as RE here. It is important to place RE to WE to limit the effect of electrolyte resistance. This setup can be also used in an open beaker. Figures 1.9b-c show three electrode system design, in which the systems consist of WE, RE, and CE. In these setups, the light enters from the side of the container. Figure 1.9d is the most advanced setup among all shown setups in the figure. The system involves a robotic probe head with CE, RE, a gas diffuser, and an optical fiber bundle which is separated from the electrolyte via a flat wall borosilicate tube [45].

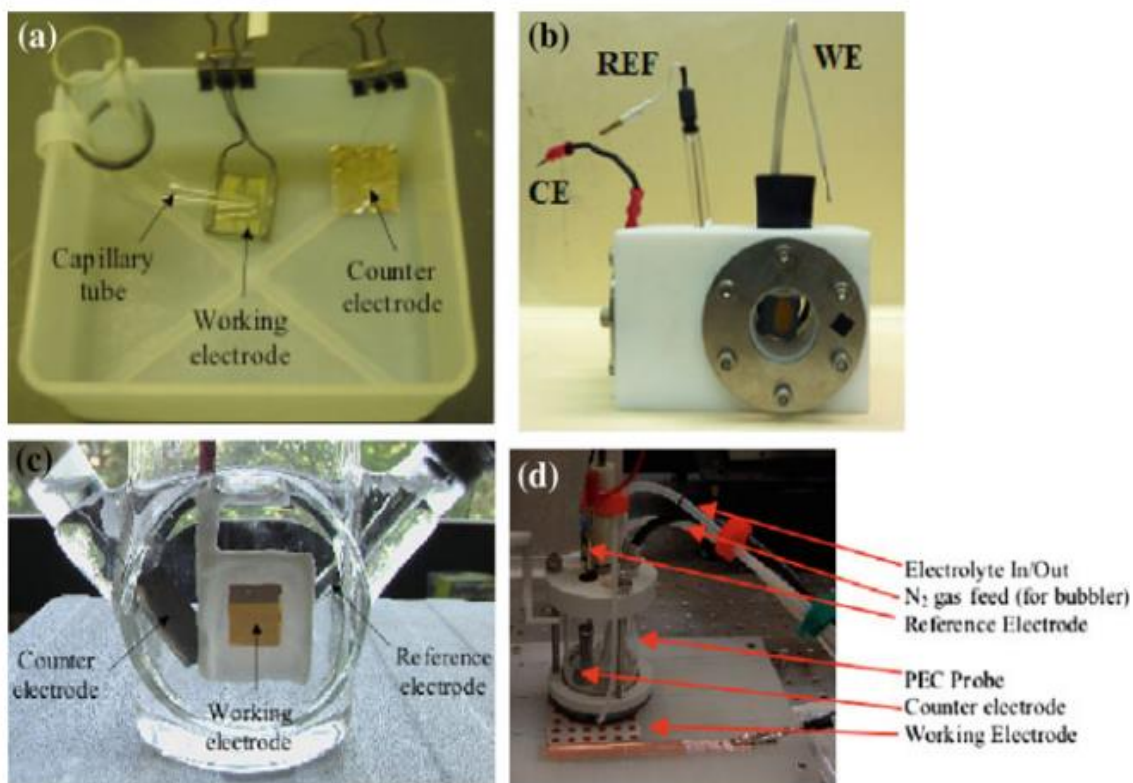


Figure 1.9. Examples of PEC configuration systems. a) open beaker with a Luggin capillary tube for the RE, b) three-port Teflon cell, c) three-port glass cell, d) robotic probe for combinatorial analysis [45].

The light source, the spectral distribution and the intensity of the sunlight are some of the most critical parameters to analyze PEC studies. The tilted angle of the sunlight reaching to the Earth's surface is dependent on the latitude and longitude of the region. Hence, it is important for scientists to adhere to spectral standards guidelines in the measurement and reporting their experiments. In accordance with this purpose, the sun illumination in a clear sky is taken as a reference. The air mass (AM) notation is often used to describe spectra since the route length of the Sun's surface through the atmosphere is the simplest parameter. The AM number stands for the amount of atmosphere traversed. It can be calculated by dividing 1 to the zenith angle of the sun, as shown below:

$$AM\# = 1/\cos\theta_{zenith} \quad (1.13)$$

Here, θ_{zenith} symbolizes the angle between the vector toward the Sun and the local vertical vector normal to the surface. The standard spectrum is decided as AM 1.5, since it represent the average annual AM value available at locations within the continental US. AM 1.5 corresponds to the light intensity of 1000 W/m² (100 mW/cm²) [45].

Photoelectrochemical hydrogen production is an uphill reaction meaning that energy input is necessary to initiate the reaction. The potential of 1.23 eV should be applied under normal operating conditions (25°C, 1 atm) [46, 47]. Thermodynamic oxidation and reduction potentials of oxygen and hydrogen are 1.23 eV and 0.0 eV, respectively.

There are three different configurations for photoelectrochemical hydrogen production systems, as shown in Figure 1.10. In Figure 1.10a and Figure 1.10b, the working electrodes are photoanode and photocathode, respectively. In Figure 1.10c, both photosensitive electrodes are photoanode and phocathode. This type of configuration is known as tandem system.

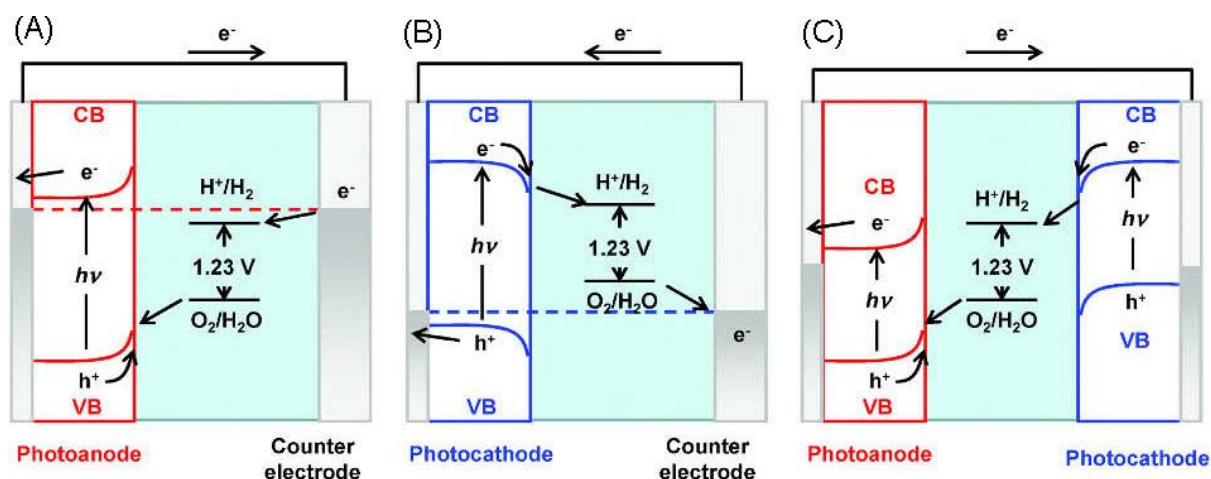


Figure 1.10. Three different configurations for PEC water splitting systems under illumination **a)** single photoanode (n-type semiconductor), **b)** single photocathode (p-type semiconductor), **c)** photoanode and photocathode tandem system [48].

1.3.3. Parameters affecting the photoelectrochemical hydrogen production

i) Material Selection: Selection of the most appropriate semiconductor photoelectrode material is the key component of PEC studies. The ideal photoelectrode should fulfill the requirements of efficient light absorption, fast charge separation and transport, high chemical stability in the aqueous medium, having band edge positions that straddle the reduction and oxidation potentials, and being economical. Up until now, there has been no semiconductor material found to meet these contradictory demands all at once. Hence, trade-offs need to be made to build composite electrodes in which different materials meet different functionalities.

The bandgap of a semiconductor material determines the spectral range of light a semiconductor can absorb. Hydrogen production in PEC requires a bandgap of 1.23 eV, plus thermodynamic losses (0.3-0.4 eV) and overpotentials at several points in order to obtain rapid reaction kinetics (0.4-0.6 eV). Thus, the bandgap needs to be at least 1.9 eV, which corresponds to the wavelength of 650 nm in spectral region. Again, it is known that below 400 nm the intensity of the sunlight decreases very quickly, imposing the upper limit bandgap of the semiconductor to be 3.1 eV.

Therefore, the optimum value of the band gap ranges between 1.9 eV and 3.1 eV, falling into the visible range of the solar spectrum [49]. Figure.1.11 represents the bandgaps and band edges of the most common semiconductors with respect to the vacuum level and NHE [50].

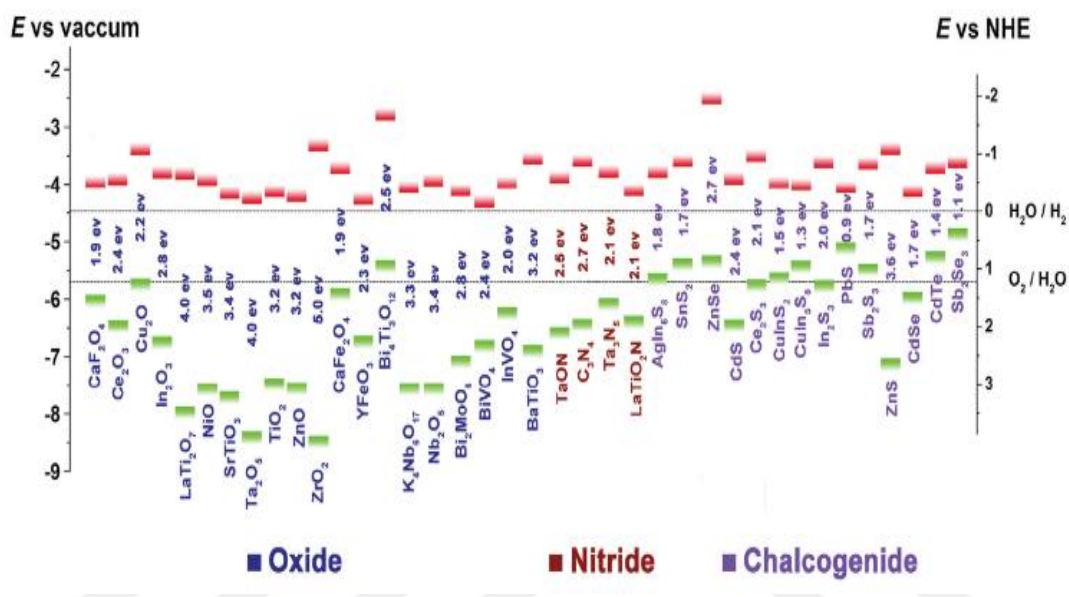


Figure 1.11. The bandgap and band edge values for the most common semiconductors with respect to the NHE and vacuum level. The horizontal red lines and green lines represent the conduction band edges and valence band edges, respectively. The dashed lines correspond to the water reduction and oxidation potentials [50].

The requirement of chemical stability directly influences the feasibility of the semiconductor. Most of the nonoxide semiconductors have the drawback of dissolving when immersed in an electrolyte. When compared to non-oxide semiconductors, oxide semiconductors are more stable in the electrolyte, but they are still susceptible to anodic or cathodic breakdown. Additionally, it is well-known that as the band gap widens, so does the stability against photocorrosion, but this fact is at odds with the efficient semiconductor electrode notion in terms of light absorption efficiency. Thus, required optimizations should be made and the most proper semiconductor needs to be chosen.

Another important issue to consider for material selection in a PEC system is the fast transportation of electron and holes. In contrary, electron and hole recombination is most likely to occur on the photoelectrode or in the space charge region. Especially if interfacial electron transfer is so slow that the concentration of minority carriers builds up at the interface and recombination is detected, which results in holes being lost before they can acquire electrons from solution species, electron and hole recombination is likely to occur either on the surface of the photoelectrode or in the space charge region [51]. The literature involves many reviews and research articles related to the minimization of recombination rate. For instance, it is well-established that the shape and structure of semiconductors play a vital role in recombination behavior of photoelectrodes. A lot of researches confirm that crystallinity is inversely proportional to the recombination rate, and dimensionality (0D: quantum dots, 1D: nanorod, nanowire, nanotube, 2D: thin films, nanosheets, 3D: dendritic α -Fe₂O₃) directly affects it as well. Nanostructuring increases light harvesting, transportation of electrons and holes, and kinetics. Nevertheless, it remarkably reduces power conversion efficiency and the durability of devices. In addition, surface energy and surface recombination are both increased due to a decrease in thermodynamic stability. On the other hand, it provides shorter carrier collection pathways and they decrease the duration of charge transfer and recombination rate. These nanostructures are employed to minimize the collection path of minority carriers and increase the volume ratio of the space charge layer to the photoelectrode bulk, which reduces bulk electron-hole recombination in photovoltaic cells.

Chemical/electrochemical corrosion is another important phenomenon to be scrutinized in PEC analyses. It principally occurs when using molecular components as linkers and non-oxide material modifiers. To avoid photocorrosion of the photoelectrodes, two methods must be used. The first step is to coat the photoelectrode surface with a protective layer, and the second step is to prevent photocorrosion by placing a catalyst on top of the layer of protection [52].

Temperature, pressure, and pH are strongly related to the PEC performance of semiconductors. Researchers have found out that working pressure enhances the band gap. Electrolyte pH conditions have a significant impact on the PEC reaction equilibrium, determining the net total charge adsorbable at the surface [53].

Up to date, there is no material to achieve and sustain 10% efficiency for solar-to-hydrogen (STH) energy conversion, which is usually considered as the minimum viable efficiency. To overcome the limitations of semiconductors, researchers have made many efforts using the state-of-the-art methods tactics to develop effective, stable, and cost-effective material system such as doping and heterostructuring [54]. Doping refers to incorporation of ions into multinary semiconductor matrices to tailor their properties to enhance PEC performance. Heterostructuring accomplishes the efficient harvest of the incident light and minimized recombination rate by coupling small band gap semiconductors with wide band gap semiconductors.

1.3.4. Metal chalcogenides and graphene-based materials in PEC studies

Chalcogenides are chemical compounds containing minimum one chalcogen element from group sixteen in the periodic table. The better electrical and optical properties of thin films made from chalcogenide materials have piqued the curiosity of many researchers. Some of the widespread known chalcogenides include cadmium chalcogenides (CdS, CdSe, CdTe), copper chalcogenides (Cu_xTe , CIT, CIS, CIGS) and zinc chalcogenides (ZnS, ZnSe, ZnTe).

Cadmium Sulfide (CdS): Cadmium sulfide (CdS) is an important functional II-VI semiconductor. Its appearance is yellow-orange to brown solid and its crystal structure is hexagonal or cubic depending on the production method. CdS has been studied extensively since it has attractive properties such as low band gap (~ 2.42 eV at 300 K), high absorption coefficient ($>10^4$), which allows the effective absorption of visible light, and size-tunability. CdS is utilized in various fields from solar cells to optoelectronics. However, there are some limitations for its photoelectrochemical

applications because of its tendency to photocorrode easily [55, 56].

Zinc Sulfide (ZnS): Zinc sulfide belongs to the II-VI family of semiconducting materials and it has drawn attention of researchers due to its better chemical stability in comparison with other chalcegonides. It is relatively less toxic, and its negative conduction band potential is higher than most of chalcegonides. It has a band gap of about 3.54 eV, which means that it needs to harvest the UV light portion of the solar spectrum [57, 58].

Cadmium Selenide (CdSe): Cadmium selenide (CdSe) is a tetrahedral semiconductor with wurtzite structure in the hexagonal modification [59]. With its total band gap of 1.7 eV, CdS has gained immensed attention in solar cells, photoelectrochemical sensors, and photocatalysis due to its favorable absorption in the visible range. Utilization of CdS/CdSe has been considered by many researchers since these materials have a particular relative position of the energy band. Namely, CB minimum of CdSe is a little higher than the CB minimum of CdS and the valance band (VB) maximum of CdS is a little lower than the VB maximum of CdSe. This situation allows for their usability in the fields of nanotechnology, electrics, optoelectronics etc. [60].

Zinc Selenide (ZnSe): Zinc Selenide (ZnSe) is one of the promising semiconductors of II-VI groups with a bandgap of 2.7 eV having green and inexpensive characteristics [61]. Its band gap energy allow light absorption of near-UV and some portion of visible light [62].

Graphene based materials: A carbon allotrope with exceptional physical qualities, graphene, a monoatomic sheet of sp^2 linked atoms, was first discovered in 2004 and has since attracted considerable attention. It is a proper candidate to be used in the areas of touch screen displays, photonics and optoelectronics, energy storage systems, photoelectrochemical and photocatalytic hydrogen production applications. Nevertheless, graphene presents valence and conduction bands that consist of bonding

π and antibonding π (π^*) orbitals, respectively, and touches the Brillouin zone corners, thereby making graphene a zero bandgap semimetallic material. This means that graphene cannot be used in a wide variety of electrical and optoelectronic devices. It is possible to chemically dope graphene with exogenous atoms that can break lattice symmetry and widen the band gap, turning it into a semiconducting material [63]. Meanwhile, other forms of graphene, graphene oxide (GO) and reduced graphene oxide (RGO), are extensively utilized, which is produced from the oxidation/exfoliation of graphite to graphene oxide (GO) and then its reduction to graphene via routes such as chemical, thermochemical, and electrochemical, respectively. GO is a material of monolayer with a high oxygen content (due to the oxygen-bearing functionalities such as carbonyl, carboxyl, epoxide groups) and characterized by a C/O ratio less than 3:1. RGO is the form of GO that has been reduced in oxygen content by the use of chemical, thermal, microwave, photochemical, and microbial/bacterial processing processes [64]. Figure 1.12 shows the representative structures of graphene, graphene oxide, and reduced graphene oxide, respectively.

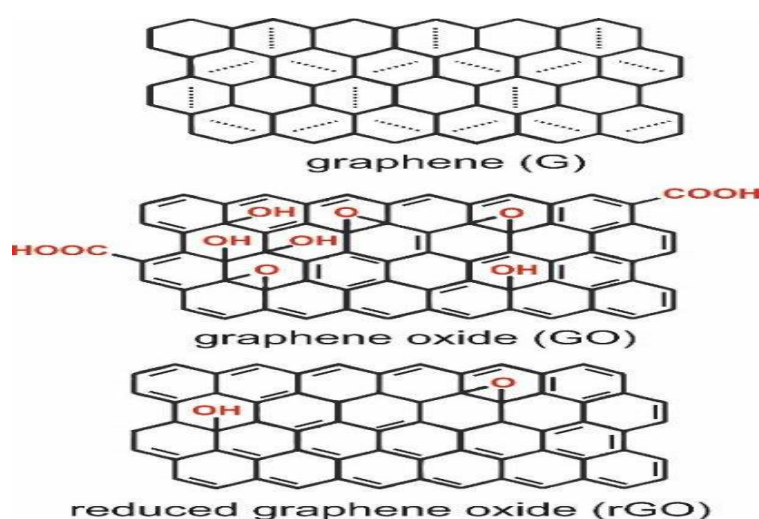


Figure 1.12. Schematics of the graphene, graphene oxide, reduced graphene oxide structure [65].

To initiate charge transfer and create a useful site for photoelectrochemical activity, restoring the sp^2 structure and reducing GO is necessary. A solid state mediator, RGO's sp^2 hybridized carbon structure exhibits high electrochemical conductivity, light transmittance, carrier mobility, and a wide surface area while in solid state. Tan et al. previously discovered that RGO, with its multi-benefit optical, structural, and electronic features, promotes efficient interfacial charge transfer between semiconductors and provides more surface active sites for water oxidation process [66]. Similarly, Prabhu et.al. synthesized WO_3 and RGO- WO_3 composites and observed two folds increase in the photocurrent of RGO- WO_3 compared to WO_3 [67].

1.3.5. Methods of thin film deposition

1.3.5.1. Physical vapor deposition

Physical vapor deposition (PVD) is one of the most prominent techniques for thin film deposition that includes the condensation of vaporized materials which are stemmed from solid/liquid sources onto various substrates [68]. The most preferred PVD processes are evaporation and sputtering. The steps used in PVD can be entitled as: (i) evaporation/sputtering of components to produce vapor phase, (ii) supersaturation of the vapor phase in an inert atmosphere to promote the condensation of metal particles, (iii) consolidation of the nanocomposite by thermal treatment under inert atmosphere [69]. Figure 1.13. shows a generalized representation of PVD technique.

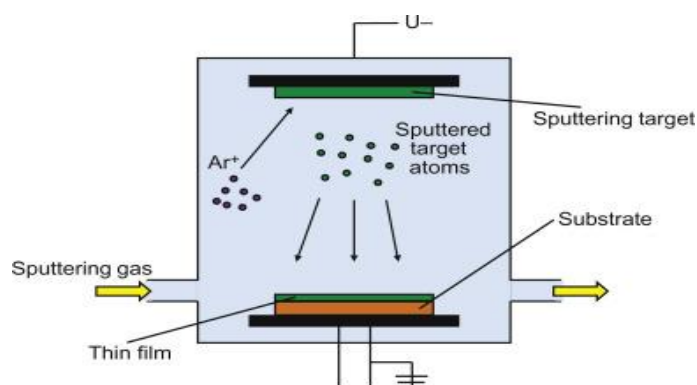


Figure 1.13. A schematical illustration of physical vapor deposition technique [70].

PVD has some advantages such as the usability of all organic and inorganic materials, yet its disadvantages cover high cost of process and low output yield, complexity of process.

1.3.5.2. Chemical vapor deposition

Chemical vapor deposition (CVD) is a versatile method in which thin films of elemental and compound semiconductors as well as metal alloys are grown on a suitable substrate by chemically reacting a volatile compound of the material to be deposited with other gaseous reactants to produce a nonvolatile solid. CVD involves a number of well-established processes, which are metal organic CVD (MOCVD), plasma-enhanced CVD (PECVD), low pressure CVD (LPCVD), laser-assisted CVD (LACVD), aerosol-assisted CVD (AACVD). The type of the process is selected based on the type of precursors and deposition conditions [71]. CVD is different from PVD in terms of chemical interaction between a gas mixture and the material surface, which in turn, results in chemical decomposition of gas constituents forming a solid film deposit. In CVD, the surface temperature is high and reaction occurs under inert atmosphere using gas precursors [72]. A schematical representation of CVD technique is presented in Figure 1.14.

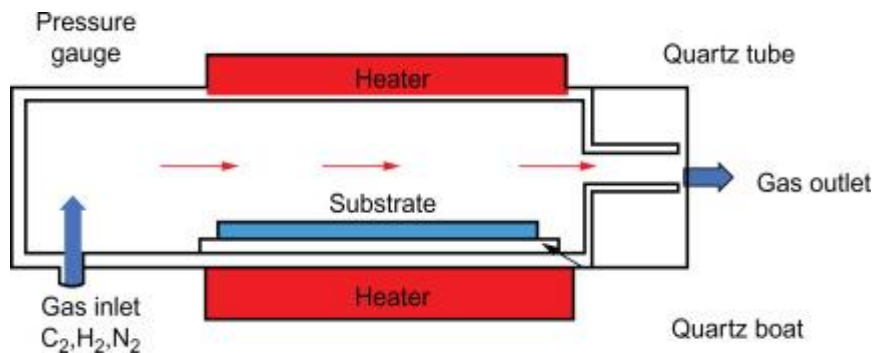


Figure 1.14. A schematical illustration of chemical vapor deposition technique [73].

In the literature, CVD is generally used to form 2D materials with large area, especially graphene. Hexagonal boron nitrides, and metal dichalcogenides are also

produced and investigated by this technique [74]. The disadvantages of CVD technique are listed as the requirement of an appropriate substrate, and high levels of temperature and pressure limits. Furthermore, high production cost is another challenge [75].

1.3.5.3. Chemical bath deposition

Chemical bath deposition (CBD) encompasses different routes to construct thin films by immersing a substrate in a liquid solution bearing precursors [76]. The reaction usually occurs at low temperature (30-80°C). Sulphide precursors used in CBD are generally thiourea, thioacetamide and thiosulphate. This method is advantageous since it doesn't require sophisticated instrumentation or other expensive equipments [77]. The most important parameters to consider are interrelated effects of solution temperature, pH, and concentration of the precursors. There are various studies regarding the metal chalcogenide formation by CBD technique [78-80]. Deposition of metal chalcogenides in CBD technique is achieved by maintaining the substrate material in contact with chemical bath including metal and chalcogenide ions using the set up given in Figure 1.15. Effect of deposition parameters, influence of annealing, bath temperature, annealing, pH, and solution concentration are investigated broadly to produce good quality metal chalcogenide thin films by CBD. The studies suggest that annealed thin films generally exhibit better properties than as-prepared ones due to increased grain sizes and transformations in their phases. Similarly, Gonzales-Panzo et al. reported that the crystalline orientation increases with increasing bath temperature [81]. In contrary, Boyle et al. stated that depositing CdS using CBD method is rather challenging because of the inefficiency of batch processing methods, such as utilization of precursor material and the conversion of this material into thin film deposit [82].

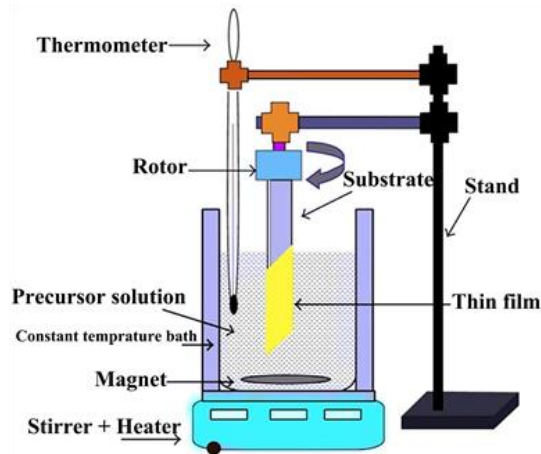


Figure 1.15. A schematical illustration of chemical bath deposition technique [83].

1.3.5.4. Spin coating

Spin coating is a common method to produce thin films of desired thickness which bases on spinning a solution of semiconductor dripped on the surface of a suitable substrate on a rotating disc. The thickness of the film is controlled by adjusting the concentration and viscosity of the solution or rotation speed. Solvent selection is another important issue to consider. In this method, aggregation of the particles can be a problem [84]. Figure 1.16 shows a schematical illustration of spin coating technique. Here, a drop of coating material is dripped into the substrate material and immediately after that the rotating disc spins around with an angular velocity. Depending on this velocity and the nature of the coating material (viscosity, percentage of solid, drying rate etc), the coating material spreads towards and off, resulting in the formation of a thin film [85].

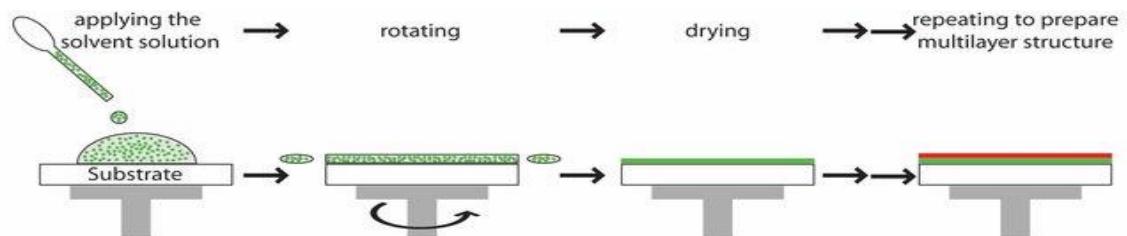


Figure 1.16. A schematical illustration of spin coating technique [86].

1.3.5.5. Dip coating

In dip coating method, a substrate is dipped into a bath with a precursor solution, remains inside for some time, and then pulled up from the solution with a constant velocity (Figure 1.17.) After the excess liquid from the substrate is drained, the solvent evaporates and forms the thin film. The parameters affecting the process are immersion time, number of dipping cycles, temperature, withdrawal speed, solution composition etc. [87]. Dip coating is more appropriate to be applied in lab-scale applications like spin coating since it doesn't require any sophisticated equipment. The main drawbacks of this deposition technique are its inefficiency in terms of time and its ability to block the screen. Additionally, some materials can hardly be deposited using this technique. For instance, the viscosity of pristine graphene based composite coating material is much lower than graphene based composite and that situation causes a worse interfacial adhesion toward a substrate for pristine graphene based composite resulting in non-uniform thin films [88].

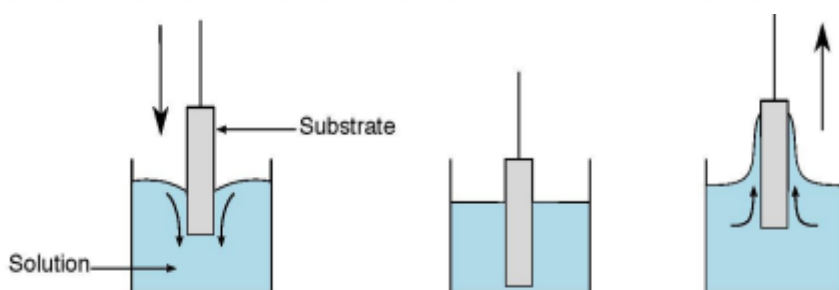


Figure 1.17. A general representation of dip coating technique [89].

1.3.5.6. Electrodeposition

Electrochemical deposition or electrodeposition is regarded as a simple and well-known process of film growth which involves the formation of a thin film onto a substrate material via the electrochemical reduction of metal ions from an electrolyte. For this process, electrical current is applied by a potentiostat. The electrode that thin

film formation occurs is the cathode, where reduction of cations of target material from an electrolyte takes place. A Pt foil or wire is used to serve as the counter electrode (anode), and it closes the circuit by injecting electrons into the electrolyte (Figure 1.18.)

On an atomic level, the electrodeposition process includes a series of steps as follows: (i) ion transportation to the electrode surface, (ii) charge transfer processes, (iii) atom incorporation into the crystal. There is a variety of electrodeposition modes: Potentiostatic, galvanostatic, pulsed potential or pulsed current, cyclic voltammetry. In potentiostatic mode, constant direct current (DC) potential is applied, whereas constant current is used in galvanostatic mode. The pulsed potential and pulsed current modes use non-DC signals [90]. Cyclic voltammetry electrodeposition is one of the most promising electrodeposition methods for obtaining high-quality data on electrochemical processes and behaviours. It reveals the locations the redox potentials of electro-active species instantly [91]. Each of these modes requires different conditions. Galvanostatic mode requires high temperatures and pre-conditioning of the electrolytic bath by adjusting pH, concentrations, precursor concentration, and use of complexing agents. Nevertheless, the deployment of cyclic voltammetric method is easier, since it can be performed at room temperature within controlled scan rates in a potential window range without the need of too many additives in the electrolytic bath [92]. Electrodeposition is beneficial since it allows the fabrication of thin films with thicknesses up to several hundred microns. However, this number is limited to only a few microns when PVD or CVD technique is used. Diverse nanostructures such as nanorods, nanowires, nanotubes, nanosheets, and composite nanostructures can be formed by electrodeposition [93, 94]. In comparison to alternative deposition procedures, electrodeposition is favoured because of its scalability, economy, and ability to cover a broad surface area while yet allowing precise composition control [90].

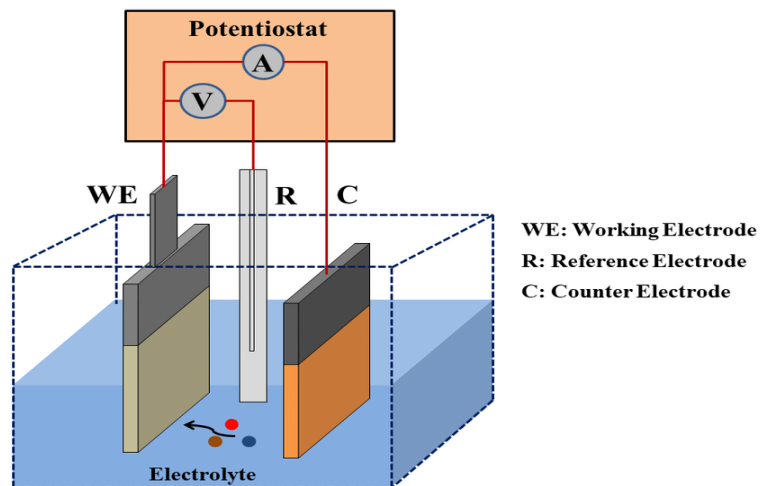


Figure 1.18. A general representation of electrodeposition technique [95].

There are some studies related to the superiority of electrodeposition technique over other deposition methods. For example, Lu et al. studied the fabrication CdS/CdSe bilayer thin films on ITO glass by chemical bath deposition and electrochemical techniques. They reported that electrodeposited thin films exhibited enhanced photoconversion efficiency in photoelectrochemical studies [60]. Kim et al. reported the cyclic voltammetric and chronoamperometric deposition of CdS. They showed that the dopant density of CdS deposited by cyclic voltmmetry was 17% more than the chronoamperometric deposited CdS. S.Z. Werta et.al. prepared $Cd_{1-x}Zn_xS$ thin films using an electrolytic bath containing cadmium chloride, zinc chloride and sodium thiosulphate under different constant potential applications and then characterized the electrodes to predict their possible usage in solar applications [96]. They concluded that increasing deposition voltage increased Zn incorporation to the structure, enhancing the performance [97].

1.3.6. Photoelectrochemical measurements

1.3.6.1. Open circuit potential

When no current is flowing through the circuit, open circuit potential (OCP), also known as open circuit voltage (OCV), equilibrium potential (EP), or rest potential, is

used to measure the potential difference between the reference electrode and the working electrode. OCP reveals information about the stability of the electrochemical system [98]. At open circuit, the Fermi level of an n-type electrode is higher than the redox potential of the electrolyte used in the system, which in turn, causes the electrons to transfer from the electrode to the electrolyte. This situation results in the formation of a space charge region (depletion region) in the electrode. The number of the ions is much more than the transferred electrons from the electrode, so there is no formation of space charge region in the electrolyte side. The Fermi energy level of the electrode equals to the energy of the redox potential of the electrolyte. The positive charges in the depletion region leads to the upward bending of the band edges at the interface [99]. For a p-type semiconductor, the situation is the reverse. Photon absorption and the e^-h^+ formation at the interface compensate this charge imbalance and cause the bands to flatten. Therefore, when the electrodes are illuminated with the light, n-type and p-type electrodes display a shift to more negative and more positive potential values, respectively [100]. Figure 1.19. shows an example representation of the potential vs. time curve of an n-type photoelectrode under light switch on-off conditions.

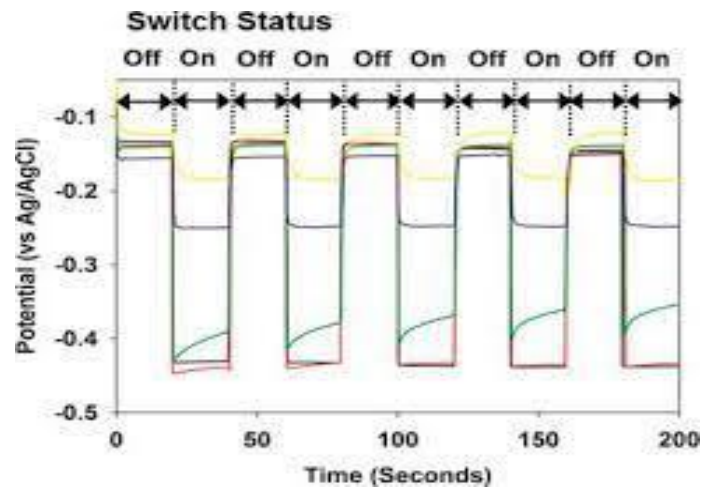


Figure 1.19. Potential vs. time curve of an n-type semiconductor under light switch on-off conditions [101].

1.3.6.2. Linear sweep voltammetry (LSV)

Linear sweep voltammetry (LSV) is based on the sweeping a linear voltage ramp from a lower limit to a higher limit as shown in Figure 1.20. LSV curve in a PEC system displays the voltammogram of the current recorded at the working electrode versus applied potential [102]. The potential value in the plot is specified in relation to the reference electrode. For n-type semiconductors, there is a plateau region where the current value is at around zero and then the current value increases in an accelerated manner to more positive values as the applied voltage is increased. The reason of the small current value in the process is due to the electron flow necessary to maintain the charged double layer at the electrode surface. As the applied potential increases, the electron flow accelerates and the transportation of electrons causes reduction in the cathode.

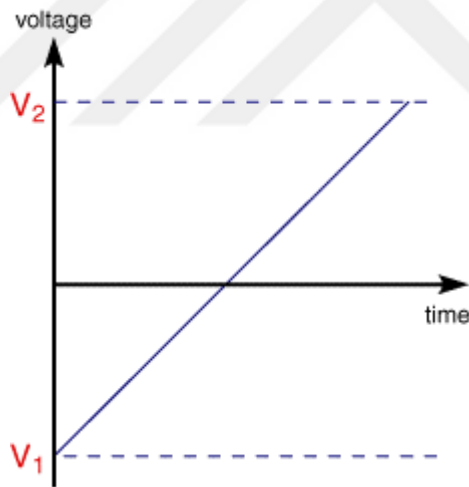


Figure 1.20. Voltage-time dependence in LSV [102].

1.3.6.3. Chronoamperometry (CA)

Stability of the tested electrode is an important parameter in PEC studies. Evaluation of electrode stability is made by performing chronoamperometry (CA) analysis, which records the photocurrent versus time. From a variety of complex bulk and surface

degradation routes, photocurrent density can be reduced. Corrosion of the electrode is a common cause of decreased performance [103]. Figure 1.21. shows a LSV curve (a) and CV curve (b) for a spray-deposited BiVO₄ photoelectrode on FTO glass under a chopped light solar irradiation. According to the figure, there is an obvious difference between the transients when the light is switched on and off. These transients indicate the existence of recombination between the electrons and holes. Photocurrent rises to its maximum value (j_0) when the light is turned on and then settles into a steady state after a period of time (j_{ss}). Due to the buildup of holes near the surface, the bulk accumulation of electrons, or the surface trapping of electrons and holes, the recombined current ($j_{ss}-j_0$) is likely to occur [49].

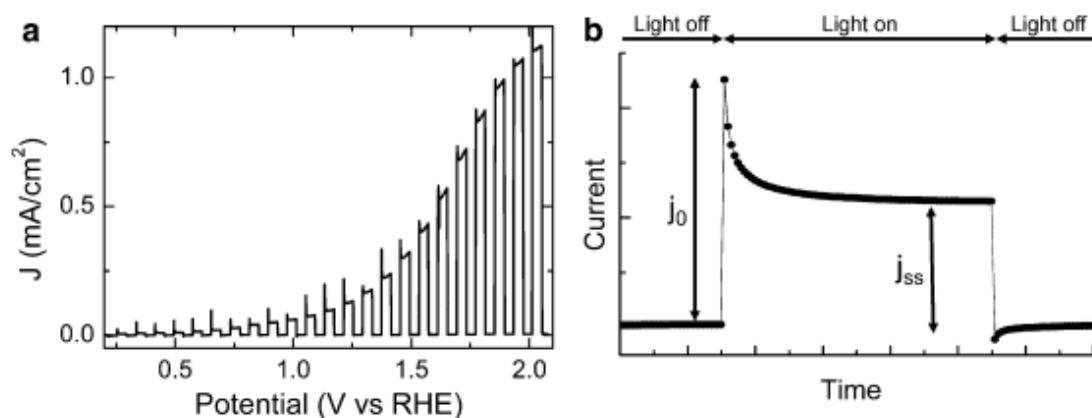


Figure 1.21. a) LSV and b) CA curves of an n-type photoelectrode under light switch on-off conditions [49].

1.3.6.4. Electrochemical impedance spectroscopy (EIS)

Electrochemical impedance spectroscopy (EIS) measures the electrical impedance of an electrode by applying an AC potential to an electrochemical cell, inducing reactions in the counter electrode and finally measuring the current passing through the cell. This analysis can be performed by a potentiostat and it can provide information about the corrosion behavior of the electrode. It also distinguishes the performance limitations of electrodes such as kinetic losses (charge-transfer activation), ohmic losses (ion and electron transport), and mass transfer losses (concentration) which

cause voltage losses. Since the frequency of the AC signal varies, the overall impedance is recorded as a function of the frequency. The impedance is represented as a complex quantity Z comprising of real part ($Z_{im}=R$) and 1 imaginary $\{Z_{im} = -\omega - c\}$. There are two types of plots, the Nyquist plot (imaginary vs real impedance axes) and the Bode plot (absolute impedance vs frequency) In the higher frequency range of the EIS spectrum (generally >10 kHz), the intercept on the real axis displays the ohmic resistance. The arc of the semicircle gives information about the charge transfer resistance. Namely, it is the difference between the real axis intercept values of the high frequency and the next lower frequency. The depression level of the semicircle in the Nyquist plot shows the electron transfer resistance behavior of the electrode [104-106]. Figure 1.22. shows an example of the Nyquist and Bode plots for an electrochemical cell.

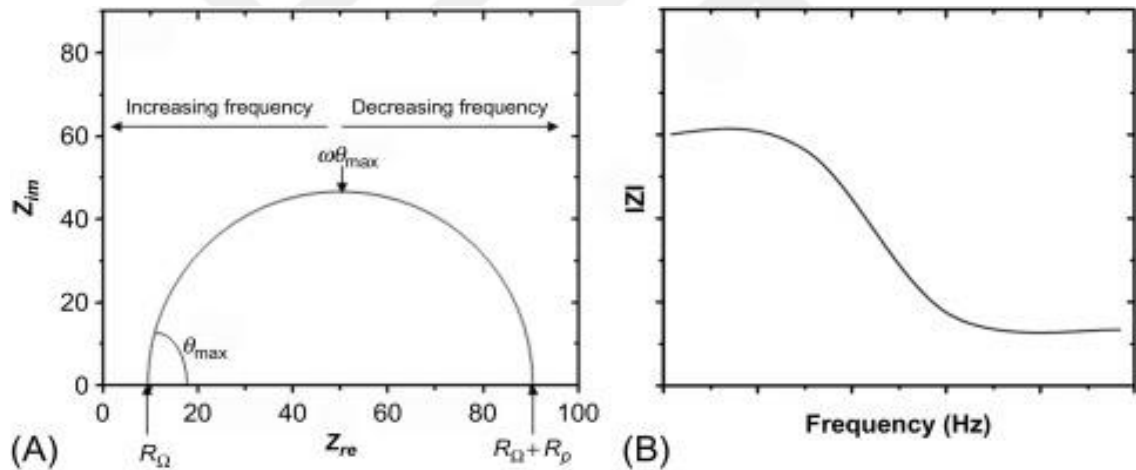


Figure 1.22. Nyquist (a) and Bode (b) plots [104].

1.3.6.5. Mott-Schottky (M-S)

Mott-Schottky (M-S) is an electrochemical impedance spectroscopy (EIS) technique. This analysis is applied to check the conductivity type of the photoelectrode (n-type or p-type), determine both the flat band potential (E_{fb}) and charge carrier density (donors or acceptors, N_d) of the photoelectrode along with the band gap (E_g). The concept of the determination of E_{fb} entails the measurement of the capacitance of the space

charge layer (C_{sc}) of the photoelectrode as a function of the applied potential (E) [103]. The relationship is given as follows:

$$1/C_{sc}^2 = (2/\epsilon_0\epsilon_s e N_D) [(V - V_{fb} - (k_B T/e))] \quad (1.14)$$

where;

ϵ_0 : permittivity of free space ($8.85 \times 10^{-12} \text{ F m}^{-1}$), ϵ_s : the dielectric constant of the deposited material, e : electronic charge, T : temperature in K, k_B : Boltzmann's constant

Flat band potential (V_{fb}) can be determined from the intercept of the x-axis of the M-S plot, where the corresponding $1/C_{sc}^2$ value reaches zero. The charge carrier density (N_D) can be calculated from the slope of the line ($2/\epsilon_0\epsilon_s e N_D$).

The N_d plays an important role in bulk and surface semiconductor properties like depletion layer width and recombination rate. The slope of the M-S plot is negative for p-type materials and positive for n-type materials [103]. Figure 1.23. displays an example of a M-S plots belonging to n-type semiconductor hematite samples [100].

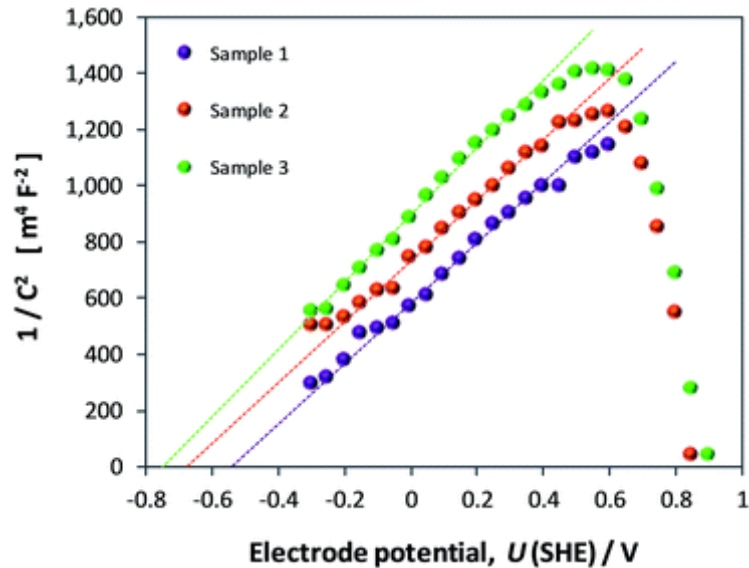


Figure 1.23. M-S curves of n-type photoelectrode samples [100].

1.3.7. Electrode characterization techniques

1.3.7.1. Scanning electron microscopy (SEM)

Scanning electron microscopy (SEM) is a material characterization technique which is used for visualization (image acquisition) and surface morphology (particle size and shape). Various signals are generated on the surface of solid specimens by electron-sample interactions when a concentrated beam of high energy electrons is utilized. They provide information about the material's structure and orientation based on the material's texture, chemical content, and crystal structure [107].

An electron gun (electron source and accelerating anode) speeds up electrons with an accelerating voltage, condensor lenses focus electrons, a vacuum chamber houses the specimen stage, and detectors collect the signals emitted by the specimen in a typical scanning electron microscope. The low-vacuum is provided inside the chamber, $0.1-10^{-4}$ Pa. Scanning electron microscopes can allow specimens up to 20 cm in diameter. The detectors define imaging modes, which are X-ray detector, back scattered electron detector, and secondary electron detector [108]

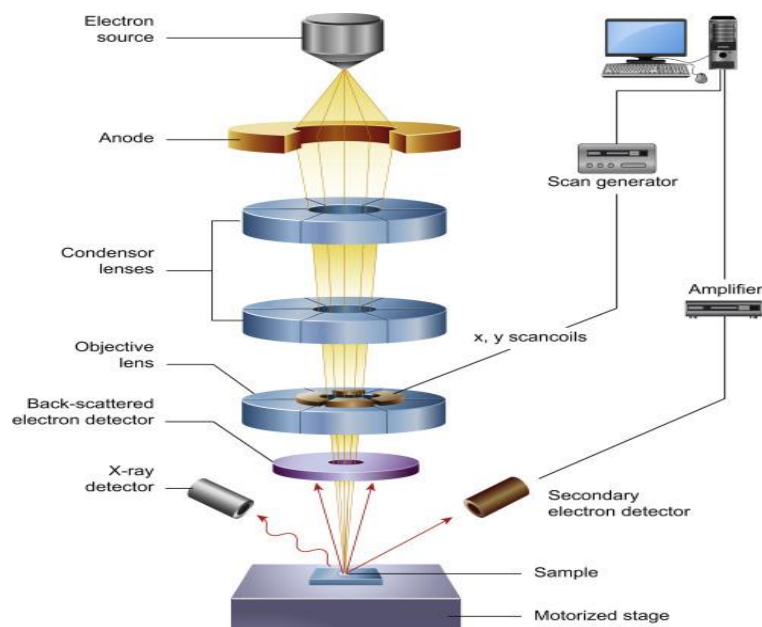


Figure 1.24. The components of a scanning electron microscope [108].

1.3.7.2. Energy dispersive X-ray spectroscopy (EDS)

Energy dispersive X-ray spectroscopy (EDS) is used to determine the elemental composition of solid materials. When an equipped SEM is employed, a high-energy electron beam is used to irradiate the atoms on the surface, resulting in the emission of distinct X-ray wavelengths with unique properties of the atomic structure of the elements. These X-ray emissions can be studied using an energy dispersive detector. After that, the elements that make up the atoms on the specimen's surface are assigned. As the name suggests, this technique is known as energy dispersive X-ray spectroscopy (EDS) [109].

1.3.7.3. X-ray diffraction (XRD)

X-ray diffraction (XRD) is one of the few non-destructive useful techniques for crystalline material characterization. It offers information related to the structure, phase, texture and other structural properties, for instance, average grain size, crystallinity, strain and crystal defects. X-ray diffractogram is obtained with monochromatic beam of X-rays scattered at specific angles from each set of lattice planes in a sample. The intensities of the peaks are determined by the atomic positions within the lattice planes. The obtained XRD pattern is specific to the material itself [110].

The main principle of this method lies behind the diffraction of X-rays by periodic atomic planes and the angle or energy-resolved detection of the diffracted signal. Bragg has investigated the geometrical interpretation of the XRD phenomenon. Bragg's law can be deduced from the geometrical conditions for diffraction given in Figure 1.25. The related formula is presented in Equation (1.15).

$$n\lambda = 2d_{hkl} \sin(\theta) \quad (1.15)$$

where n is the diffraction order, λ is the wavelength of the incident beam, d_{hkl} is the lattice spacing in nm, θ is the angle of the diffraction beam in degrees.

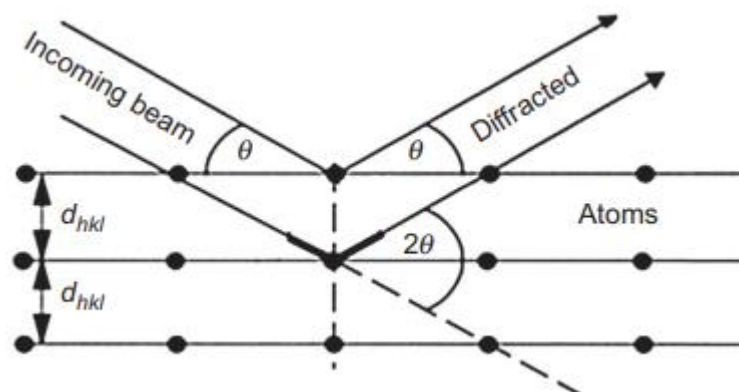


Figure 1.25. Schematic representation of Bragg's diffraction [111].

1.3.7.4. X-ray photoelectron spectroscopy (XPS)

X-ray photoelectron spectroscopy (XPS) is a quantitative analysis of elemental surface composition and it is useful to detect all elements with the exception of hydrogen and helium by determining binding states of elements [112, 113]. It involves the detection of elements in a sample with the emission of photoelectrons from a sample as a result of X-ray photon irradiation. The photoelectron lines such as Auger lines and satellite peaks have different binding energies and they help identify chemical states of the sample [113].

1.3.7.5. Raman spectroscopy (RS)

Raman spectroscopy (RS) is a widely used analytical tool in the field of vibrational spectroscopy. It is chiefly performed on solid or liquid samples to study the vibrational, rotational, and other low-frequency modes in a specimen and provide fingerprint information about the materials structure [114].

The main principle of Raman spectroscopy is based on the excitement of a molecule from its initial electronic state to a higher level. As a result, the molecule will return to

its final state and emit a photon. Rayleigh scattering occurs when the released photon's frequency matches the incident photon's frequency (elastic scattering). A photon's energy state can be changed if its final state is higher than its initial state, which is known as Stokes RS (Stokes Raman scattering). In the reverse case, anti-Stokes RS (anti-Stokes Raman scattering) will be observed [115]. Raman scattering is regarded as inelastic scattering since the frequency and the energy of the photon are changed. Difference in Raman shift between incident and radiated photons can be determined by comparing their wavelengths [116]. By this way, Raman spectroscopy probes the chemical composition of a sample by revealing the Raman shift values in cm^{-1} .

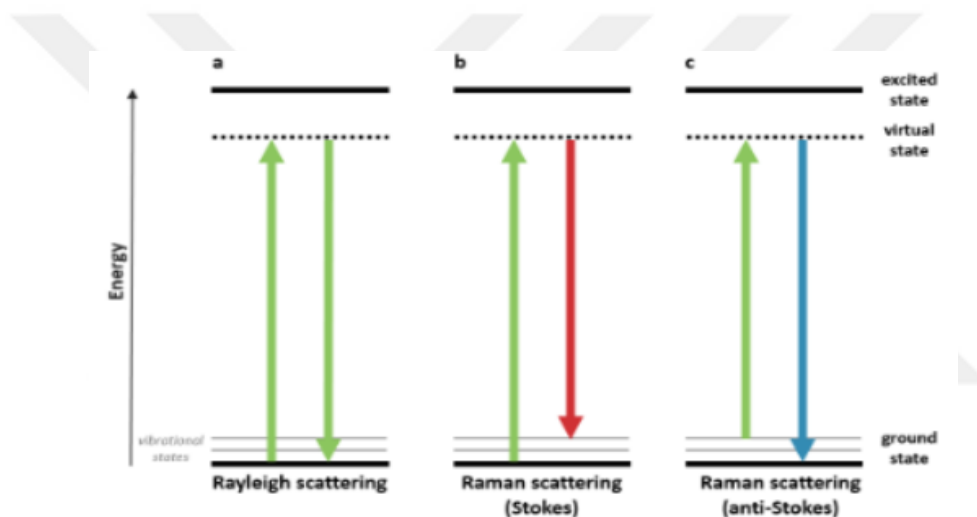


Figure 1.26. Energy transitions in Raman spectroscopy [115].

1.3.7.6. UV-visible spectroscopy (UV-vis spectroscopy)

Spectrum analysis in the UV-visible region can be done quickly and easily using UV-visible spectroscopy, a technique that uses spectroscopy to quantify how much of an object's reflected light passes through it (380-750 nm)[117]. UV-visible spectroscopy is helpful to determine the band gap of thin films. To do this; Kubelka-Munk equation is applied, which is;

$$ah\nu = B(h\nu - E_g)^n \tag{1.15}$$

Here, α is the absorption coefficient, $h\nu$ is the incident photon energy, B is the absorption edge width parameter, E_g is the band gap, and 'n' is the exponent dependent on direct or indirect transitions across the band gap [118].

Figure 1.27. gives an illustration of the components of a UV-vis spectrophotometer, which are a light source, a monochromator, sample, and a detector. The monochromator emits monochromatic light from the light source. The dispersion device splits light into a spectrum according to the wavelength of the light. The entrance and exit slits determine the spectral resolution. The detector detects how much light is transmitted or reflected through the sample by converting the light signal into the electric signal.

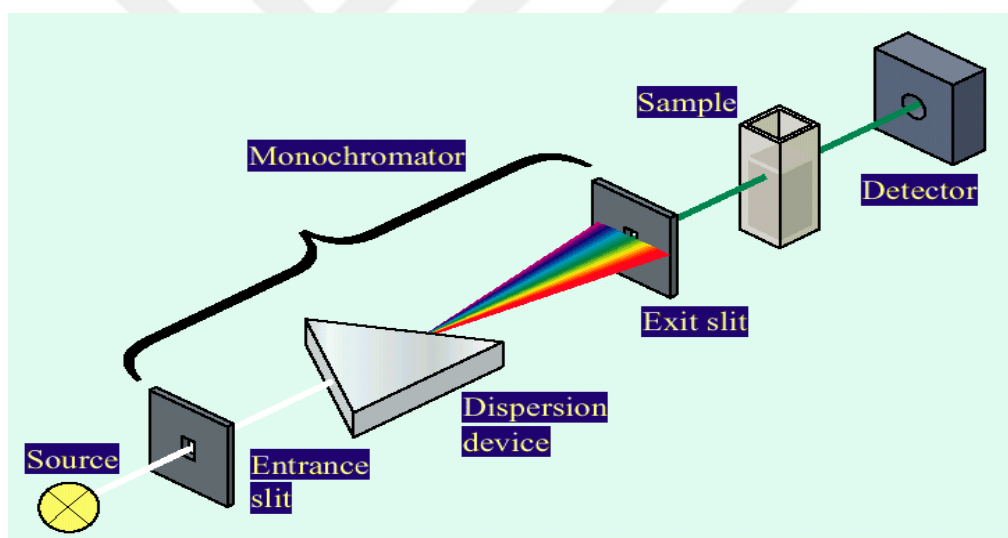


Figure 1.27. A schematical illustration of a UV-vis spectrophotometer [119].

1.4. Literature Survey on Photoelectrochemical Studies

Photoelectrochemical (PEC) hydrogen generation system is generally considered as an electrolysis system which mainly depends on harvesting some portion of solar light to achieve water splitting. Here, photoelectrodes act as absorbents of solar light to transfer charge through an external circuit. Thus, photoelectrodes can be regarded as the main component of a PEC system. An ideal photoelectrode has the abilities of good charge

separation, charge transport, high stability against photocorrosion and chemical corrosion, and economical viability. After the pioneering work of Fujishima and Honda demonstrating water splitting concept with TiO_2 in 1972, the studies related to the photoelectrochemical hydrogen generation and photoelectrode modification engineering have been steered in the way of using metal oxides as photoelectrodes at first. The reported studies suggest that metal oxide photoelectrodes remain stable even in harsh PEC conditions, yet they demonstrate low efficiency due to the intrinsically wide band gap and low charge carrier mobility. In contrast, photoelectrodes prepared using III-V group of semiconductors yield an extraordinary ($\sim 12.4\%$) solar-to-hydrogen conversion efficiency, but this time they suffer from poor stability. In the past decades, transition metal chalcogenides (TMCs) have been adequately investigated to increase the PEC performance, which are chemical compounds bearing sulfides, selenides or tellurides. They have emerged as better electrochemical conductive with narrow band gap and more economical materials than metal oxides [120, 121]. Among these semiconductors, cadmium sulfide (CdS) has been extensively studied due to its low band gap value (around 2.4 eV) and its capability to absorb visible light up to 520 nm [122]. However, its instability is an obstacle to its practical usage in PEC studies [123]. To overcome this drawback, $\text{Cd}_x\text{Zn}_{1-x}\text{S}$ thin films can be formed to improve charge separation efficiency since ZnS has the same coordination mode as CdS [124]. Thus, the flexible alteration of band gap values with constituent stoichiometries has been the devotion of the scientists to investigate the ternary $\text{Cd}_x\text{Zn}_{1-x}\text{S}$ thin films. Even so, there are still some restraints for $\text{Cd}_x\text{Zn}_{1-x}\text{S}$, such as the insufficient dispersion of active sites, low efficiency of electron-hole separation and weak migration ability of the photoexcited charge carriers [125, 126]. The PEC studies based on the decoration of $\text{Cd}_x\text{Zn}_{1-x}\text{S}$ particles with graphene derivatives increase the rate of electron transport with the merits of improved carrier mobility, electrical conductivity, and prevention of recombination [127]. Especially, utilization of reduced graphene oxide (RGO) rather than graphene oxide (GO) is relatively advantageous to enhance the PEC performance [128]. The large π -

conjugated system of RGO contributes to its electron donor characteristics [129, 130]. There are several studies reported in the literature regarding the RGO decoration on semiconductors, and their results reveal that RGO exhibits an important role in PEC analyses [131-135]. These studies indicate that CdS, CdZnS, GO-CdS, or RGO-CdS thin films have been constructed with different deposition methods, for instance, electrodeposition [96], chemical bath deposition [136], chemical vapor deposition [137], and spray pyrolysis [138]. Electrodeposition is superior to other deposition techniques, because it offers some advantages such as ease of control of the deposit reactions, economic viability, allowance for the reactions to take place at low temperatures, simplicity, and ease of manufacturability, particularly for the quaternary compounds [139, 140].

There are no known reports of one-step development of RGO-binary metal chalcogenide composites, according to our knowledge, such as RGO-CdZnS thin films, using the electrodeposition method. In the literature, there are a few studies for the electrodeposited CdZnS for different applications [96, 97, 141]. For instance, S.Z. Werta et.al. prepared $Cd_{1-x}Zn_xS$ thin films from an electrolytic bath including cadmium chloride, zinc chloride and sodium thiosulphate under constant potential applications and then characterized the electrodes to predict their possible usage in solar applications [96]. In a recent study, B. B. Panda et.al. fabricated ZnS–CdS thin film photoelectrodes by electrodeposition method with constant current and tested these electrodes for natural dye sensitized solar cells [97]. In the literature, preparation of GO-CdS or RGO-CdS with the electrodeposition method was generally carried out with two steps. First of all, GO or RGO layers were coated on the electrode surface with different methods and then CdS layer was electrodeposited on the GO or RGO layer with constant potentiometric or amperometric methods. Although, there are some studies on the synthesis and applications of GO-CdS structures [142-146], there are a few studies on the RGO-CdZnS which were prepared with different techniques. For instance, in our previous

studies, we reported photocatalytic and PEC activities of RGO-CdZnS structures prepared with solvothermal and hydrothermal methods [132, 147-149].

It was well described in the literature that improvement of the transport rate of the photogenerated charge carriers of the semiconductors with conductive carbon based supports, such as GO and RGO, enhanced PEC hydrogen evolution performance [150-152]. For this reason, it might be an interesting route to prepare novel composite structures on the photoelectrode by improvement the interaction between the RGO and CdZnS particles.

CdSe and ZnSe are also one of the most popular semiconductors among PEC studies. Thus, CdZnSSe semiconductors are fascinating due to their controllable compositions and particular sizes [153]. They exhibit the characteristic features of CdS, CdSe, ZnS, and ZnSe which have high absorption coefficient, wide range of band gap energy, high sensitivity, good chemical stability and electrical properties. RGO with CdZnSSe ensures to ease the electron transfer, advance the photocurrent response and prevent photocorrosion of CdZnSSe, providing to display high PEC performance [154, 155]. The study reported by Li et al. emphasize the vital role of RGO nanosheets on $\text{Co}_3\text{O}_4/\text{Co}(\text{OH})_2/\text{RGO}$ photocatalysts and their results indicated that RGO enhanced the photocurrent by decreasing the nanoparticle aggregation and increasing the charge transfer rate [156]. In the recent past, the number of studies of CdZnSSe composites and photoelectrodes in the photoelectrochemical field has been increased, yet there is no reported work regarding the contribution of RGO in CdZnSSe thin films fabricated by one-step electrodeposition strategy. Zhuang et al. reported a study designating to photoelectrochemical performance of CdSe@TiO₂ core-shell nanorod arrays obtained by electrochemical deposition and their study reported a photocurrent density of 2.1 mA cm⁻² under visible light irradiation [157]. In addition, Ayal et al. developed CdSe supported titanium dioxide nanotube arrays as a semiconductor electrode for photoelectrochemical application by using electrodeposition technique. This study reveals that incorporating CdSe into titanium dioxide nanotube arrays provides a

notable enhancement in the photoelectrochemical properties. They reported the maximum photocurrent density of 1.94 mA cm^{-2} [158]. Izi et al. fabricated ZnS thin films on a Mo substrate by electrodeposition and spray pyrolysis methods and concluded that electrodeposited ZnS had relatively lower band gap [159]. Kumarage et al. studied the effect of deposition method on the photoelectrochemical performance of CdS thin films. They disclosed that electrodeposited CdS thin films exhibited better photoelectrochemical characteristics than chemical bath deposited CdS thin films due to their improved interparticle connections and homogeneity [160]. Riveros et al. electrodeposited composition-graded stacked $\text{CdS}_x\text{Se}_{(1-x)}$ thin films, but they did not perform any application of the films. They firstly deposited CdS and then exchanged S with Se in the structure with gradual addition of SeO_2 in the electrodeposition bath. However, this method consisted of successive electrodeposition steps [161].

Combining CdZnSSe with other semiconductors such as selenides of copper, molybdenum and nickel has not been reported in the literature. Yet, there are some studies related to the increased PEC performance of semiconductors when they are combined. He et al. studied MoS_2/CdS photoelectrodes and they stated that MoS_2/CdS exhibited a photocurrent density almost five times that of the pristine MoS_2 [162]. Patil et al. synthesized photoactive $\text{Zn}_{1-x}\text{Cu}_{2x}\text{Se}$ photoelectrodes and concluded that they had the best photoconversion efficiency (1.65%) with $\text{Zn}_{0.90}\text{Cu}_{0.10}\text{Se}$.

Herein, a new electrochemical method was proposed to prepare new photoanodes bearing CdZnS, RGO-CdZnS, CdZnSSe, RGO-CdZnSSe, CdZnNiSSe, CdZnMoSSe, CdZnCuSSe, RGO- CdZnNiSSe composites and then these photoanodes were tested in the PEC system to investigate the effect of the synthesis method to the performance of PEC hydrogen evolution reaction. In order to enhance the photoelectrochemical activity in PEC process, a facile one-step electrodeposition-electroreduction method was developed to form composite thin films on indium tin oxide coated glass substrate (ITO) with the repetitive cyclic voltammetry (rCV) at room temperature. With this new method, nanoparticles were immobilized among the RGO sheets by electrodeposition

and electrochemical reduction of GO simultaneously. Between the RGO sheets, the nanoparticles will be immobilized, preventing leakage and aggregation, which will limit photocorrosion of deposited nanoparticles and contribute to increase the active sites on the composite for the PEC process.



2. MATERIAL AND METHOD

2.1. Materials

For solvothermal synthesis of RGO-Cd_{0.60}Zn_{0.40}S-Pt composites: To synthesize and rinse graphene oxide and reduced graphene oxide, the graphite powder (Acros-organics), potassium permanganate (KMnO₄) (Sigma-Aldrich), hydrogen peroxide solution (30%) (H₂O₂) (Merck), hydrazine hydrate solution (35%) (Sigma-Aldrich), sulfuric acid (96%) (H₂SO₄) (Merck), hydrochloric acid (37%) (HCl) (Merck), methanol and ethanol (Merck) were purchased [163]. Cadmium acetate (Cd(CH₃COO)₂) (Merck), zinc acetate (Zn(CH₃COO)₂) (Merck), and dimethyl sulfoxide (DMSO)(Aldrich) were used for the solvothermal synthesis of RGO-Cd_{0.60}Zn_{0.40}S. Pt loading was conducted with hexachloroplatinic acid (H₂PtCl₆·6H₂O)(Alfa Aesar). Sodium sulfite (Na₂SO₃) (Acros-organics), sodium sulfide nonahydrate (Na₂S·9H₂O) (Acros-organics) and ultra-pure water were used for sacrificial reagent preparation. Ultra-pure water had the resistivity of 18.2 MΩ cm (at 25 °C) Milli-Q, Millipore.

For electrodeposition studies of RGO-CdZnMSSe (M=Ni, Cu, Mo), cadmium acetate dihydrate, (CH₃COO)₂·2H₂O) (Acros Organics), zinc acetate dihydrate, (Zn(CH₃COO)₂·2H₂O) (Acros Organics), Cu(CH₃COO)₂ (Alfa Aesar), Na₂MoO₄·2H₂O (Sigma-Aldrich), Ni(NO₃)₂·6H₂O (Carlo-Erba) sodium thiosulfate (Na₂S₂O₃) (Sigma-Aldrich) and sodium selenosulfate (Na₂SeSO₃) were used as the sources of Cd, Zn, Cu, Mo, Ni, S, Se precursors, respectively. Ethylenediaminetetraacetic acid (EDTA) (Carlo Erba) acted as a complexing agent during thin film formation. The pH of the electrolytic bath was adjusted with sodium hydroxide (Sigma-Aldrich). Graphene oxide (GO) was produced by using graphite powder (Acros-organics), H₂SO₄ (Aldrich), H₃PO₄ (Merck), KMnO₄ (Sigma-Aldrich) and H₂O₂ (30%) (Aldrich). For washing procedure of fabricated GO, ultra-pure water HCl (30%) and absolute ethanol (Merck) were used in order. Thin film formation was conducted on ITO coated glass substrate with a sheet resistance of 6~8 ohm/sq, which was purchased from Biotain Hong Kong Co., Ltd. The

mixture including sodium sulfite (Na_2SO_3) (Sigma-Aldrich), and sodium sulfide nonahydrate ($\text{Na}_2\text{S}\cdot 9\text{H}_2\text{O}$) (Acros Organics) served as the electrolyte to determine the performance of prepared photoelectrodes.

2.2 Preparation of Graphene Oxide (GO) and Reduced Graphene Oxide (RGO)

GO was synthesized in a mixture of concentrated H_2SO_4 (120.0 mL) / H_3PO_4 (13.3 mL), 1.0 g of graphite powder and 6.0 g of KMnO_4 in a three-neck round bottom flask. The mixture was sonicated until the particles were uniformly dispersed. After that, the three-neck round bottom flask was heated under a reflux condenser in a temperature-controlled jacket to $50\text{ }^\circ\text{C}$ and maintained at this temperature for 12 h. Finally, the mixture was cooled down to the room temperature and it was poured onto 100 mL of ice with 30% H_2O_2 (1.0 mL). The mixture was centrifuged, and the supernatant was discarded away followed by the successive washing the remaining solid with deionized water (3x), 30% HCl (3x), and ethanol (3x). At the end of this process, the resulting material was left to vacuum-dry at $40\text{ }^\circ\text{C}$ overnight [164].



Figure 2.1. a) Solvothermal synthesis of GO, b) Resulting product (GO mixture) of solvothermal synthesis.

Hydrazine reduction of GO yielded RGO as a byproduct. To do that, 300.0 ml of ultra-pure water and 0.60 g of GO powder were ultrasonicated in a flask for a while. When

the uniform distribution of GO particles was observed, 2.0 ml of hydrazine (35%) was added into the mixture and it was kept at 100°C for 24 hours using a water-cooled condenser. The slurry was washed many times with water and methanol after centrifugation. The finished product was dried in the ambient conditions and the black RGO powder was collected [165-167].

2.3 Preparation of Photoelectrodes by Solvothermal and Electrodeposition Method

The RGO-Cd_{0.60}Zn_{0.40}S-Pt composite was synthesized by the solvothermal method. A 500 ml flask was filled with a mixture of RGO, Cd(CH₃COO)₂, Zn(CH₃COO)₂ and DMSO, and it was ultrasonicated for 30 min. The optimum percentage of RGO and Pt in the composite had been determined as 1.0% and 0.5%, respectively [168]. The temperature of the mixture was increased up to 180°C and kept at this temperature for 12 h under a water-cooled condenser. After the solvothermal reaction, the mixture was centrifuged and rinsed with ethanol and acetone, 3 times for each, and then it was dried in a vacuum-oven at 70 °C for 2 h. For Pt loading (0.5%), a photodeposition technique was applied, in which, a certain amount of RGO-Cd_{0.6}Zn_{0.4}S was continuously dispersed in 50 ml of 0.35 M Na₂S/0.25 M Na₂SO₃ aqueous solution with a magnetic stirrer, and a predetermined volume of hexachloroplatinate acid (H₂PtCl₆.6H₂O) was slowly dripped into the solution. Afterwards, UV irradiation was applied to the surface of the mixture by using Max-303 Xenon Light Source 300 W (≤420 nm) for 2 h and RGO-Cd_{0.60}Zn_{0.40}S-Pt was synthesized.

Indium tin oxide (ITO) coated glass was used to serve as a substrate for coating and it was cut into slices with the dimensions of 1 cm x 0.8 cm. Before coating, ITO coated glass slides were cleaned with acetone, ethanol, and ultrapure water in an ultrasonic bath for 10 minutes for each. After that, 5.0 mg of RGO-Cd_{0.60}Zn_{0.40}S-Pt was dispersed in 2.0 ml of ethanol, and 15 µL of suspension was dripped onto the conductive part of the ITO surface which was placed on the disc of the spin coater (Model P6700). The thin films were spun clockwise with the speed rate of 4000 rpm for 30 s and this was

repeated 25 times with intermittent preheating at 150°C on a hot plate before each run. Finally, coated thin films were annealed in a muffle furnace at the temperature of 500°C for an hour and the temperature was kept constant. To prepare the RGO-Cd_{0.60}Zn_{0.40}S-Pt photoanode, the end of copper wire was fixed to the surface of the ITO with a silver paste. The uncoated conductive parts of the ITO along with the silver paste were covered with silicon with a silicon gun. After that, photoelectrochemical analyses were performed. Figure 2.2. schematizes the pathway of this process.

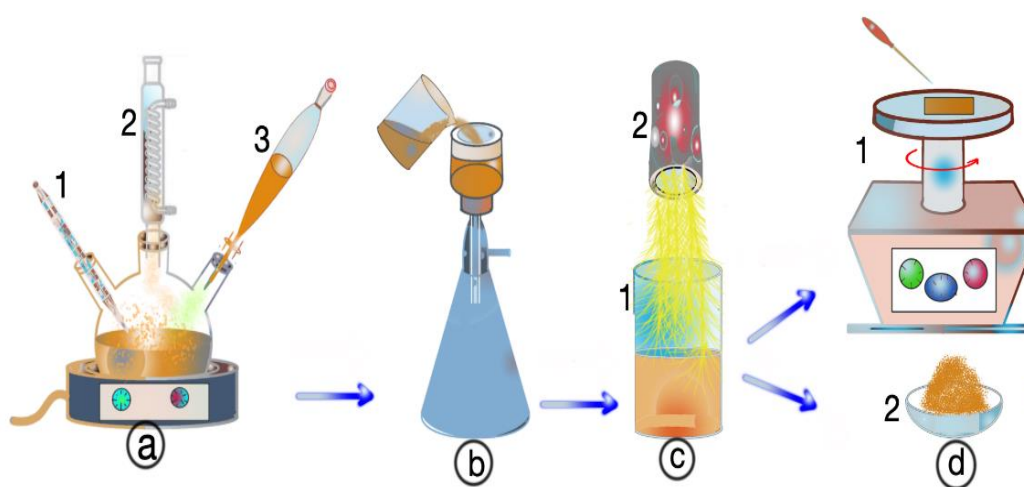


Figure 2.2. Synthesis, photoelectrode preparation, and photocatalytic-photoelectrochemical measurements pathway. **a)** Synthesis of RGO-Cd_{0.60}Zn_{0.40}S composite with solvothermal method under reflux (1: thermometer, 2: condenser, 3: separation funnel); **b)** filtering, drying and annealing of the particles; **c)** photoreduction of Pt on RGO-Cd_{0.60}Zn_{0.40}S particles under UV light excitation (1: RGO-Cd_{0.60}Zn_{0.40}S dispersed Na₂S/Na₂SO₃ electrolyte, 2: light source); **d)** Preparation of the RGO-Cd_{0.60}Zn_{0.40}S-Pt particles for applications (1: coating on ITO with a spin coater, 2: RGO-Cd_{0.60}Zn_{0.40}S-Pt particles).

Electrodeposited Cd_xZn_{1-x}S (x = 0.0, 0.2, 0.5, 0.8, 1.0) thin films were fabricated using the repetitive cyclic voltammetry (rCV). At room temperature, all electrochemical experiments were carried out. The aqueous solution of required concentration of Cd(CH₃COO)₂·2H₂O, Zn(CH₃COO)₂·2H₂O and Na₂S₂O₃ was used as the electrolyte for

the one-pot electrodeposition reactions. The ITO slices were used as the substrate of the working electrode. Prior to the experiments, ITO slices were adequately rinsed with ultrapure water, cleaned with detergent, distilled water, isopropanol and acetone. Electrodeposition experiments were performed in a three-electrode cell configuration with a working electrode (ITO), a counter electrode (Pt wire), and a reference electrode (Ag/AgCl in saturated KCl). The rCVs were performed at the 100 mV s^{-1} scan rate within the potential range from -1.7 to $0.2 \text{ V vs. Ag/AgCl}$ [46]. A pushing rod was used to insert an alumina ceramic crucible boat filled with freshly deposited thin films into the long quartz tube. After that, one end of the cylinder was connected to the Ar gas cylinder with a plastic pipe and the other one end to a beaker which was filled with water. The flow rate of Ar gas was adjusted and the atmosphere inside the quartz tube consisted of 100% of Ar by passing the Ar gas for 15 minutes. Consequently, the tube furnace was heated to 350°C , 450°C , and 550°C at $15^\circ\text{C}/\text{min}$ and kept at these temperatures for an hour. The cooling rate of the tube furnace was set $20^\circ\text{C}/\text{min}$. After the annealing process was over, the samples were withdrawn from the tube furnace and prepared for PEC performance analyses. The best photoelectrochemical performance was achieved with $\text{Cd}_{0.8}\text{Zn}_{0.2}\text{S}$ composition, thus further modifications were carried out with this structure. RGO- $\text{Cd}_{0.8}\text{Zn}_{0.2}\text{S}$ photoelectrodes were prepared using the same procedure as $\text{Cd}_x\text{Zn}_{1-x}\text{S}$ preparation. However, different amounts of GO powder were added into the electrolyte for RGO- $\text{Cd}_{0.8}\text{Zn}_{0.2}\text{S}$ photoelectrodes. The concentration values of the GO in the electrolyte were 0.10 mg mL^{-1} , 0.25 mg mL^{-1} , 0.50 mg mL^{-1} . The fabricated thin films were abbreviated as RGO(0.10)- $\text{Cd}_{0.8}\text{Zn}_{0.2}\text{S}$, RGO(0.25)- $\text{Cd}_{0.8}\text{Zn}_{0.2}\text{S}$, and RGO(0.50)- $\text{Cd}_{0.8}\text{Zn}_{0.2}\text{S}$. The next step of electrode modification was to optimize the photoelectrochemical performance by changing S/Se composition in $\text{Cd}_{0.8}\text{Zn}_{0.2}\text{S}_x\text{Se}_{1-x}$ composite. The aqueous electrolytic bath for electrodeposition reactions consisted of required concentrations of $\text{Cd}(\text{CH}_3\text{COO})_2 \cdot 2\text{H}_2\text{O}$, $\text{Zn}(\text{CH}_3\text{COO})_2 \cdot 2\text{H}_2\text{O}$, $\text{Na}_2\text{S}_2\text{O}_3$, Na_2SeSO_3 and EDTA. The pH of the electrolytic bath was tuned at 8.7. Here, Na_2SeSO_3 solution was prepared at 80°C for 4 hours after dispersing $\text{Na}_2\text{S}_2\text{O}_3$ and Se powder in

ultrapure water. Rinsed and cleaned ITO coated glass slices served as the substrates of the working electrode. Electrodeposition technique was conducted in a standard three-electrode system. The repetitive cyclic voltammetry technique was conducted at the rate of 100 mV s^{-1} between -1.5 - 1.0 V vs. Ag/AgCl . After that, $\text{ITO}/\text{Cd}_{0.8}\text{Zn}_{0.2}\text{S}_x\text{Se}_{1-x}$ photoelectrodes were thermally treated in a horizontal tube furnace at 450°C in Ar for 1 hour. The aforementioned rCV parameters were applied for photoelectrode construction. $\text{ITO}/\text{Cd}_{0.8}\text{Zn}_{0.2}\text{S}_{0.2}\text{Se}_{0.8}$ was found as the photoelectrode yielding the highest photocurrent density. Afterwards, $\text{RGO}(0.25)\text{-Cd}_{0.8}\text{Zn}_{0.2}\text{S}_{0.2}\text{Se}_{0.8}$ was electrodeposited on ITO surface since the optimized concentration of GO in electrolytic bath had been determined as 0.25 mg mL^{-1} . For the final modification part, the effect of M (M: Ni, Cu, Mo) on the photoelectrochemical performance of CdZnSSe and RGO-CdZnSSe photoelectrode was investigated. To do this, $\text{Cd}_{0.8}\text{Zn}_{0.2}\text{Ni}_{0.2}\text{S}_{0.2}\text{Se}_{0.8}$, $\text{Cd}_{0.8}\text{Zn}_{0.2}\text{Cu}_{0.2}\text{S}_{0.2}\text{Se}_{0.8}$, $\text{Cd}_{0.8}\text{Zn}_{0.2}\text{Mo}_{0.2}\text{S}_{0.2}\text{Se}_{0.8}$, $\text{RGO}(0.25)\text{-Cd}_{0.8}\text{Zn}_{0.2}\text{Ni}_{0.2}\text{S}_{0.2}\text{Se}_{0.8}$ thin film structures were produced. Cyclic voltammetry (CV) experiments were run on a standard three-electrode cell (ITO: working electrode, Pt wire: counter electrode, Ag/AgCl : reference electrode) containing precursor solution for each type of fabricated thin film to monitor the prospective currents and potentials. The solutions consisted of $\text{Cd}(\text{CH}_3\text{COO})_2 \cdot 2\text{H}_2\text{O}$, $\text{Zn}(\text{CH}_3\text{COO})_2 \cdot 2\text{H}_2\text{O}$, $\text{Cu}(\text{CH}_3\text{COO})_2$, $\text{Na}_2\text{MoO}_4 \cdot 2\text{H}_2\text{O}$, $\text{Ni}(\text{NO}_3)_2 \cdot 6\text{H}_2\text{O}$, $\text{Na}_2\text{S}_2\text{O}_3$ and Na_2SeSO_3 as Cd, Zn, Cu, Mo, Ni, S, Se precursors, respectively. EDTA was used as complexing agent to chelate with the cations of Cd, Zn, Ni, Cu and Mo. The experiment was carried out in room conditions. An argon environment was used for 1 hour to anneal the thin films made from ITO-coated glass slices before being stored for further analysis.

In order to be able to perform PEC performance tests, Ag paste (Electrofix silver conductive paste) was used to bond the surface of the conductive part of the ITO coated glass with a copper wire to help form a conductive pathway. A silicon glue gun with 11 mm silicon glue hot melt stick was used to cover the uncoated conductive surfaces and edges of the thin films.

2.4 Characterization Techniques

Scanning Electron Microscopy (SEM) with an EDAX detector attachment was used to analyze the microstructure and morphology of thin films (Carl Zeiss 300VP) operating at an accelerated voltage of 15.0 kV. XRD pattern was collected on a (Bruker D2 Phaser) X-ray diffractometer under Cu-K α radiation ($\lambda=1.54056 \text{ \AA}$) with a step size of 0.02° in the angular 2θ range of 10° - 80° . Raman spectra were recorded with a Raman spectrometer (STEX-100) with the laser excitation wavelength of 538 nm in back scattering geometry. The PG instruments T92+ UV/VIS spectrophotometer was used to monitor the UV-vis diffuse reflectance spectra (UV-vis DRS) of the samples. The X-ray photoelectron spectroscopy (XPS) measurements were carried out by Thermo-Scientific spectrophotometer (Al-K α (1486.7 eV)-X-ray source with the beam size of 400 nm diameter).

2.5 Photoelectrochemical Measurements

Photoelectrochemical analyses of all photoelectrodes were performed in a three-electrode system with the Gamry 1500B Potentiostat/Galvanostat as the electrochemical workstation. PEC properties of thin films were investigated in a standard three-electrode PEC cell configuration (Reference 1000B Potentiostat/Galvanostat/ZRA). In this configuration, photoanodes, Pt wire, and Ag/AgCl were used as the working electrode, the counter electrode, and the reference electrode, respectively. All the electrodes were immersed in a $0.35 \text{ mol dm}^{-3} \text{ Na}_2\text{S}/0.25 \text{ mol dm}^{-3} \text{ Na}_2\text{SO}_3$ sacrificial electrolyte (pH=13.0) throughout PEC analyses. The area of $1 \text{ cm} \times 0.8 \text{ cm}$ of photoanodes was exposed to solar light illumination with the power intensity held at $1.0 \times 10^3 \text{ W m}^{-2}$ by using HAL-320 Compact Xenon Light Source Solar Simulator. Open circuit potential (OCP) measurements, linear sweep voltammograms (LSV) and chronoamperometry (CA) analyses were monitored under transient light conditions. LSV for the photoanodes were obtained with the scan rate of 5 mV s^{-1} . Electrochemical impedance spectroscopy (EIS) was carried out in dark conditions. The amplitude of the sinusoidal

wave was 10 mV and the employed frequency range was from 10^5 to 10^{-2} Hz. Mott-Shottky (M-S) analysis was carried out at an AC frequency of 1 kHz with an amplitude of 5 mV.

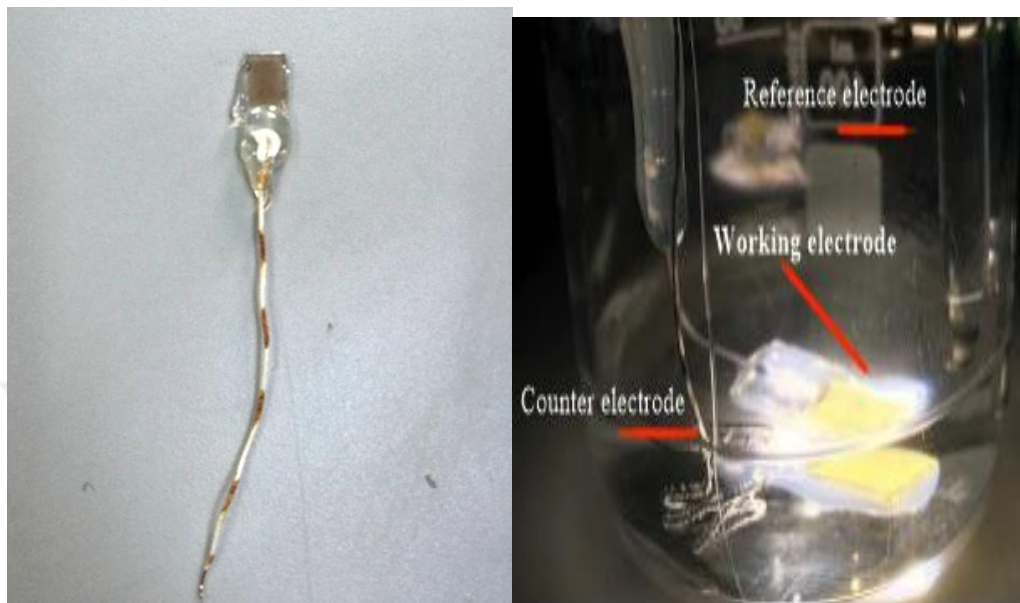


Figure 2.3. a) A photoelectrode ready-to-be tested (left) and b) a three-electrode set-up (right) for photoelectrochemical analyses.

3. RESULTS AND DISCUSSION

3.1. Characterization and Photoelectrochemical Analyses of Solvothermally Prepared RGO-Cd_{0.60}Zn_{0.40}S-Pt Photoelectrodes

Scanning electron microscopy (SEM) analysis was performed for the morphological characterization of RGO-Cd_{0.60}Zn_{0.40}S-Pt with FEI Quanta FEG-450 using 20 kV beam voltage at the magnifications of 5000, b) 25000 and c) 50000 (Figure 3.1.). SEM image in Figure 3.1a illustrates the homogeneous distribution of RGO-Cd_{0.60}Zn_{0.40}S-Pt composites on ITO surface. SEM images recorded with higher magnifications clearly show the RGO sheets and globular particles decorated on the RGO sheets as seen in Figure 3.1b-c. Furthermore, the globules' dimensions are within the range of 250-400 nm.

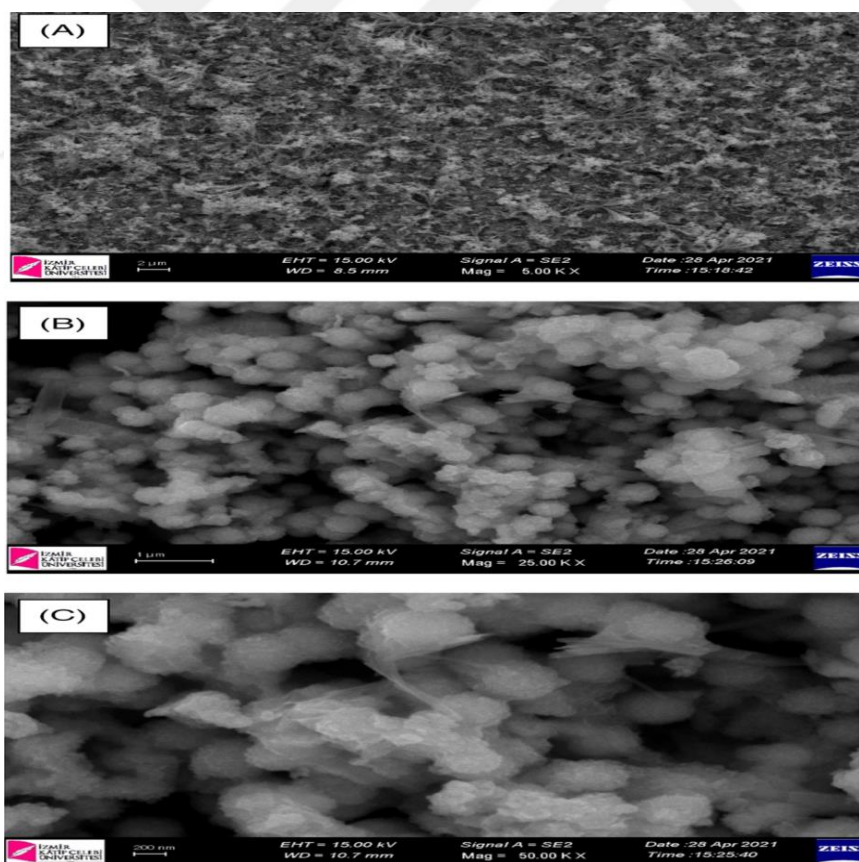


Figure 3.1. SEM images of RGO-Cd_{0.60}Zn_{0.40}S-Pt at a) 5000, b) 25000 and c) 50000 magnifications.

Figure 3.2a demonstrates the XRD diffractogram of RGO-Cd_{0.60}Zn_{0.40}S-Pt thin film. The pattern exhibits three prominent diffraction peaks at $2\theta = 27.142^\circ$, 44.419° , 52.524° , which are assigned to the lattice planes of (111), (220), and (311), respectively [169]. These peaks are well indexed to the cubic phase of Cd_(1-x)Zn_xS, which corresponds to the Card no. 01-079-6257 given by Joint Committee on Powder Diffraction Standards (JCPDS) [170]. No Pt diffraction peak in the pattern may be on the account of the low content of Pt loading or the incorporation of Pt content into the RGO-Cd_{0.60}Zn_{0.40}S structure [171, 172]. Although Pt diffraction peak in the pattern are not clearly observed in the XRD diffractogram. The presence of Pt in the structure is recorded with the EDS spectrum for the RGO-Cd_{0.60}Zn_{0.40}S-Pt composite (Figure 3.2b). The spectrum verifies the presence of Cd, Zn, S, C, O, Pt, In, and Sn elements. C and O elements are attributed to RGO, while In, Sn, and O indicates the presence of ITO.

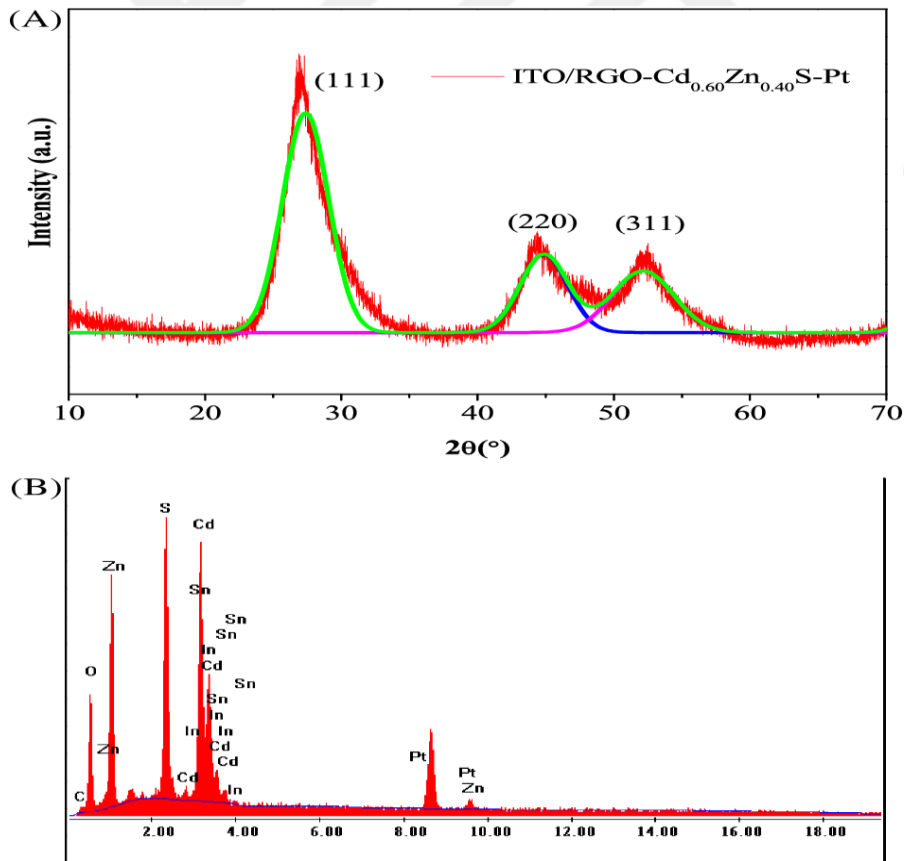


Figure 3.2. a) XRD pattern of RGO-Cd_{0.60}Zn_{0.40}S-Pt, b) EDS spectrum of RGO-Cd_{0.60}Zn_{0.40}S-Pt.

Figure 3.3. displays the Raman spectrum of RGO-Cd_{0.60}Zn_{0.40}S-Pt thin film recorded with 532 nm excitation laser source. The spectrum reveals peaks centered at 310 cm⁻¹, 613 cm⁻¹, 1010 cm⁻¹, 1355 cm⁻¹, and 1605 cm⁻¹. The peak position of longitudinal optical (1LO) phonon band is dependent on the composition of the CdZnS structure. The observed 1LO peak at 310 cm⁻¹ confirms the presence of Cd_{0.60}Zn_{0.40}S, since it is located between the wavenumbers of 300 cm⁻¹ (bulk CdS) and 325 cm⁻¹ (bulk ZnS). The peaks at ca. 613 cm⁻¹ and 1010 cm⁻¹ are recognized as second-order longitudinal optical (2LO) and third-order longitudinal optical (3LO) phonon bands, respectively. The spectrum consists of D (1355 cm⁻¹) and G (1605 cm⁻¹) bands corresponding to the RGO decoration in RGO-Cd_{0.60}Zn_{0.40}S-Pt structure. The RGO's I_D/I_G ratio measures the degree of abnormality in the D band. To resolve the D and G bands, Origin software is used through, and I_D/I_G is calculated as 1.04 by using Gaussian fitting.

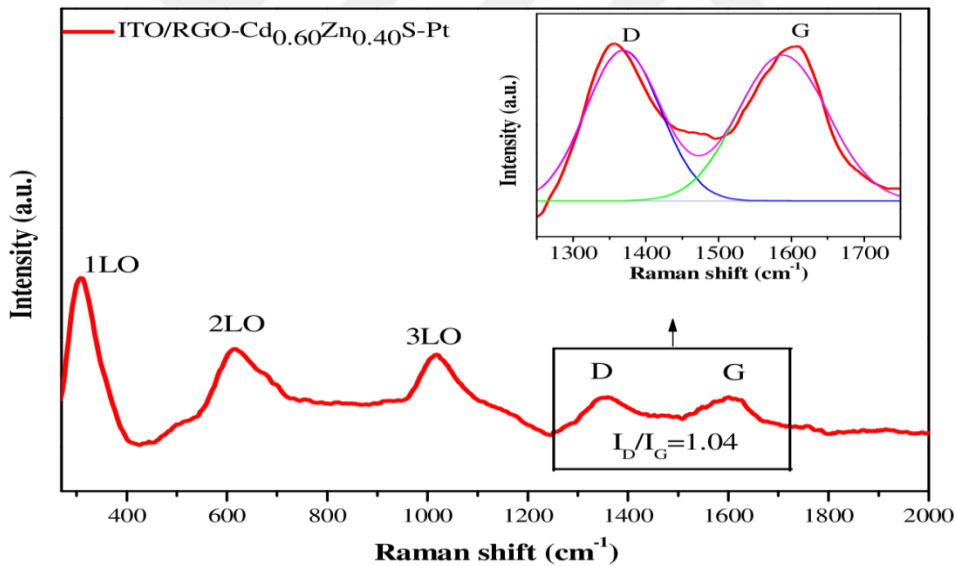


Figure 3.3. Raman spectrum of ITO/RGO-Cd_{0.60}Zn_{0.40}S-Pt photoelectrode. (Inset: Gaussian fitting of the D and G bands).

Figure 3.4 represents the UV-vis DRS spectra (a) and Tauc plots (b) of RGO-Cd_{0.60}Zn_{0.40}S-Pt powder and ITO/RGO-Cd_{0.60}Zn_{0.40}S-Pt electrode. The band gaps of these materials are estimated from the reflectance vs wavelength graph using the Tauc equation of the Kubelka-Munk method:

$$(\ln F(R\alpha)) = A(\ln(h\nu - E_g))^n \quad (3.1)$$

Here, $h\nu$ is the incident photon energy, R is the reflectance, $F(R\alpha)$ is the function, which is proportional to the extinction coefficient (α), A is the proportionality constant, E_g is the band gap, and n depends on the nature of the material, and it is taken as $\frac{1}{2}$, which is the direct allowed transition. While the band gap of RGO-Cd_{0.60}Zn_{0.40}S-Pt particles was reported as 2.30 eV, coating of these particles on ITO surface as ITO/RGO-Cd_{0.60}Zn_{0.40}S-Pt photoelectrode shifts the band gap to 2.28 eV, which are found by extrapolating the linear fit of the curves to the abscissa axis. The slight red shift in the band gap of the ITO/RGO-Cd_{0.60}Zn_{0.40}S-Pt photoelectrode with respect to the powder may be resulted from the further thermal treatment of the electrode after coating.

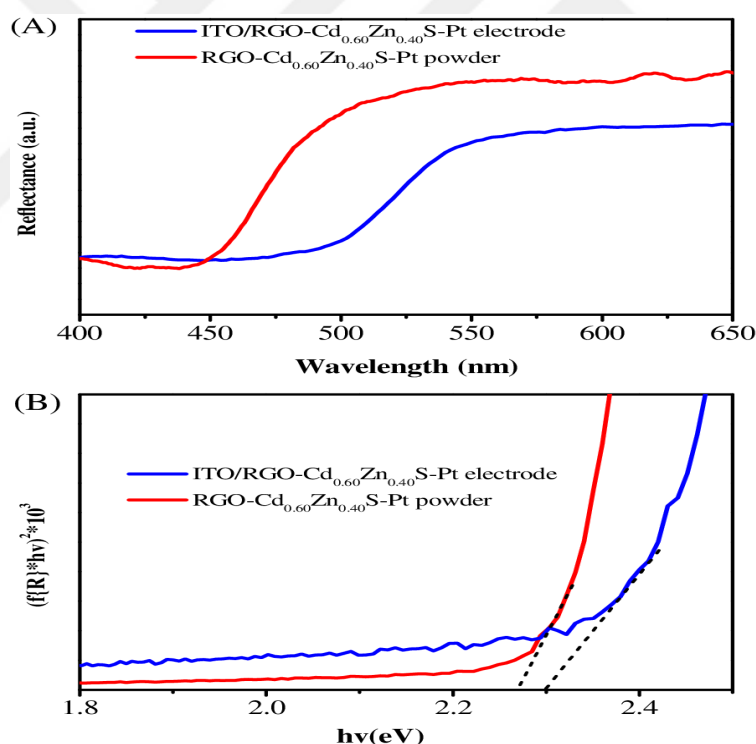


Figure 3.4. a) UV-vis DRS and b) Tauc plots of RGO-Cd_{0.60}Zn_{0.40}S and RGO-Cd_{0.60}Zn_{0.40}S-Pt.

Open-circuit potential (OCP), linear sweep voltammetric (LSV), and chronoamperometric (CA) analyses of the PEC system were performed with 0.25 mol

dm⁻³ Na₂S/0.35 mol dm⁻³ Na₂SO₃ electrolyte. The open-circuit potential response of RGO-Cd_{0.60}Zn_{0.40}S-Pt photoelectrode under transient light was recorded as shown in Figure 3.5a. The photoelectrode behaves as n-type semiconductor since the potential decreases when the light is on, and it increases again as the light is turned off. The E_{ocp} drop of RGO-Cd_{0.60}Zn_{0.40}S-Pt photoelectrode is observed as 184 mV in the electrolyte. Linear sweep voltammetry (LSV) (Figure 3.5b.) and chronoamperometry (CA) (Figure 3.5c.) analysis under transient light illumination were carried out to enlighten the PEC activities of RGO-Cd_{0.60}Zn_{0.40}S-Pt photoelectrode. The photogenerated currents are strongly correlated to the degree of charge separation during the PEC process. Consistent with the LSV analyses, the photocurrent value of RGO-Cd_{0.60}Zn_{0.40}S-Pt electrode is enhanced from 1.20 mA cm⁻². Yet, the formation of spikes is eye-catching, which implies the existence of charge recombination.

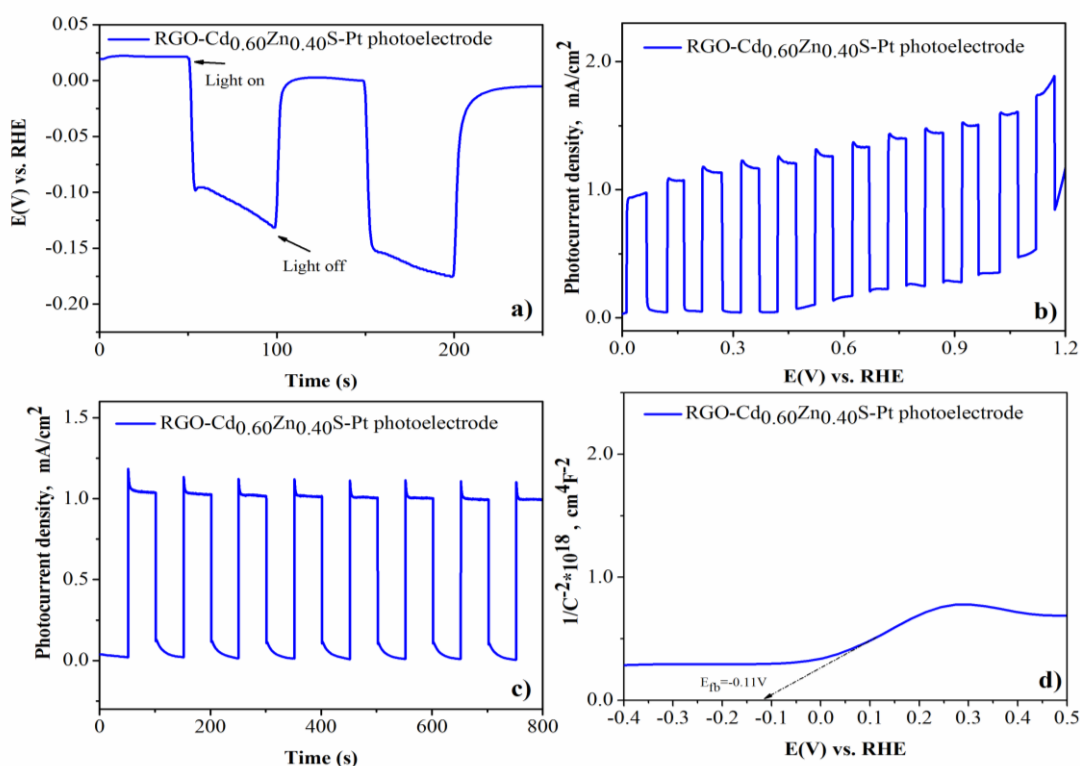


Figure 3.5. a) Open circuit potential (OCP), b) Linear sweep voltammetry (LSV), c) Chronoamperometric (I-t), d) Mott-Schottky (M-S) curves of RGO-Cd_{0.60}Zn_{0.40}S-Pt photoelectrode.

At the semiconductor/liquid interface, the flat band potential (E_{fb}) and donor density can be determined with great precision by the use of M-S technique. (Figure 3.5d.) Generally, the flat band potential is obtained from the M-S relationship of the capacitance vs the applied potential [173]. Namely, the flat band potential of the photoelectrodes can be estimated by extrapolating the M-S plot and taking the intercept of the x-axis as the V_{fb} [174]. The V_{fb} values of RGO-Cd_{0.60}Zn_{0.40}S-Pt in the electrolyte is determined as -0.11 V vs. RHE. The sign and magnitude of the linear region slope of the M-S curve give important clues related to the carrier concentration and the type (n or p) of the photoelectrode. Fig. 3.5d shows that the photoelectrode has n-type characteristics, with electrons as the majority carriers, based on the linear fit of the M-S curve [175]. The electron donor density (N_d) of RGO-Cd_{0.60}Zn_{0.40}S-Pt photoelectrode is calculated as $0.82 \times 10^{18} \text{ cm}^{-3}$.

Figure 3.6. shows the applied bias photon-to-current conversion efficiency (ABPE) plot of RGO-Cd_{0.60}Zn_{0.40}S-Pt photoelectrode against the applied potential by evaluating the results of the LSV curves [176]. The applied bias photon to current conversion efficiency (ABPE) value is proportional to the amount of energy consumed during the reaction and is calculated using Equation (3.2) [177]:

$$ABPE(\%) = |J_{pc}| \times ((1.23 - V_b)/P_{light}) \times 100 \quad (3.2)$$

where V_{app} represents the applied external potential vs RHE, J_{ph} stands for the current density at the V_{app} , and $P_{incident}$ is the power density of the incident light (100 mW cm^{-2} , AM 1.5G). According to the Figure 3.6., RGO-Cd_{0.60}Zn_{0.40}S-Pt yields the maximum photoconversion efficiency of 1.03% in Na₂S/Na₂SO₃ electrolyte.

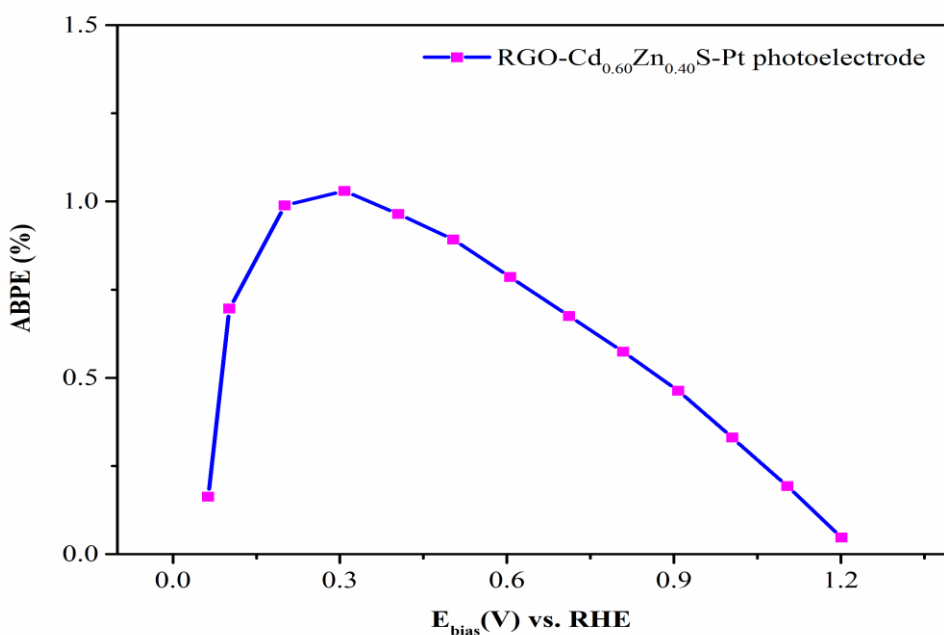


Figure 3.6. ABPE plot of RGO-Cd_{0.60}Zn_{0.40}S-Pt photoelectrode.

3.2. Characterization and Photoelectrochemical Analyses of Electrodeposited Photoelectrodes

3.2.1 Electrochemical Deposition, Characterization and Photoelectrochemical Performance of CdZnS and RGO-CdZnS Photoelectrodes

The facile co-electrodepositions of Cd_xZn_{1-x}S thin films (x=0.0, 0.2, 0.5, 0.8, 1.0) were carried out from the Cd(CH₃COO)₂·2H₂O and/or Zn(CH₃COO)₂·2H₂O aqueous solution at the concentrations varying between 0.00 and 0.02 mol dm⁻³ (depending on the x value) containing 0.040 mol dm⁻³ Na₂S₂O₃, as sulfur source [178]. A three-electrode arrangement was used for 10 consecutive cycles of rCV at a scan rate of 100 mV s⁻¹ in the range of -1.7 to 0.2 V vs. AgCl. Figure 3.7. displays the CV curves for the co-electrodeposition of CdS, ZnS, and Cd_{0.8}Zn_{0.2}S on ITO substrate. As shown in Figure 3.7a, performing rCVs at the cathodic potentials eases the growth of the CdS thin films by blocking the limitation of thickness, decreasing the defects, and increasing crystallite sizes. Hence, constructing high-quality thin films via the cathodic method is a relatively relevant method. rCVs for the CdS electrodeposition exhibit two cathodic peaks

centered approximately at -1.0 V and -1.3 V vs. Ag/AgCl and two anodic peaks at around -0.9 V and -0.4 V vs. Ag/AgCl. The intensities of the peak current decrease with the small potential shift of the cathodic and anodic waves as the cycle number increases. The cathodic peak at -1.00 V can be attributed to the reduction of $S_2O_3^{2-}$ ions. Cd^{2+} cations are reduced to Cd^0 at -1.3 V, and the dissolution of Cd^0 takes place at -0.4 V [180] and then it is deposited on the electrode surface as solid CdS particles.

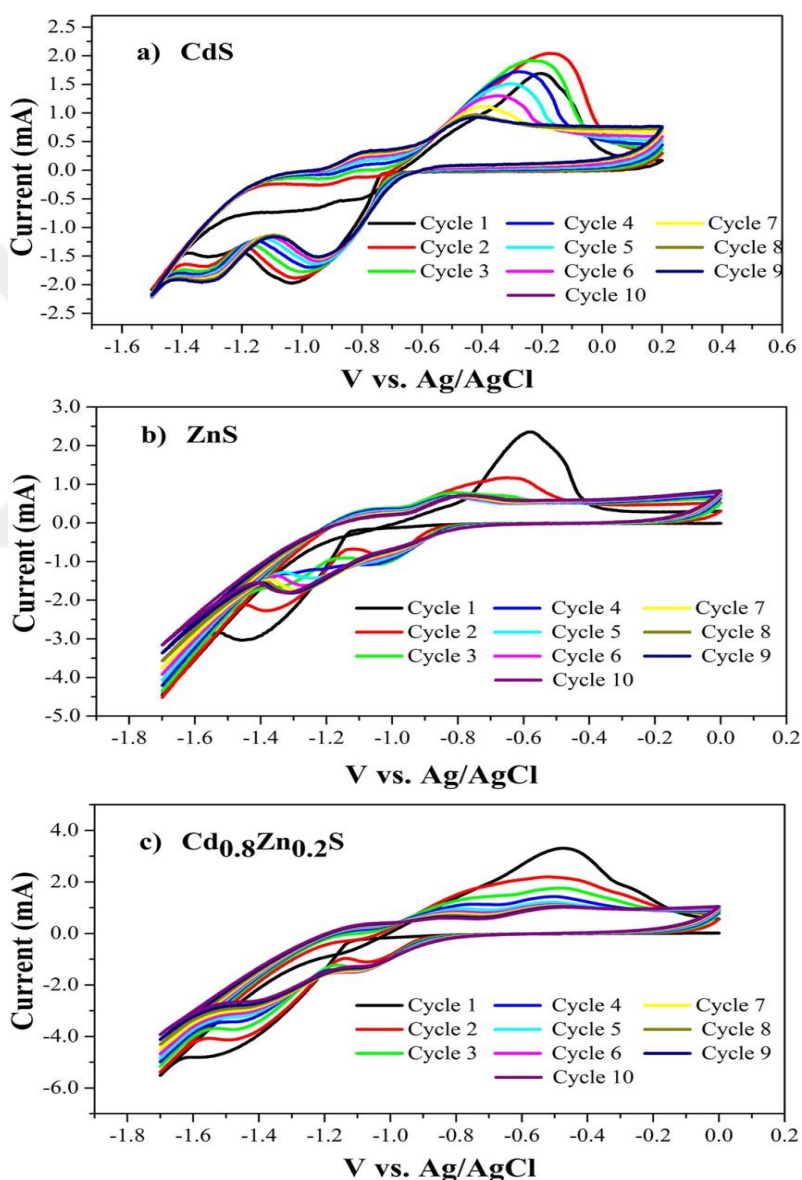


Figure 3.7. rCV curves for the fabrication of **a)** CdS, **b)** ZnS, **c)** $Cd_{0.8}Zn_{0.2}S$ thin films in the aqueous solution consisting of $Cd(CH_3COO)_2 \cdot 2H_2O$, $Zn(CH_3COO)_2 \cdot 2H_2O$ and $Na_2S_2O_3$ mixture at 100 mV s^{-1} scan rate.

Figure 3.7b represents the formation of ZnS thin film from the aqueous solution of $0.02 \text{ mol dm}^{-3} \text{ Zn}(\text{CH}_3\text{COO})_2 \cdot 2\text{H}_2\text{O}$ and $0.040 \text{ mol dm}^{-3} \text{ Na}_2\text{S}_2\text{O}_3$. During the cathodic scan, the cathodic peaks which appear at around -1.00 V and -1.30 V vs Ag/AgCl are assigned to the $\text{S}_2\text{O}_3^{2-}$ and Zn^{2+} reduction, respectively. The distinct peak at around -0.50 V vs. Ag/AgCl designates the Zn oxidation, while the faint peak which appears at -0.80 V vs. Ag/AgCl can be originated from the oxidation of $\text{S}_2\text{O}_3^{2-}$.

Figure 3.7c displays the rCVs of $\text{Cd}_{0.8}\text{Zn}_{0.2}\text{S}$ thin film which was deposited on the ITO electrode at the scan rate of 100 mV s^{-1} . The cathodic peak at -0.90 V during the forward scan is assigned to the reduction of $\text{S}_2\text{O}_3^{2-}$ ions. The reduction of Cd^{2+} and Zn^{2+} ions are observed at the same potential (the peak at -1.30 V). Apart from Figure 3.7a and Figure 3.7b, Figure 3.7c has two subsequent anodic peaks at around -0.40 V and -0.70 V vs. Ag/AgCl that may be ascribed to the re-oxidation of Cd and Zn, respectively. Cd^{2+} and Zn^{2+} ions react with S^{2-} and are deposited as CdZnS film on the ITO surface.

RGO- $\text{Cd}_{0.8}\text{Zn}_{0.2}\text{S}$ thin films were constructed with the same procedure as $\text{Cd}_x\text{Zn}_{1-x}\text{S}$ preparation with the addition of GO powder to the electrolyte. The concentrations of the GO in the electrolyte were chosen as 0.10 mg mL^{-1} , 0.25 mg mL^{-1} , 0.50 mg mL^{-1} to find out the optimized amount of the RGO in the composite structure. The rCV response observed during the fabrication of RGO(0.25)- $\text{Cd}_{0.8}\text{Zn}_{0.2}\text{S}$ thin film is illustrated in Figure 3.8. as an example. When the CV curves of RGO(0.25)- $\text{Cd}_{0.8}\text{Zn}_{0.2}\text{S}$ and $\text{Cd}_{0.8}\text{Zn}_{0.2}\text{S}$ are analyzed closely, two major differences draw attention. The first one of these is that the peak current for the construction of RGO(0.25)- $\text{Cd}_{0.8}\text{Zn}_{0.2}\text{S}$ thin film is reasonably higher than that of $\text{Cd}_{0.8}\text{Zn}_{0.2}\text{S}$ thin film. The second difference shows that RGO decoration causes the shifting of the oxidation and reduction peaks. Moreover, when the potential is swept towards negative potentials, the intensity of cathodic current for RGO- $\text{Cd}_{0.8}\text{Zn}_{0.2}\text{S}$ is relatively higher, which may refer to the irreversible reduction of GO to RGO and reduction of Cd^{2+} simultaneously. The characteristic anodic peak at around 0.10 V is assigned to the redox reaction of the RGO sheet on the ITO surface. As shown in Figure 3.8, during the first CV cycles, RGO sheet is coated on the ITO

surface due to the reduction of GO at around -1.0 V. Then, $\text{Cd}_{0.8}\text{Zn}_{0.2}\text{S}$ particles are decorated on the RGO sheet as a result of the reduction of Cd^{2+} and Zn^{2+} ions at -1.30 V and then reoxidized during the reverse scan. During the consecutive rCV cycles, new RGO- $\text{Cd}_{0.8}\text{Zn}_{0.2}\text{S}$ layers are formed on the electrode surface. As a result of the optimized 10 rCV cycles, $\text{Cd}_{0.8}\text{Zn}_{0.2}\text{S}$ could be immobilized among the RGO sheets.

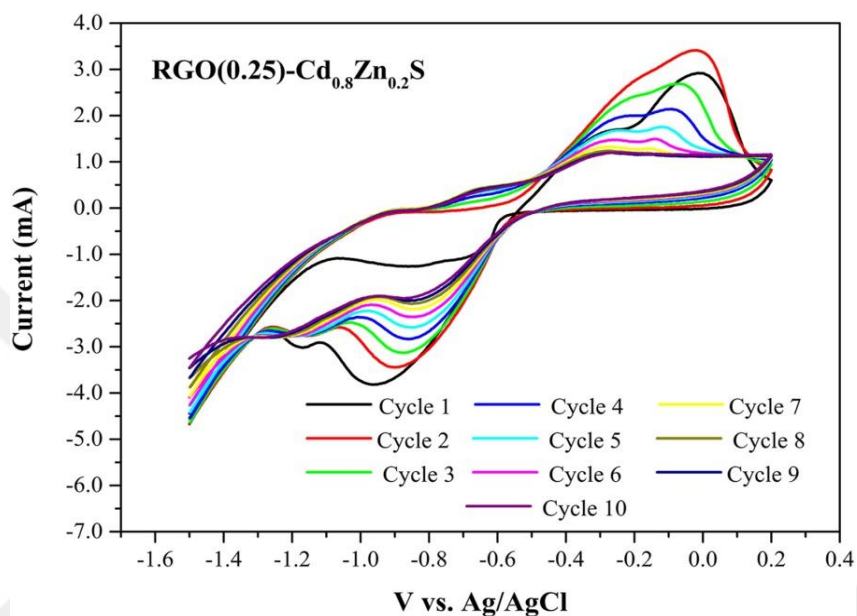


Figure 3.8. rCV responses of ITO electrode recorded during the fabrication of RGO(0.25)- $\text{Cd}_{0.8}\text{Zn}_{0.2}\text{S}$ thin film in the electrolyte consisting of RGO, $\text{Cd}(\text{CH}_3\text{COO})_2 \cdot 2\text{H}_2\text{O}$, $\text{Zn}(\text{CH}_3\text{COO})_2 \cdot 2\text{H}_2\text{O}$ and $\text{Na}_2\text{S}_2\text{O}_3$ mixture at 100 mVs^{-1} scan rate.

Coating of the RGO sheets on the previously deposited $\text{Cd}_{0.8}\text{Zn}_{0.2}\text{S}$ particles during the consecutive rCV cycles prevent accumulation of the new $\text{Cd}_{0.8}\text{Zn}_{0.2}\text{S}$ particles on the previously deposited ones. Similar voltammetric responses were observed for all electrodeposited RGO- $\text{Cd}_{0.8}\text{Zn}_{0.2}\text{S}$ composite structures with peak current differences due to the different amount of GO added to the electrolyte.

Raman spectroscopy is one of the best tools to characterize the lattice properties and probe the band structure, as well as the crystallinity in a material system [181]. In this study, this tool is used for the confirmation of the presence of as-synthesized GO (Figure 3.8.) $\text{Cd}_x\text{Zn}_{1-x}\text{S}$ ($x=0.0, 0.2, 0.5, 0.8, 1.0$), annealed $\text{Cd}_{0.8}\text{Zn}_{0.2}\text{S}$ and RGO-

$\text{Cd}_{0.8}\text{Zn}_{0.2}\text{S}$ thin films (Figure 3.9.). The presence of GO can be proven by two distinct peaks, which are assigned to D (1356 cm^{-1}) and G (1601 cm^{-1}) bands, respectively. The D band is linked to structural defects in the GO-nanocomposite structure, whereas the G band is linked to in-plane stretching vibrations of sp^2 bonded carbon atoms in both rings and chains. [182, 183].

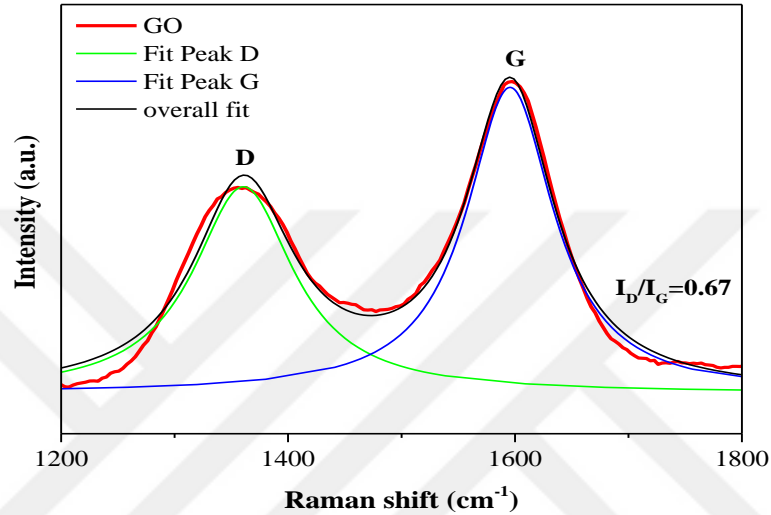


Figure 3.9. Raman spectrum of GO.

Figure 3.10a displays the Raman spectra of $\text{Cd}_x\text{Zn}_{1-x}\text{S}$ ($x=0.0, 0.2, 0.5, 0.8, 1.0$) thin films. The peak position of the 1LO phonon mode is blue-shifted as the Cd/Zn value decreases. CdS exhibits a Raman peak at 301 cm^{-1} , while the Raman peak of ZnS is located at 324 cm^{-1} [184].

According to Figure 3.10b, the prominent first-order longitudinal optical (1LO) phonon mode and the second overtone (2LO) phonon mode of relatively less intensity were located at 312 cm^{-1} and 614 cm^{-1} , respectively [185]. Figure 3.10c represents the Raman spectrum of RGO(0.25)- $\text{Cd}_{0.8}\text{Zn}_{0.2}\text{S}$ thin film annealed at 450°C , which is the optimum annealing temperature. In addition to the aforementioned peaks, three different peaks are also observed at 905 cm^{-1} , 1344 cm^{-1} , and 1606 cm^{-1} , which are assigned to the third-order longitudinal optical (3LO) phonon mode of $\text{Cd}_{0.8}\text{Zn}_{0.2}\text{S}$, D band and G band of RGO, respectively. The Raman spectra of GO (Figure 3.9.) and RGO reveal that

I_D/I_G ratio of GO, 0.65, shifts to 1.03 in the case of RGO as the average number of sp^2 domains decreases [186].

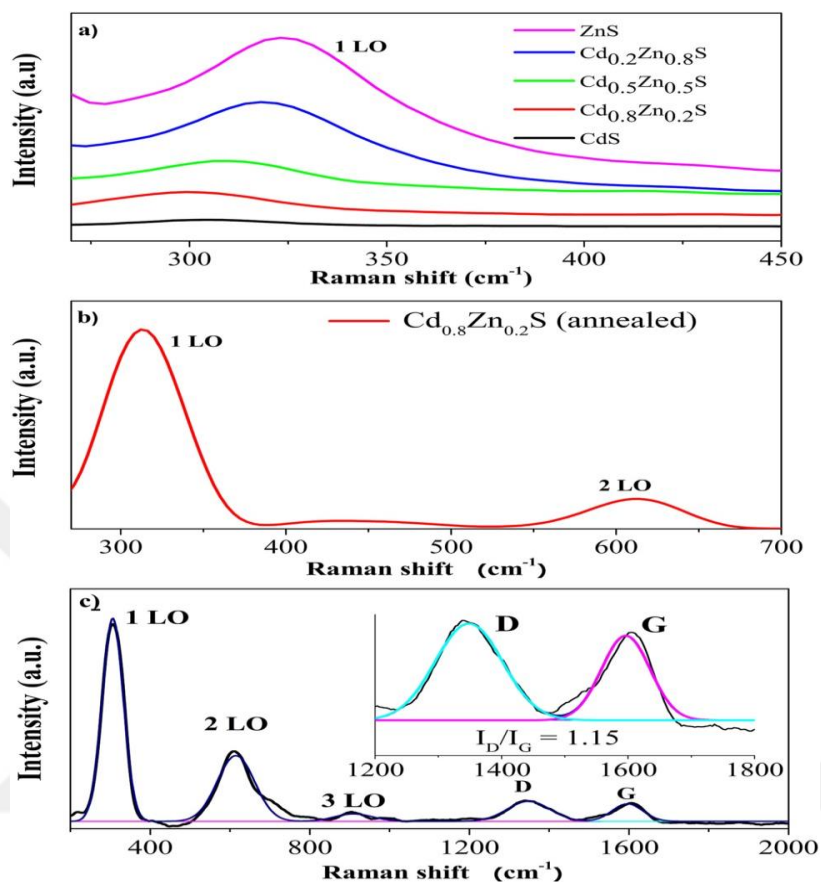


Figure 3.10. Raman spectra of **a)** as-synthesized $Cd_xZn_{1-x}S$ ($x = 0.0, 0.2, 0.5, 0.8, 1.0$), **b)** annealed $Cd_{0.8}Zn_{0.2}S$ and **c)** RGO(0.25)- $Cd_{0.8}Zn_{0.2}S$ thin films.

SEM images of electrodeposited RGO(0.25)- $Cd_{0.8}Zn_{0.2}S$ thin film are represented in Figure 3.11. According to Figure 3.11a., RGO (0.25)- $Cd_{0.8}Zn_{0.2}S$ thin film exhibits almost uniform surface morphology with partial agglomeration [187]. At higher magnification (Figure 3.11b.), RGO sheets are clearly seen with the decoration of $Cd_{0.8}Zn_{0.2}S$ nanoparticles.

Figure 3.11c displays the XRD pattern of RGO (0.25)- $Cd_{0.8}Zn_{0.2}S$ thin film. The figure shows that the diffraction peaks positioned at 2θ values $24.3^\circ, 25.7^\circ, 27.4^\circ, 35.8^\circ, 42.5^\circ, 46.5^\circ, 51.0^\circ$ match well with the (100), (002), (101), (102), (110), (103), and (112) planes of hexagonal $Cd_{0.8}Zn_{0.2}S$, respectively (JCPDS card no: 65-3414) [188]. The

well-resolved broad peak centered at 26.5° and the small diffraction peak at 46.3° are assigned to the presence of (002) and (102) planes of RGO, respectively [189]. The diffractogram also exhibits peaks of ITO substrate (JCPDS card no: 06-0416 (In_2O_3) and 41-1445 (SnO_2)) [190]. The mean crystallite size was determined using the Debye-Scherrer's formula:

$$D = \frac{0.9\lambda_{\text{Ka1(Cu)}}}{\beta_{2\theta} \cos\theta_{\text{max}}} \quad (3.3)$$

β : full-width at half maxima (FWHM) in radians, λ : wavelength of X-rays, D : crystallite size, θ : diffraction angle [191]. The crystallite sizes were in the range of 14.3-36.0 nm, and the mean crystallite size was calculated as 25.7 nm.

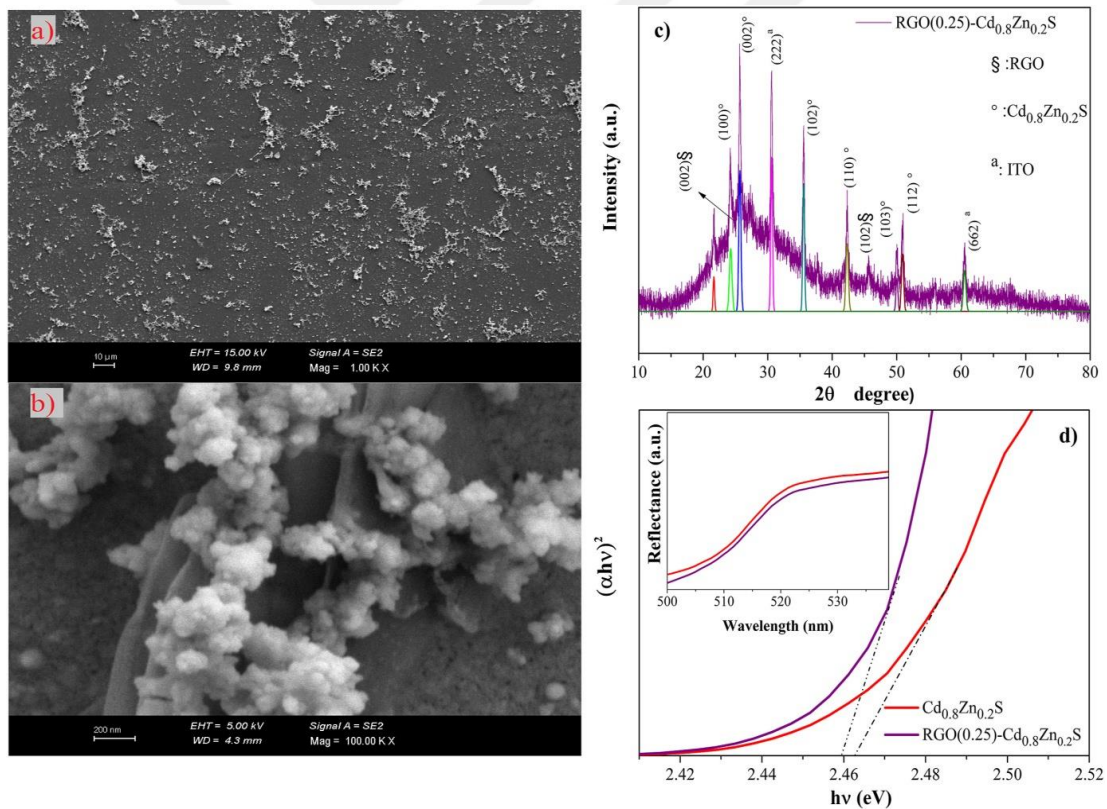


Figure 3.11. SEM images of RGO (0.25)- Cd_{0.8}Zn_{0.2}S at **a)** low and **b)** high magnification. **c)** XRD pattern of RGO(0.25)-Cd_{0.8}Zn_{0.2}S thin film. **d)** UV-vis DRS and Tauc plots of Cd_{0.8}Zn_{0.2}S and RGO(0.25)-Cd_{0.8}Zn_{0.2}S thin films annealed at 450°C.

The UV-vis diffuse reflectance spectra (UV-vis DRS) and Tauc's plots of Cd_{0.8}Zn_{0.2}S (annealed at 450°C) and RGO(0.25)- Cd_{0.8}Zn_{0.2}S (annealed at 450°C) thin films are given in Figure 3.11d. Both spectra demonstrate that the reflection peaks are comparatively similar. The band gap energy values were determined using the Tauc's plot by extrapolating the linear portion of the curve to intersect the hν axis. The band gap values of Cd_{0.8}Zn_{0.2}S (annealed at 450°C) and RGO(0.25)- Cd_{0.8}Zn_{0.2}S (annealed at 450°C) are almost identical (2.46 eV).

EDS spectra indicate the presence of Cd, S, C, and O in RGO (0.25)-Cd_{0.8}Zn_{0.2}S thin film annealed at 450°C (Figure 3.12.). In, Si, and O peaks are also observed which come from the ITO and the glass substrate. RGO in the composite is proven with the existence of C and O elements.

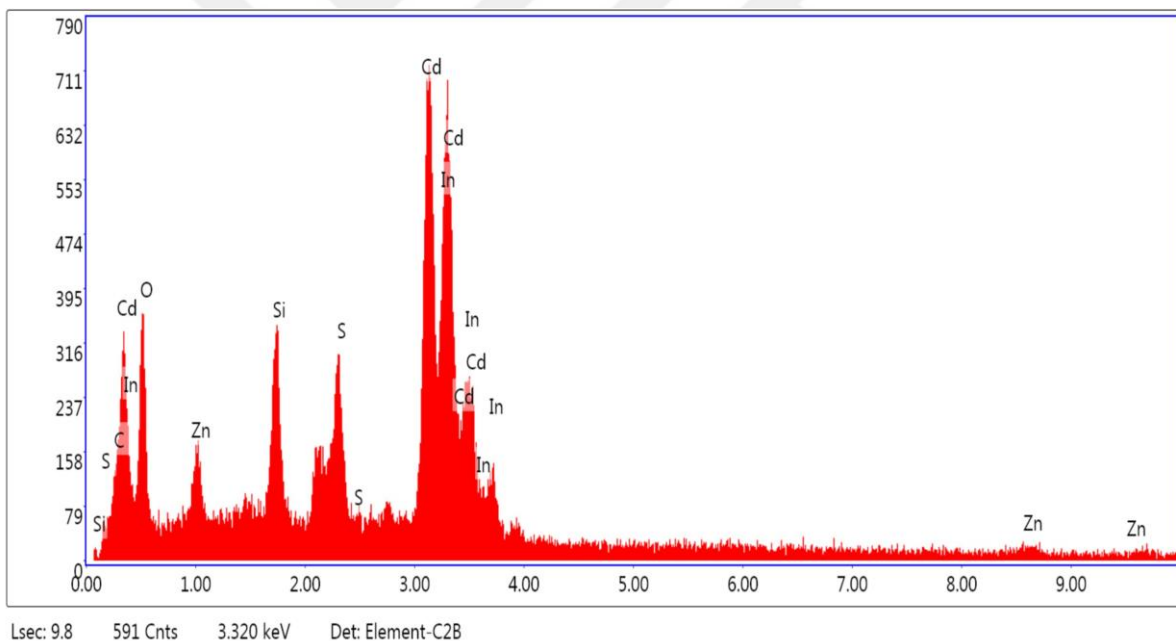


Figure 3.12. EDS spectrum of RGO(0.25)-Cd_{0.8}Zn_{0.2}S thin film annealed at 450°C.

PEC analyses were performed to check the photo-response of photoelectrodes under the presence and absence of illumination. Open circuit potentials (OCPs) of photoelectrodes were measured to investigate the electron-hole generation and transport [192]. OCP measurements were performed under transient solar light illumination with the power intensity held at $1.0 \times 10^3 \text{ W m}^{-2}$ using HAL-320 Solar Simulator. Figure 3.13 shows the

OCP curves of $\text{Cd}_x\text{Zn}_{1-x}\text{S}$ ($x=0.0, 0.2, 0.5, 0.8, 1.0$) (Figure 3.13a), annealed $\text{Cd}_{0.8}\text{Zn}_{0.2}\text{S}$ (350°C and 450°C) (Figure 3.13b), and RGO(0.10, 0.25, 0.50)- $\text{Cd}_{0.8}\text{Zn}_{0.2}\text{S}$ photoelectrodes annealed at 450°C (Figure 3.13c). The reason for choosing to proceed with the $\text{Cd}_{0.8}\text{Zn}_{0.2}\text{S}$ based photoelectrodes (Figure 3.13b and Figure 3.13c) can be explained by its relatively good photo-response, which can also be confirmed by its linear sweep voltammetry (LSV) and chronoamperometry (CA) analyses, compared to other $\text{Cd}_x\text{Zn}_{1-x}\text{S}$ ($x=0.0, 0.2, 0.5, 1.0$) thin films. The photopotentials in Figure 3.13. were measured versus an Ag/AgCl reference electrode, and the potentials were translated to the RHE scale by applying the Nernst equation, as shown in the following equation [193]:

$$E_{\text{RHE}} = E_{\text{Ag/AgCl}} + E^0_{\text{Ag/AgCl}} + 0.059\text{pH} \quad (3.4)$$

where E_{RHE} represents the potential versus RHE, $E_{\text{Ag/AgCl}}$ and $E^0_{\text{Ag/AgCl}}$ indicate potential measured vs. the Ag/AgCl reference electrode, and standard reduction potential of Ag/AgCl reference electrode (0.1976 V vs. RHE at 25°C), respectively.

All photoelectrodes studied in this work, exhibit n-type characteristics since the OCP curves display a negative shift just after the illumination due to the excited photoelectron transfer from photoelectrodes. OCPs reach stabilized values when equilibrium is reached. Subsequently, when the light is turned off, OCPs go towards more positive potential values. The higher values of potential changes indicate that the photoelectrodes exhibit better separation efficiency of photogenerated charges [194]. Figure 3.13a displays the OCP curves of as-synthesized $\text{Cd}_x\text{Zn}_{1-x}\text{S}$ photoelectrodes in the time range from 400 s to 1400 s. The reason for omitting the time interval of 0 s-100 s is the instability of the as-synthesized photoelectrodes. According to the figure, it is clear to say that photoelectrodes with higher Cd/Zn values yield higher OCP values. Namely, the OCP values of ZnS, $\text{Cd}_{0.2}\text{Zn}_{0.8}\text{S}$, $\text{Cd}_{0.5}\text{Zn}_{0.5}\text{S}$, $\text{Cd}_{0.8}\text{Zn}_{0.2}\text{S}$, and CdS are 9 mV, 72 mV, 172 mV, 226 mV, and 185 mV, respectively. This behavior of $\text{Cd}_{0.8}\text{Zn}_{0.2}\text{S}$ can be explained by its greater accumulation of photoinduced charges [195].

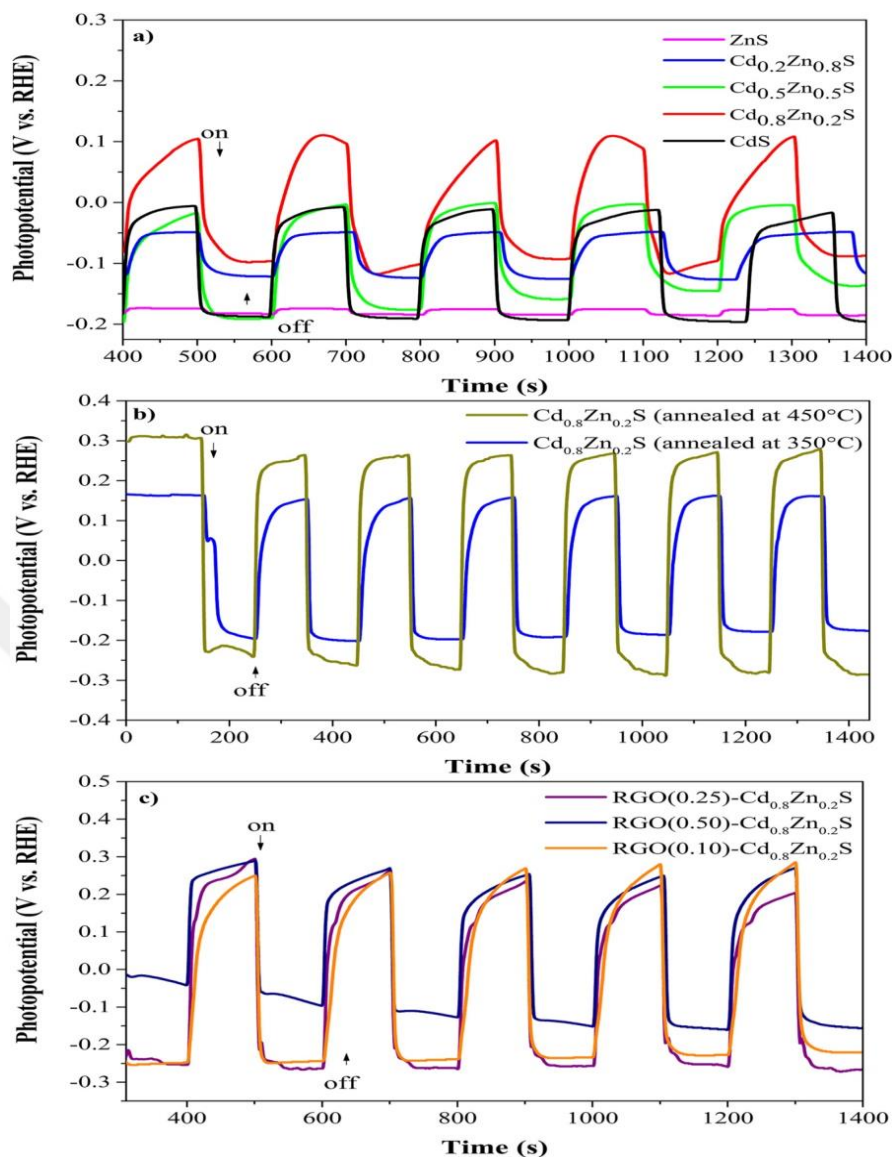


Figure 3.13. Open circuit potential (OCP) curves of **a)** as-synthesized $\text{Cd}_x\text{Zn}_{1-x}\text{S}$ ($x=0.0, 0.2, 0.5, 0.8, 1.0$) photoelectrodes, **b)** $\text{Cd}_{0.8}\text{Zn}_{0.2}\text{S}$ photoelectrodes annealed at 350°C and 450°C, **c)** RGO(0.10, 0.25, 0.50)- $\text{Cd}_{0.8}\text{Zn}_{0.2}\text{S}$ photoelectrodes annealed at 450°C.

Figure 3.13b shows the OCP curves of $\text{Cd}_{0.8}\text{Zn}_{0.2}\text{S}$ photoelectrodes annealed at 350°C and 450°C in an argon atmosphere for 1 h. OCP values of the electrodes annealed at 350°C and 450°C are 357 mV and 506 mV, respectively. Further increasing the annealing temperature decomposes the ITO structure and reduces the conductivity of the electrode.

The enhancement of OCPs of annealed $\text{Cd}_{0.8}\text{Zn}_{0.2}\text{S}$ photoelectrodes can result from the uniform adherence of the deposited thin films on the ITO surface and removal of recombination sites (traps) from the electronic structure under heat treatment in an argon atmosphere. Even though annealed $\text{Cd}_{0.8}\text{Zn}_{0.2}\text{S}$ photoelectrodes exhibit superior properties compared to as-synthesized photoelectrodes, decorating them with RGO promotes mobility of the photogenerated electrons from $\text{Cd}_{0.8}\text{Zn}_{0.2}\text{S}$. Furthermore, RGO increases conductivity and hinders the photo corrosion of $\text{Cd}_{0.8}\text{Zn}_{0.2}\text{S}$ photoelectrodes (Figure 3.13c) [196].

Figure 3.14. shows the linear sweep voltammograms (LSVs) of $\text{Cd}_x\text{Zn}_{1-x}\text{S}$ ($x=0.0, 0.2, 0.5, 0.8, 1.0$) (Figure 3.14a), annealed $\text{Cd}_{0.8}\text{Zn}_{0.2}\text{S}$ ($350^\circ\text{C}, 450^\circ\text{C}$) (Figure 3.14b), and RGO (0.10, 0.25, 0.50)- $\text{Cd}_{0.8}\text{Zn}_{0.2}\text{S}$ photoelectrodes annealed at 450°C (Figure 3.14c). LSV curves of $\text{Cd}_x\text{Zn}_{1-x}\text{S}$ ($x=0.0, 0.2, 0.5, 0.8, 1.0$) photoelectrodes demonstrate minuscule transient spikes which indicate that surface recombination rate is not very high, which is evident in Figure 3.14a. However, $\text{Cd}_{0.8}\text{Zn}_{0.2}\text{S}$ photoelectrode exhibits the most improved photoactivity among all photoelectrodes in Figure 3.14a. $\text{Cd}_{0.8}\text{Zn}_{0.2}\text{S}$ photoelectrode was then annealed in an argon atmosphere at 350°C and 450°C for 1 h. As Figure 3.14b suggests, the enhancement in the photocurrent densities of annealed photoelectrodes may be attributed to the improved crystallinity [197] and possession of more compact and densified structure through annealing [198]. LSV responses of $\text{Cd}_{0.8}\text{Zn}_{0.2}\text{S}$ photoelectrodes were also investigated after RGO decoration and annealing process at 450°C , which is the temperature that minimizes the recombination rate of photoinduced charges. Figure 3.14c shows the LSV curves of RGO(0.10)- $\text{Cd}_{0.8}\text{Zn}_{0.2}\text{S}$, RGO(0.25)- $\text{Cd}_{0.8}\text{Zn}_{0.2}\text{S}$, and RGO(0.50)- $\text{Cd}_{0.8}\text{Zn}_{0.2}\text{S}$ photoelectrodes. Among all tested photoelectrodes, the photo-response of RGO(0.25)- $\text{Cd}_{0.8}\text{Zn}_{0.2}\text{S}$ is the most pronounced one. The first reason for that is the remarkably good bounding of $\text{Cd}_{0.8}\text{Zn}_{0.2}\text{S}$ to the surface of RGO sheets through the van der Waals force and improved interfacial contact that was supplied by the encapsulation of $\text{Cd}_{0.8}\text{Zn}_{0.2}\text{S}$ by the RGO [130]. The second reason is that RGO(0.25)- $\text{Cd}_{0.8}\text{Zn}_{0.2}\text{S}$ photoelectrode possesses the optimum amount of

RGO, since excess RGO might prevent the absorption of light and cause a decrease of the $\text{Cd}_{0.8}\text{Zn}_{0.2}\text{S}$ relative content. This situation leads to the reduction of the number of electrons excited from the valence band to the conduction band of $\text{Cd}_{0.8}\text{Zn}_{0.2}\text{S}$ [199].

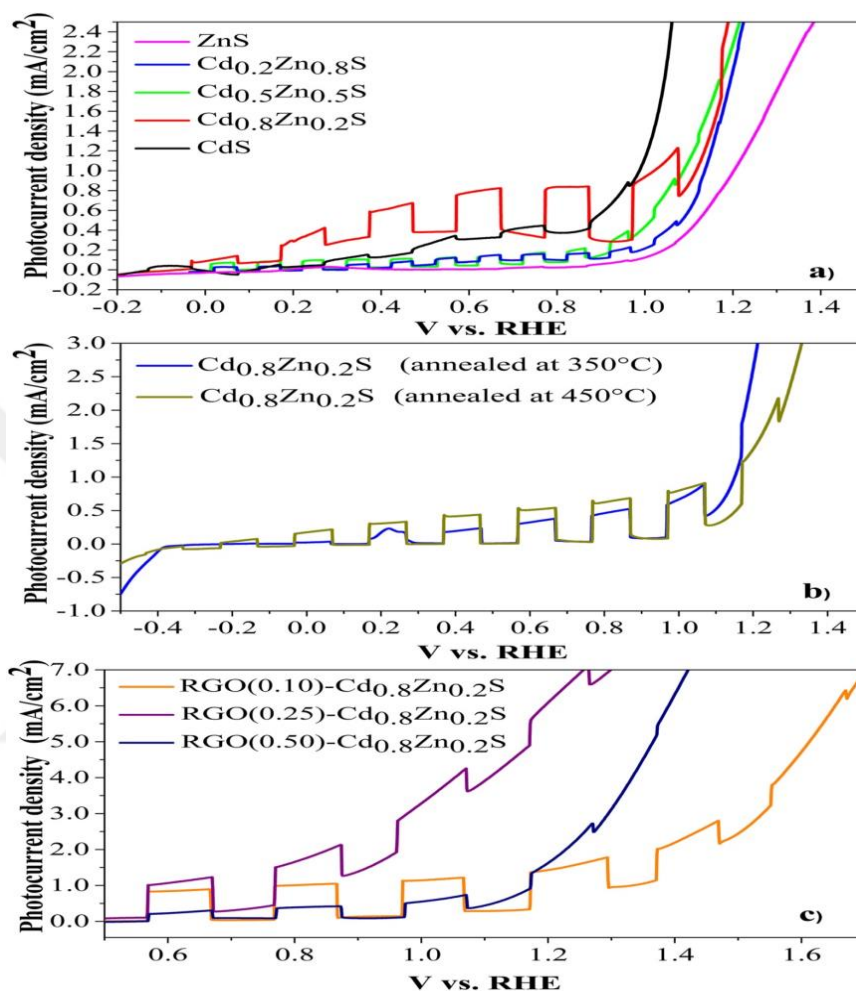


Figure 3.14. Linear sweep voltammetry (LSV) curves of **a)** as-synthesized $\text{Cd}_x\text{Zn}_{1-x}\text{S}$ ($x=0.0, 0.2, 0.5, 0.8, 1.0$) photoelectrodes, **b)** $\text{Cd}_{0.8}\text{Zn}_{0.2}\text{S}$ photoelectrodes annealed at 350°C and 450°C, **c)** RGO(0.10, 0.25, 0.50)- $\text{Cd}_{0.8}\text{Zn}_{0.2}\text{S}$ photoelectrodes annealed at 450°C.

The instantaneous photo-responses of photoelectrodes were studied by applying chronoamperometry (CA) analysis for switch-on and switch-off conditions in 50 s intervals. As depicted in Figure 3.15a, increasing Cd/Zn value from 0.0 to 0.8 in $\text{Cd}_x\text{Zn}_{1-x}\text{S}$ composition boosts the photocurrent density almost 18 folds, reaching from 25 $\mu\text{A cm}^{-2}$ to 438 $\mu\text{A cm}^{-2}$. The photocurrent density values are 193, 117, and 83 $\mu\text{A cm}^{-2}$

cm^{-2} for CdS, $\text{Cd}_{0.5}\text{Zn}_{0.5}\text{S}$, and $\text{Cd}_{0.2}\text{Zn}_{0.8}\text{S}$ photoelectrodes, respectively. However, it is worthy to note that increasing Zn composition in photoelectrodes improves the stability of photoinduced charges. At the end of the 600th second, 21% of the photogenerated electrons of $\text{Cd}_{0.8}\text{Zn}_{0.2}\text{S}$ photoelectrode is degraded. Nevertheless, 100% of photostability is obtained for ZnS photoelectrode. Thus, annealing $\text{Cd}_{0.8}\text{Zn}_{0.2}\text{S}$ thin films was performed to compensate this handicap, since many reports in the literature underscore the enhancement of PEC performance through annealing, by altering the morphology of thin films [200-202].

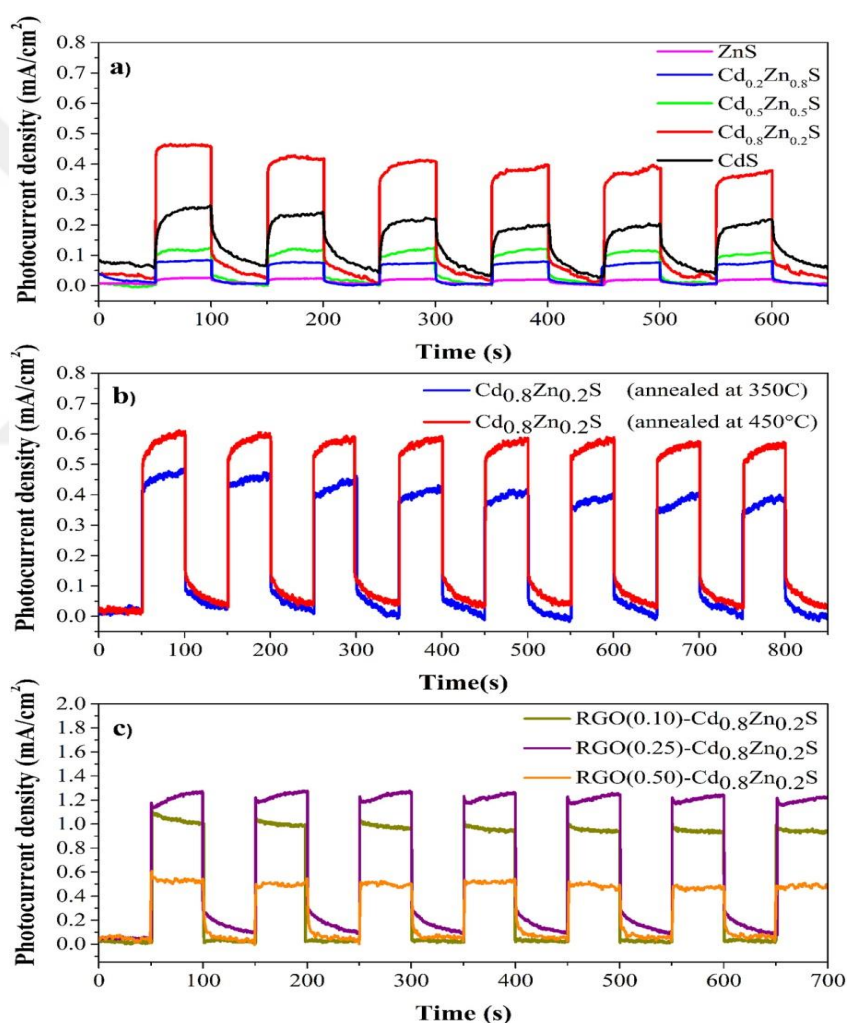


Figure 3.15. Chronoamperometric I-t curves of **a)** as-synthesized $\text{Cd}_x\text{Zn}_{1-x}\text{S}$ ($x=0.0, 0.2, 0.5, 0.8, 1.0$) photoelectrodes, **b)** $\text{Cd}_{0.8}\text{Zn}_{0.2}\text{S}$ photoelectrodes annealed at 350°C and 450°C, **c)** RGO(0.10, 0.25, 0.50)- $\text{Cd}_{0.8}\text{Zn}_{0.2}\text{S}$ photoelectrodes annealed at 450°C.

As the literature survey suggests, photocurrent density values increase from $438 \mu\text{A cm}^{-2}$ (as-synthesized $\text{Cd}_{0.8}\text{Zn}_{0.2}\text{S}$) to 460 and $597 \mu\text{A cm}^{-2}$ values for the photoelectrodes annealed at 350°C , and 450°C , respectively (Figure 3.15b). Moreover, the photostability of annealed $\text{Cd}_{0.8}\text{Zn}_{0.2}\text{S}$ photoelectrodes is enhanced when compared to as-synthesized $\text{Cd}_{0.8}\text{Zn}_{0.2}\text{S}$ photoelectrode due to the improved lattice structure and decrease of defects. In the case of RGO decoration (Figure 3.15c), the photocurrent is quite stable and photocurrent decay is considerably minimal. RGO(0.25)- $\text{Cd}_{0.8}\text{Zn}_{0.2}\text{S}$ photoelectrode exhibits the best PEC performance with the photocurrent value of 1.38 mA cm^{-2} . The photocurrent values of RGO(0.10)- $\text{Cd}_{0.8}\text{Zn}_{0.2}\text{S}$ and RGO(0.50)- $\text{Cd}_{0.8}\text{Zn}_{0.2}\text{S}$ photoelectrodes are 1.05 mA cm^{-2} and 0.52 mA cm^{-2} , respectively. Figure 3.15c implies that the GO concentration should be at an optimum concentration value [203] while co-electrodepositing RGO- $\text{Cd}_{0.8}\text{Zn}_{0.2}\text{S}$ thin films from aqueous solutions.

The rate of hydrogen production of RGO (0.25)- $\text{Cd}_{0.8}\text{Zn}_{0.2}\text{S}$ is estimated using the Faraday's law:

$$n.z=Q/F \quad (3.5)$$

where n is the number of electrons moving per mole of molecules, z is the electrochemical equivalent of the substance, Q is the charge, F is the Faraday's constant (96485 C mol^{-1}). Q is calculated by integrating photocurrent vs. time curve. Thus, the hydrogen production rate of RGO (0.25)- $\text{Cd}_{0.8}\text{Zn}_{0.2}\text{S}$ photoelectrode is calculated as $26.2 \mu\text{moles h}^{-1}$.

Table 3.1. represents the performances of some CdZnS and RGO based photoelectrodes stated in the literature. As shown in the table, there are different photoelectrode preparation methods such as spray pyrolysis [204], chemical bath deposition [123, 205] doctor blading method [203, 206] pulse electrodeposition [207] successive ion layer adsorption and reaction (SILAR) [208], drop coating [209]. In these studies, the photocurrent densities of photoelectrodes were reported between $8.9 \mu\text{A cm}^{-2}$ - $366 \mu\text{A cm}^{-2}$ based on given experimental conditions.

Table 3.1. A representative summary of the performance of Cd, Zn, S, RGO bearing photoelectrodes stated in the literature.

Photoelectrode/ Substrate	Preparation method	Treatment temperatu re	Sacrificial Reagent	Light intensity (mW cm ⁻²)	Photocurrent density (mA cm ⁻²)	Ref.
CdS on FTO	Spray pyrolysis	-	0.1 mol dm ⁻³ Na ₂ S/0.01 mol dm ⁻³ Na ₂ SO ₃	65	0.21	[204]
Zn _{0.2} Cd _{0.8} S on ITO	Chemical bath deposition	-	Na ₂ S/ Na ₂ SO ₃	100	0.20	[123]
Graphene- Zn _{0.8} Cd _{0.2} S	Doctor blading method	-	0.1 mol dm ⁻³ PBS	-	~0.09	[206]
CdS on FTO	Pulse electrodeposition	200°C in Ar	0.1 mol dm ⁻³ Na ₂ S/0.03 mol dm ⁻³ Na ₂ SO ₃	100	~0.2	[207]
CdS on ITO	SILAR method	-	50 mmol Na ₂ S	55	0.125	[208]
CdS on FTO	Chemical bath deposition	350°C in air	0.1 mol dm ⁻³ Na ₂ S/0.01 mol dm ⁻³ Na ₂ SO ₃	80	0.37	[205]
RGO-CdS on ITO	Doctor blading method	450°C in N ₂	0.1 mol dm ⁻³ KNO ₃	-	~0.08	[203]
RGO-CdS:Mn on ITO	One-step drop coating	-	0.1 mol dm ⁻³ KCl/ 5.0 mM K ₃ Fe(CN) ₆ /K ₄ Fe(CN) ₆	-	0.25	[209]
Cd_{0.8}Zn_{0.2}S on ITO	One step electrodeposition	450°C in Ar	0.35 mol dm⁻³ Na₂S/0.25 mol dm⁻³ Na₂SO₃	100	0.597	This work
RGO(0.25)- Cd_{0.8}Zn_{0.2}S on ITO	One step electrodeposition	450°C in Ar	0.35 mol dm⁻³ Na₂S/0.25 mol dm⁻³ Na₂SO₃	100	1.38	This work

The surface doping effect on the charge transfer of RGO(0.25)- Cd_{0.8}Zn_{0.2}S was analyzed by applying electrochemical impedance spectroscopy (EIS). Figure 3.16a represents the Nyquist plots of Cd_{0.8}Zn_{0.2}S and RGO(0.25)- Cd_{0.8}Zn_{0.2}S photoelectrodes annealed at 450°C, without light illumination over a wide range of frequency (10⁻²-10⁵ Hz). The Nyquist plots display arcs in the high frequency area, which proves a single relaxation mechanism during the electrical process [210]. As seen from the inset graph of Figure 3.16a, solution resistance (R_s) values for Cd_{0.8}Zn_{0.2}S and RGO(0.25)- Cd_{0.8}Zn_{0.2}S photoelectrodes are found as 13.46 ohm and 2.56 ohm, respectively. This result suggests that the interaction on the photoelectrode/electrolyte interface is much

better for RGO(0.25)- $\text{Cd}_{0.8}\text{Zn}_{0.2}\text{S}$ photoelectrode [211]. To unveil the charge transfer resistance (R_{ct}) at the photoelectrode/electrolyte interface, the radius of the arc can be considered. The arc radius of RGO(0.25)- $\text{Cd}_{0.8}\text{Zn}_{0.2}\text{S}$ photoelectrode is quite smaller than $\text{Cd}_{0.8}\text{Zn}_{0.2}\text{S}$ photoelectrode revealing the low resistance of RGO(0.25)- $\text{Cd}_{0.8}\text{Zn}_{0.2}\text{S}$, which in turn, eases the separation of e^-/h^+ pairs. Figure 3.16b shows the employed generalized Randles circuit with a finite-length Warburg element. Here, R_s accounts for the series resistance for ohmic and contact effects. R_{ct} is assigned the charge transfer resistance between the electrolyte and photoelectrode interface, and CPE (constant phase element) is the interfacial capacitance parameter [212].

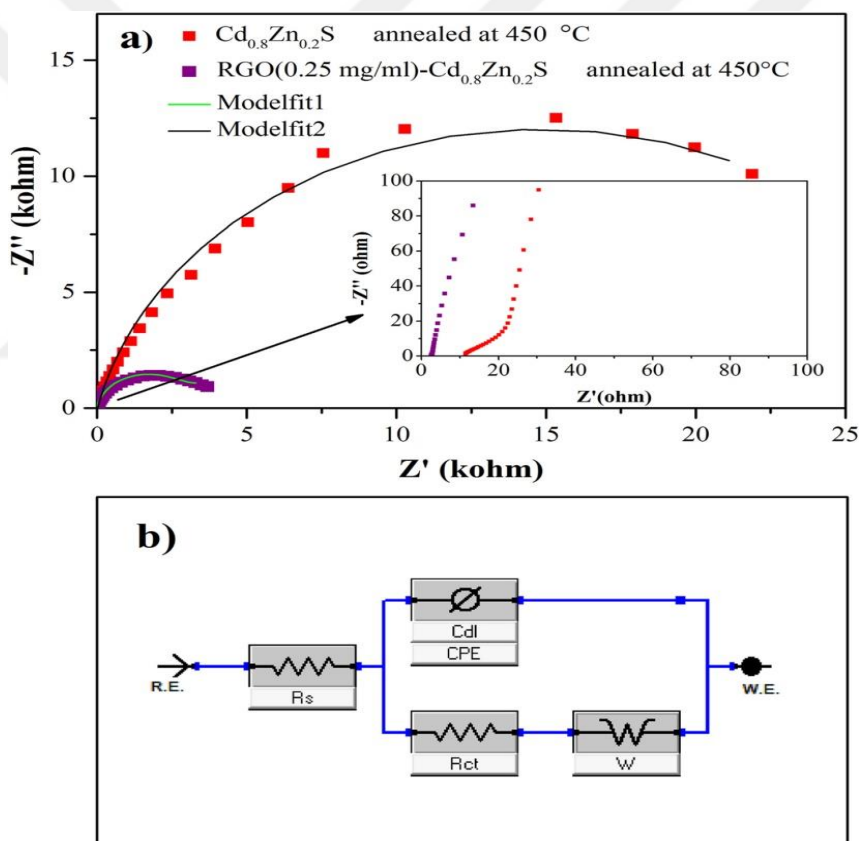


Figure 3.16. a) Nyquist plots of $\text{Cd}_{0.8}\text{Zn}_{0.2}\text{S}$ and RGO(0.25)- $\text{Cd}_{0.8}\text{Zn}_{0.2}\text{S}$ photoelectrodes annealed at 450°C . (Frequency range: 10^{-2} - 10^5 Hz). b) Equivalent circuit model used for EIS data fitting. (R.E.: Reference electrode, W.E: Working electrode, R_s : Series resistance, R_{ct} : Charge transfer resistance, CPE: Constant phase element, W: Finite-length Warburg element).

The fitted data to the experimental Nyquist plots are listed in Table 3.2.

Table 3.2. Fitting results for EIS of Cd_{0.8}Zn_{0.2}S and RGO(0.25)- Cd_{0.8}Zn_{0.2}S photoelectrodes annealed at 450°C.

Photoelectrode	R_s (Ω)	CPE (10⁻⁵sⁿΩ⁻¹)	n (CPE)	W (Ω.s^{-1/2})	R_{ct} (10³Ω cm²)
Cd _{0.8} Zn _{0.2} S	13.46	9.67	0.87	1.06*10 ²	29.60
RGO(0.25)- Cd _{0.8} Zn _{0.2} S	2.56	6.75	0.93	1.42*10 ⁻³	2.97

Mott-Schottky (M-S) analysis provides an insight into the calculation of charge carrier density, determination of flat band potential value, as well as the nature of the photoelectrodes. Here, the M-S plot of the photoelectrode yielding the best PEC properties, RGO(0.25)- Cd_{0.8}Zn_{0.2}S, is given in Figure 3.17. The slope of the M-S plot is positive, which confirms that the photoelectrode exhibits n-type properties. The charge carrier density (N_D) and flat band potential (V_{fb}) were obtained using Mott-Schottky (M-S) equation [213]:

$$1/C^2 = (2/\epsilon_0\epsilon_s e N_D) [(V - V_{fb} - (k_B T/e))] \quad (3.6)$$

where;

C: interfacial capacitance

ε₀: permittivity of free space (8.85 x 10⁻¹² F m⁻¹)

ε_s: the dielectric constant of the deposited material

e: electronic charge

T: temperature in K

k_B: Boltzmann's constant

The M-S plot's x-axis intercept, where the associated 1/C² value reaches zero, was used to determine the flat band potential (V_{fb}). The charge carrier density (N_D) was evaluated

from the slope of the line ($2/\epsilon_0\epsilon_s e N_D$). Thus, V_{fb} and N_D values of the RGO(0.25)- $Cd_{0.8}Zn_{0.2}S$ are -0.44 V vs. RHE and $2.53 \times 10^{18} \text{ cm}^{-3}$, respectively.

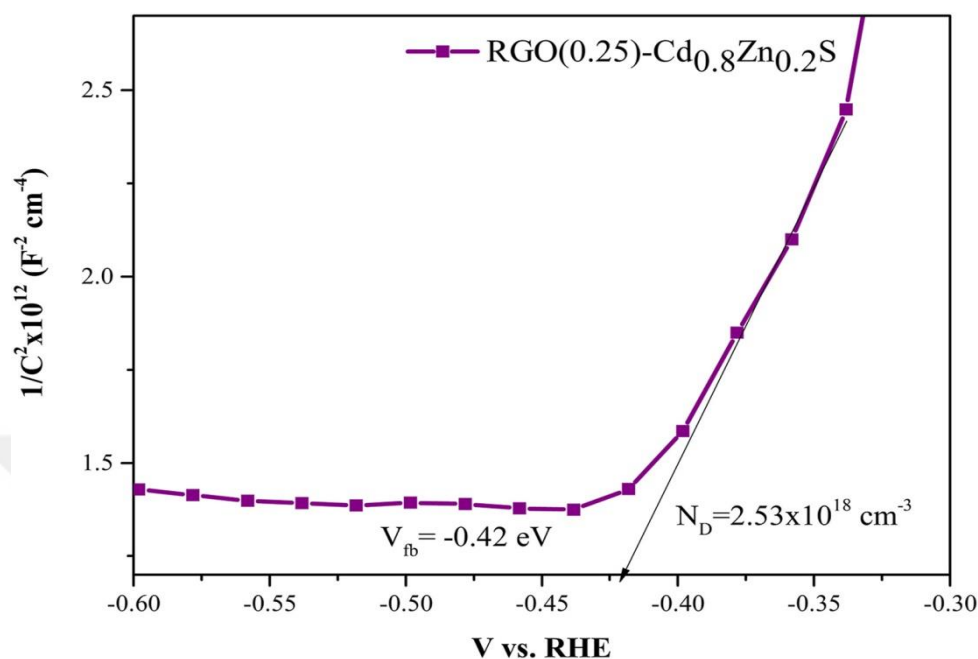


Figure 3.17. M-S plot of ITO/RGO(0.25)- $Cd_{0.8}Zn_{0.2}S$ photoelectrode annealed at 450°C.

It is stated in the literature that the conduction band (CB) edge of an n-type semiconductor is placed at less than 0.1 V of its flat band potential [214]. Therefore, the position of the CB of ITO/RGO(0.25)- $Cd_{0.8}Zn_{0.2}S$ photoelectrode can be predicted as -0.52 V vs. RHE. Since the band gap value of this photoelectrode was calculated as 2.46 eV, the valence band (VB) of RGO(0.25)- $Cd_{0.8}Zn_{0.2}S$ becomes 1.94 eV. Figure 3.18. is quite helpful to enlighten the PEC mechanism of the ITO/RGO(0.25)- $Cd_{0.8}Zn_{0.2}S$ photoelectrode in Na_2S/Na_2SO_3 electrolyte system. Hole formation occurs when electrons from the VB to CB are stimulated by solar radiation, and the photoelectrode is irradiated. Then, the electrons are transported to the Pt cathode to generate H_2 . The photogenerated holes possessing high energy in the VB would oxidize the material when they cannot be quickly removed. In order to avoid this drawback, S^{2-} ions in the electrolyte act as a sacrificial reagent to stabilize the photoelectrode and these ions instantaneously remove holes producing S_2^{2-} by compensating the loss of S^{2-} (Figure

3.18). SO_3^{2-} ions coming from Na_2SO_3 is used to convert S_2^{2-} to $\text{S}_2\text{O}_3^{2-}$ ($\text{S}_2^{2-} + 2\text{SO}_3^{2-} \rightarrow 2\text{S}_2\text{O}_3^{2-} + 2\text{e}^-$). As a result, the hydrogen generation of the PEC system is enhanced and stabilization is ensured by introducing $\text{Na}_2\text{S}/\text{Na}_2\text{SO}_3$ electrolyte as the sacrificial reagent [215].

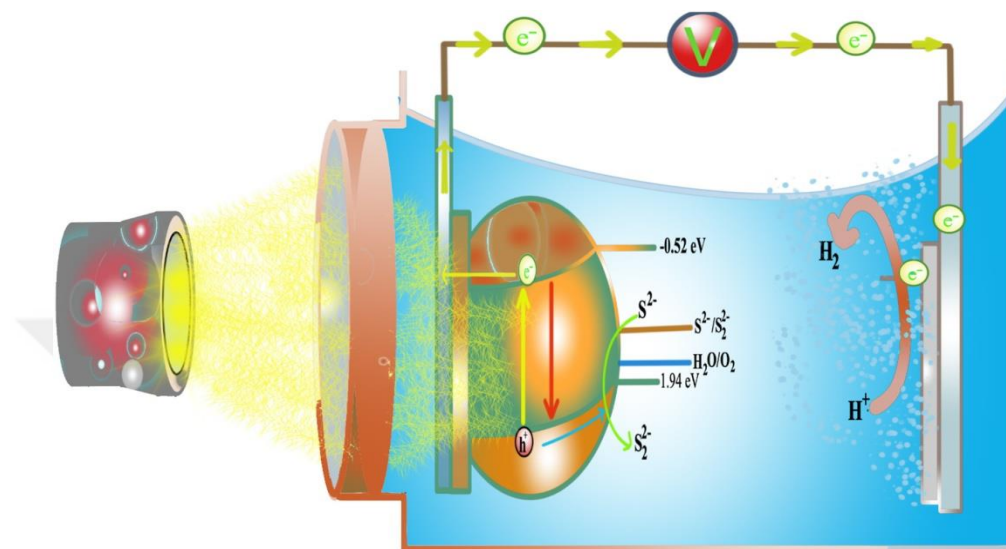


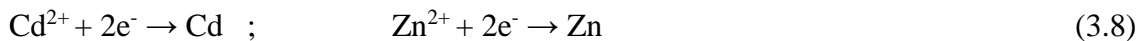
Figure 3.18. Band diagram of ITO/RGO(0.25)- $\text{Cd}_{0.8}\text{Zn}_{0.2}\text{S}$ electrode in PEC hydrogen evolution system.

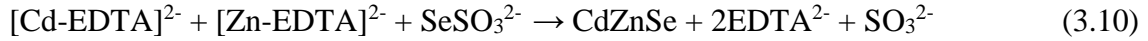
3.2.2. Electrochemical Deposition, Characterization and Photoelectrochemical Performance of CdZnSSe and RGO-CdZnSSe Photoelectrodes

Electrodeposition with the repetitive cyclic voltammetry (rCV) method was used for the synthesis of $\text{Cd}_{0.8}\text{Zn}_{0.2}\text{S}_x\text{Se}_{1-x}$ ($x=0.0, 0.2, 0.5, 0.8, 1.0$) thin films. The aqueous electrolytic bath for electrodeposition reactions consisted of required concentrations of $\text{Cd}(\text{CH}_3\text{COO})_2 \cdot 2\text{H}_2\text{O}$, $\text{Zn}(\text{CH}_3\text{COO})_2 \cdot 2\text{H}_2\text{O}$, $\text{Na}_2\text{S}_2\text{O}_3$, Na_2SeSO_3 and EDTA. The pH of the electrolytic bath was tuned at 8.7. Here, Na_2SeSO_3 solution was prepared at 80°C for 4 hours after dispersing Na_2SO_3 and Se powder in ultrapure water. Rinsed and cleaned ITO coated glass slices served as the substrates of the working electrode. Electrodeposition technique was conducted in a standard three-electrode system. The repetitive cyclic voltammetry technique was conducted at the rate of 100 mV s^{-1} between -1.5 - 1.0 V vs. Ag/AgCl . After that, $\text{ITO}/\text{Cd}_{0.8}\text{Zn}_{0.2}\text{S}_x\text{Se}_{1-x}$ photoelectrodes were thermally treated in a horizontal tube furnace at 350°C in Ar for 1 hour. The $\text{Cd}_{0.8}\text{Zn}_{0.2}\text{S}_{0.2}\text{Se}_{0.8}$ was determined as the best photochemical photoelectrode with the

highest performance. RGO- $\text{Cd}_{0.8}\text{Zn}_{0.2}\text{S}_{0.2}\text{Se}_{0.8}$ photoelectrodes were prepared according to procedure of $\text{Cd}_{0.8}\text{Zn}_{0.2}\text{S}_x\text{Se}_{1-x}$ mentioned above. Besides, the electrolyte also included different amounts of GO powder such as 0.10 mg/ml, 0.25 mg/ml, 0.50 mg/ml to be able to increase and evaluate the photoelectrochemical performance. These thin films were named as RGO(0.10)- $\text{Cd}_{0.8}\text{Zn}_{0.2}\text{S}_{0.2}\text{Se}_{0.8}$, RGO(0.25)- $\text{Cd}_{0.8}\text{Zn}_{0.2}\text{S}_{0.2}\text{Se}_{0.8}$, and RGO(0.50)- $\text{Cd}_{0.8}\text{Zn}_{0.2}\text{S}_{0.2}\text{Se}_{0.8}$.

Figure 3.19. shows the CV curves of $\text{Cd}_{0.8}\text{Zn}_{0.2}\text{S}$ (Figure 3.19a), $\text{Cd}_{0.8}\text{Zn}_{0.2}\text{Se}$ (Figure 3.19b), and $\text{Cd}_{0.8}\text{Zn}_{0.2}\text{S}_{0.2}\text{Se}_{0.8}$ (Figure 3.19c). $\text{Cd}_{0.8}\text{Zn}_{0.2}\text{Se}$ formation was enabled by preparing an aqueous electrolytic bath composed of $\text{Cd}(\text{CH}_3\text{COO})_2$, $\text{Zn}(\text{CH}_3\text{COO})_2$, Na_2SeSO_3 , EDTA, and NaOH. The reason for adding EDTA into the bath is that it avoids the precipitation of the formed hydroxylated Cd(II) and Zn(II) compounds in the pH range between 7-14. Additionally, EDTA is a quite strong ligand so that it can maintain stability of cadmium and zinc ions in the solution. NaOH is used to stabilize the pH of the bath at 8.7. Unlike acidic environment, carrying out co-electrodeposition process in alkaline medium hinders the detrimental effects of hydrogen and improves the overall quality of the growing deposit [216]. The CV voltammogram of $\text{Cd}_{0.8}\text{Zn}_{0.2}\text{Se}$ formation exhibits two cathodic peaks and one anodic peak, located at ca. -1.1, -1.3, -0.6 V vs. Ag/AgCl, respectively. $[\text{Cd-EDTA}]^{2-}$ and $[\text{Zn-EDTA}]^{2-}$ complexes in the electrolytic bath requires a larger overpotential for reduction than needed for Cd^{2+} and Zn^{2+} ions reduction onto ITO surface, because a larger current is necessary break $[\text{Cd-EDTA}]^{2-}$ and $[\text{Zn-EDTA}]^{2-}$ complexes [217]. Zhang et al. also confirmed that the presence of Cd-EDTA complexes shifts the deposition of cadmium to more negative potential values [218]. The cathodic peak at -1.1 V vs. Ag/AgCl can be ascribed to the deposition of Cd from Cd-EDTA complex. In an alkaline bath as used in this study, the peak at ca. -1.3 V vs. Ag/AgCl is related to the reduction of selenosulfate ions. The anodic dissolution of $\text{Cd}_{0.8}\text{Zn}_{0.2}\text{Se}$ occurs at -0.6 V vs. Ag/AgCl. The reactions (3.7, 3.8, 3.9) and the overall reaction (3.10) taking place in the electrodeposition process are [219, 220]:





$\text{Cd}_{0.8}\text{Zn}_{0.2}\text{S}$ deposition takes place in an aqueous bath solution including $\text{Cd}(\text{CH}_3\text{COO})_2$, $\text{Zn}(\text{CH}_3\text{COO})_2$, $\text{Na}_2\text{S}_2\text{O}_3$, EDTA, and NaOH at pH=8.7. There are two cathodic peaks at -1.1 and -1.3 V vs. Ag/AgCl, and two anodic peaks at -1.1 and -0.7 V vs. Ag/AgCl.

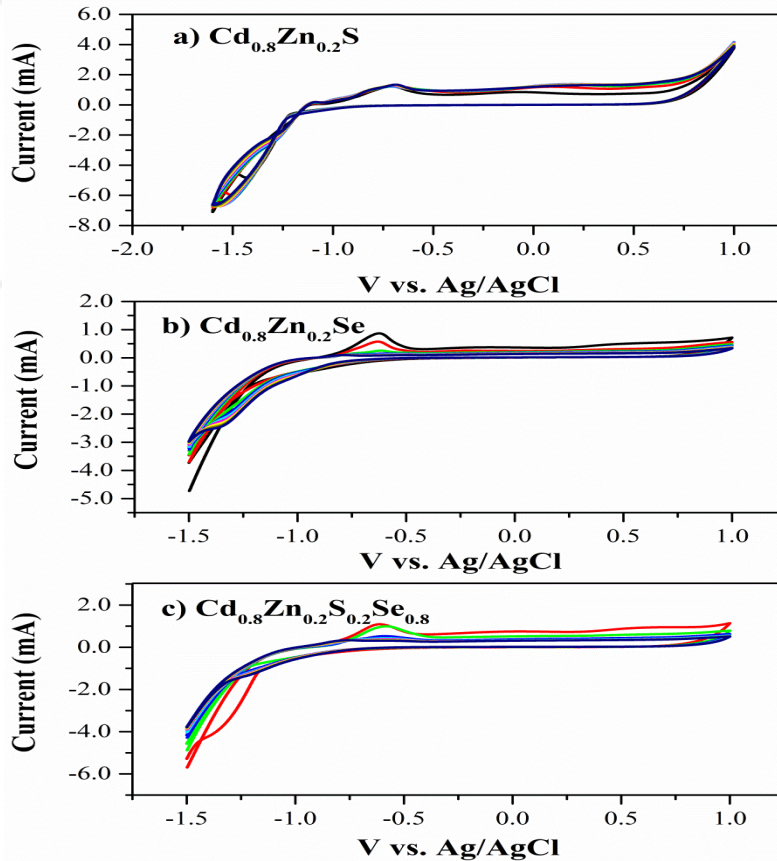


Figure 3.19. rCVs of a) $\text{Cd}_{0.8}\text{Zn}_{0.2}\text{S}$, b) $\text{Cd}_{0.8}\text{Zn}_{0.2}\text{S}$, c) $\text{Cd}_{0.8}\text{Zn}_{0.2}\text{S}_{0.2}\text{Se}_{0.8}$ thin film construction.

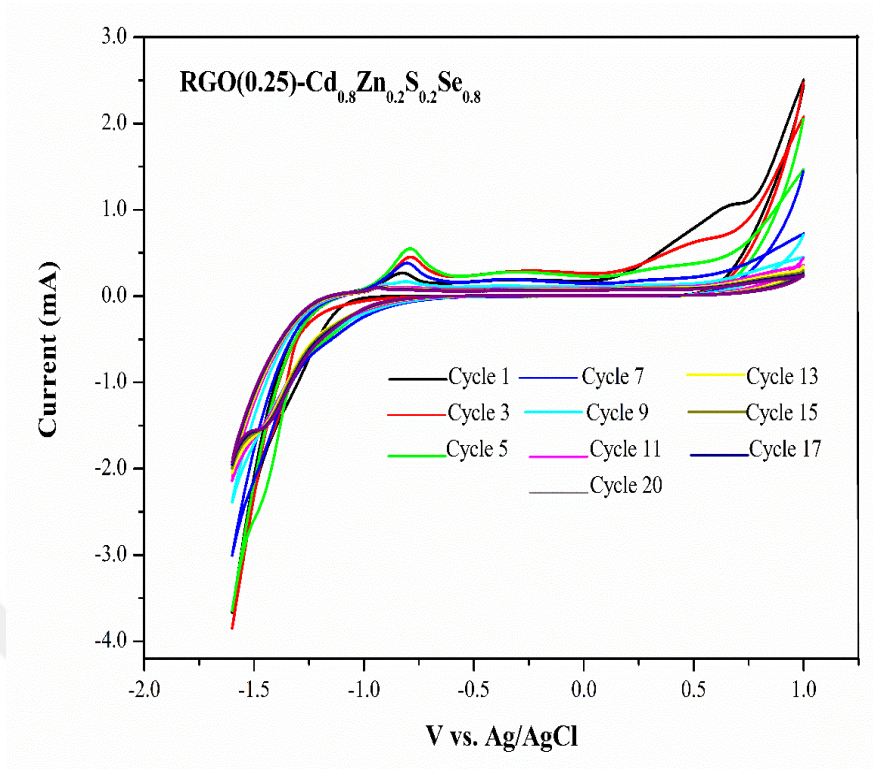


Figure 3.20. rCV curve for the fabrication of RGO- $\text{Cd}_{0.8}\text{Zn}_{0.2}\text{S}_{0.2}\text{Se}_{0.8}$.

Figure 3.21. shows the Raman spectra of $\text{Cd}_{0.8}\text{Zn}_{0.2}\text{S}_{0.2}\text{Se}_{0.8}$ (Figure 3.21a) and RGO(0.25)- $\text{Cd}_{0.8}\text{Zn}_{0.2}\text{S}_{0.2}\text{Se}_{0.8}$ (Figure 3.21b) recorded with laser excitation at 532 nm. The bands positioned at 177 cm^{-1} , 202 cm^{-1} , 418 cm^{-1} , and 615 cm^{-1} belong to the Raman modes of TO (transverse optical phonon), 1LO (longitudinal optical phonon) and 2LO bands of CdZnSSe [222].

D and G bands of RGO are discussed in Figure 3.9. in detail. In Figure 3.9, the peaks of synthesized GO were fitted to Lorentzian functions ($R^2=0.992$), while RGO gave the best fit to Gaussian functions ($R^2=0.989$). GO exhibits peaks called as D and G bands at 1359 cm^{-1} and 1596 cm^{-1} .

The D and G bands positioned at 1359 cm^{-1} and 1562 cm^{-1} belong to RGO. The intensity ratio (I_D/I_G) for GO is calculated as 0.65. Upon reduction of GO during electrodeposition, I_D/I_G increases to 0.82 due to the restoration of sp^2 carbon atoms and decrease in mean sizes of sp^2 domains. Furthermore, the positions of the D and G bands shift and get closer to each other for RGO [223].

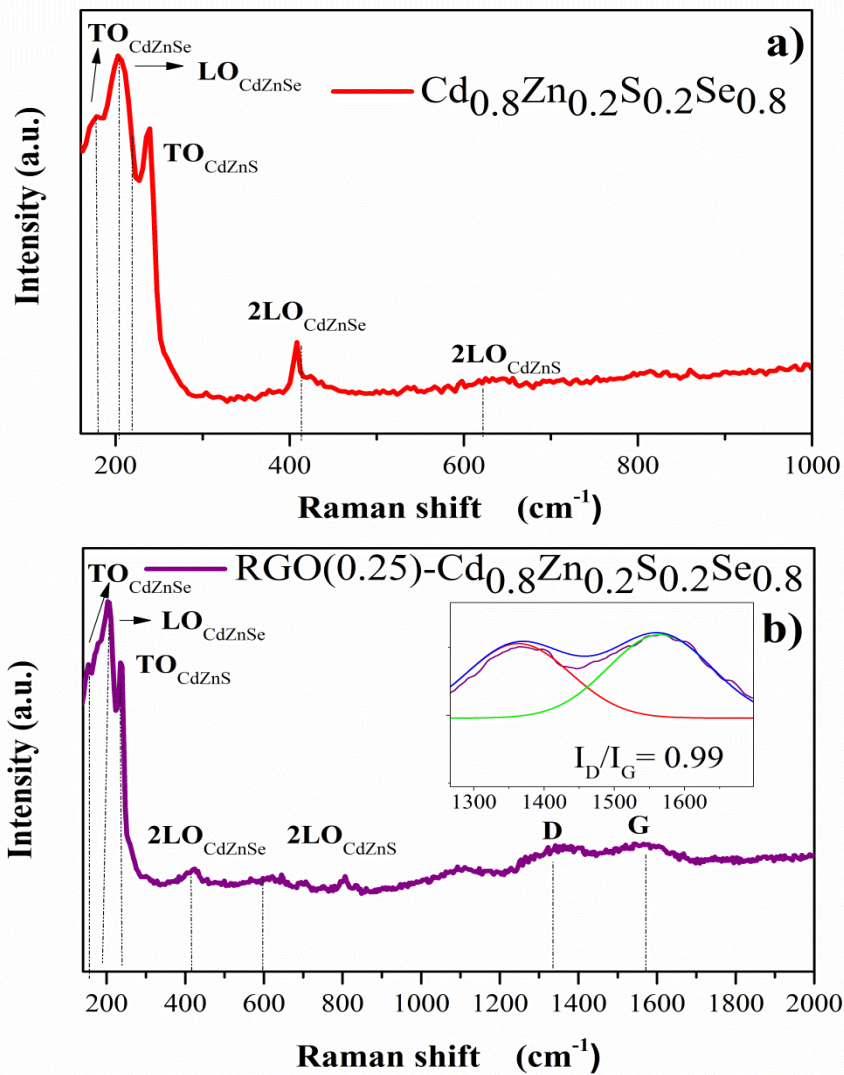


Figure 3.21. Raman spectra of **a)** $\text{Cd}_{0.8}\text{Zn}_{0.2}\text{S}_{0.2}\text{Se}_{0.8}$, **b)** $\text{RGO-Cd}_{0.8}\text{Zn}_{0.2}\text{S}_{0.2}\text{Se}_{0.8}$ thin films.

The FESEM images of $\text{Cd}_{0.8}\text{Zn}_{0.2}\text{S}_{0.2}\text{Se}_{0.8}$ and $\text{RGO}(0.25)\text{-Cd}_{0.8}\text{Zn}_{0.2}\text{S}_{0.2}\text{Se}_{0.8}$ thin films are presented on Figure 3.22. FESEM images were recorded at low (Figure 3.22a) and high (Figure 3.22b) magnifications.

Based on Figure 3.22a, thin films have compact and dense surface morphology with some cluster formation on some points. However, with the presence of RGO in the structure, the cluster formation has been diminished and smoother surface has been achieved. At high magnification (Figure 3.22b), RGO sheets are clearly observed around $\text{Cd}_{0.8}\text{Zn}_{0.2}\text{S}_{0.2}\text{Se}_{0.8}$ particles.

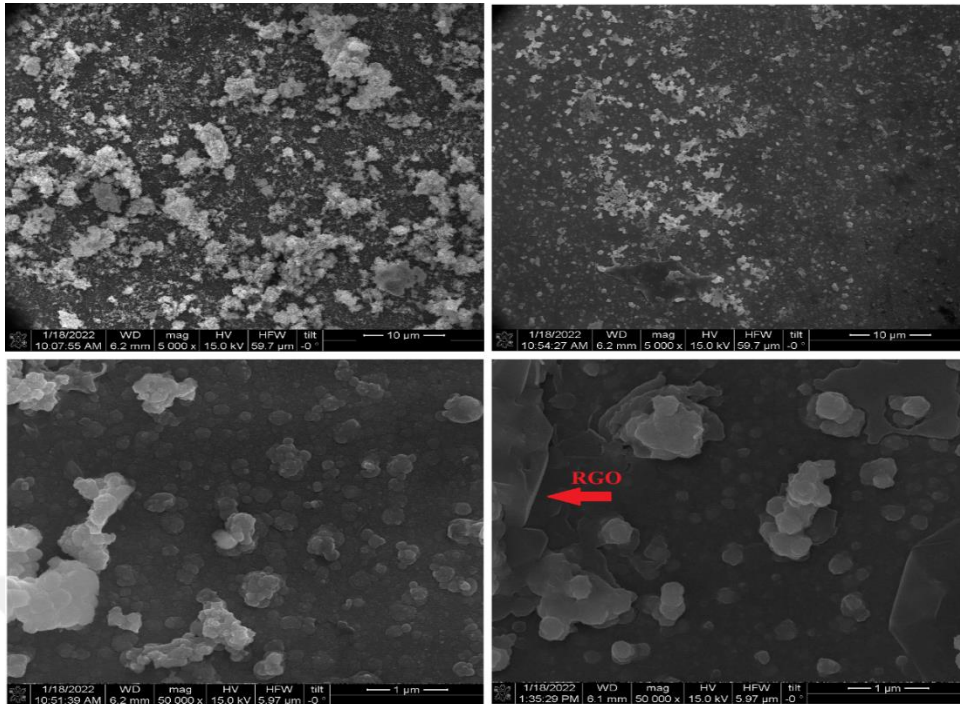


Figure 3.22. FESEM images of $\text{Cd}_{0.8}\text{Zn}_{0.2}\text{S}_{0.2}\text{Se}_{0.8}$ and $\text{RGO-Cd}_{0.8}\text{Zn}_{0.2}\text{S}_{0.2}\text{Se}_{0.8}$ thin films at **a)** low (x5000) and **b)** high (x50000) magnifications.

EDS spectra demonstrates the existence of Cd, Zn, S, Se, C, and O in $\text{RGO (0.25)-Cd}_{0.8}\text{Zn}_{0.2}\text{S}_{0.2}\text{Se}_{0.8}$ thin film fabricated on ITO (Figure 3.23). Furthermore, the detected In, Si, and O peaks are attributed to originate from the ITO and the glass substrate. RGO in the composite thin film is verified with the presence of C and O elements.

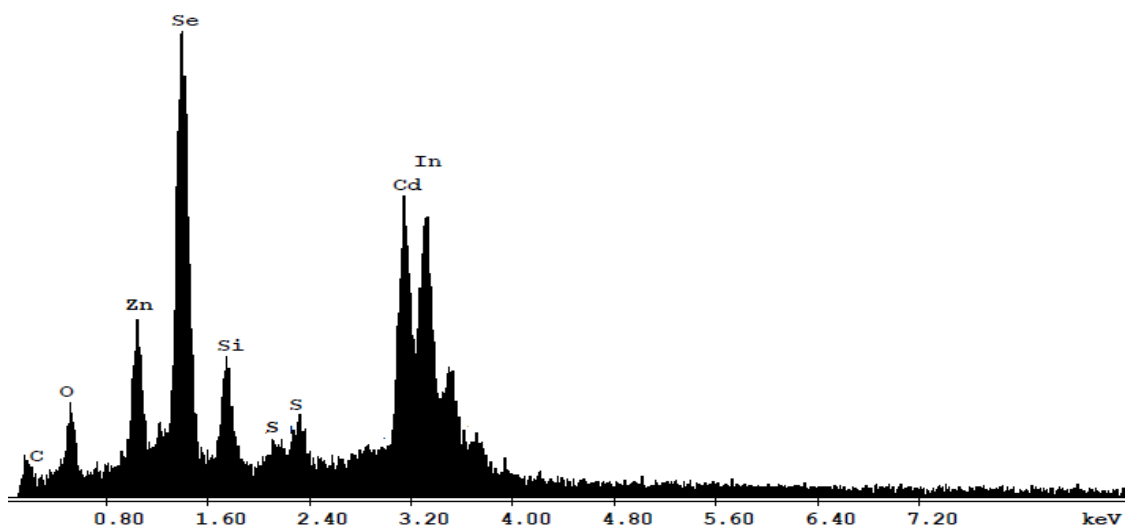


Figure 3.23. EDS spectrum of $\text{RGO(0.25)-Cd}_{0.8}\text{Zn}_{0.2}\text{S}_{0.2}\text{Se}_{0.8}$ photoelectrode.

To investigate the chemical states and surface chemical compositions of composites, XPS measurements were performed. (Figure 3.24.) The XPS full spectrum (survey) scan confirms the presence of the characteristic peaks of Cd 3d, Zn 2p, S 2p, and Se 3d. Each XPS spectrum is deconvoluted into peaks by Gaussian fitting through Origin software. The C1s element on survey spectrum can be assigned to the trace hydrocarbon coming from the XPS instrument since it is used as the reference peak [224].

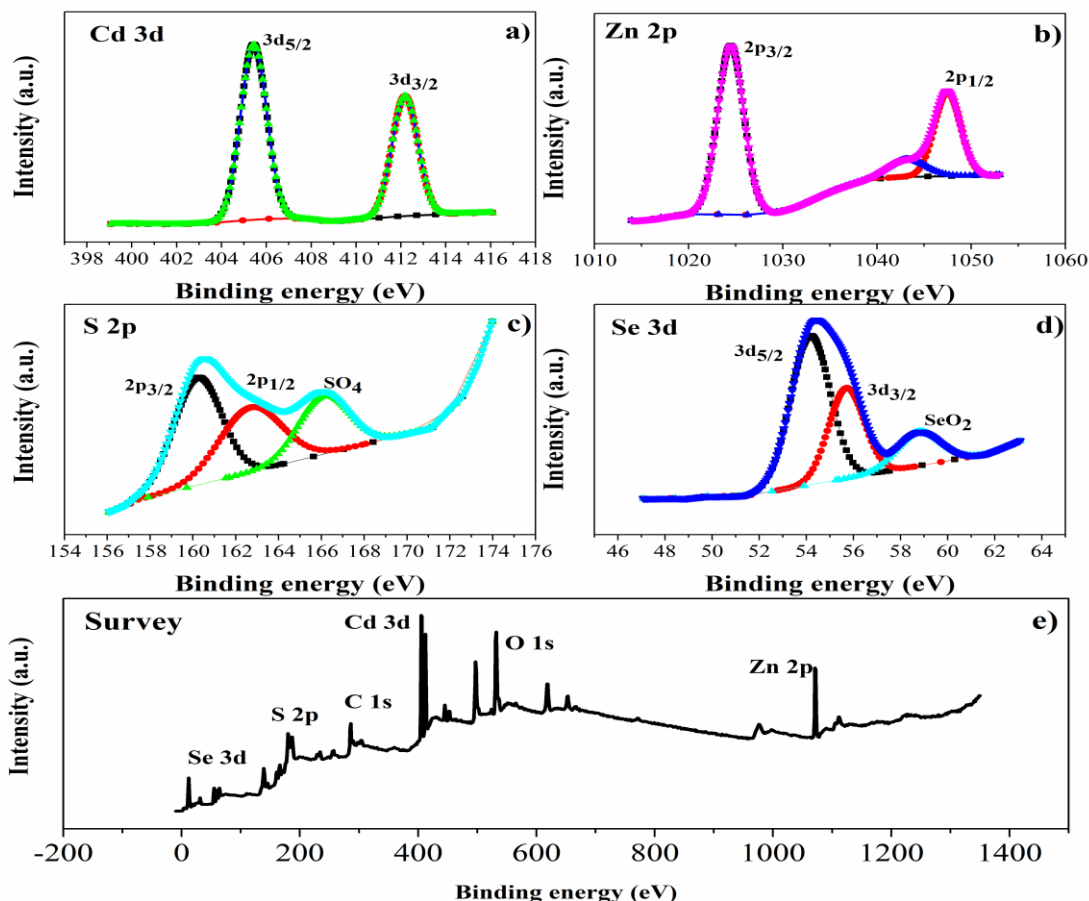


Figure 3.24. X-ray photoelectron spectroscopy (XPS) spectra of Cd_{0.8}Zn_{0.2}S_{0.2}Se_{0.8}. **a)** Cd 3d, **b)** Zn 2p, **c)** S 2p, **d)** Se 3d, **e)** Survey.

The binding energies of Cd 3d are positioned at 405.5 eV (3d_{5/2}) and 412.2 eV (3d_{3/2}) and the difference in binding energy between two peaks is 6.7 eV indicating that Cd is present in the form of Cd²⁺ [225]. The Zn 2p spectrum is fitted by deconvoluting the two 2p_{3/2} and 2p_{1/2} peaks at 1024 eV and 1047 eV impaired with a satellite peak, respectively [226]. The spin-orbit splitting of Zn 2p_{3/2} and 2p_{1/2} is 23 eV which is attributed to ZnS and ZnSe bonding.

S 2p XPS spectrum displays 2 noticeable peaks located at 160.6 eV and 163.0 eV, which is related with the core levels of and $2p_{3/2}$ and $2p_{1/2}$, respectively. Se 3d spectrum is deconvoluted into peaks at 54.5, 53.6 eV which are assigned to $3d_{3/2}$ and Se $3d_{5/2}$. The broad peak at 58.8 eV can arise from Se-oxygen bonding structure, which results from the oxidation state of Se species [227].

Figure 3.25. represents the XPS spectra of RGO- $\text{Cd}_{0.8}\text{Zn}_{0.2}\text{S}_{0.2}\text{Se}_{0.8}$. Apart from the Cd 3d, Zn 2p, S 2p and Se 3d spectra, the peaks of C 1s and O 1s spectra are also investigated. C 1s spectrum is decomposed into three peaks composed of C-C/C=C (285.0 eV), C-O (286.8 eV), C=O (289.2 eV), indicating the presence of RGO [228]. Oxygenated functional groups of RGO are observed in the form of C=O/O=C-OH (529.7 eV), C-O (531.7 eV), H_2O (533.7 eV), C-OH (536.0 eV) groups [229].

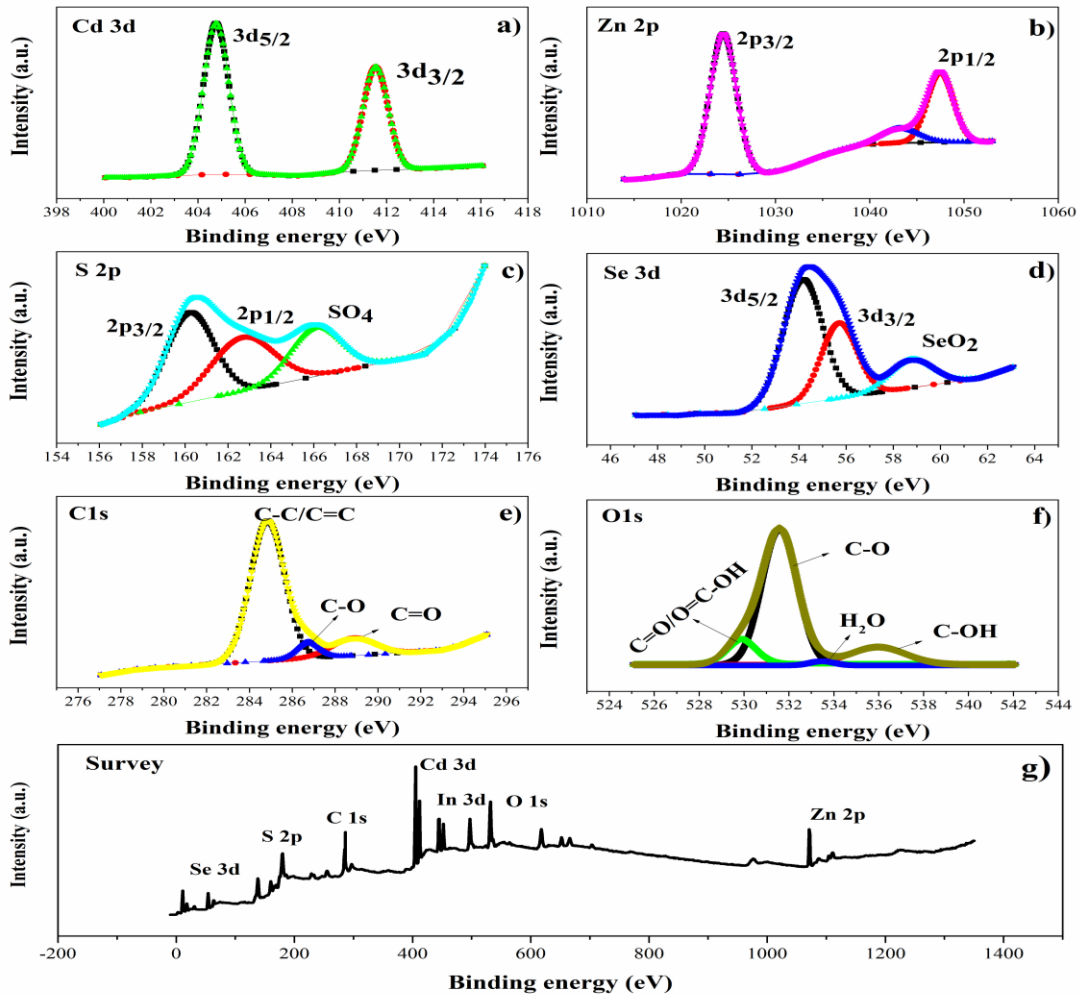


Figure 3.25. X-ray photoelectron spectroscopy (XPS) spectra of RGO- $\text{Cd}_{0.8}\text{Zn}_{0.2}\text{S}_{0.2}\text{Se}_{0.8}$. a) Cd 3d, b) Zn 2p, c) S 2p, d) Se 3d, e) C 1s, f) O 1s, g) Survey.

Figure 3.26a shows the XRD patterns for $\text{Cd}_{0.8}\text{Zn}_{0.2}\text{Se}$, $\text{Cd}_{0.8}\text{Zn}_{0.2}\text{S}_{0.2}\text{Se}_{0.8}$, and RGO- $\text{Cd}_{0.8}\text{Zn}_{0.2}\text{S}_{0.2}\text{Se}_{0.8}$ and they indicate peaks centered at around $2\theta=24.1^\circ$, 25.4° , 27.3° , 42.1° , 49.9° . These peaks can be ascribed to the (100), (002), (101), (110), (112) planes of hexagonal structure of CdZnSSe (JCPDS Card no. 49-1459) [230]. The (002) and (102) planes of RGO is at $2\theta= 26.40^\circ$ and 45.18° , respectively. Thus, the pattern of RGO- $\text{Cd}_{0.8}\text{Zn}_{0.2}\text{S}_{0.2}\text{Se}_{0.8}$ reveals that the intensity of RGO peaks is higher than $\text{Cd}_{0.8}\text{Zn}_{0.2}\text{Se}$, $\text{Cd}_{0.8}\text{Zn}_{0.2}\text{S}_{0.2}\text{Se}_{0.8}$. The average crystallite size has been calculated by deconvoluting peaks to determine the full-width-half-maximum (FWHM) and peak positions. Accordingly, Debye-Scherrer's formula was employed [231]:

$$D=(0.9\lambda_{\text{K}\alpha 1}(\text{Cu})) / (\beta_{2\theta} \cos \theta_{\text{max}}) \quad (3.3)$$

where k is a constant equal to 0.9, λ is the wavelength of X-ray used, β is the full-width-half-maximum (FWHM), θ is the diffraction angle. The average crystallite size is calculated as 94 nm.

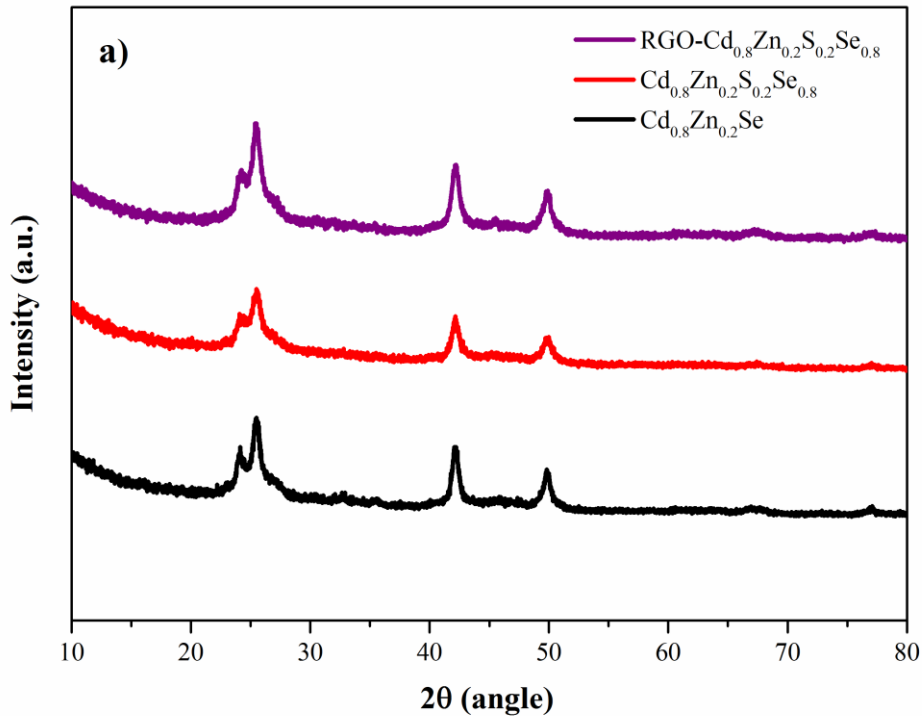


Figure 3.26. XRD patterns of $\text{Cd}_{0.8}\text{Zn}_{0.2}\text{Se}$, $\text{Cd}_{0.8}\text{Zn}_{0.2}\text{S}_{0.2}\text{Se}_{0.8}$, RGO- $\text{Cd}_{0.8}\text{Zn}_{0.2}\text{S}_{0.2}\text{Se}_{0.8}$ thin films.

To evaluate the optical properties of photoelectrodes, UV-vis DRS spectra were recorded. Figure 3.27. shows that introducing RGO to the $\text{Cd}_{0.8}\text{Zn}_{0.2}\text{S}_{0.2}\text{Se}_{0.8}$ photoelectrode leads to slight red-shift of the absorption edge because of the less transparency of fabricated photoelectrode [232]. The band gap values of RGO(0.25)- $\text{Cd}_{0.8}\text{Zn}_{0.2}\text{S}_{0.2}\text{Se}_{0.8}$ and $\text{Cd}_{0.8}\text{Zn}_{0.2}\text{S}_{0.2}\text{Se}_{0.8}$ are estimated based on Kubelka-Munk function [233]:

$$(\alpha h\nu)^2 = A(h\nu - E_g) \quad (3.1)$$

where α , $h\nu$, A and E_g are absorption coefficient, photon energy, proportionality constant, and band gap, respectively. The band gap energies are determined as 1.75, 1.84, 1.80 and 2.47 eV for $\text{Cd}_{0.8}\text{Zn}_{0.2}\text{Se}$, $\text{Cd}_{0.8}\text{Zn}_{0.2}\text{S}_{0.2}\text{Se}_{0.8}$, RGO (0.25)- $\text{Cd}_{0.8}\text{Zn}_{0.2}\text{S}_{0.2}\text{Se}_{0.8}$, and $\text{Cd}_{0.8}\text{Zn}_{0.2}\text{S}$ photoelectrodes.

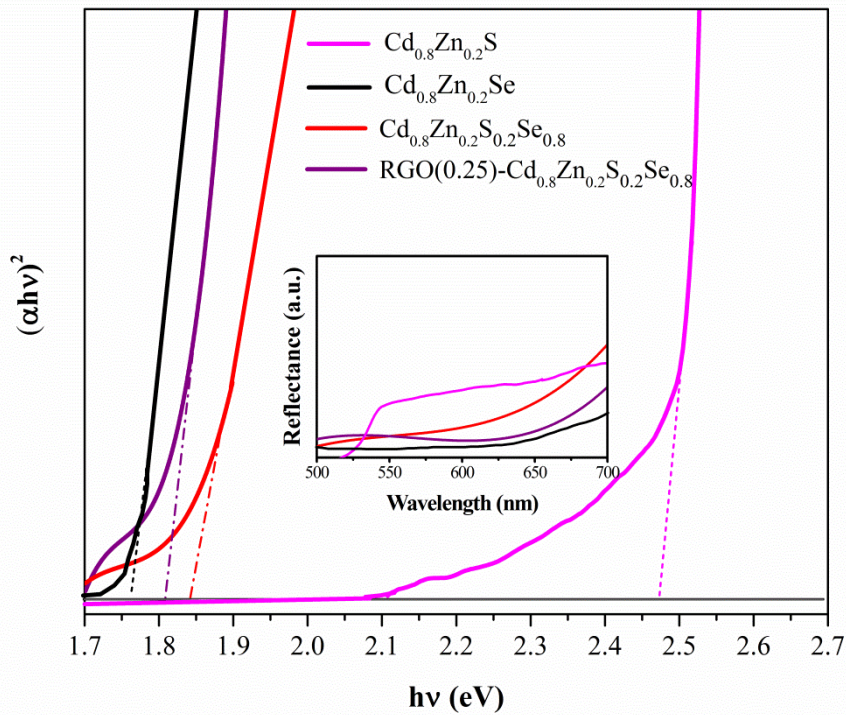


Figure 3.27. UV-vis DRS (inset) and Tauc plots of $\text{Cd}_{0.8}\text{Zn}_{0.2}\text{S}$, $\text{Cd}_{0.8}\text{Zn}_{0.2}\text{Se}$, $\text{Cd}_{0.8}\text{Zn}_{0.2}\text{S}_{0.2}\text{Se}_{0.8}$ and RGO- $\text{Cd}_{0.8}\text{Zn}_{0.2}\text{S}_{0.2}\text{Se}_{0.8}$ thin films.

Photoelectrochemical performances of photoelectrodes were studied through a three electrode system in $\text{Na}_2\text{S}/\text{Na}_2\text{SO}_3$ sacrificial reagent. Here, sulfide (S^{2-}) and sulfite (SO_3^{2-}) anions act as efficient reducing agents to scavenge photogenerated holes to

oxidize S^{2-} into disulfide (S_2^{2-}) anions, and SO_3^{2-} into sulfate (SO_4^{2-}) and dithionate $S_2O_6^{2-}$ [234]. PEC properties of photoelectrodes were investigated in a standard three-electrode configuration. Figure 3.28. displays the linear sweep voltammograms (LSVs) of fabricated photoelectrodes under chopped 1 Sun (AM 1.5G) illumination. Figure 3.28a. represents the LSV curves of $Cd_{0.8}Zn_{0.2}S$, $Cd_{0.8}Zn_{0.2}S_{0.8}Se_{0.2}$, $Cd_{0.8}Zn_{0.2}S_{0.5}Se_{0.5}$, $Cd_{0.8}Zn_{0.2}S_{0.2}Se_{0.8}$, $Cd_{0.8}Zn_{0.2}Se$ annealed at $350^\circ C$ in argon gas flow for 1 h. Annealing treatment is necessary to improve the contact between the thin film and ITO substrate in order to suppress electron-hole charge recombination [235]. Linear sweep voltammograms (LSVs) were obtained in a potential range between -0.2 V vs. RHE and 1.8 V vs. RHE. RHE stands for the reversible hydrogen electrode (RHE) scale converted by using the Nerst equation [236]:

$$V_{RHE} = V_{Ag/AgCl} + 0.059 \times pH + V^0_{Ag/AgCl} \quad (3.4)$$

where $V^0_{Ag/AgCl} = 0.197$ V and $pH_{electrolyte} = 13.0$

According to Figure 3.28a, $CdS_{0.2}Se_{0.8}$ photoelectrode exhibits relatively higher photocurrent density among all tested photoelectrodes. This situation arises from the low rate of electron-hole recombination rate experienced during LSV analysis. Besides, the best performance of $CdS_{0.2}Se_{0.8}$ photoelectrode is accompanied by the most negative shift of its onset potential.

Figure 3.28b represents linear sweep voltammograms of RGO(0.10)- $Cd_{0.8}Zn_{0.2}S_{0.2}Se_{0.8}$, RGO(0.25)- $Cd_{0.8}Zn_{0.2}S_{0.2}Se_{0.8}$, RGO(0.50)- $Cd_{0.8}Zn_{0.2}S_{0.2}Se_{0.8}$ photoelectrodes. The light was switched on and off at regular intervals causing a fast current upshot followed by decay. RGO acts as a conductive-bridge linker, promotes electron-hole separation, and improves photocurrent to different degrees [237]. Several reports in the literature are in agreement with this statement [134, 150, 238, 239]. Nevertheless, excessive mass loading of RGO in the photoelectrode may result in blocking the active species and prevention of the light absorption. As a consequence, an optimization of RGO amount is required to utilize solar energy effectively and improve the photoelectrochemical performance [240]. Clearly, Figure 3.28b suggests that RGO(0.25)- $Cd_{0.8}Zn_{0.2}S_{0.2}Se_{0.8}$ exhibits superior photoelectrochemical characteristics.

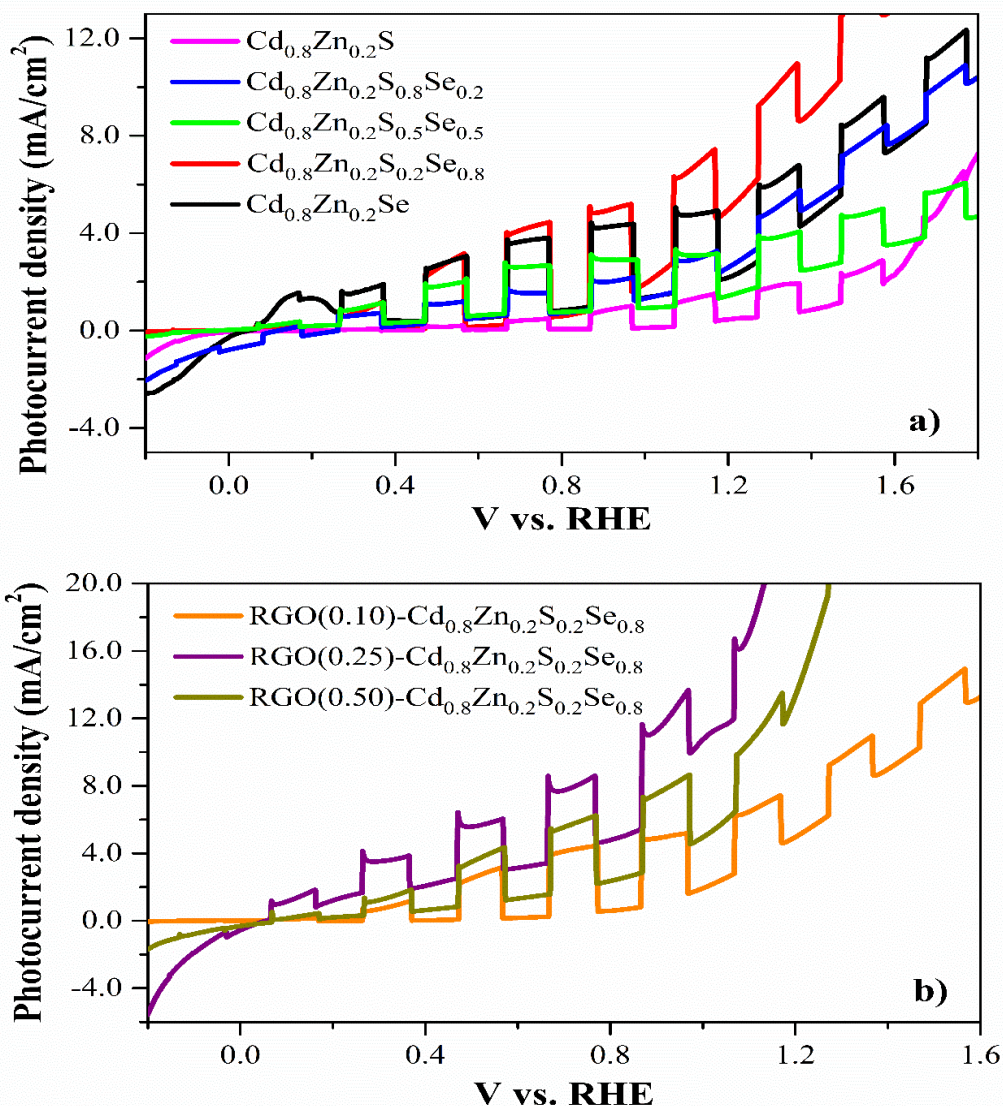


Figure 3.28. LSV curves of **a)** $\text{Cd}_{0.8}\text{Zn}_{0.2}\text{S}_x\text{Se}_{1-x}$ ($x=0.0, 0.2, 0.5, 0.8, 1.0$) and **b)** $\text{RGO}(0.10, 0.25, 0.50)\text{-Cd}_{0.8}\text{Zn}_{0.2}\text{S}_{0.2}\text{Se}_{0.8}$ photoelectrodes.

The transient photocurrent density (I)-time (t) curves of $\text{Cd}_{0.8}\text{Zn}_{0.2}\text{S}$, $\text{Cd}_{0.8}\text{Zn}_{0.2}\text{S}_{0.8}\text{Se}_{0.2}$, $\text{Cd}_{0.8}\text{Zn}_{0.2}\text{S}_{0.5}\text{Se}_{0.5}$, $\text{Cd}_{0.8}\text{Zn}_{0.2}\text{S}_{0.2}\text{Se}_{0.8}$, $\text{Cd}_{0.8}\text{Zn}_{0.2}\text{Se}$ (Figure 3.29a), and $\text{RGO}(0.10)\text{-Cd}_{0.8}\text{Zn}_{0.2}\text{S}_{0.2}\text{Se}_{0.8}$, $\text{RGO}(0.25)\text{-Cd}_{0.8}\text{Zn}_{0.2}\text{S}_{0.2}\text{Se}_{0.8}$, $\text{RGO}(0.50)\text{-Cd}_{0.8}\text{Zn}_{0.2}\text{S}_{0.2}\text{Se}_{0.8}$ (Figure 3.29b) photoelectrodes were obtained for six light on-light off cycles at 50 s intervals. The I - t curves illustrated in Figure 3.29a show that $\text{Cd}_{0.8}\text{Zn}_{0.2}\text{S}$, $\text{Cd}_{0.8}\text{Zn}_{0.2}\text{S}_{0.8}\text{Se}_{0.2}$, $\text{Cd}_{0.8}\text{Zn}_{0.2}\text{S}_{0.5}\text{Se}_{0.5}$, $\text{Cd}_{0.8}\text{Zn}_{0.2}\text{S}_{0.2}\text{Se}_{0.8}$, $\text{Cd}_{0.8}\text{Zn}_{0.2}\text{Se}$ exhibit the photocurrent densities of 0.94, 1.34, 2.34, 4.08, 3.07 mA cm^{-2} at 0.8 V bias (vs. Ag/AgCl) under chopped solar light irradiation (150 W Xe light, light intensity: 100 mW cm^{-2}) It is observed that all $\text{Cd}_{0.8}\text{Zn}_{0.2}\text{S}_x\text{Se}_{1-x}$ ($x=0.0, 0.2, 0.5, 0.8, 1.0$) photoelectrodes demonstrate a steep rise in

photocurrent, yet the photocurrent drops rapidly when the light is on. During repetitive on-off illumination cycles, all photoelectrodes reveal n-type conductivity characteristics. Figure 3.29b indicates that RGO suppresses the recombination of photoinduced charges. Namely, the photocurrent density of $\text{Cd}_{0.8}\text{Zn}_{0.2}\text{S}_{0.2}\text{Se}_{0.8}$ jumps from 4.08 mA cm^{-2} , to 4.21 , 5.00 , and 4.51 mA cm^{-2} for RGO(0.10)- $\text{Cd}_{0.8}\text{Zn}_{0.2}\text{S}_{0.2}\text{Se}_{0.8}$, RGO(0.25)- $\text{Cd}_{0.8}\text{Zn}_{0.2}\text{S}_{0.2}\text{Se}_{0.8}$, RGO(0.50)- $\text{Cd}_{0.8}\text{Zn}_{0.2}\text{S}_{0.2}\text{Se}_{0.8}$ photoelectrodes, respectively.

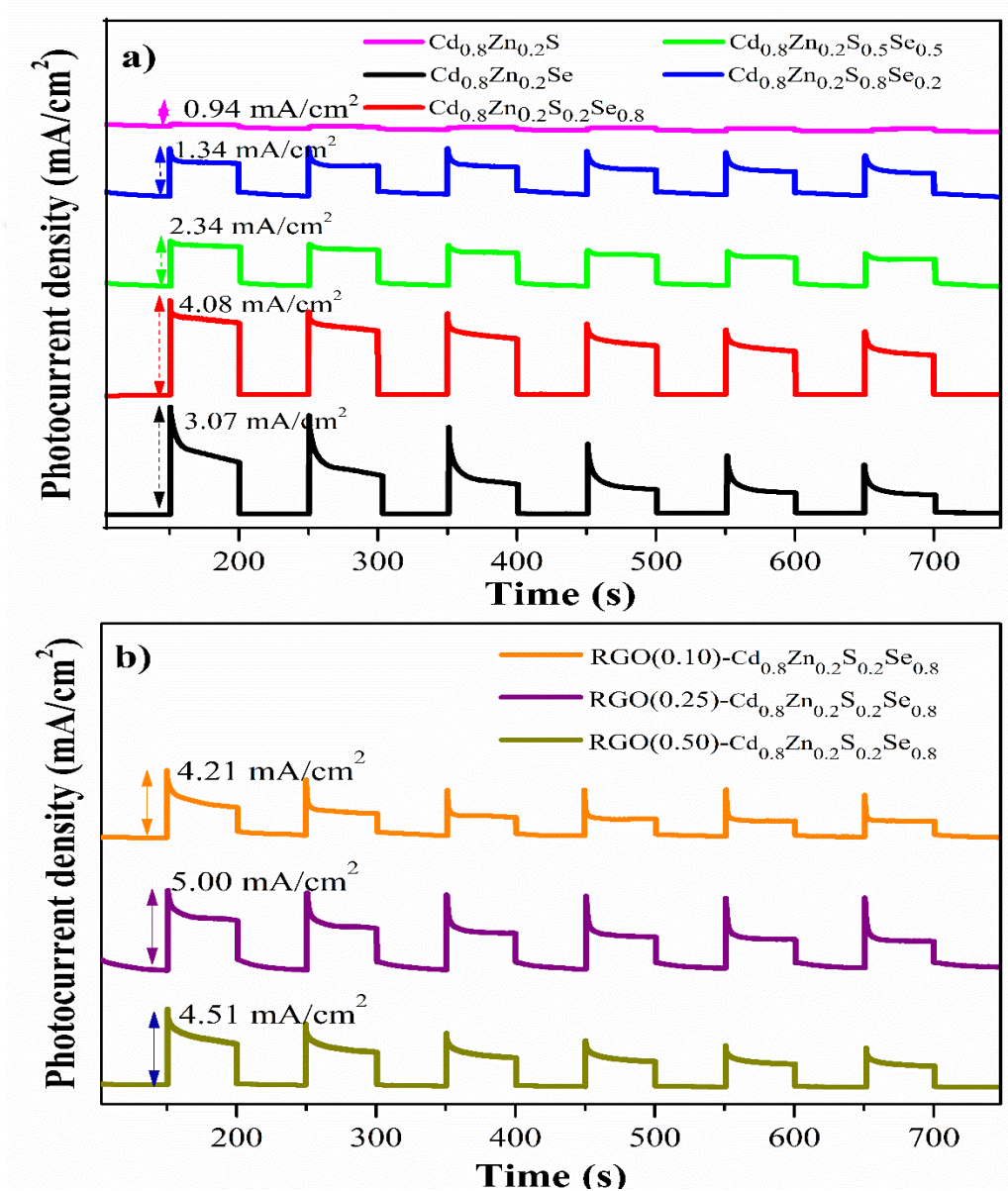


Figure 3.29. Chronoamperometric I-t curves of **a)** $\text{Cd}_{0.8}\text{Zn}_{0.2}\text{S}_x\text{Se}_{1-x}$ ($x=0.0, 0.2, 0.5, 0.8, 1.0$) and **b)** RGO(0.10, 0.25, 0.50)- $\text{Cd}_{0.8}\text{Zn}_{0.2}\text{S}_{0.2}\text{Se}_{0.8}$ photoelectrodes.

Table 3.3. A representative summary of the performance of Cd, Zn, S, Se, RGO bearing photoelectrodes reported in literature.

Photoelectrode/ Substrate	Preparation method	Temperature	Sacrificial reagent	Light intensity (mW cm ⁻²)	Photocurrent density (mA/cm ²)	Ref.
CdSe /ITO	Galvanostatic electrodeposition	350°C (Ar)	Na ₂ S/Na ₂ SO ₃	100	3.00	[241]
CdS _{0.2} Se _{0.8} /FTO	Spray pyrolysis	-	Na ₂ S+S+NaOH	20	1.02	[242]
CdSe _{0.6} S _{0.4} /ITO	Spin coating	-	Na ₂ SO ₄	100	0.68	[243]
CdSe/ZnSe/ZnO/FTO	Electrodeposition/consecutive ion replacement reaction	-	Na ₂ S/Na ₂ SO ₃	100	3.2	[244]
Cu:CdS _{0.7} Se _{0.3} /Pt	PVD/DC sputtering	-	Na ₂ SO ₄	100	0.82	[245]
CdSe/RGO/TiO ₂ /Ti	CV electrodeposition	400°C (N ₂)	Na ₂ SO ₄	170	~1	[246]
CdS/ ITO	Chemical bath deposition (CBD)	-	Na ₂ SO ₃	87.5	0.09	[247]
TiO ₂ /RGO/CdS/FTO	SILAR	350°C (NH ₃)	Na ₂ S	90	~3	[248]
TiO ₂ /CdS/MoS ₂ /FTO	CBD and SILAR	-	Na ₂ S/ Na ₂ SO ₃	100	3.25	[249]
Cd_{0.8}Zn_{0.2}S_{0.2}Se_{0.8}/ITO	One step electrodeposition	350°C in Ar	Na₂S/Na₂SO₃	100	4.08	This work
RGO(0.25)- Cd_{0.8}Zn_{0.2}S_{0.2}Se_{0.8}/ITO	One step electrodeposition	350°C in Ar	Na₂S/Na₂SO₃	100	5.00	This work

Table 3.3. represents a brief summary of the photocurrent densities of some related photoelectrodes stated in literature. There are some methods to fabricate CdS, CdSe, ZnS, ZnSe and RGO based photoelectrodes such as electrodeposition, spray pyrolysis, spin coating, drop coating, chemical bath deposition, successive ionic layer adsorption and reaction. However, there is no report which is based on a facile, one-step electrodeposition of RGO-CdZnSSe on any substrate.

Hydrogen production rate of RGO-Cd_{0.8}Zn_{0.2}S_{0.2}Se_{0.8} photoelectrode is determined with the Faraday's law given below:

$$n.z=Q/F \quad (3.5)$$

n represents number of electrons per mole, z is the electrochemical equivalent of the material, Q stands for the charge, and F is Faraday's constant ($F=96485 \text{ C mol}^{-1}$). Finally, the hydrogen production rate of RGO-Cd_{0.8}Zn_{0.2}S_{0.2}Se_{0.8} photoelectrode is 94.9 $\mu\text{moles h}^{-1}$

EIS analysis was used to study the charge transfer at the semiconductor-electrolyte junction. EIS measurements were performed in the frequency range of 100 kHz-0.1 Hz under dark conditions. Figure 3.30a displays Nyquist plots of the photoelectrodes. The semicircular radius and inclined line are associated with mechanism of charge transfer and photoelectrode kinetics. The smaller the semicircular radius is, the lower the charge transfer resistance [250]. Experimental results were fitted using equivalent Randles circuit model with a Warburg element as given in Figure 3.30b. R_s corresponds to series resistance which combines ITO, sacrificial electrolyte, and external contact for the electrochemical device. R_{ct} accounts for the charge transfer resistance at the semiconductor-electrolyte junction [251]. Constant phase element (CPE) defines the capacitance resulting from the formation of double layer in the photoelectrode. The adopted EIS fitting model yields R_s values for RGO(0.25)-Cd_{0.8}Zn_{0.2}S_{0.2}Se_{0.8}, Cd_{0.8}Zn_{0.2}S_{0.2}Se_{0.8}, Cd_{0.8}Zn_{0.2}Se and Cd_{0.8}Zn_{0.2}S as 7.3 $\Omega \text{ cm}^{-2}$, 13.6 $\Omega \text{ cm}^{-2}$, 13.8 $\Omega \text{ cm}^{-2}$, 16.6 $\Omega \text{ cm}^{-2}$, respectively. Small R_{ct} values (RGO(0.25)-Cd_{0.8}Zn_{0.2}S_{0.2}Se_{0.8}: 145.1 $\Omega \text{ cm}^{-2}$, Cd_{0.8}Zn_{0.2}Se: 383.8 $\Omega \text{ cm}^{-2}$, Cd_{0.8}Zn_{0.2}S_{0.2}Se_{0.8}: 715.5 $\Omega \text{ cm}^{-2}$, Cd_{0.8}Zn_{0.2}S: 1530.0 $\Omega \text{ cm}^{-2}$) indicate the fast movement of electrons on the surface of the photoelectrode [252]. CPE values for RGO(0.25)-Cd_{0.8}Zn_{0.2}S_{0.2}Se_{0.8}, Cd_{0.8}Zn_{0.2}Se, Cd_{0.8}Zn_{0.2}S_{0.2}Se_{0.8} and Cd_{0.8}Zn_{0.2}S are obtained as 19.80×10^{-5} , 13.90×10^{-5} , 5.39×10^{-5} , 6.22×10^{-5} , respectively.

Table 3.4. Fitting results for EIS of RGO(0.25)-Cd_{0.8}Zn_{0.2}S_{0.2}Se_{0.8}, Cd_{0.8}Zn_{0.2}S_{0.2}Se_{0.8}, Cd_{0.8}Zn_{0.2}Se and Cd_{0.8}Zn_{0.2}S photoelectrodes.

Photoelectrode	R_s (Ω)	CPE ($10^{-5} \text{s}^n \Omega^{-1}$)	W ($\Omega \cdot \text{s}^{-1/2}$)	R_{ct} ($\Omega \text{ cm}^2$)
Cd _{0.8} Zn _{0.2} S	16.60	6.22	6.84×10^{-4}	1530.0
Cd _{0.8} Zn _{0.2} Se	13.80	5.39	4.00×10^{-3}	383.8
Cd _{0.8} Zn _{0.2} S _{0.2} Se _{0.8}	13.60	13.90	3.57×10^{-4}	715.5
RGO(0.25)-Cd _{0.8} Zn _{0.2} S _{0.2} Se _{0.8}	7.30	19.80	3.71×10^{-3}	145.1

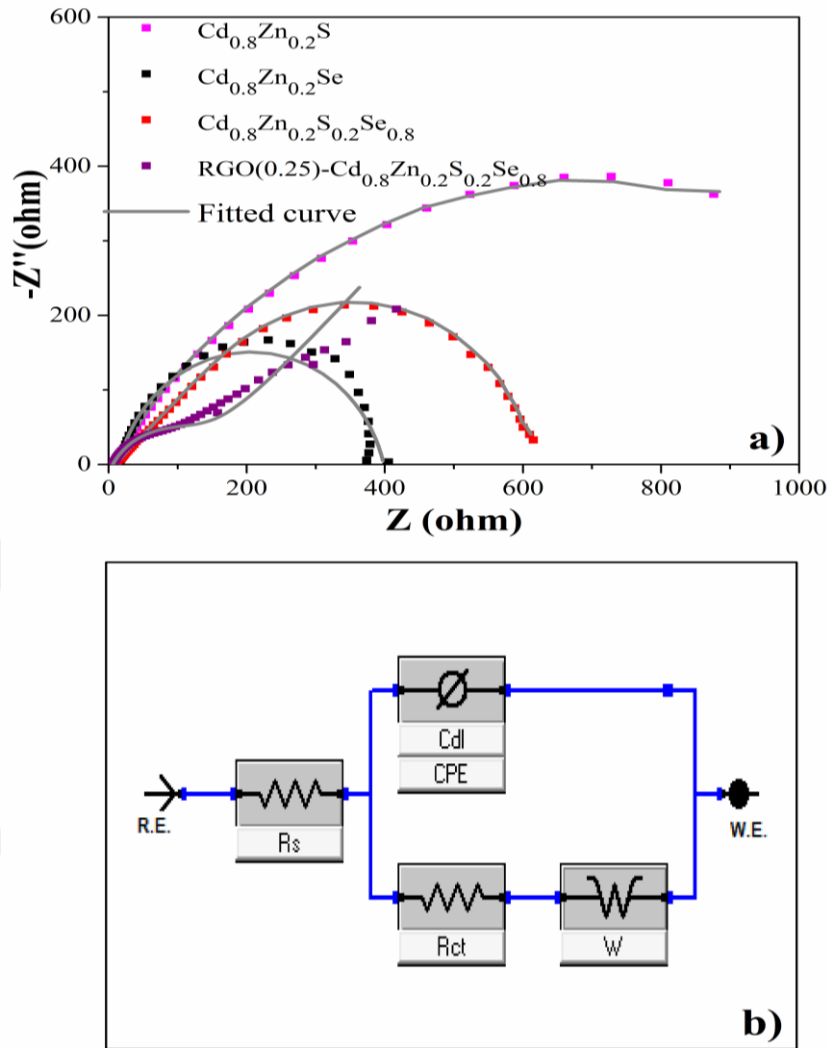


Figure 3.30. Nyquist plots of **a)** $\text{Cd}_{0.8}\text{Zn}_{0.2}\text{S}$, $\text{Cd}_{0.8}\text{Zn}_{0.2}\text{Se}$, $\text{Cd}_{0.8}\text{Zn}_{0.2}\text{S}_{0.2}\text{Se}_{0.8}$, $\text{RGO}(0.25)\text{-Cd}_{0.8}\text{Zn}_{0.2}\text{S}_{0.2}\text{Se}_{0.8}$ and **b)** Equivalent circuit model used for EIS data fitting (R.E.: Reference electrode, W.E.: Working electrode, R_s : Series resistance, R_{ct} : Charge transfer resistance, CPE: Constant phase element, W: Finite-length Warburg element).

Mott-Schottky (M-S) analysis is applied to clarify the band structure, identify the conductivity (n-type or p-type) and determine the flat band potential (V_{fb}) of a photoelectrode [253]. M-S analysis was performed at 100 Hz frequency in dark condition. M-S equation is given below [150]:

$$1/C^2 = (2/\epsilon_0 \epsilon_e N A^2) (V - V_{fb} - KT/e) \quad (3.6)$$

C: capacitance of space charge region, e: electron charge (1.603×10^{-19} C), K: Boltzmann constant (1.38×10^{-23} J/K), T: absolute temperature (K), ϵ : dielectric constant of semiconductor, ϵ_0 : permittivity of vacuum (8.854×10^{-12} F m⁻¹), N: charge carrier density, A: area of the photoelectrode, V: applied potential, V_{fb} : flat band potential. (KT/e is neglected at room temperature under 1 atm pressure).

Equation (3.6) states that the photoelectrode's charge carrier density is inversely proportional to the linear component of the M-S curve [254]. In Figure 3.31, the slope of RGO(0.25)-Cd_{0.8}Zn_{0.2}S_{0.2}Se_{0.8} is associated with its charge carrier density (charge donor density for n-type, N_D) and photocurrent. The positive slope of photoelectrode suggests that it has n-type conductivity. The flat band potential value of RGO (0.25)-Cd_{0.8}Zn_{0.2}S_{0.2}Se_{0.8} is determined from the intercept of the linear part of M-S plot. The flat band potential term provides a qualitative insight of the degree of band bending at the Schottky interface. Higher shift of band bending confirms that photoinduced charge recombination will be hard at the interface, and hence, photoelectrochemical performance can be significantly improved [255]. The V_{fb} and N_D of RGO(0.25)-Cd_{0.8}Zn_{0.2}S_{0.2}Se_{0.8} are observed as -0.32 V vs. RHE and 4.44×10^{18} cm⁻³, respectively. There are no reports related to the N_D values of RGO-CdZnSSe photoelectrodes in the literature, yet a few reports are available for the N_D of CdSSe photoelectrodes. For instance, de Los Angeles Hernandez Perez et al. have calculated the N_D of CdS_{0.25}Se_{0.75} as 1.39×10^{18} cm⁻³ [247]. The V_{fb} values for Cd_{0.8}Zn_{0.2}S, Cd_{0.8}Zn_{0.2}Se, and Cd_{0.8}Zn_{0.2}S_{0.2}Se_{0.8} photoelectrodes are determined as -0.33, -0.25 and -0.23 V vs. RHE.

M-S parameters are presented on Table 3.5.

Table 3.5. M-S parameters for RGO(0.25)-Cd_{0.8}Zn_{0.2}S_{0.2}Se_{0.8}, Cd_{0.8}Zn_{0.2}S_{0.2}Se_{0.8}, Cd_{0.8}Zn_{0.2}Se and Cd_{0.8}Zn_{0.2}S photoelectrodes.

Photoelectrodes	V_{fb} (V vs. RHE)	N_D (cm ⁻³)
RGO(0.25)-Cd _{0.8} Zn _{0.2} S _{0.2} Se _{0.8}	-0.32	4.44×10^{18}
Cd _{0.8} Zn _{0.2} S _{0.2} Se _{0.8}	-0.23	3.12×10^{18}
Cd _{0.8} Zn _{0.2} Se	-0.25	2.97×10^{18}
Cd _{0.8} Zn _{0.2} S	-0.33	2.82×10^{18}

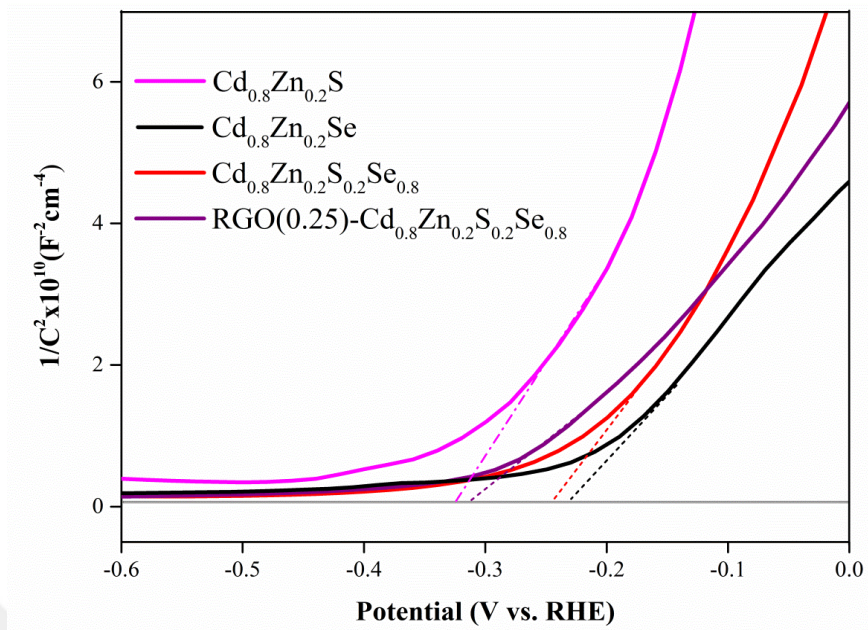


Figure 3.31. M-S plots of $Cd_{0.8}Zn_{0.2}S$, $Cd_{0.8}Zn_{0.2}Se$, $Cd_{0.8}Zn_{0.2}S_{0.2}Se_{0.8}$, and $RGO(0.25)-Cd_{0.8}Zn_{0.2}S_{0.2}Se_{0.8}$ photoelectrodes.

ABPE is calculated according to Equation (3.12) [177]. As shown in Figure 3.32., the maximum ABPE values for $Cd_{0.8}Zn_{0.2}S_{0.2}Se_{0.8}$ and $RGO(0.25)-Cd_{0.8}Zn_{0.2}S_{0.2}Se_{0.8}$ were estimated as 2.15% and 3.07%.

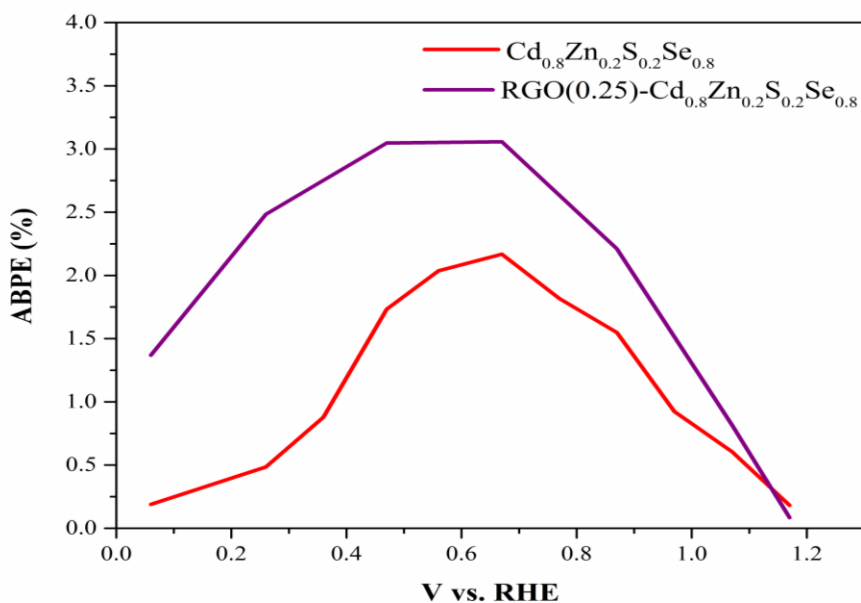


Figure 3.32. ABPE values for $Cd_{0.8}Zn_{0.2}S_{0.2}Se_{0.8}$ and $RGO(0.25)-Cd_{0.8}Zn_{0.2}S_{0.2}Se_{0.8}$ photoelectrodes.

Figure 3.33. displays a schematical representation of the band diagram of RGO-Cd_{0.8}Zn_{0.2}S_{0.2}Se_{0.8} photoelectrode and the mechanism of hydrogen production during PEC analysis in aqueous Na₂S/Na₂SO₃ sacrificial electrolyte. RGO-Cd_{0.8}Zn_{0.2}S_{0.2}Se_{0.8} behaves as a photoanode since it has excess electrons (e⁻). When the photoanode is exposed to light, electrons are excited from the valence band (VB) to the conduction band (CB) followed by electron flow through external circuit to Pt cathode leading to hydrogen production [52]. The positions of CB and VB are depicted as -0.46 eV and 1.35 eV vs. RHE, respectively. These values are obtained from M-S analysis and Tauc plot of Kubelka-Munk's function of RGO-Cd_{0.8}Zn_{0.2}S_{0.2}Se_{0.8} photoelectrode. During PEC hydrogen production in Na₂S/Na₂SO₃ sacrificial electrolyte, the reactions taking part at the VB side are:



Meanwhile, H⁺ ion is reduced to H₂ gas at the cathode part.

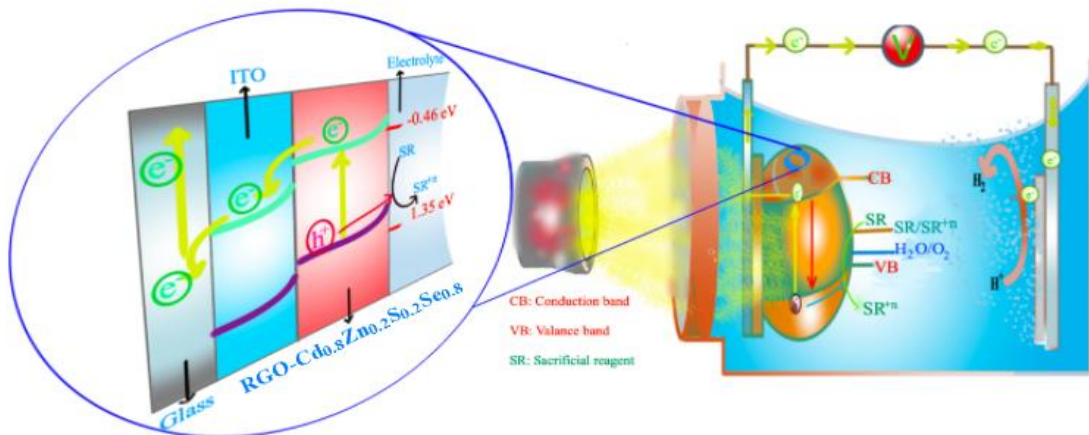


Figure 3.33. Band diagram of RGO-Cd_{0.8}Zn_{0.2}S_{0.2}Se_{0.8} photoelectrode in PEC hydrogen production system.

3.2.3. Electrochemical Deposition, Characterization and Photoelectrochemical Performance of CdZnMSeS (M: Ni, Cu, Mo) and RGO-CdZnNiSeS Photoelectrodes

Figure 3.34. displays the CV curves for the fabrication of CdS, CdSe, ZnS, ZnSe, NiS, NiSe, CuS, CuSe, NiS, NiSe, MoS₂, MoSe₂ thin films separately. The aqueous electrolytic bath involves the precursor salt solutions (Cd(CH₃COO)₂.2H₂O, Zn(CH₃COO)₂.2H₂O, Cu(CH₃COO)₂, Na₂MoO₄.2H₂O, Ni(NO₃)₂.6H₂O, Na₂S₂O₃, Na₂SeSO₃) and EDTA as complexing agent. The pH of the electrolytic bath is adjusted to 8.7 with NaOH. The CV analyses were performed at 100 mV s⁻¹ scan rate. As described earlier, the CV curve for CdS formation on ITO exhibits two cathodic peaks at -1.1 and -1.3 V vs. Ag/AgCl, and two anodic peaks at -1.1 and -0.7 V vs. Ag/AgCl corresponding to the reduction of [Cd-EDTA]²⁻ complexes, reduction of S₂O₃²⁻, oxidation of S₂O₃²⁻, oxidation and dissolution of Cd.

The CV curve for CdSe gives two cathodic peaks and one anodic peak, located at ca. -1.1, -1.3, -0.7 V vs. Ag/AgCl. These peaks are ascribed to the reduction of Cd²⁺ ions from [Cd-EDTA]²⁻ complexes, reduction of selenosulfate ions, and anodic dissolution of CdSe, respectively.

ZnS and NiS formation curves display similar patterns to CdS, while the peaks attributed to the ZnSe and NiSe thin film construction are observed in the similar potential range to CdSe. The difference of the CV voltammogram of CuS from other S containing compounds may be explained with the existence of two stripping anodic peaks at positive potential limits related with the oxidation of copper compounds [256].

Levinas et al. electrodeposited MoS₂ thin films on a foam based photoelectrode and the behavior of the cyclic voltammetric electrodeposition of MoS₂ thin film was quite similar to the one we have obtained in our CV voltammogram [257].

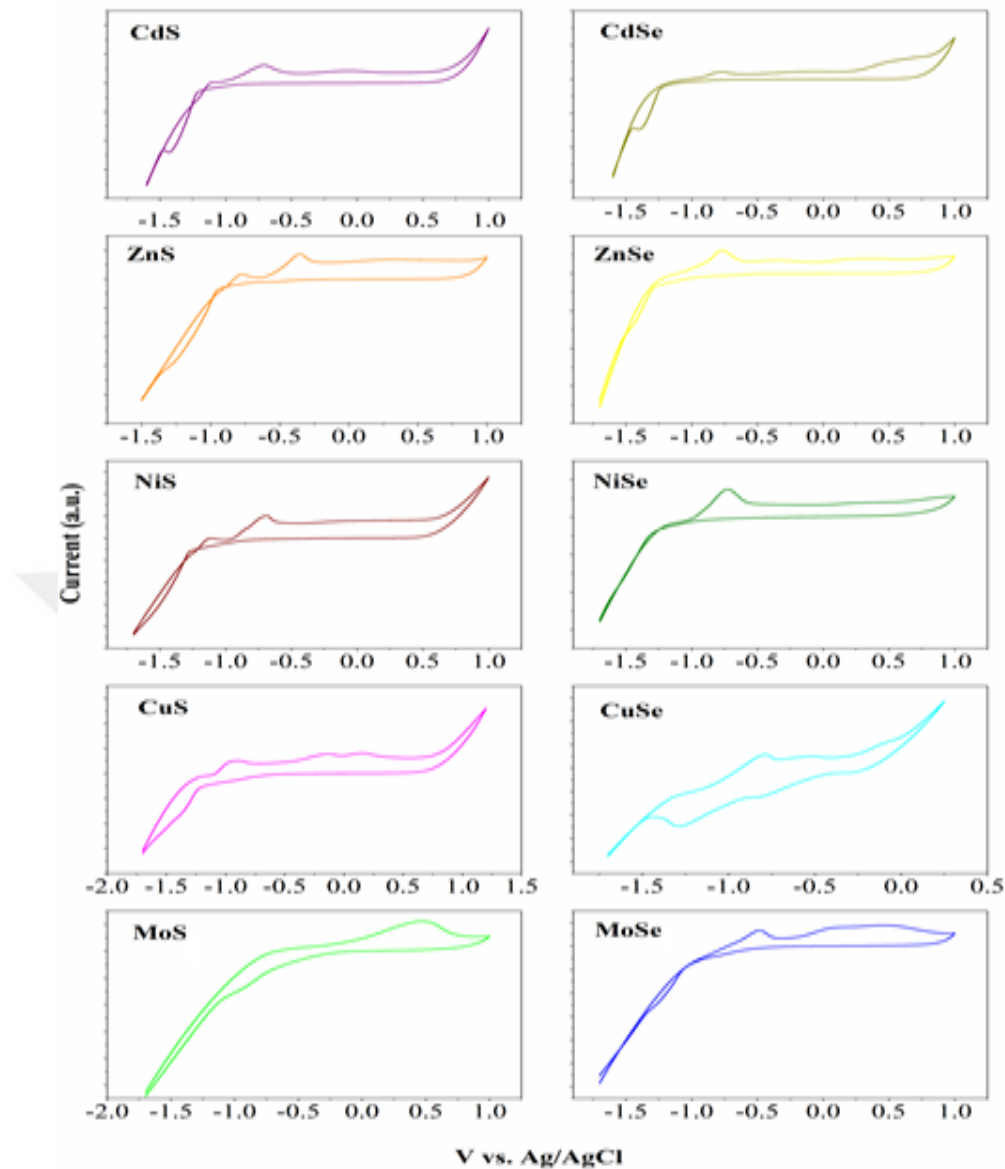


Figure 3.34. CV curves for the fabrication of CdS, CdSe, ZnS, ZnSe, CuS, CuSe, MoS₂, MoSe₂ thin films.

Figure 3.35 represents the CV curves for Cd_{0.6}Zn_{0.2}Mo_{0.2}S_{0.2}Se_{0.8} (Figure 3.35a.), Cd_{0.6}Zn_{0.2}Cu_{0.2}S_{0.2}Se_{0.8} (Figure 3.35b), Cd_{0.6}Zn_{0.2}Ni_{0.2}S_{0.2}Se_{0.8} (Figure 3.35c), and RGO-Cd_{0.6}Zn_{0.2}Ni_{0.2}S_{0.2}Se_{0.8} (Figure 3.35d), thin films. The CV curves given in Figure 3.35a, Figure 3.35b and Figure 3.35c display the characteristic peaks of CdS, CdSe, ZnS, ZnSe, NiS, NiSe, CuS, CuSe, MoS₂, MoSe₂. However, the composition of the thin films causes some peaks to become more distinct than the others.

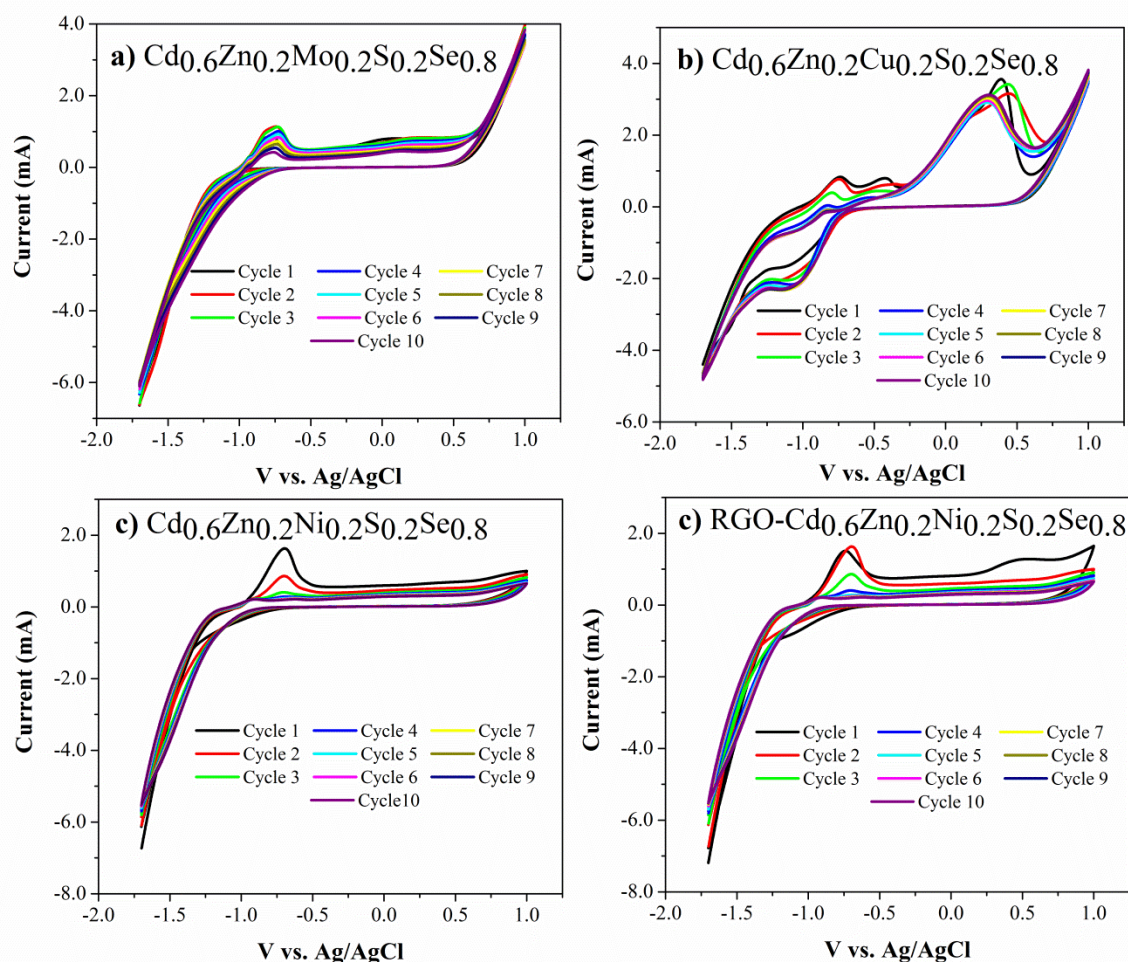


Figure 3.35. CV curves for the fabrication of **a)** $\text{Cd}_{0.6}\text{Zn}_{0.2}\text{Mo}_{0.2}\text{S}_{0.2}\text{Se}_{0.8}$, **b)** $\text{Cd}_{0.6}\text{Zn}_{0.2}\text{Cu}_{0.2}\text{S}_{0.2}\text{Se}_{0.8}$, **c)** $\text{Cd}_{0.6}\text{Zn}_{0.2}\text{Ni}_{0.2}\text{S}_{0.2}\text{Se}_{0.8}$ and **d)** $\text{RGO-Cd}_{0.6}\text{Zn}_{0.2}\text{Ni}_{0.2}\text{S}_{0.2}\text{Se}_{0.8}$ thin films.

The Raman spectra of the $\text{Cd}_{0.6}\text{Zn}_{0.2}\text{Mo}_{0.2}\text{S}_{0.2}\text{Se}_{0.8}$, $\text{Cd}_{0.6}\text{Zn}_{0.2}\text{Cu}_{0.2}\text{S}_{0.2}\text{Se}_{0.8}$, $\text{Cd}_{0.6}\text{Zn}_{0.2}\text{Ni}_{0.2}\text{S}_{0.2}\text{Se}_{0.8}$ and $\text{RGO-Cd}_{0.6}\text{Zn}_{0.2}\text{Ni}_{0.2}\text{S}_{0.2}\text{Se}_{0.8}$ photoelectrodes excited with 532 nm of an Ar^+ ion laser are given in Figure 3.36. The bands positioned at 177 cm^{-1} , 202 cm^{-1} , 418 cm^{-1} , and 615 cm^{-1} belong to the Raman modes of TO (transverse optical phonon), 1LO (longitudinal optical phonon) and 2LO bands of CdZnSSe. Apart from that, the peaks at 248 cm^{-1} and 404 cm^{-1} are corresponded to the out-of-plane A_{1g} vibration mode of $\text{Cd}_{0.6}\text{Zn}_{0.2}\text{Mo}_{0.2}\text{S}_{0.2}\text{Se}_{0.8}$ [258, 259]. The presence of CuSe and CuS are addressed to the peaks at around 1100 cm^{-1} (antisymmetric stretching mode of CuSe) and 470 cm^{-1} (S-S vibration of CuS) [260, 261]. A_{1g} Raman mode of NiSe is clearly

obvious at 202 cm^{-1} since it increases the intensity of the TO peak considerably [262]. The existence of RGO is confirmed with the overlapping of D and G bands.

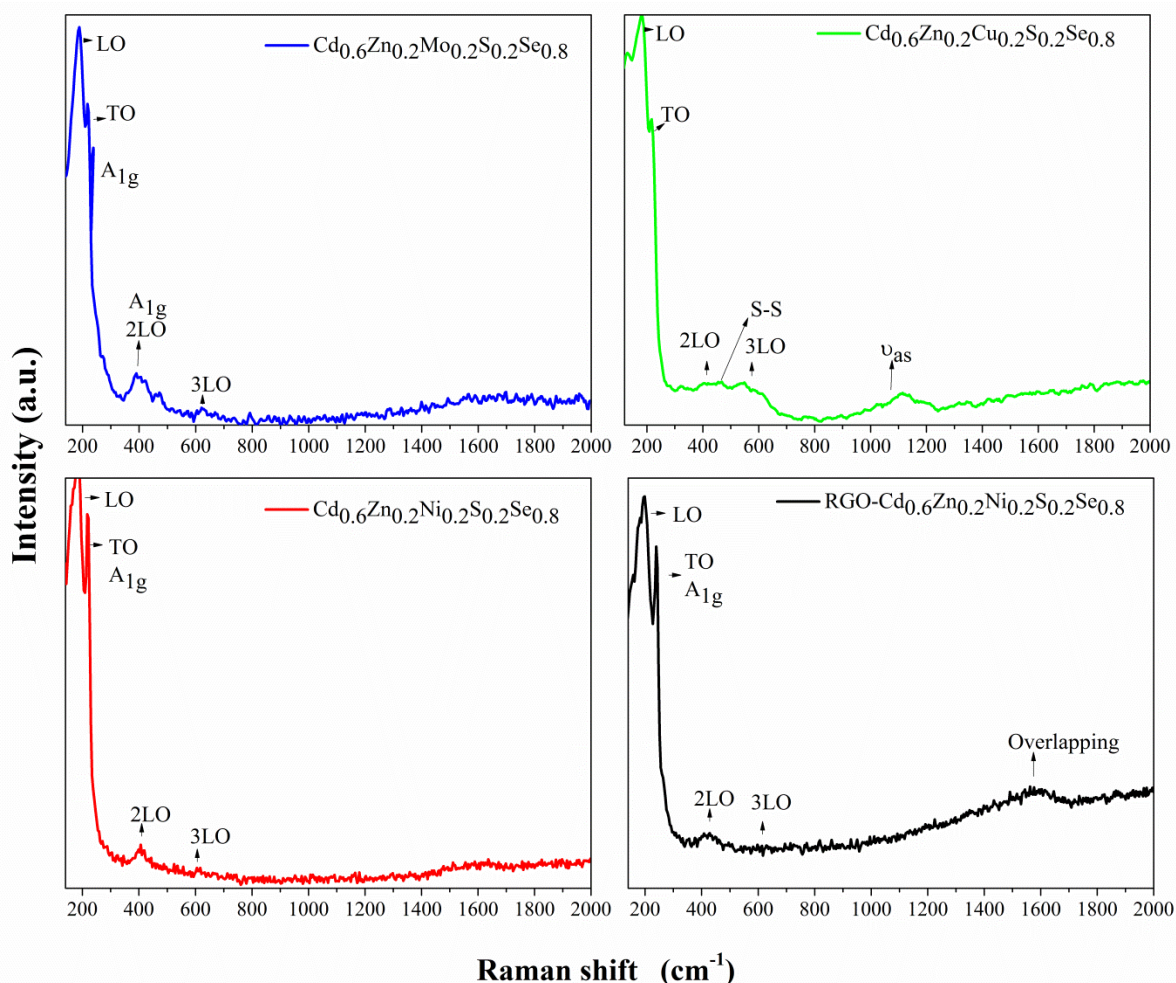


Figure 3.36. Raman spectra of $\text{Cd}_{0.6}\text{Zn}_{0.2}\text{Mo}_{0.2}\text{S}_{0.2}\text{Se}_{0.8}$, $\text{Cd}_{0.6}\text{Zn}_{0.2}\text{Cu}_{0.2}\text{S}_{0.2}\text{Se}_{0.8}$, $\text{Cd}_{0.6}\text{Zn}_{0.2}\text{Ni}_{0.2}\text{S}_{0.2}\text{Se}_{0.8}$ and RGO- $\text{Cd}_{0.6}\text{Zn}_{0.2}\text{Ni}_{0.2}\text{S}_{0.2}\text{Se}_{0.8}$ photoelectrodes.

The field emission scanning electron microscopy (FESEM) images of $\text{Cd}_{0.6}\text{Zn}_{0.2}\text{Ni}_{0.2}\text{S}_{0.2}\text{Se}_{0.8}$ and RGO- $\text{Cd}_{0.6}\text{Zn}_{0.2}\text{Ni}_{0.2}\text{S}_{0.2}\text{Se}_{0.8}$ are presented in Figure 3.37a-b with magnification of 200000x. It is clearly detected that the RGO nanosheets are embedded in the CdZnNiSse particles. Thus, the RGO nanosheets act as bridges for the connection between different CdZnNiSse particles, improving the photoelectrochemical performance through the separation of photo-generated carriers. The energy dispersive X-ray spectrometer (EDS) results reveals that the peaks corresponding to Cd, Zn, Ni, S, Se, O, and C elements which verifies the targeted composition of the related structure on the surface of ITO (Figure 3.37c). It is clear from the CdZnNiSse particles' signals,

as well as the Raman spectrum, that RGO is present in this structure, as evidenced by the signals from Cd, Zn, Ni, S, and Se.

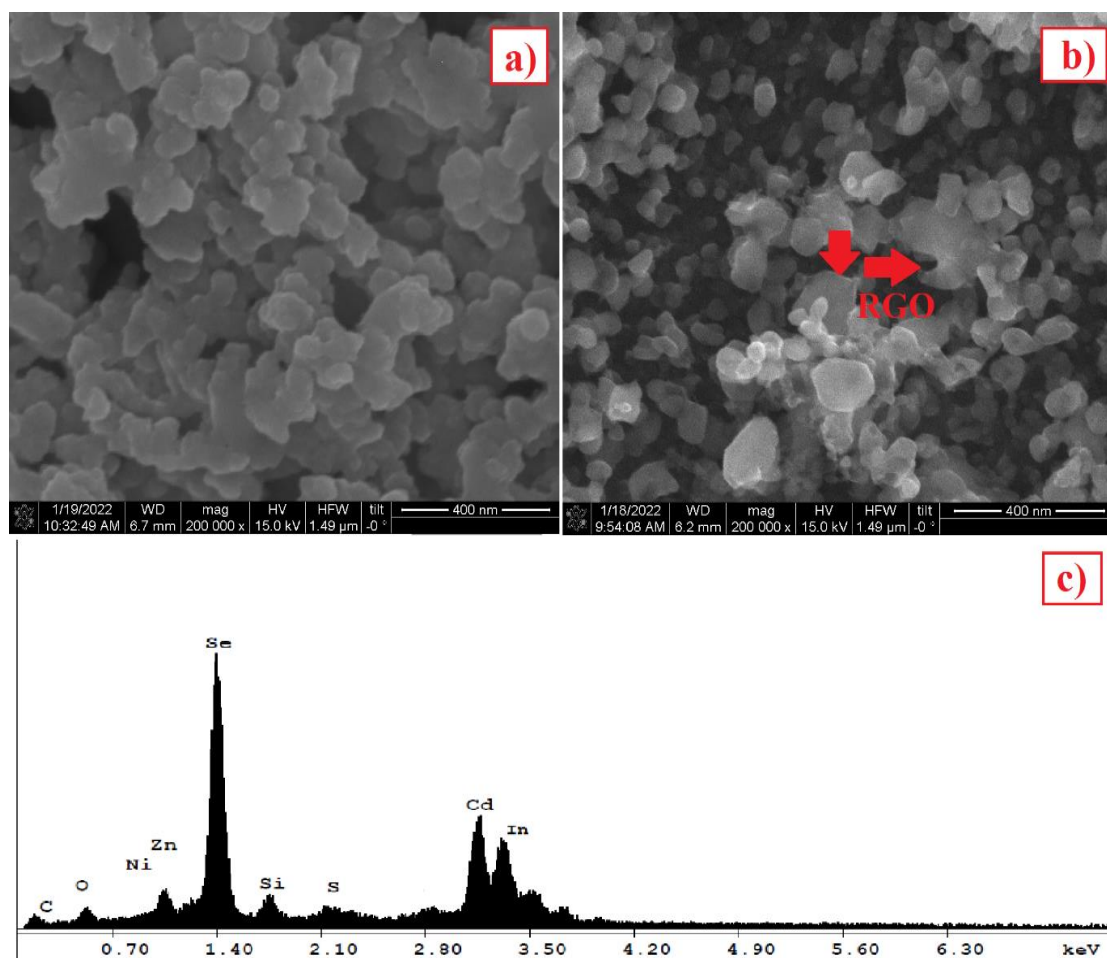


Figure 3.37. FESEM images of the fabricated photoelectrodes at magnification of 200000x. **a)** $\text{Cd}_{0.6}\text{Zn}_{0.2}\text{Ni}_{0.2}\text{S}_{0.2}\text{Se}_{0.8}$, **b)** $\text{RGO-Cd}_{0.6}\text{Zn}_{0.2}\text{Ni}_{0.2}\text{S}_{0.2}\text{Se}_{0.8}$.

The magnificated 5000x FESEM images of $\text{Cd}_{0.6}\text{Zn}_{0.2}\text{Ni}_{0.2}\text{S}_{0.2}\text{Se}_{0.8}$, $\text{Cd}_{0.6}\text{Zn}_{0.2}\text{Cu}_{0.2}\text{S}_{0.2}\text{Se}_{0.8}$ and $\text{Cd}_{0.6}\text{Zn}_{0.2}\text{Mo}_{0.2}\text{S}_{0.2}\text{Se}_{0.8}$ and $\text{RGO-Cd}_{0.6}\text{Zn}_{0.2}\text{Ni}_{0.2}\text{S}_{0.2}\text{Se}_{0.8}$ are further given in Figure 3.38.

According to Figure 3.38., the more uniform surface is achieved with the presence of RGO in the $\text{RGO-Cd}_{0.6}\text{Zn}_{0.2}\text{Ni}_{0.2}\text{S}_{0.2}\text{Se}_{0.8}$ photoelectrode compared to the fabricated other photoelectrodes. In addition, the observed agglomeration on the surface of $\text{Cd}_{0.6}\text{Zn}_{0.2}\text{Ni}_{0.2}\text{S}_{0.2}\text{Se}_{0.8}$ photoelectrode is relatively less than $\text{Cd}_{0.6}\text{Zn}_{0.2}\text{Cu}_{0.2}\text{S}_{0.2}\text{Se}_{0.8}$ and $\text{Cd}_{0.6}\text{Zn}_{0.2}\text{Mo}_{0.2}\text{S}_{0.2}\text{Se}_{0.8}$.

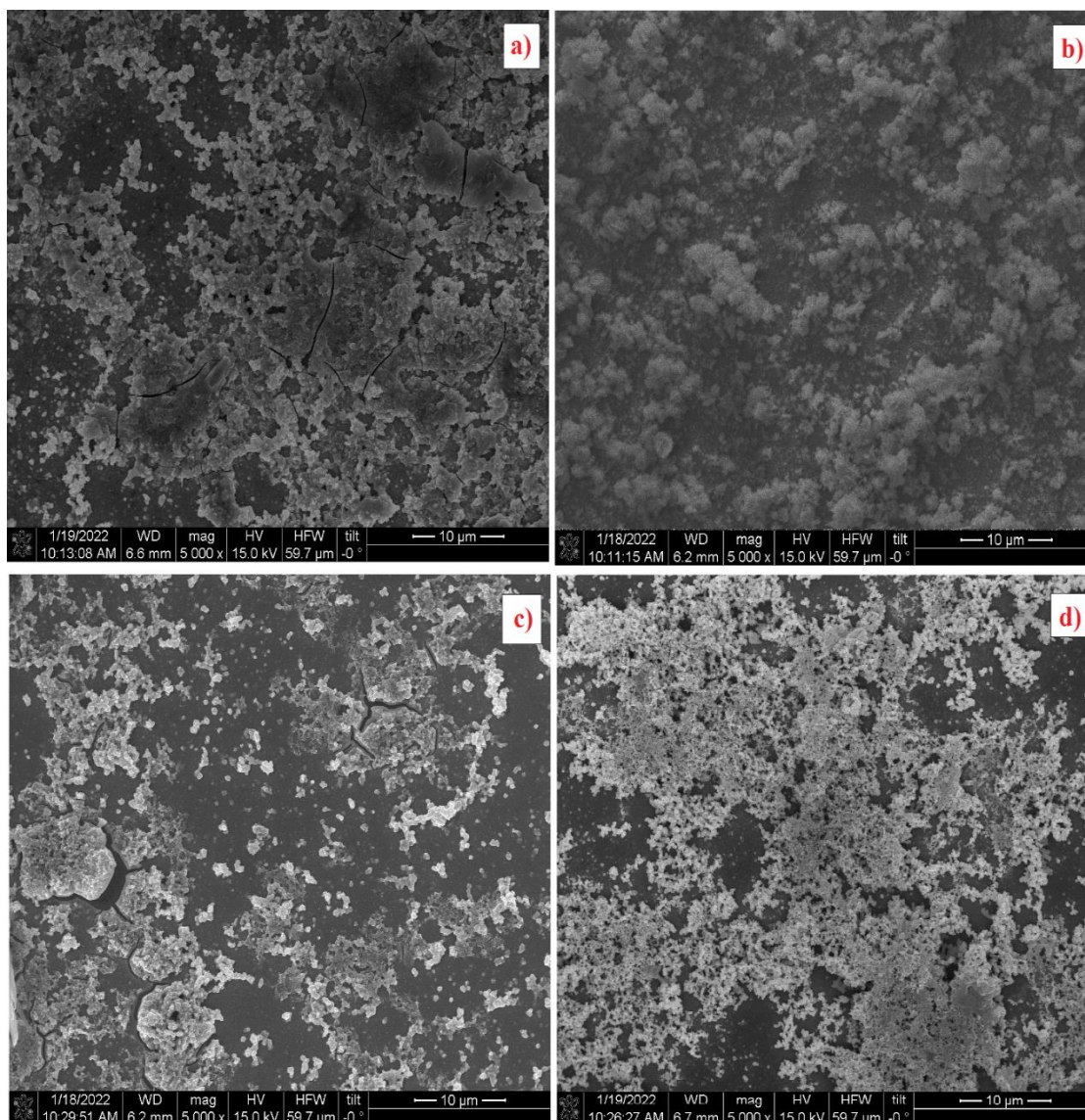


Figure 3.38. FESEM images of the prepared structures on ITO substrate at magnification of 5000x. **a)** $\text{Cd}_{0.6}\text{Zn}_{0.2}\text{Mo}_{0.2}\text{S}_{0.2}\text{Se}_{0.8}$ **b)** $\text{Cd}_{0.6}\text{Zn}_{0.2}\text{Cu}_{0.2}\text{S}_{0.2}\text{Se}_{0.8}$ **c)** $\text{Cd}_{0.6}\text{Zn}_{0.2}\text{Ni}_{0.2}\text{S}_{0.2}\text{Se}_{0.8}$ **d)** $\text{RGO-Cd}_{0.6}\text{Zn}_{0.2}\text{Ni}_{0.2}\text{S}_{0.2}\text{Se}_{0.8}$.

The oxidation states and chemical composition of $\text{Cd}_{0.6}\text{Zn}_{0.2}\text{Ni}_{0.2}\text{S}_{0.2}\text{Se}_{0.8}$ photoelectrode is typically analyzed by performing XPS (Figure 3.39.). The survey spectrum confirms the existence of Cd 3d, Zn 2p, Ni 2p, S 2p, Se 3d, O 1s oxidation states. The characteristic C 1s peak at 284.4 eV on survey spectrum is used as the reference peak [263]. The peaks of Cd 3d are located at 405.5 eV ($3d_{5/2}$) and 412.2 eV ($3d_{3/2}$). The XPS spectrum of Zn 2p reveals the binding energies at 1024 eV ($2p_{3/2}$) and 1047 eV ($2p_{1/2}$) impaired with a satellite peak. The presence of Ni is testified in the XPS spectrum of Ni 2p. The two typical peaks centered at around 855.7 eV and 874.6 eV are assigned to the

$2p_{3/2}$ and $2p_{1/2}$ oxidation states with their two satellite peaks [106]. S 2p spectrum is resolved into two peaks at 160.6 eV and 163.0 eV, corresponding to the $2p_{3/2}$ and $2p_{1/2}$ oxidation states, respectively. Further, the small peak at 166.5 eV indicates the presence of S-O bonding due to the partial oxidation of S edges in the structure [264]. Se 3d spectrum displays a doublet Se 3d spectrum is deconvoluted into peaks at 54.5, 53.6 eV which are assigned to $3d_{3/2}$ and Se $3d_{5/2}$. The broad peak at 58.8 eV can arise from Se-oxygen bonding structure.

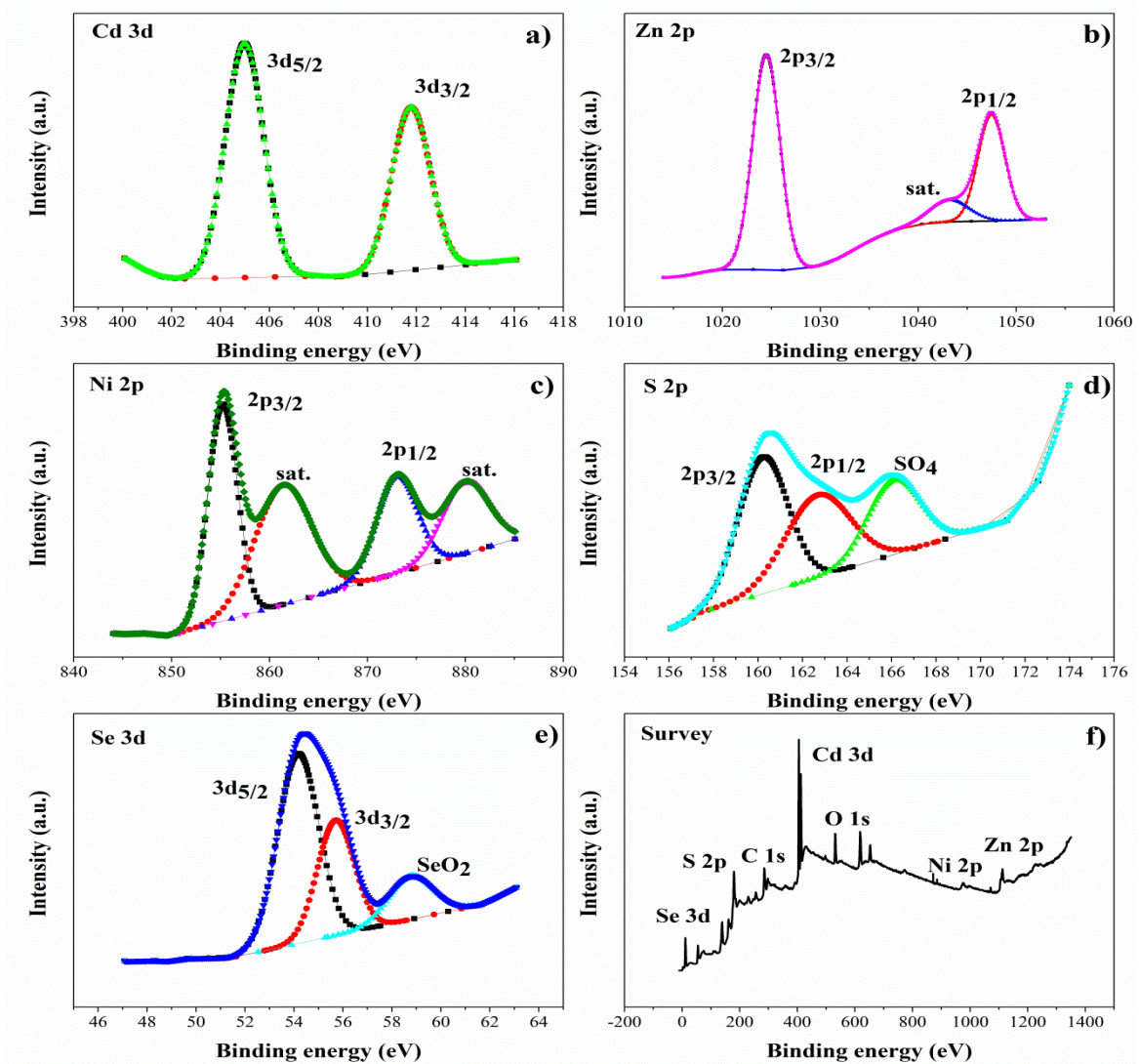


Figure 3.39. X-ray photoelectron spectroscopy (XPS) spectra of $\text{Cd}_{0.6}\text{Zn}_{0.2}\text{Ni}_{0.2}\text{S}_{0.2}\text{Se}_{0.8}$. a) Cd 3d, b) Zn 2p, c) Ni 2p, d) S 2p, e) Se 3d, f) Survey.

Figure 3.40 gives the XPS spectra of RGO- $\text{Cd}_{0.6}\text{Zn}_{0.2}\text{Ni}_{0.2}\text{S}_{0.2}\text{Se}_{0.8}$. RGO presence in $\text{Cd}_{0.6}\text{Zn}_{0.2}\text{Ni}_{0.2}\text{S}_{0.2}\text{Se}_{0.8}$ can be identified by the C 1s and O 1s spectra. The intensity of the C 1s peak on the survey spectrum is much higher than the one on the survey

spectrum of $\text{Cd}_{0.6}\text{Zn}_{0.2}\text{Ni}_{0.2}\text{S}_{0.2}\text{Se}_{0.8}$, which is in well correspondence with the RGO structure. The XPS spectrum of C1s is broad and asymmetric, indexing to the existence of carbon containing species. C 1s spectrum is deconvoluted into the peaks assigned to the C-C/C=C (285.0 eV), C-O (286.8 eV), C=O (289.2 eV). Oxygenated functional groups of RGO are observed in the form of C=O/O=C-OH (529.7 eV), C-O (531.7 eV), H_2O (533.7 eV), C-OH (536.0 eV) groups.

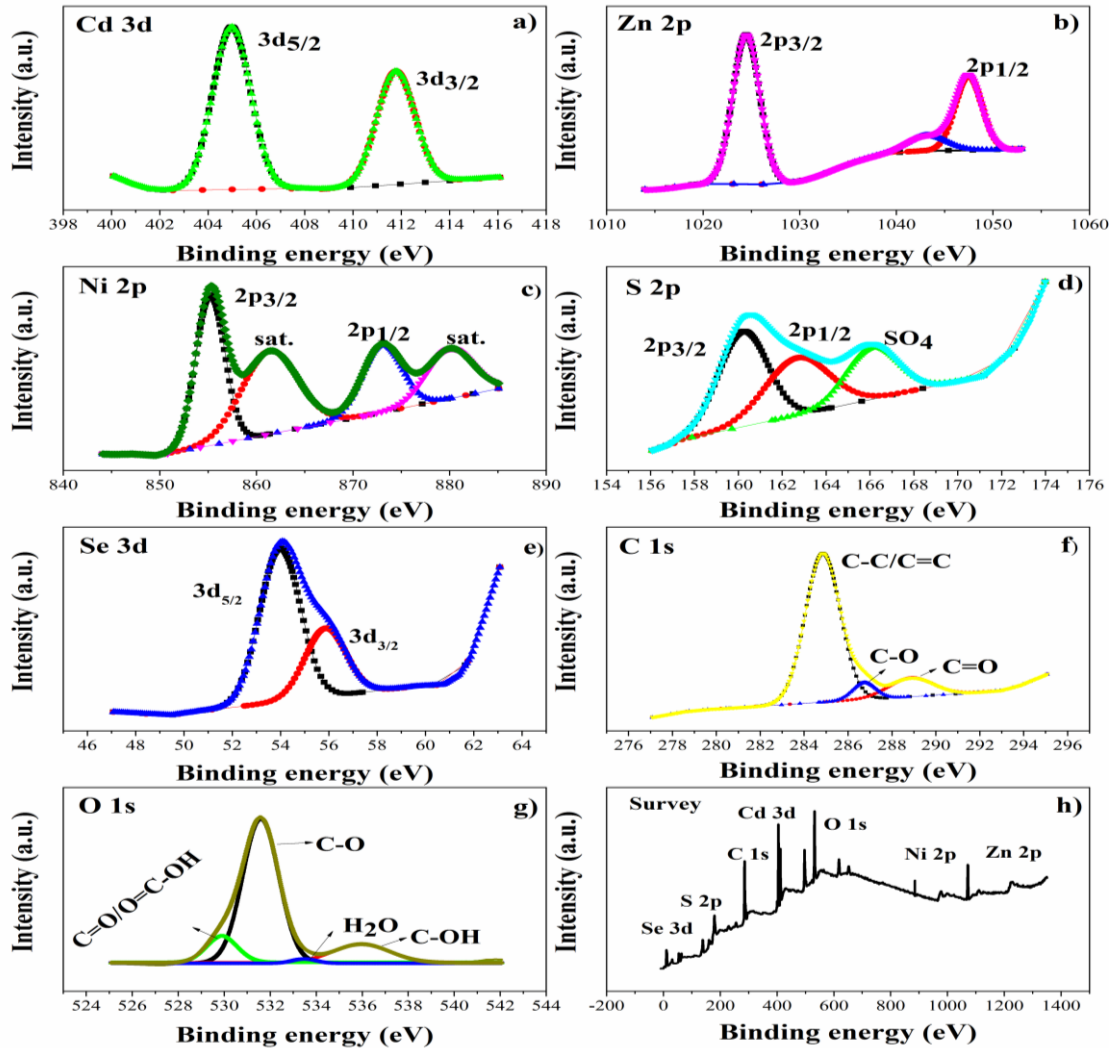


Figure 3.40. X-ray photoelectron spectroscopy (XPS) spectra of RGO- $\text{Cd}_{0.6}\text{Zn}_{0.2}\text{Ni}_{0.2}\text{S}_{0.2}\text{Se}_{0.8}$. a) Cd 3d, b) Zn 2p, c) Ni 2p, d) S 2p, e) Se 3d, f) C 1s, g) O 1s, h) Survey.

Figure 3.41 gives the XRD patterns belonging to $\text{Cd}_{0.6}\text{Zn}_{0.2}\text{Mo}_{0.2}\text{S}_{0.2}\text{Se}_{0.8}$, $\text{Cd}_{0.6}\text{Zn}_{0.2}\text{Cu}_{0.2}\text{S}_{0.2}\text{Se}_{0.8}$, $\text{Cd}_{0.6}\text{Zn}_{0.2}\text{Ni}_{0.2}\text{S}_{0.2}\text{Se}_{0.8}$ and RGO- $\text{Cd}_{0.6}\text{Zn}_{0.2}\text{Ni}_{0.2}\text{S}_{0.2}\text{Se}_{0.8}$ thin films. The diffraction peaks of NiSe appears at $2\theta=30.2^\circ, 33.0^\circ, 45.4^\circ, 50.0^\circ, 60.2^\circ, 62.0^\circ$

and 68.0° . This pattern is consistent with the literature [265, 266]. Accordingly, the peaks at $2\theta=30^\circ, 35^\circ, 45^\circ$ ve 55° represents NiS formation. The peaks located at $2\theta=27.7^\circ, 30.2^\circ, 32.3^\circ, 41.6^\circ, 46.0^\circ$ and 55.9° de proves the existence of CuS [267]. MoS and MoSe formation is confirmed with the location of peaks at $2\theta=33^\circ, 35^\circ, 45^\circ$ ve 55° [268]. Apart from that, RGO- $\text{Cd}_{0.6}\text{Zn}_{0.2}\text{Ni}_{0.2}\text{S}_{0.2}\text{Se}_{0.8}$ exhibits a relatively broad peak between $2\theta=20^\circ-30^\circ$ diffraction angle. The reason for that might lie behind the fact that the diffraction peaks belonging to RGO overlaps with other peaks [269]. The average crystallite size for RGO- $\text{Cd}_{0.6}\text{Zn}_{0.2}\text{Ni}_{0.2}\text{S}_{0.2}\text{Se}_{0.8}$ is calculated as 55.8 nm.

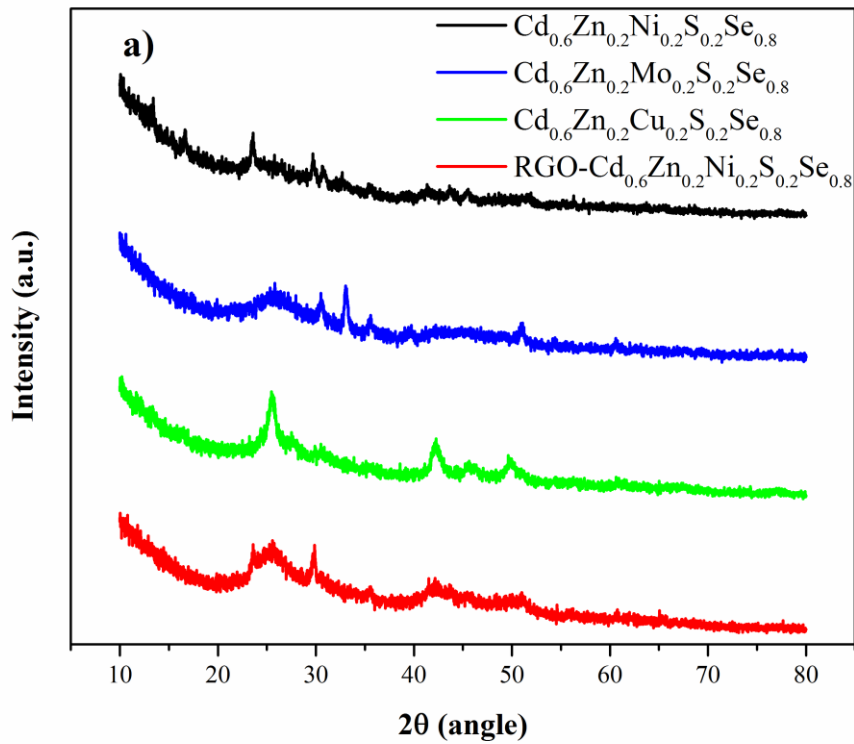


Figure 3.41. XRD patterns of $\text{Cd}_{0.6}\text{Zn}_{0.2}\text{Mo}_{0.2}\text{S}_{0.2}\text{Se}_{0.8}$, $\text{Cd}_{0.6}\text{Zn}_{0.2}\text{Cu}_{0.2}\text{S}_{0.2}\text{Se}_{0.8}$, $\text{Cd}_{0.6}\text{Zn}_{0.2}\text{Ni}_{0.2}\text{S}_{0.2}\text{Se}_{0.8}$ and RGO- $\text{Cd}_{0.6}\text{Zn}_{0.2}\text{Ni}_{0.2}\text{S}_{0.2}\text{Se}_{0.8}$ thin film.

Figure 3.42 displays the UV-vis DRS (inset) and Tauc plots of RGO- $\text{Cd}_{0.6}\text{Zn}_{0.2}\text{Ni}_{0.2}\text{S}_{0.2}\text{Se}_{0.8}$ and $\text{Cd}_{0.6}\text{Zn}_{0.2}\text{Ni}_{0.2}\text{S}_{0.2}\text{Se}_{0.8}$ thin films. The band gap values for RGO- $\text{Cd}_{0.6}\text{Zn}_{0.2}\text{Ni}_{0.2}\text{S}_{0.2}\text{Se}_{0.8}$ and $\text{Cd}_{0.6}\text{Zn}_{0.2}\text{Ni}_{0.2}\text{S}_{0.2}\text{Se}_{0.8}$ are calculated as 1.83 and 1.84 eV, respectively.

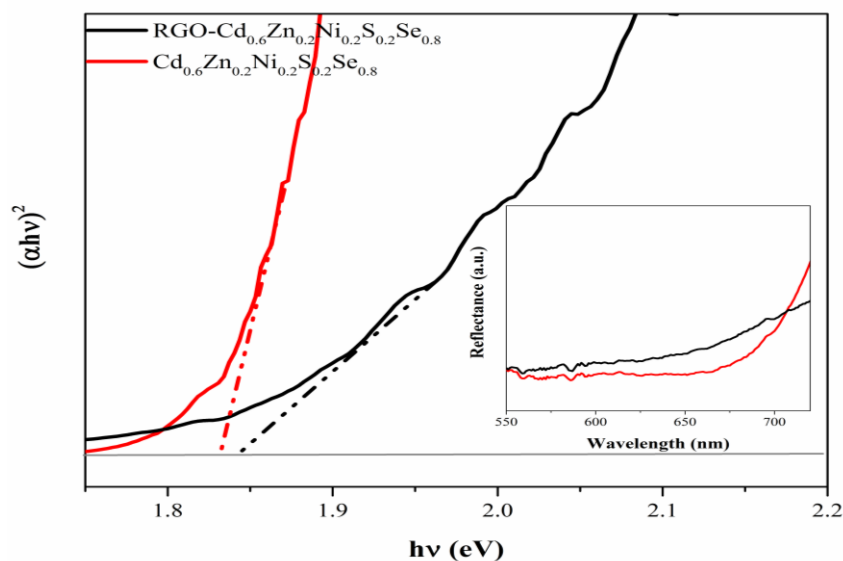


Figure 3.42. UV-vis DRS (inset) and Tauc plots of RGO-Cd_{0.6}Zn_{0.2}Ni_{0.2}S_{0.2}Se_{0.8} and Cd_{0.6}Zn_{0.2}Ni_{0.2}S_{0.2}Se_{0.8} thin films.

Linear sweep voltammetry (LSV) analyses were performed in an aqueous electrolyte (0.25 mol dm⁻³ Na₂S/0.35 mol dm⁻³ Na₂SO₃) by switching the light on and off at 0.1 V intervals. RGO-Cd_{0.6}Zn_{0.2}Ni_{0.2}S_{0.2}Se_{0.8} photoelectrode generates the highest photocurrent density at 0.8 V vs. RHE. In comparison, Cd_{0.6}Zn_{0.2}Ni_{0.2}S_{0.2}Se_{0.8} photoelectrode yields close, yet apparently lower photocurrent density. In terms of LSV, the performances of Cd_{0.6}Zn_{0.2}Cu_{0.2}S_{0.2}Se_{0.8} and Cd_{0.6}Zn_{0.2}Mo_{0.2}S_{0.2}Se_{0.8} photoelectrodes comes after Cd_{0.6}Zn_{0.2}Ni_{0.2}S_{0.2}Se_{0.8} photoelectrode.

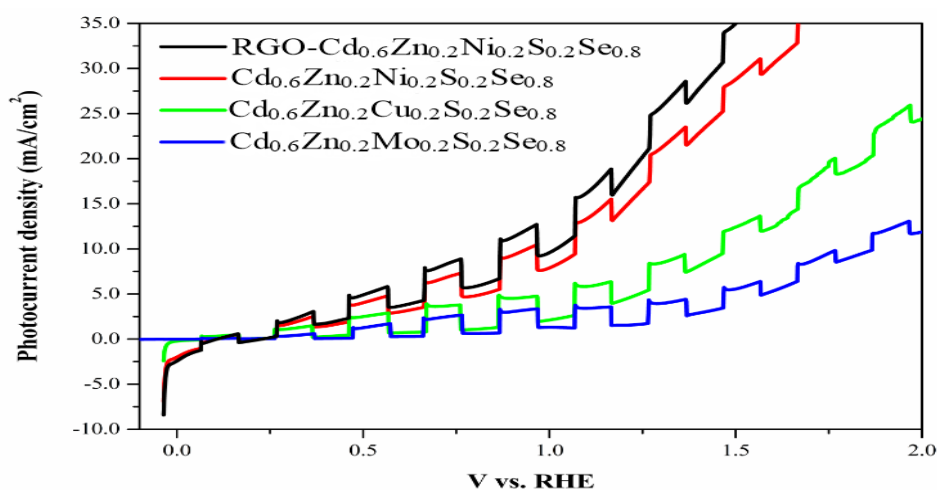


Figure 3.43. LSV curves of Cd_{0.6}Zn_{0.2}Mo_{0.2}S_{0.2}Se_{0.8}, Cd_{0.6}Zn_{0.2}Cu_{0.2}S_{0.2}Se_{0.8}, Cd_{0.6}Zn_{0.2}Ni_{0.2}S_{0.2}Se_{0.8} and RGO-Cd_{0.6}Zn_{0.2}Ni_{0.2}S_{0.2}Se_{0.8} photoelectrodes.

The transient photocurrents of photoelectrodes were illustrated in Figure 3.44. Photocurrent density of 5.34 mA cm^{-2} was achieved with the RGO- $\text{Cd}_{0.6}\text{Zn}_{0.2}\text{Ni}_{0.2}\text{S}_{0.2}\text{Se}_{0.8}$ photoelectrode, which outperforms all other tested photoelectrodes in terms of photogenerated charge carrier separation efficiency and photocorrosion. The photocurrent density of RGO- $\text{Cd}_{0.6}\text{Zn}_{0.2}\text{Ni}_{0.2}\text{S}_{0.2}\text{Se}_{0.8}$ is followed by $\text{Cd}_{0.6}\text{Zn}_{0.2}\text{Ni}_{0.2}\text{S}_{0.2}\text{Se}_{0.8}$, $\text{Cd}_{0.6}\text{Zn}_{0.2}\text{Cu}_{0.2}\text{S}_{0.2}\text{Se}_{0.8}$ and $\text{Cd}_{0.6}\text{Zn}_{0.2}\text{Mo}_{0.2}\text{S}_{0.2}\text{Se}_{0.8}$ photoelectrodes, which corresponds to 5.08, 3.16, 2.53 mA cm^{-2} , respectively.

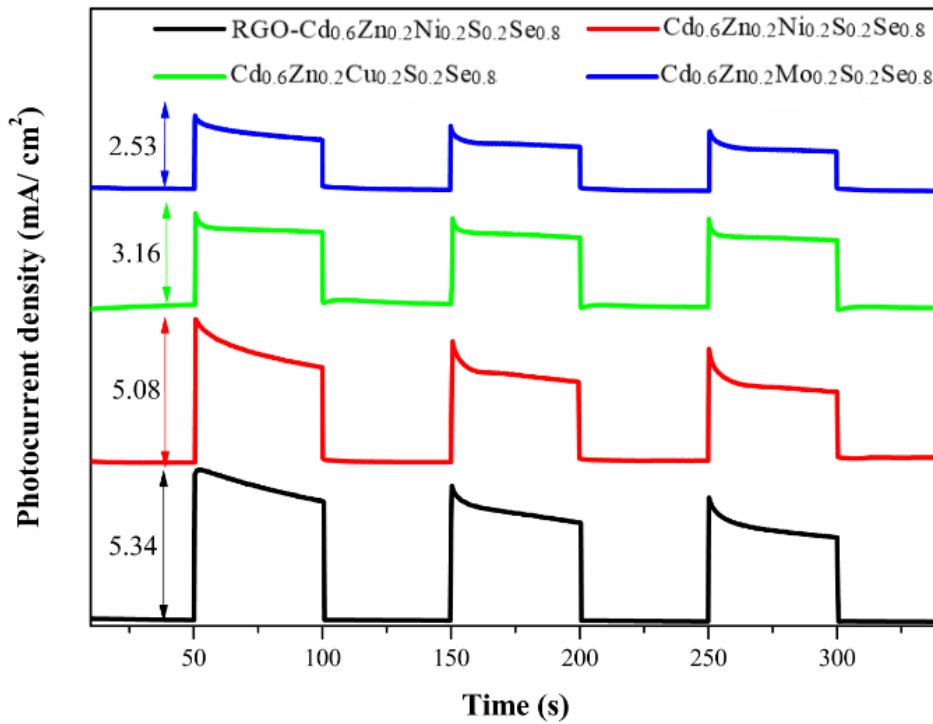


Figure 3.44. Chronoamperometric (CA) curves of $\text{Cd}_{0.6}\text{Zn}_{0.2}\text{Mo}_{0.2}\text{S}_{0.2}\text{Se}_{0.8}$, $\text{Cd}_{0.6}\text{Zn}_{0.2}\text{Cu}_{0.2}\text{S}_{0.2}\text{Se}_{0.8}$, $\text{Cd}_{0.6}\text{Zn}_{0.2}\text{Ni}_{0.2}\text{S}_{0.2}\text{Se}_{0.8}$ and RGO- $\text{Cd}_{0.6}\text{Zn}_{0.2}\text{Ni}_{0.2}\text{S}_{0.2}\text{Se}_{0.8}$ photoelectrodes.

Table 3.6. Literature survey on related photoelectrodes.

Photoelectrode /Substrate	Preparation Method	Temp.	Sacrificial reagent	Light intensity (mWcm ⁻²)	Photocurrent density	Ref.
TiO ₂ /CuPc /FTO	Electrophoretic deposition	450°C	0.1 mol dm ⁻³ Na ₂ SO ₄	100	2.40 mA cm ⁻²	[270]
TiO ₂ /CuPc/NiFe-LDH	Layer by layer method	-	0.5 mol dm ⁻³ Na ₂ SO ₄	100	2.10 mA cm ⁻²	[271]
CoPc (NH ₂) ₄ /BiVO ₄ /FTO	Electrodeposition	450°C (Air)	0.1 mol dm ⁻³ PO ₄ ³⁻ Tampon Çözelti	100	3.02 mA cm ⁻²	[272]
MoS _x /BP/BVO/FTP	Electrodeposition	450°C (Air)	0.2 mol dm ⁻³ Na ₂ SO ₄ 1.2 mol dm ⁻³ H ₂ SO ₄	100	2.1 mA cm ⁻²	[273]
P3HT/MoS ₂ /ITO	Spin Coating	-	0.1 mol dm ⁻³ LiClO ₄ / Acetonitrile 0.1 mol dm ⁻³ TBATFB/Acetonitrile	24.2	183.16 μA cm ⁻²	[274]
CuO/ Cu foils	Electrodeposition	300°C (Air)	1.0 mol dm ⁻³ Na ₂ SO ₄ 0.1 mol dm ⁻³ Na ₂ SO ₄	100	1.4 mA cm ⁻²	[275]
NiO _x /pn-GaN	Electrodeposition	500°C (O ₂)	1 mol dm ⁻³ NaCl	100	0.19 mA cm ⁻²	[276]
Cu ₂ O/CuO/ FTO	Electrodeposition	450°C	0.5 mol dm ⁻³ Na ₂ SO ₄	100	2.5 mA cm ⁻²	[277]
Cu ₂ O/ CuO//FTO	Electrodeposition	400°C (Air)	0.5 mol dm ⁻³ Na ₂ SO ₄	100	3.15 mA cm ⁻²	[278]
RGO(0.25)-Cd_{0.6}Zn_{0.2}Ni_{0.2}S_{0.2}Se_{0.8}	One-step electrodeposition	350°C	0.25 mol dm⁻³ Na₂S-0.35 mol dm⁻³ Na₂SO₃	100	5.34 mA cm⁻²	This work

Electrochemical impedance spectroscopy (EIS) was used to further explore the charge transport and kinetics (Figure 3.45a). The Nyquist plots suggest that the photoelectrodes exhibit similar solution resistance, but quite different charge transport resistance. The charge transfer resistance of Cd_{0.6}Zn_{0.2}Ni_{0.2}S_{0.2}Se_{0.8} has decreased significantly upon including RGO in photoelectrode composition and charge transfer at the semiconductor-electrolyte interface is promoted. On the contrary, the behavior of the Nyquist plot for Cd_{0.6}Zn_{0.2}Mo_{0.2}S_{0.2}Se_{0.8} photoelectrode can be responsible for the low photocurrent

density. Nyquist curves are fitted using equivalent Randles circuit model with a Warburg element as given in Figure 3.45b. This model includes the elements of the solution resistance (R_s), the Warburg impedance (W), charge transfer resistance (R_{ct}), and the constant phase element (CPE).

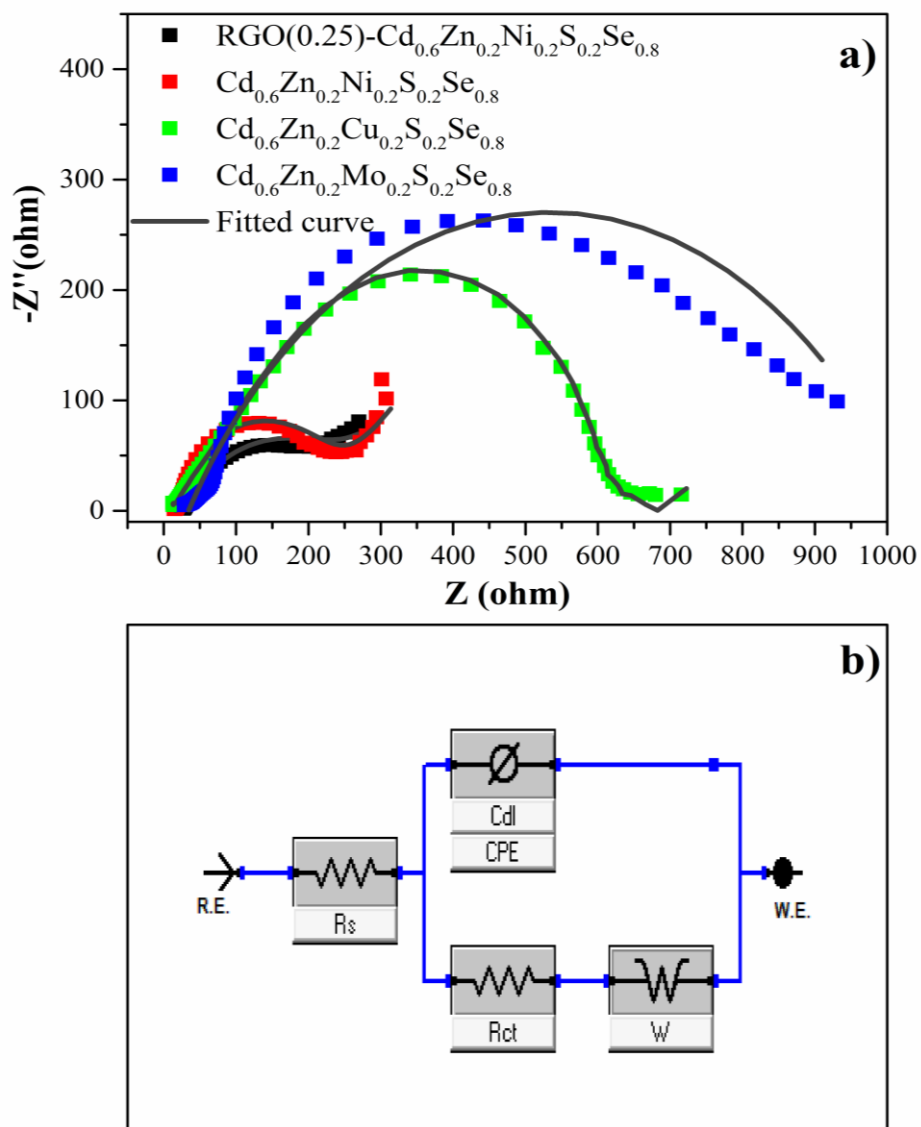


Figure 3.45. a) Nyquist plots and fitted curves of $Cd_{0.6}Zn_{0.2}Mo_{0.2}S_{0.2}Se_{0.8}$, $Cd_{0.6}Zn_{0.2}Cu_{0.2}S_{0.2}Se_{0.8}$, $Cd_{0.6}Zn_{0.2}Ni_{0.2}S_{0.2}Se_{0.8}$ and RGO- $Cd_{0.6}Zn_{0.2}Ni_{0.2}S_{0.2}Se_{0.8}$ photoelectrodes. b) Equivalent circuit model used for EIS data fitting (R.E.: Reference electrode, W.E.: Working electrode, R_s : Series resistance, R_{ct} : Charge transfer resistance, CPE: Constant phase element, W: Finite-length Warburg element).

The calculated EIS parameters according to the EIS model are presented on Table 3.7.

Table 3.7. Fitting results for EIS of $\text{Cd}_{0.6}\text{Zn}_{0.2}\text{Mo}_{0.2}\text{S}_{0.2}\text{Se}_{0.8}$, $\text{Cd}_{0.6}\text{Zn}_{0.2}\text{Cu}_{0.2}\text{S}_{0.2}\text{Se}_{0.8}$, $\text{Cd}_{0.6}\text{Zn}_{0.2}\text{Ni}_{0.2}\text{S}_{0.2}\text{Se}_{0.8}$ and RGO- $\text{Cd}_{0.6}\text{Zn}_{0.2}\text{Ni}_{0.2}\text{S}_{0.2}\text{Se}_{0.8}$ photoelectrodes.

Photoelectrode	R_s (Ω)	CPE ($10^{-4}\text{s}^n\Omega^{-1}$)	W ($\Omega\cdot\text{s}^{-1/2}$)	R_{ct} ($\Omega\text{ cm}^2$)
$\text{Cd}_{0.6}\text{Zn}_{0.2}\text{Mo}_{0.2}\text{S}_{0.2}\text{Se}_{0.8}$	34.27	2.78	$2.78\cdot 10^{-4}$	998.5
$\text{Cd}_{0.6}\text{Zn}_{0.2}\text{Cu}_{0.2}\text{S}_{0.2}\text{Se}_{0.8}$	11.70	1.39	$1.42\cdot 10^{-3}$	647.7
$\text{Cd}_{0.6}\text{Zn}_{0.2}\text{Ni}_{0.2}\text{S}_{0.2}\text{Se}_{0.8}$	26.02	1.95	$1.06\cdot 10^{-2}$	245.3
RGO- $\text{Cd}_{0.6}\text{Zn}_{0.2}\text{Ni}_{0.2}\text{S}_{0.2}\text{Se}_{0.8}$	16.40	3.71	$8.90\cdot 10^{-3}$	223.9

Mott-Schottky (M-S) analysis is performed for RGO- $\text{Cd}_{0.6}\text{Zn}_{0.2}\text{Ni}_{0.2}\text{S}_{0.2}\text{Se}_{0.8}$, $\text{Cd}_{0.6}\text{Zn}_{0.2}\text{Ni}_{0.2}\text{S}_{0.2}\text{Se}_{0.8}$, $\text{Cd}_{0.6}\text{Zn}_{0.2}\text{Cu}_{0.2}\text{S}_{0.2}\text{Se}_{0.8}$ and $\text{Cd}_{0.6}\text{Zn}_{0.2}\text{Mo}_{0.2}\text{S}_{0.2}\text{Se}_{0.8}$ photoelectrodes. Practically, above the flatband potential the photoresponse can be initiated [173]. M-S plots were collected at a frequency of 100 Hz in the dark. Figure 3.46. shows the M-S plots for RGO- $\text{Cd}_{0.6}\text{Zn}_{0.2}\text{Ni}_{0.2}\text{S}_{0.2}\text{Se}_{0.8}$, $\text{Cd}_{0.6}\text{Zn}_{0.2}\text{Ni}_{0.2}\text{S}_{0.2}\text{Se}_{0.8}$, $\text{Cd}_{0.6}\text{Zn}_{0.2}\text{Cu}_{0.2}\text{S}_{0.2}\text{Se}_{0.8}$ and $\text{Cd}_{0.6}\text{Zn}_{0.2}\text{Mo}_{0.2}\text{S}_{0.2}\text{Se}_{0.8}$ photoelectrodes.

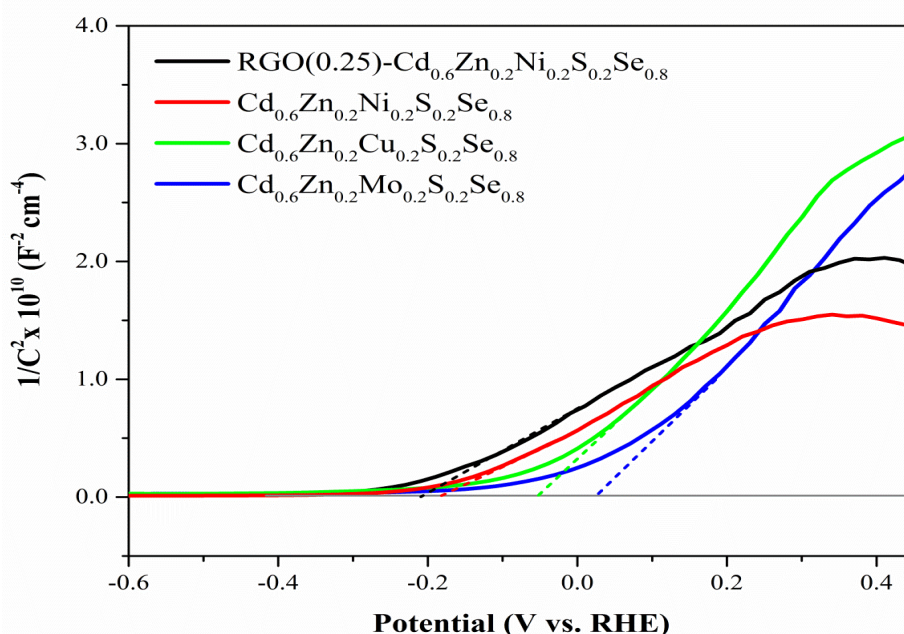


Figure 3.46. M-S plots for RGO- $\text{Cd}_{0.6}\text{Zn}_{0.2}\text{Ni}_{0.2}\text{S}_{0.2}\text{Se}_{0.8}$, $\text{Cd}_{0.6}\text{Zn}_{0.2}\text{Ni}_{0.2}\text{S}_{0.2}\text{Se}_{0.8}$, $\text{Cd}_{0.6}\text{Zn}_{0.2}\text{Cu}_{0.2}\text{S}_{0.2}\text{Se}_{0.8}$ and $\text{Cd}_{0.6}\text{Zn}_{0.2}\text{Mo}_{0.2}\text{S}_{0.2}\text{Se}_{0.8}$ photoelectrodes.

According to the Figure 3.46., the flat band potentials of RGO-Cd_{0.6}Zn_{0.2}Ni_{0.2}S_{0.2}Se_{0.8}, Cd_{0.6}Zn_{0.2}Ni_{0.2}S_{0.2}Se_{0.8}, Cd_{0.6}Zn_{0.2}Cu_{0.2}S_{0.2}Se_{0.8} and Cd_{0.6}Zn_{0.2}Mo_{0.2}S_{0.2}Se_{0.8} photoelectrodes are determined as -0.24, -0.18, -0.05, and 0.02 V vs. RHE. Yet, linear sweep voltammetry (LSV) results suggest that the onset potentials are shifted to more positive side, which designates the lack of efficient electron-hole extracting mechanism. Therefore, an external bias is necessary to initiate photoresponse. RGO-Cd_{0.6}Zn_{0.2}Ni_{0.2}S_{0.2}Se_{0.8} photoelectrode, on the other hand, has a minimal external bias, which is in line with prior findings.

The slope of the M-S plot is inversely proportional to the N_d value of a photoelectrode. Indeed, the slope of the M-S curve of RGO-Cd_{0.6}Zn_{0.2}Ni_{0.2}S_{0.2}Se_{0.8} is apparently the largest [279].

Charge carrier density values of photoelectrodes are calculated based on Eq (3.24):

$$1/C^2=(2/\epsilon_0\epsilon_eNA^2)(V-V_{fb}-KT/e) \quad (3.6)$$

C: capacitance of space charge region, e: electron charge (1.603 x 10⁻¹⁹ C), K: Boltzmann constant (1.38 x 10⁻²³ J/K), T: absolute temperature (K), ε: dielectric constant of semiconductor, ε₀: permittivity of vacuum (8.854 x 10⁻¹² F m⁻¹), N: charge carrier density, A: area of the photoelectrode, V: applied potential, V_{fb}: flat band potential. (KT/e is neglected at room temperature under 1 atm pressure).

The flat band potentials (V_{fb}) and charge donor density values (N_d) derived from M-S plots are summarized in Table 3.8.

Table 3.8. M-S parameters for RGO-Cd_{0.6}Zn_{0.2}Ni_{0.2}S_{0.2}Se_{0.8}, Cd_{0.6}Zn_{0.2}Ni_{0.2}S_{0.2}Se_{0.8}, Cd_{0.6}Zn_{0.2}Cu_{0.2}S_{0.2}Se_{0.8} and Cd_{0.6}Zn_{0.2}Mo_{0.2}S_{0.2}Se_{0.8} photoelectrodes.

Photoelectrode	N _d (cm ⁻³)	V _{fb} (V vs. RHE)
RGO-Cd _{0.6} Zn _{0.2} Ni _{0.2} S _{0.2} Se _{0.8}	4.88 x 10 ¹⁸	-0.24
Cd _{0.6} Zn _{0.2} Ni _{0.2} S _{0.2} Se _{0.8}	4.44 x 10 ¹⁸	-0.18
Cd _{0.6} Zn _{0.2} Cu _{0.2} S _{0.2} Se _{0.8}	4.17 x 10 ¹⁸	-0.05
Cd _{0.6} Zn _{0.2} Mo _{0.2} S _{0.2} Se _{0.8}	2.80 x 10 ¹⁸	0.02

Figure 3.47. illustrates the band diagram of RGO-Cd_{0.6}Zn_{0.2}Ni_{0.2}S_{0.2}Se_{0.8} photoelectrode in PEC studies. The conduction band and valence band energies are determined as -0.34 eV and 1.50 eV, respectively.

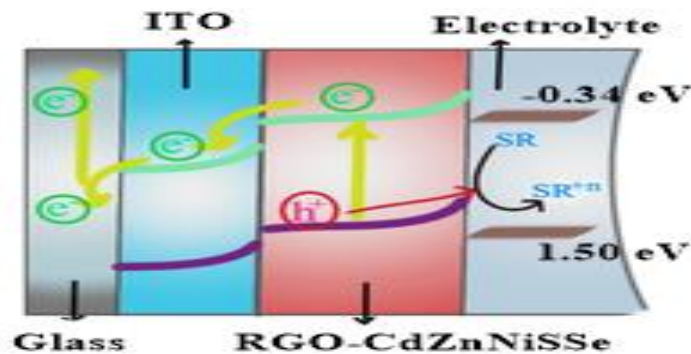


Figure 3.47. Band diagram of RGO-Cd_{0.6}Zn_{0.2}Ni_{0.2}S_{0.2}Se_{0.8} photoelectrode in PEC hydrogen production system.

The ABPE vs. V vs. RHE curves for Cd_{0.6}Zn_{0.2}Ni_{0.2}S_{0.2}Se_{0.8} and RGO-Cd_{0.6}Zn_{0.2}Ni_{0.2}S_{0.2}Se_{0.8} photoelectrodes are given in Figure 3.48. According to the figure, the maximum ABPE values for Cd_{0.6}Zn_{0.2}Ni_{0.2}S_{0.2}Se_{0.8} and RGO-Cd_{0.6}Zn_{0.2}Ni_{0.2}S_{0.2}Se_{0.8} photoelectrodes are determined as 2.31% and 3.18%, respectively.

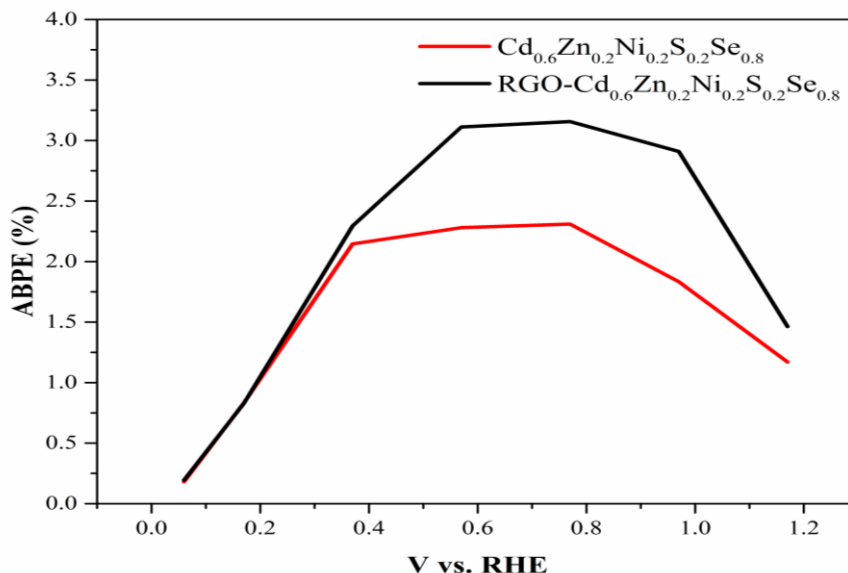


Figure 3.48. ABPE values for Cd_{0.6}Zn_{0.2}Ni_{0.2}S_{0.2}Se_{0.8} and RGO-Cd_{0.6}Zn_{0.2}Ni_{0.2}S_{0.2}Se_{0.8} photoelectrodes.

4. CONCLUSIONS

This study systematically investigates the electrodeposition of CdZnS, CdZnSSe, CdZnNiSSe, CdZnCuSSe, CdZnMoSSe, RGO-CdZnS, RGO-CdZnSSe, RGO-CdZnNiSSe photoelectrodes on ITO substrate by repetitive cyclic voltammetry at room temperature to determine their PEC performances. The repetitive cyclic voltammetry technique was performed at the rate of 100 mV s^{-1} . As-prepared photoelectrodes were thermally annealed in Ar atmosphere at different temperatures for 1 h using a horizontal tube furnace. The photoelectrochemical activities of photoelectrodes were examined using a standard three-electrode system in $\text{Na}_2\text{S}/\text{Na}_2\text{SO}_3$ sacrificial reagent under chopped 1 Sun illumination (100 mW cm^{-2}). All the electrodes were immersed in a $0.35 \text{ mol dm}^{-3} \text{ Na}_2\text{S}/0.25 \text{ mol dm}^{-3} \text{ Na}_2\text{SO}_3$ sacrificial electrolyte ($\text{pH}=13.0$) throughout PEC analyses. The area of $1 \text{ cm} \times 0.8 \text{ cm}$ of photoanodes was exposed to solar light illumination with the power intensity held at $1.0 \times 10^3 \text{ W m}^{-2}$. Open circuit potential (OCP) measurements, linear sweep voltammograms (LSV) and chronoamperometry (CA) analyses were monitored under transient light conditions. LSV for the photoanodes were obtained with the scan rate of 5 mV s^{-1} . Electrochemical impedance spectroscopy (EIS) measurement was performed in dark conditions. The amplitude of the sinusoidal wave was 10 mV and the employed frequency range was from 10^5 to 10^{-2} Hz. Mott-Shottky (M-S) analysis was carried out at an AC frequency of 1 kHz with an amplitude of 5 mV.

Prior to performing the photoelectrochemical investigations, all of the produced photoelectrodes were characterized. Scanning Electron Microscopy (SEM) with an EDAX detector attachment operating at 15.0 kV was used to analyze the microstructure and morphology of thin films. Under Cu-K α radiation with a step size of 0.02° , an XRD pattern was acquired on an X-ray diffractometer. In back scattering geometry, Raman spectrometer was used to capture Raman spectra at a 538 nm laser excitation wavelength. An ultraviolet-visible diffuse reflectance spectrophotometer (UV-vis DRS) was used to record the UV-vis DRS spectra of samples. Thermo-Scientific spectrophotometer (Al-K α (1486.7 eV)- X-ray source with the beam diameter of 400 nm diameter) was utilized for the XPS measurements.

At first, $\text{Cd}_x\text{Zn}_{1-x}\text{S}$ ($x=0.0, 0.2, 0.5, 0.8, 1.0$) photoelectrodes were fabricated from the aqueous solution consisting of $\text{Cd}(\text{CH}_3\text{COO})_2 \cdot 2\text{H}_2\text{O}$, $\text{Zn}(\text{CH}_3\text{COO})_2 \cdot 2\text{H}_2\text{O}$ and

Na₂S₂O₃. Among all the tested photoelectrodes, Cd_{0.8}Zn_{0.2}S yielded the best results. Yet, it needed some modifications to suppress photocorrosion in the presence of sacrificial electrolyte during PEC analyses. Annealing at 350°C and 450°C, and RGO decoration of Cd_{0.8}Zn_{0.2}S prevented severe corrosion problems as well as increase photoinduced electron number and lessen e⁻-h⁺ recombination rate. The photostability of annealed (especially at 450 °C) Cd_{0.8}Zn_{0.2}S photoelectrode was enhanced to a large extent in comparison with as-synthesized Cd_{0.8}Zn_{0.2}S photoelectrode due to the improved lattice structure and decrease of defects. Increasing Cd/Zn value from 0.0 to 0.8 in Cd_xZn_{1-x}S composition boosted the photocurrent density almost 18 folds, reaching from 25 μA cm⁻² to 438 μA cm⁻². The photocurrent density values were obtained as 193, 117, and 83 μA cm⁻² for CdS, Cd_{0.5}Zn_{0.5}S, and Cd_{0.2}Zn_{0.8}S photoelectrodes, respectively. These results showed that it is worthy to note that increasing Zn composition in photoelectrodes improved the stability of photoinduced charges. Furthermore, it was seen that it is important to keep RGO composition in RGO-Cd_{0.8}Zn_{0.2}S photoelectrode at an optimum value since the overabundance of RGO avoids the absorption of light. This situation causes the reduction of the number of electrons excited from the valence band to the conduction band of Cd_{0.8}Zn_{0.2}S. The maximum ABPE values of Cd_{0.8}Zn_{0.2}S (annealed at 450°C) and RGO(0.25)- Cd_{0.8}Zn_{0.2}S were estimated as 0.86% and 1.02%, respectively.

Secondly, the photoelectrochemical activities of Cd_{0.8}Zn_{0.2}S_xSe_{1-x} and RGO-Cd_{0.8}Zn_{0.2}S_{0.2}Se_{0.8} photoelectrodes were investigated for the first time in literature. Yet, there has been no any study reporting the one-step electrodeposition of CdZnSSe bearing photoanodes in the literature. Due to the narrow band gap values of CdSe and ZnSe compared to the CdS and ZnS, different S/Se compositions were modulated in the Cd_{0.8}Zn_{0.2}S_xSe_{1-x} photoelectrode composition. To fabricate Cd_{0.8}Zn_{0.2}S_xSe_{1-x} photoelectrodes, an aqueous electrolytic bath consisting of Cd(CH₃COO)₂, Zn(CH₃COO)₂, Na₂SeSO₃, EDTA, and NaOH was prepared. EDTA was used to avoid the precipitation of the formed hydroxylated Cd(II) and Zn(II) compounds in the presence of Na₂SeSO₃. The photoelectrochemical activities of photoelectrodes were examined using a standard three-electrode system in Na₂S/Na₂SO₃ sacrificial reagent under chopped 1 Sun illumination (100 mW cm⁻²). Photoelectrodes were thermally annealed at 350°C in argon to adhere the thin film onto the ITO substrate. The results of

photoelectrochemical analyses revealed that $\text{Cd}_{0.8}\text{Zn}_{0.2}\text{S}_{0.2}\text{Se}_{0.8}$ photoelectrode exhibited the highest photocurrent density among $\text{Cd}_{0.8}\text{Zn}_{0.2}\text{S}_x\text{Se}_{1-x}$ photoelectrodes. In addition, including RGO in $\text{Cd}_{0.8}\text{Zn}_{0.2}\text{S}_{0.2}\text{Se}_{0.8}$ structure suppressed the recombination of photoinduced charges and consequently enhanced the photoelectrochemical activity. RGO(0.25)- $\text{Cd}_{0.8}\text{Zn}_{0.2}\text{S}_{0.2}\text{Se}_{0.8}$ photoelectrode was determined as the photoelectrode yielding the highest photocurrent and efficiency. Namely, $\text{Cd}_{0.8}\text{Zn}_{0.2}\text{S}$, $\text{Cd}_{0.8}\text{Zn}_{0.2}\text{S}_{0.8}\text{Se}_{0.2}$, $\text{Cd}_{0.8}\text{Zn}_{0.2}\text{S}_{0.5}\text{Se}_{0.5}$, $\text{Cd}_{0.8}\text{Zn}_{0.2}\text{S}_{0.2}\text{Se}_{0.8}$, $\text{Cd}_{0.8}\text{Zn}_{0.2}\text{Se}$ exhibited the photocurrent densities of 0.94, 1.34, 2.34, 4.08, 3.07 mA cm^{-2} (vs. Ag/AgCl) under chopped solar light irradiation. The photocurrent density of $\text{Cd}_{0.8}\text{Zn}_{0.2}\text{S}_{0.2}\text{Se}_{0.8}$ jumped from 4.08 mA cm^{-2} , to 4.21, 5.00, and 4.51 mA cm^{-2} for RGO(0.10)- $\text{Cd}_{0.8}\text{Zn}_{0.2}\text{S}_{0.2}\text{Se}_{0.8}$, RGO(0.25)- $\text{Cd}_{0.8}\text{Zn}_{0.2}\text{S}_{0.2}\text{Se}_{0.8}$, RGO(0.50)- $\text{Cd}_{0.8}\text{Zn}_{0.2}\text{S}_{0.2}\text{Se}_{0.8}$ photoelectrodes, respectively. The maximum ABPE values for $\text{Cd}_{0.8}\text{Zn}_{0.2}\text{S}_{0.2}\text{Se}_{0.8}$ and RGO(0.25)- $\text{Cd}_{0.8}\text{Zn}_{0.2}\text{S}_{0.2}\text{Se}_{0.8}$ were estimated as 2.15% and 3.07%.

Finally, $\text{Cd}_{0.6}\text{Ni}_{0.2}\text{Zn}_{0.2}\text{S}_{0.2}\text{Se}_{0.8}$, $\text{Cd}_{0.6}\text{Cu}_{0.2}\text{Zn}_{0.2}\text{S}_{0.2}\text{Se}_{0.8}$, $\text{Cd}_{0.6}\text{Mo}_{0.2}\text{Zn}_{0.2}\text{S}_{0.2}\text{Se}_{0.8}$ photoelectrodes were fabricated from the aqueous solutions of $\text{Cd}(\text{CH}_3\text{COO})_2 \cdot 2\text{H}_2\text{O}$, $\text{Zn}(\text{CH}_3\text{COO})_2 \cdot 2\text{H}_2\text{O}$, $\text{Cu}(\text{CH}_3\text{COO})_2$, $\text{Na}_2\text{MoO}_4 \cdot 2\text{H}_2\text{O}$, $\text{Ni}(\text{NO}_3)_2 \cdot 6\text{H}_2\text{O}$, $\text{Na}_2\text{S}_2\text{O}_3$ and Na_2SeSO_3 as Cd, Zn, Cu, Mo, Ni, S, Se precursors, respectively. EDTA was used as complexing agent to chelate with the cations of Cd, Zn, Ni, Cu and Mo. As-prepared photoelectrodes were thermally annealed in a horizontal tube furnace at 350°C for an hour. The photocurrent density of RGO- $\text{Cd}_{0.6}\text{Zn}_{0.2}\text{Ni}_{0.2}\text{S}_{0.2}\text{Se}_{0.8}$ was followed by $\text{Cd}_{0.6}\text{Zn}_{0.2}\text{Ni}_{0.2}\text{S}_{0.2}\text{Se}_{0.8}$, $\text{Cd}_{0.6}\text{Zn}_{0.2}\text{Cu}_{0.2}\text{S}_{0.2}\text{Se}_{0.8}$ and $\text{Cd}_{0.6}\text{Zn}_{0.2}\text{Mo}_{0.2}\text{S}_{0.2}\text{Se}_{0.8}$ photoelectrodes, which corresponds to 5.08, 3.16, 2.53 mA cm^{-2} , respectively. The maximum ABPE values for $\text{Cd}_{0.6}\text{Zn}_{0.2}\text{Ni}_{0.2}\text{S}_{0.2}\text{Se}_{0.8}$ and RGO- $\text{Cd}_{0.6}\text{Zn}_{0.2}\text{Ni}_{0.2}\text{S}_{0.2}\text{Se}_{0.8}$ photoelectrodes were determined as 2.31% and 3.18%, respectively.

In all EIS analyses, Nyquist plots were fitted through equivalent Randles model with Warburg impedance. R_{ct} , R_s , CPE, n , W parameters were found to be consistent with the photoelectrochemical performance of photoelectrodes.

Characterization techniques such as SEM, FESEM, Raman, XRD, EDS, UV-vis was applied to reveal the existence of elements in the composition of photoelectrodes as well as interpret the surface morphology, vibrational states, and chemical and electronic states of the atoms, band gap energy values and crystallographic structure.

All in all, the main idea of this thesis study emerges from using a facile, efficient, low-

cost technique to deposit thin films to perform as photoelectrodes. In the literature, electrodeposition is known as a versatile and cost-effective method to fabricate photoelectrodes but harvesting a large portion of the solar light efficiently is still an issue to solve. To solve this, one-step simultaneous electrodeposition using cyclic voltammetry (CV) was carried out and optimizations on photoelectrode composition, annealing temperature, pH, RGO composition, potential range arrangement on CV were made. Initially, the photocurrent value was $25 \mu\text{A cm}^{-2}$ (ZnS) and at the end of the study with necessary modifications, 5.34 mA cm^{-2} photocurrent density was achieved with RGO-Cd_{0.6}Zn_{0.2}Ni_{0.2}S_{0.2}Se_{0.8}.



REFERENCES

- [1] Acikgoz, C., (2011). Renewable energy education in Turkey. *Renewable Energy*, 36, 608-11.
- [2] Abu-Rumman, G., Khdair, A.I., Khdair, S.I., (2020). Current status and future investment potential in renewable energy in Jordan: An overview, *Heliyon*, 6(2), e03346.
- [3] Musa, S.D., Zhonghua, T., Ibrahim, A.O., Habib, M., (2018). China's energy status: a critical look at fossils and renewable options, *Renewable and Sustainable Energy Reviews*, 81, 2281-90.
- [4] Martins, F., Felgueiras, C., Smitková, M., (2018). Fossil fuel energy consumption in European countries, *Energy Procedia*, 153, 107-11.
- [5] Saidi, K., Omri, A., (2020). The impact of renewable energy on carbon emissions and economic growth in 15 major renewable energy-consuming countries, *Environmental Research*, 109567.
- [6] Apergis, E., Apergis, N., (2017). The role of rare earth prices in renewable energy consumption: the actual driver for a renewable energy world, *Energy Economics*, 62, 33-42.
- [7] Dawood, F., Anda, M., Shafiullah, G., (2020). Hydrogen production for energy: An overview, *International Journal of Hydrogen Energy*.
- [8] Ike, G.N., Usman, O., Alola, A.A., Sarkodie, S.A. (2020). Environmental quality effects of income, energy prices and trade: The role of renewable energy consumption in G-7 countries. *Science of The Total Environment*, 137813.
- [9] Elayyachy, M., Elkodadi, M., Aouniti, A., Ramdani, A., Hammouti, B., Malek, F., et al., (2005). New bipyrazole derivatives as corrosion inhibitors for steel in hydrochloric acid solutions. *Mater Chem Phys.*, 93, 281-5.
- [10] Goel, M., (2005). *Energy Sources and Global Warming*. New Delhi, India: Allied Publishers Pvt. Ltd.
- [11] Verma, C., Saji, V.S., Quraishi, M., Ebenso, E., (2020). Pyrazole derivatives as environmental benign acid corrosion inhibitors for mild steel: experimental and computational studies. *Journal of Molecular Liquids.*, 298, 111943.
- [12] Abe, J., Ajenifuja, E., Popoola, O., (2019). Hydrogen energy, economy and storage: review and recommendation. *International Journal of Hydrogen Energy*.

- [13] Abdin, Z., Zafaranloo, A., Rafiee, A., Mérida, W., Lipiński, W., Khalilpour, K.R., (2020). Hydrogen as an energy vector. *Renewable and Sustainable Energy Reviews*. 120, 109620.
- [14] *The Future of Hydrogen: Seizing today's opportunities* (2019).
- [15] *Europe H. Hydrogen Applications* (2017).
- [16] Hanley, E.S., Deane, J., Gallachóir, B.Ó., (2018). The role of hydrogen in low carbon energy futures—A review of existing perspectives. *Renewable and Sustainable Energy Reviews*. 82, 3027-45.
- [17] Acar, C., Dincer, I., (2019). Review and evaluation of hydrogen production options for better environment. *Journal of Cleaner Production*.
- [18] Dincer, I., Acar, C., (2015). Review and evaluation of hydrogen production methods for better sustainability. *International Journal of Hydrogen Energy*, 40, 11094-111.
- [19] Kalamaras, C.M., Efstathiou, A.M., (2013). Hydrogen production technologies: current state and future developments, Hindawi.
- [20] Nikolaidis, P., Poullikkas, A., (2017). A comparative overview of hydrogen production processes. *Renewable and Sustainable Energy Reviews*, 67, 597-611.
- [21] Holladay, J.D., Hu, J., King, D.L., Wang, Y., (2009). An overview of hydrogen production technologies. *Catalysis Today*, 139, 244-60.
- [22] Bakhtyari, A., Makarem, M., Rahimpour, M., (2017). Hydrogen production through pyrolysis. *Encyclopedia of Sustainability Science and Technology*, Springer New York, New York, NY.
- [23] Ismagilov, Z., Matus, E., Ismagilov, I., Sukhova, O., Yashnik, S., Ushakov, V., et al (2019). Hydrogen production through hydrocarbon fuel reforming processes over Ni based catalysts. *Catalysis Today*, 323, 166-82.
- [24] Barbir, F., (2006). PEM fuel cells. *Fuel Cell Technology*: Springer, 27-51.
- [25] LeValley, T.L., Richard, A.R., Fan, M., (2014). The progress in water gas shift and steam reforming hydrogen production technologies—a review. *International Journal of Hydrogen Energy*, 39, 16983-7000.
- [26] Baruah, R., Dixit, M., Basarkar, P., Parikh, D., Bhargav, A., (2015). Advances in ethanol autothermal reforming. *Renewable and Sustainable Energy Reviews*, 51, 1345-53.

- [27] Luque, R., Speight, J., (2014). Gasification for synthetic fuel production: fundamentals, processes and applications, Elsevier.
- [28] Pyrolysis. 2020.
- [29] Chaubey, R., Sahu, S., James, O.O., Maity, S., (2013). A review on development of industrial processes and emerging techniques for production of hydrogen from renewable and sustainable sources. *Renewable and Sustainable Energy Reviews*, 443-62.
- [30] da Silva Veras, T., Mozer, T.S., da Silva César, A., (2017). Hydrogen: trends, production and characterization of the main process worldwide. *International Journal of Hydrogen Energy*, 42, 2018-33.
- [31] Pandey, B., Prajapati, Y.K., Sheth, P.N., (2019). Recent progress in thermochemical techniques to produce hydrogen gas from biomass: A state of the art review, *International Journal of Hydrogen Energy*.
- [32] Ontario-Ministry of Agriculture FaRA. Biomass Combustion.
- [33] Shahbaz, M., Al-Ansari, T., Aslam, M., Khan, Z., Inayat, A., Athar, M., et al (2020). A state of the art review on biomass processing and conversion technologies to produce hydrogen and its recovery via membrane separation. *International Journal of Hydrogen Energy*.
- [34] Chi, J., Yu, H., (2018). Water electrolysis based on renewable energy for hydrogen production. *Chinese Journal of Catalysis*, 39, 390-4.
- [35] Tahir, M., Tasleem, S., Tahir, B., (2020). Recent development in band engineering of binary semiconductor materials for solar driven photocatalytic hydrogen production. *International Journal of Hydrogen Energy*.
- [36] Fajrina, N., Tahir, M., (2019). A critical review in strategies to improve photocatalytic water splitting towards hydrogen production. *International Journal of Hydrogen Energy*, 44, 540-77.
- [37] Zhang, Y., Heo, Y.J., Lee, J.W., Lee, J.H., Bajgai, J., Lee, K.J., et al. (2018). Photocatalytic hydrogen evolution via water splitting: A short review. *Catalysts*, 8 (655).
- [38] Zhou, H., Liu, J., Xu, J.J, Zhang, S., Chen, H.Y. (2019). Advances in DNA/RNA detection using nanotechnology. *Advances in Clinical Chemistry*, 91, 31-98.
- [39] Carmichael, P. (2016). *Materials and Devices for Photoelectrochemical and*

Photocatalytic Water Splitting, UCL (University College London).

- [40] Zhang, Z., Yates, Jr J.T., (2012). Band bending in semiconductors: chemical and physical consequences at surfaces and interfaces. *Chemical Reviews*, 112, 5520-51.
- [41] Brajter-Toth, A. (2003). *Electroanalytical Methods: Guide to Experiments and Applications*, ACS Publications, New York.
- [42] Pletcher, D. (2019). *A first course in electrode processes*: Royal Society of Chemistry.
- [43] Zhang, Q., Uchaker, E., Candelaria, S.L., Cao, G., (2013). Nanomaterials for energy conversion and storage. *Chemical Society Reviews*, 42, 3127-71.
- [44] Peerakiatkhajohn, P., Yun, J.H., Wang, S., Wang, L., (2016). Review of recent progress in unassisted photoelectrochemical water splitting: from material modification to configuration design. *Journal of Photonics for Energy*, 7, 012006.
- [45] Chen, Z., Dinh, H.N., Miller, E., (2013). *Photoelectrochemical water splitting*: Springer.
- [46] Bajorowicz, B., Kobylański, M., Malankowska, A., Mazierski, P., Nadolna, J., Pieczyńska, A., et al (2018). Application of metal oxide-based photocatalysis.
- [47] Ghosh, S., Basu, R.N., (2019). *Nanoscale Characterization. Noble Metal-Metal Oxide Hybrid Nanoparticles*: Elsevier, p. 65-93.
- [48] Li, R., (2017). Latest progress in hydrogen production from solar water splitting via photocatalysis, photoelectrochemical, and photovoltaic-photoelectrochemical solutions. *Chinese Journal of Catalysis*, 38, 5-12.
- [49] Van de Krol, R., Grätzel, M., (2012). *Photoelectrochemical hydrogen production*: Springer.
- [50] Lu, Q., Yu, Y., Ma, Q., Chen, B., Zhang, H., (2016). 2D transition-metal-dichalcogenide-nanosheet-based composites for photocatalytic and electrocatalytic hydrogen evolution reactions. *Advanced Materials*, 28, 1917-33.
- [51] Giménez, S., Bisquert, J., (2016). *Photoelectrochemical solar fuel production*: Springer.
- [52] Ahmed, M., Dincer, I., (2019). A review on photoelectrochemical hydrogen production systems: challenges and future directions. *International Journal of Hydrogen Energy*, 44, 2474-507.
- [53] Joy, J., Mathew, J., George, S.C., (2018). *Nanomaterials for photoelectrochemical*

- water splitting–review. *International Journal of Hydrogen Energy*, 43, 4804-17.
- [54] Chiu, Y.H., Lai, T.H., Kuo, M.Y., Hsieh, P.Y., Hsu, Y.J., (2019). Photoelectrochemical cells for solar hydrogen production: Challenges and opportunities. *APL Materials*, 7, 080901.
- [55] Yang, Y., Chen, H., Bao, X., (2003). Synthesis and optical properties of cds semiconductor nanocrystallites encapsulated in a poly (ethylene oxide) matrix. *Journal of Crystal Growth*, 252, 251-6.
- [56] Li, C., Yang, S., Zheng, B., Zhou, T., Yuan, H., Xiao, D., (2012). Cadmium sulfide nanotubes thin films: Characterization and photoelectrochemical behavior. *Thin Solid Films*, 520, 2520-5.
- [57] Hankare, P., Chate, P., Sathe, D., (2009). Zinc sulphide semiconductor electrode synthesis and the photoelectrochemical application. *Journal of Alloys and compounds*, 487, 367-9.
- [58] Gaikwad, A., Betty, C., Kumar, A., Sasikala, R., (2018). Microflowers of Pd doped ZnS for visible light photocatalytic and photoelectrochemical applications. *Materials Science in Semiconductor Processing*, 86, 139-45.
- [59] Palik, E.D., (1998). *Handbook of optical constants of solids*. Academic press.
- [60] Li, X., Yang, Q., Hua, H., Chen, L., He, X., Hu, C., et al (2015). CdS/CdSe core/shell nanowall arrays for high sensitive photoelectrochemical sensors. *Journal of Alloys and Compounds*, 630, 94-9.
- [61] Sitara, E., Nasir, H., Mumtaz, A., Ehsan, M.F., Sohail, M., Iram, S., et al.(2021). Enhanced photoelectrochemical water splitting using zinc selenide/graphitic carbon nitride type-II heterojunction interface. *International Journal of Hydrogen Energy*.
- [62] Kuehnel, M.F., Creissen, C.E., Sahn, C.D., Wielend, D., Schlosser, A., Orchard, K.L., et al (2019). ZnSe Nanorods as Visible-Light Absorbers for Photocatalytic and Photoelectrochemical H₂ Evolution in Water. *Angewandte Chemie*, 131, 5113-7.
- [63] Rosman, N.N., Yunus, R.M., Minggu, L.J., Arifin, K., Salehmin, M.N.I., Mohamed, M.A., et al (2018). Photocatalytic properties of two-dimensional graphene and layered transition-metal dichalcogenides based photocatalyst for photoelectrochemical hydrogen generation: An overview. *International Journal of Hydrogen Energy*, 43, 18925-45.
- [64] Rowley-Neale, S.J., Randviir, E.P., Dena, A.S.A., Banks, C.E., (2018). An

overview of recent applications of reduced graphene oxide as a basis of electroanalytical sensing platforms. *Applied Materials Today*, 10, 218-26.

[65] Carneiro, P., Morais, S., Pereira, M.C., (2019). Nanomaterials towards biosensing of Alzheimer's disease biomarkers. *Nanomaterials*, 9(1663).

[66] Tan, H.L., Tahini, H.A., Wen, X., Wong, R.J., Tan, X., Iwase, A., et al., (2016). Interfacing BiVO₄ with reduced graphene oxide for enhanced photoactivity: a tale of facet dependence of electron shuttling. *Small*, 12, 5295-302.

[67] Prabhu, S., Cindrella, L., Kwon, O.J., Mohanraju, K., (2017). Green synthesis of rGO-WO₃ composite and its efficient photoelectrochemical water splitting. *International Journal of Hydrogen Energy*, 42, 29791-6.

[68] Verissimo, N., Chung, S., Webster, T., (2015). New nanoscale surface modifications of metallic biomaterials. *Surface Coating and Modification of Metallic Biomaterials*: Elsevier, 249-73.

[69] Rane, A.V., Kanny, K., Abitha, V., Thomas, S., (2018). Methods for synthesis of nanoparticles and fabrication of nanocomposites. *Synthesis of inorganic nanomaterials*: Elsevier, 121-39.

[70] Bhagyaraj, S.M., Oluwafemi, S.O., Kalarikkal, N., Thomas, S., (2018). Synthesis of inorganic nanomaterials: Advances and Key Technologies.

[71] Benelmekki, M., Erbe, A., (2019). Nanostructured thin films—background, preparation and relation to the technological revolution of the 21st century. *Frontiers of Nanoscience*: Elsevier, 1-34.

[72] Tahir, M.B., Rafique, M., Rafique, M.S., (2020). *Nanotechnology and Photocatalysis for Environmental Applications*: Elsevier.

[73] Korotcenkov, G., (2020). *Metal Oxide Powder Technologies: Fundamentals, Processing Methods and Applications*: Elsevier.

[74] Bhowmik, S., Rajan, A.G., (2022). Chemical Vapor Deposition of 2D Materials: A Review of Modeling, Simulation, and Machine Learning Studies. *iScience*, 103832.

[75] Pottathara, Y.B., Thomas, S., Kalarikkal, N., Grohens, Y., Kokol, V., (2019). *Nanomaterials synthesis: design, fabrication and applications*: Elsevier.

[76] De Guire, M.R., Bauermann, L.P., Parikh, H., Bill, J., (2013). Chemical bath deposition. *Chemical Solution Deposition of Functional Oxide Thin Films*: Springer, 319-39.

- [77] Mane, R., Lokhande, C., (2000). Chemical deposition method for metal chalcogenide thin films. *Materials Chemistry and Physics*, 65, 1-31.
- [78] Qiu, J., Weng, B., Ge, W., McDowell, L.L., Cai, Z., Shi, Z., (2017). A broadband Pb-chalcogenide/CdS solar cells with tandem quantum-dots embedded in the bulk matrix (QDiM) absorption layers by using chemical bath deposition. *Solar Energy Materials and Solar Cells*, 172, 117-23.
- [79] Abbas, K., Aamir, M., Mehmood, R.F., Sher, M., Akhtar, J., (2022). Deposition of morphology-tailored CdS thin films by chemical bath approach. *Materials Today: Proceedings*.
- [80] Skorniyakov, L., Uritskaya, A., (2021). Effect of diffusion on the formation of chemically deposited films of CdS and other chalcogenides. *Thin Solid Films*, 735, 138878.
- [81] Ho, S.M., (2015). Chalcogenide thin films prepared using chemical bath deposition method. *Research Journal of Applied Sciences, Engineering and Technology*, 11, 1058-65.
- [82] Boyle, D., Bayer, A., Heinrich, M., Robbe, O., O'Brien, P., (2000). Novel approach to the chemical bath deposition of chalcogenide semiconductors. *Thin Solid Films*, 361, 150-4.
- [83] Rathod, K.C., Kamble, P.D., Sanadi, K.R., Kamble, G.S., Guar, M.L., Garadkar, K.M., (2021). Photovoltaic application study of zinc telluride thin films grown by chemical bath deposition method. *Advances in Materials Physics and Chemistry*, 11, 131-44.
- [84] Puniredd, S., Pisula, W., Müllen, K., (2013). Influence of Film Morphology on Optical and Electronic Properties of Organic Materials. *Woodhead Publ Ser Electron Opt Mater*, 39, 83-101.
- [85] Makhlof, A., (2011). Current and advanced coating technologies for industrial applications. *Nanocoatings and ultra-thin films: Elsevier*, 3-23.
- [86] Busuioc, C., Jinga, S.I., Andronescu, E., (2012). Barium magnesium tantalate thin films obtained by sol-gel processing. *Revista Romana de Materiale*, 42, 299-305.
- [87] Lončarević, D., Čupić, Ž., (2019). The perspective of using nanocatalysts in the environmental requirements and energy needs of industry. *Industrial Applications of Nanomaterials: Elsevier*, 91-122.

- [88] Kakaei, K., Esrafil, M.D., Ehsani, A., (2019). Graphene and anticorrosive properties. *Interface Science and Technology*, Elsevier, 303-37.
- [89] van Stam, J., Andersén, M., Moons, E., (2016). Comparing morphology in dip-coated and spin-coated polyfluorene: Fullerene films. *Organic Photovoltaics XVII: SPIE*, 15-24.
- [90] Manivannan, R., Victoria, S.N., (2018). Preparation of chalcogenide thin films using electrodeposition method for solar cell applications—A review. *Solar Energy*, 173, 1144-57.
- [91] Lee, H., Lee, J-H., Hwang, Y-H., Kim, Y., (2014). Cyclic voltammetry study of electrodeposition of CuGaSe₂ thin films on ITO-glass substrates. *Current Applied Physics*, 14, 18-22.
- [92] Jana, A., Hazra, M., Datta, J., (2017). Periodic voltammetry as a successful technique for synthesizing CdSe semiconductor films for photo-electrochemical application. *Journal of Solid State Electrochemistry*, 21, 3083-91.
- [93] Gamburg, Y.D., Zangari, G., (2011). *Theory and practice of metal electrodeposition: Springer Science & Business Media*.
- [94] Prakash, S., Yeom, J., (2014). *Advanced fabrication methods and techniques. Nanofluidics and Microfluidics: Systems and Applications*, 87-170.
- [95] Ho, S.M., SA, V., Ahmed, G., Vidya, N.S., (2018). A review of nanostructured thin films for gas sensing and corrosion protection. *Mediterranean Journal of Chemistry*, 7.
- [96] Werta, S., Echendu, O., Egbo, K., Dejene, F., (2019). Electrochemical deposition and characterization of thin-film Cd_{1-x}Zn_xS for solar cell application: The effect of cathodic deposition voltage. *Thin Solid Films*, 689, 137511.
- [97] Panda, B., Mahapatra, P., Ghosh, M., (2020). Electrodeposited mixed ZnS–CdS photoelectrode for natural dye-sensitized solar cells (NDSSC). *Indian Journal of Physics*, 1-9.
- [98] Research P. Open Circuit Potential.
- [99] Muhibbullah, M., Haleem, A.M.A., (2015). Estimation of the Open Circuit Voltage of a pn Junction Based on Photoelectrochemical Measurements. *Transactions of the Materials Research Society of Japan*, 40, 247-52.
- [100] Hankin, A., Bedoya-Lora, F.E., Alexander, J.C., Regoutz, A., Kelsall, G.H., (2019). Flat band potential determination: avoiding the pitfalls. *Journal of Materials*

Chemistry A, 7, 26162-76.

[101] Park, J.H., Zhou, H., Percival, S.J., Zhang, B., Fan, F-R.F., Bard, A.J., (2013). Open circuit (mixed) potential changes upon contact between different inert electrodes—size and kinetic effects. *Analytical Chemistry*, 85, 964-70.

[102] Cambridge Uo.

[103] Chen, Z., Dinh, H., Miller, E., (2013). *Photoelectrochemical Water Splitting: Standards, Experimental Methods, and Protocols*, Springer-Verlag, New York.

[104] Nnamchi, P.S., Obayi, C.S., (2018). *Electrochemical Characterization of Nanomaterials. Characterization of Nanomaterials: Elsevier*, 103-27.

[105] Zhang, J., Xie, Z., Zhang, J., Tang, Y., Song, C., Navessin, T., et al., (2006). High temperature PEM fuel cells. *Journal of Power Sources*, 160, 872-91.

[106] Huang, H., Zhao, Y., Bai, Y., Li, F., Zhang, Y., Chen, Y., (2020). Conductive metal–organic frameworks with extra metallic sites as an efficient electrocatalyst for the hydrogen evolution reaction. *Advanced Science*, 7, 2000012.

[107] Wang, Z., Liu, Z., Chen, J., Yang, H., Luo, J., Gao, J., et al., (2019). Self-assembly of three-dimensional CdS nanosphere/graphene networks for efficient photocatalytic hydrogen evolution. *Journal of Energy Chemistry*, 31, 34-8.

[108] Inkson, B., (2016). *Scanning electron microscopy (SEM) and transmission electron microscopy (TEM) for materials characterization. Materials characterization using nondestructive evaluation (NDE) methods: Elsevier*.

[109] Ebnesajjad, S., Ebnesajjad, C., (2013). *Surface treatment of materials for adhesive bonding: William Andrew*.

[110] Kohli, R., Mittal, K., (2018). *Developments in Surface Contamination and Cleaning: Applications of Cleaning Techniques: Volume 11: Elsevier*.

[111] Epp, J., (2016). *X-ray diffraction (XRD) techniques for materials characterization. Materials characterization using nondestructive evaluation (NDE) methods: Elsevier*.

[112] Mather, R., (2009). *Surface modification of textiles by plasma treatments. Surface modification of textiles: Elsevier*.

[113] Martin, P.M., (2009). *Handbook of deposition technologies for films and coatings: science, applications and technology, William Andrew*.

[114] Adya, A.K., Canetta, E., (2014). *Nanotechnology and its applications to animal biotechnology. Animal Biotechnology: Elsevier*.

- [115] Chen, W., Wang, J., Wan, F., Wang, P., (2019). Review of optical fibre sensors for electrical equipment characteristic state parameters detection. *High Voltage*, 4, 271-81.
- [116] McGregor, H., Wang, W., Short, M., Zeng, H., (2016). Clinical utility of Raman spectroscopy: current applications and ongoing developments. *Advanced Health Care Technology*, 2, 13-29.
- [117] Mishra, J., Sharma, R.K., Misra, K., (2018). *Characterization Techniques for Herbal Products. Management of High Altitude Pathophysiology: Elsevier.*
- [118] Batra, V., Kotru, S., Varagas, M., Ramana, C., (2015). Optical constants and band gap determination of $\text{Pb}_{0.95}\text{La}_{0.05}\text{Zr}_{0.54}\text{Ti}_{0.46}\text{O}_3$ thin films using spectroscopic ellipsometry and UV-visible spectroscopy. *Optical Materials*, 49, 123-8.
- [119] Wang, H., Chu, P.K., (2013). *Surface characterization of biomaterials. Characterization of biomaterials: Elsevier.*
- [120] Moridon, S.N.F., Arifin, K., Yunus, R.M., Minggu, L.J., Kassim, M.B., (2021). Photocatalytic water splitting performance of TiO_2 sensitized by metal chalcogenides: A review. *Ceramics International*.
- [121] Zhao, J., Wang, J., Chen, Z., Ju, J., Han, X., Deng, Y., (2021). Metal chalcogenides: An emerging material for electrocatalysis. *APL Materials*, 9, 050902.
- [122] Fatahi, P., Roy, A., Bahrami, M., Hoseini, S.J., (2018). Visible-light-driven efficient hydrogen production from CdS nanoRods anchored with co-catalysts based on transition metal alloy nanosheets of NiPd, NiZn, and NiPdZn. *ACS Applied Energy Materials*, 1, 5318-27.
- [123] Wu, P., Liu, Z., Guo, Z., Li, X., Zhao, L., (2019). $\text{Zn}_{1-x}\text{Cd}_x\text{S}$ nanowall photoanode prepared via seed layer epitaxial growth method and modified by dual co-catalyst for photoelectrochemical water splitting. *Applied Surface Science*, 467, 65-74.
- [124] Qiu, J., Zhang, X-F., Zhang, X., Feng, Y., Li, Y., Yang, L., et al., (2018). Constructing $\text{Cd}_{0.5}\text{Zn}_{0.5}\text{S}@ \text{ZIF-8}$ nanocomposites through self-assembly strategy to enhance Cr (VI) photocatalytic reduction. *Journal of Hazardous Materials*, 349, 234-41.
- [125] Mathew, J., Anila, E., (2018). Hydrothermal assisted chemical bath deposition of (Cd: Zn) S thin film with high photosensitivity and low dark current. *Solar Energy*, 172, 165-70.
- [126] Oh, J.Y., Yu, J.M., Chowdhury, S.R., Lee, T.I., Misra, M., (2019). Significant

impact of Pd nanoparticle and CdS nanolayer of Pd@CdS@ZnO core-shell nanorods on enhancing catalytic, photoelectrochemical and photocurrent generation activity. *Electrochimica Acta*, 298, 694-703.

[127] An, H., Yan, X., Li, H., Yang, B., Wei, J., Yang, G., (2019). Increased Active Sites by in Situ Growth of CoP Quantum Dots on CdS/rGO To Achieve Efficient Photocatalytic H₂ Production. *ACS Applied Energy Materials*, 2, 4195-204.

[128] Qin, Q., Bai, X., Hua, Z., (2017). Electrochemical synthesis of well-dispersed CdTe nanoparticles on reduced graphene oxide and its photoelectrochemical sensing of catechol. *Journal of Electrochemical Society*, 64, H241.

[129] Li, L., Li, B., Liu, H., Li, M., Wang, B., (2020). Photoelectrochemical sensing of hydrogen peroxide using TiO₂ nanotube arrays decorated with RGO/CdS. *Journal of Alloys and Compounds*, 815, 152241.

[130] Ibrahim, I., Lim, H., Huang, N., Pandikumar, A., (2016). Cadmium sulphide-reduced graphene oxide-modified photoelectrode-based photoelectrochemical sensing platform for copper (II) ions. *PloS One*, 11.

[131] Tayebi, M., Kolaei, M., Tayyebi, A., Masoumi, Z., Belbasi, Z., Lee, B-K., (2019). Reduced graphene oxide (RGO) on TiO₂ for an improved photoelectrochemical (PEC) and photocatalytic activity. *Solar Energy*, 190, 185-94.

[132] Akyüz, D., Ayaz, R.M.Z., Yılmaz, S., Uğuz, Ö., Sarıoğlu, C., Karaca, F., et al., (2019). Metal chalcogenide based photocatalysts decorated with heteroatom doped reduced graphene oxide for photocatalytic and photoelectrochemical hydrogen production. *International Journal of Hydrogen Energy*, 44, 18836-47.

[133] Lin, H-S., Lin, L-Y., (2017). Improving visible-light responses and electric conductivities by incorporating Sb₂S₃ and reduced graphene oxide in a WO₃ nanoplate array for photoelectrochemical water oxidation. *Electrochimica Acta*, 252, 235-44.

[134] Nasiri, M., Sangpour, P., Yousefzadeh, S., Bagheri, M., (2019). Elevated temperature annealed α -Fe₂O₃/reduced graphene oxide nanocomposite photoanode for photoelectrochemical water oxidation. *Journal of Environmental and Chemical Engineering*, 7, 102999.

[135] Subramanyam, P., Vinodkumar, T., Nepak, D., Deepa, M., Subrahmanyam, C., (2019). Mo-doped BiVO₄@ reduced graphene oxide composite as an efficient photoanode for photoelectrochemical water splitting. *Catalysis*, 325, 73-80.

- [136] Ampong, F.K., Awudza, J.A., Nkum, R., Boakye, F., Thomas, P.J., O'Brien, P., (2015). Ternary cadmium zinc sulphide films with high charge mobilities. *Solid State Science*, 40, 50-4.
- [137] Foo, C., Lim, H., Pandikumar, A., Huang, N., Ng, Y., (2016). Utilization of reduced graphene oxide/cadmium sulfide-modified carbon cloth for visible-light-prompt photoelectrochemical sensor for copper (II) ions. *Journal of Hazardous Materials*, 304, 400-8.
- [138] Rajathi, S., Sankarasubramanian, N., Ramanathan, K., Senthamizhselvi, M., (2012). Structural and optoelectronic properties of pyrolytically sprayed CdZnS thin films. *Chalcogenide Letters*, 9, 495-500.
- [139] Ikhioya, I., Jonah, N., Okanigbuan, O. Surface morphological, structural and optical properties on cadmium zinc sulphide (CdZnS) ternary compound prepared by electrodeposition technique. *Nigerian Annals of Natural Sciences*.
- [140] Beraich, M., Taibi, M., Guenbour, A., Zarrouk, A., Boudalia, M., Bellaouchou, A., et al., (2019). Preparation and characterization of Cu₂CoSnS₄ thin films for solar cells via co-electrodeposition technique: Effect of electrodeposition time. *Optik*, 193, 162996.
- [141] Lokhande, C., Yermune, V., Pawar, S., (1988). Electrodepositions of CdS, ZnS and Cd_{1-x}Zn_xS films. *Materials Chemistry and Physics*, 20, 283-92.
- [142] Wang, X., Tian, H., Yang, Y., Wang, H., Wang, S., Zheng, W., et al (2012). Reduced graphene oxide/CdS for efficiently photocatalytic degradation of methylene blue. *Journal of Alloys and Compounds*, 524, 5-12.
- [143] Huo, P., Zhou, M., Tang, Y., Liu, X., Ma, C., Yu, L., et al., (2016). Incorporation of N-ZnO/CdS/Graphene oxide composite photocatalyst for enhanced photocatalytic activity under visible light. *Journal of Alloys and Compounds*, 670,198-209.
- [144] Gao, P., Liu, J., Sun, D.D., Ng, W., (2013). Graphene oxide-CdS composite with high photocatalytic degradation and disinfection activities under visible light irradiation. *Journal of Hazardous Materials*, 250, 412-20.
- [145] An, X., Yu, X., Jimmy, C.Y., Zhang, G., (2013). CdS nanorods/reduced graphene oxide nanocomposites for photocatalysis and electrochemical sensing. *Journal of Materials Chemistry A*, 1, 5158-64.
- [146] Lin, R., Shen, L., Ren, Z., Wu, W., Tan, Y., Fu, H., et al. (2014). Enhanced

photocatalytic hydrogen production activity via dual modification of MOF and reduced graphene oxide on CdS. *Chemical Communications*, 50, 8533-5.

[147] Akyüz, D., Koca, A., (2018). Photocatalytic hydrogen production with reduced graphene oxide (RGO)-CdZnS nano-composites synthesized by solvothermal decomposition of dimethyl sulfoxide as the sulfur source. *Journal of Photochemistry and Photobiology A*, 364, 625-34.

[148] Tanişik, İ., Uğuz, Ö., Akyüz, D., Ayaz, R.M.Z., Sarioğlu, C., Karaca, F., et al., (2020). Solar-hydrogen production with reduced graphene oxide supported $CdxZn1-xS$ photocatalysts. *International Journal of Hydrogen Energy*, 45, 34845-56.

[149] Ayaz, R.Z., Akyüz, D., Uğuz, Ö., Tanşik, İ., Sarioğlu, C., Karaca, F., et al., (2020). Photoelectrochemical performance of thermally sulfurized $CdxZn1-xS$ photoanode: Enhancement with reduced graphene oxide support. *Renewable Energy*, 162, 182-95.

[150] Ranjan, R., Kumar, M., Sinha, A., (2019). Development and characterization of rGO supported CdSMoS₂ photoelectrochemical catalyst for splitting water by visible light. *International Journal of Hydrogen Energy*, 44, 16176-89.

[151] Ranjan, R., Kumar, M., Sinha, A., (2019). CdS supported on electrochemically reduced rGO for photo reduction of water to hydrogen. *International Journal of Hydrogen Energy*, 44, 10573-84.

[152] Ali, M.B., Jo, W-K., Elhouichet, H., Boukherroub, R., (2017). Reduced graphene oxide as an efficient support for CdS-MoS₂ heterostructures for enhanced photocatalytic H₂ evolution. *International Journal of Hydrogen Energy*, 42,16449-58.

[153] Chen, Y., Ren, X., Zhang, K., Wang, L., (2019). Structure and photoluminescence of ZnS/CdS_{1-x}Sex nanocomposite prepared by a two-step process. *Materials Science in Semiconductor Processing*, 100, 42-7.

[154] Li, L., Li, B., Liu, H., Li, M., Wang, B., (2018). Photoelectrochemical sensing of hydrogen peroxide using TiO₂ nanotube arrays decorated with RGO/CdS. *Journal of Alloys and Compounds*, 815, 152241.

[155] Shen, Q., Shi, X., Fan, M., Han, L., Wang, L., Fan, Q., (2015). Highly sensitive photoelectrochemical cysteine sensor based on reduced graphene oxide/CdS: Mn nanocomposites. *Journal of Electroanalytical Chemistry*, 759, 61-6.

[156] Li, H., Sun, C., Zhao, Y., Xu, X., Yu, H., (2018). Facile synthesis of recyclable

Co₃O₄/Co(OH)₂/RGO ternary heterostructures with synergistic effect for photocatalysis. *Journal of Nanoparticle Research*, 20, 1-13.

[157] Zhuang, H., Liu, X., Li, F., Xu, W., Lin, L., Cai, Z., (2019). Construction of CdSe@TiO₂ core-shell nanorod arrays by electrochemical deposition for efficient visible light photoelectrochemical performance. *International Journal of Energy Research*, 43, 7197-205.

[158] Ayal, A.K., Zainal, Z., Lim, H.N., Talib, Z.A., Lim, Y-C., Chang, S-K., et al. (2018). Fabrication of CdSe nanoparticles sensitized TiO₂ nanotube arrays via pulse electrodeposition for photoelectrochemical application. *Materials Research Bulletin*, 106, 257-62.

[159] Izi, M., Heidari, G., Khoie, S.M., Najafi, J., (2017). Comparison of ZnS thin films fabricated by electrodeposition and spray pyrolysis methods. *Surface Engineering and Applied Electrochemistry*, 53, 245-9.

[160] Kumarage, W., Wijesundera, R., Kaur, N., Zappa, D., Seneviratne, V., Jayalath, C., et al., (2019). A Comparative Assessment: Chemical Bath Deposited and Electrodeposited CdS Films. *International Journal of Electroactive Materials*, 7, 1-6.

[161] Riveros, G., Baez, C., Ramírez, D., Pereyra, C.J., Marotti, R.E., Romero, R., et al., (2016). Electrodeposition and characterization of composition-graded CdS_xSe(1-x) multilayer thin film structures. *Journal of Alloys and Compounds*, 686, 235-44.

[162] He, G., Zhang, Y., He, Q., (2019). MoS₂/CdS heterostructure for enhanced photoelectrochemical performance under visible light. *Catalysts*, 9 (379).

[163] Uğuz, Ö., Koca, A., (2021). Hybrid photoelectrochemical–photocatalytic hydrogen evolution reaction with reduced graphene oxide–binary metal chalcogenide composites. *International Journal of Energy Research*, 45, 19303-15.

[164] Marcano, D.C., Kosynkin, D.V., Berlin, J.M., Sinitskii, A., Sun, Z., Slesarev, A., et al. (2010). Improved synthesis of graphene oxide. *ACS Nano*, 4, 4806-14.

[165] Akyüz, D., Ayaz, R.M.Z., Yılmaz, S., Uğuz, Ö., Sarioğlu, C., Karaca, F., et al., (2019). Metal chalcogenide based photocatalysts decorated with heteroatom doped reduced graphene oxide for photocatalytic and photoelectrochemical hydrogen production. *International Journal of Hydrogen Energy*, 44, 18836-47.

[166] Tanişik, İ., Uğuz, Ö., Akyüz, D., Ayaz, R.M.Z., Sarioğlu, C., Karaca, F., et al. (2020). Solar-hydrogen production with reduced graphene oxide supported Cd_xZn_{1-x}S

photocatalysts. *International Journal of Hydrogen Energy*.

[167] Ayaz, R.Z., Akyüz, D., Uğuz, Ö., Tanişik, İ., Sarioğlu, C., Karaca, F., et al., (2020). Photoelectrochemical performance of thermally sulfurized $Cd_xZn_{1-x}S$ photoanode: Enhancement with reduced graphene oxide support. *Renewable Energy*.

[168] Akyüz, D., Koca, A., (2018). Photocatalytic hydrogen production with reduced graphene oxide (RGO)-CdZnS nano-composites synthesized by solvothermal decomposition of dimethyl sulfoxide as the sulfur source. *Journal of Photochemistry and Photobiology A: Chemistry*, 364, 625-34.

[169] Yakoubi, A., Chaabane, T.B., Aboulaich, A., Mahiou, R., Balan, L., Medjahdi, G., et al., (2016). Aqueous synthesis of Cu-doped CdZnS quantum dots with controlled and efficient photoluminescence. *Journal of Luminescence*, 175, 193-202.

[170] Akyüz, D., Özkaya, A.R., Koca, A., (2020). Photocatalytic and photoelectrochemical performances of Mo, Ni and Cu decorated metal chalcogenides. *Materials Science in Semiconductor Processing*, 116, 105127.

[171] Jin, J., Yu, J., Liu, G., Wong, P.K., (2013). Single crystal CdS nanowires with high visible-light photocatalytic H_2 -production performance. *Journal of Materials Chemistry A*, 1, 10927-34.

[172] Horoz, S., (2018). Structural, optical and photovoltaic properties of Co (3%): CdZnS nanoparticles. *Indian Journal of Pure & Applied Physics (IJPAP)*, 56, 759-64.

[173] Deshpande, A., Kelkar, S., Rayalu, S., Ogale, S., (2014). Orthorhombic/cubic Cd_2SnO_4 nanojunctions: enhancing solar water splitting efficiency by the suppression of charge recombination. *Journal of Materials Chemistry A*, 2, 492-9.

[174] Li, Q., Shan, F., Sun, B., Song, Y., Wang, F., Ji, J., (2017). Photo-assisted electrocatalysis of CdSMoS₂ hybrid for hydrogen evolution reaction: Morphology-dependent photoelectroactivity of p-n junction photocathode under bias potential. *International Journal of Hydrogen Energy*, 42, 5549-59.

[175] Liu, C., Qiu, Y., Wang, F., Wang, K., Liang, Q., Chen, Z., (2017). Design of Core-Shell-Structured ZnO/ZnS Hybridized with Graphite-Like C₃N₄ for Highly Efficient Photoelectrochemical Water Splitting. *Advanced Materials Interfaces*, 4, 1700681.

[176] Gao, B., Wang, T., Fan, X., Gong, H., Li, P., Feng, Y., et al., (2019). Enhanced water oxidation reaction kinetics on a BiVO₄ photoanode by surface modification with

Ni₄O₄ cubane. *Journal of Materials Chemistry A*, 7, 278-88.

[177] Gopalakrishnan, S., Jeganathan, K., (2017). Facile fabrication of silicon nanowires as photocathode for visible-light induced photoelectrochemical water splitting. *International Journal of Hydrogen Energy*, 42, 22671-6.

[178] Uğuz, Ö., Budak, Ö., Koca, A., (2021). Simultaneous electrodeposition of electrochemically reduced graphene oxide-binary metal chalcogenide composites to enhance photoelectrochemical performance. *International Journal of Hydrogen Energy*.

[179] Zarębska, K., Skompska, M., (2011). Electrodeposition of CdS from acidic aqueous thiosulfate solution—Investigation of the mechanism by electrochemical quartz microbalance technique. *Electrochimica Acta*, 56, 5731-9.

[180] Mammadov, M., Aliyev, A.S., Elrouby, M., (2012). Electrodeposition of cadmium sulfide. *International Journal of Thin Film Science and Technology*, 1, 43-53.

[181] Wu, J-B., Lin, M-L., Cong, X., Liu, H-N., Tan, P-H., (2018). Raman spectroscopy of graphene-based materials and its applications in related devices. *Chemical Society Reviews*, 47, 1822-73.

[182] Zhao, B., Hao, R., Wang, Z., Zhang, H., Hao, Y., Zhang, C., et al., (2018). Green synthesis of multi-dimensional plasmonic coupling structures: Graphene oxide gapped gold nanostars for highly intensified surface enhanced Raman scattering. *Chemical Engineering Journal*, 349, 581-7.

[183] Pandey, A., Qureshi, A., (2017). Surface modified graphene oxide nanosheets by gold ion implantation as a substrate for surface enhanced Raman scattering. *Journal of Alloys and Compounds*, 703, 500-7.

[184] Zellagui, R., Dehdouh, H., Sahraoui, T., Chaumont, D., Adnane, M., (2019). Effect of zinc/cadmium proportion in CdS layers deposited by CBD method. *International Multidisciplinary Research Journal*, 08-12.

[185] Zakria, M., Khan, T.M., Nasir, A., Mahmood, A., (2015). Annealing-induced effects on structural and optical properties of Cd_{1-x}Zn_xS thin films for optoelectronic applications. *Materials Science- Poland*, 33, 677-84.

[186] Fang, S., Huang, D., Lv, R., Bai, Y., Huang, Z-H., Gu, J., et al., (2017). Three-dimensional reduced graphene oxide powder for efficient microwave absorption in the S-band (2–4 GHz). *Rsc Advances*, 7, 25773-9.

[187] Mustafa, G., Chowdhury, M., Saha, D., Hussain, S., Islam, O., (2012). Annealing

effects on the properties of chemically deposited CdS thin films at ambient condition. Dhaka University Journal of Science, 60, 283-8.

[188] Liang, Y., Shao, M., Liu, L., Hu, J., Cui, W., (2014). Synthesis of Cd_{1-x}Zn_xS/K₄Nb₆O₁₇ Composite and its Photocatalytic Activity for Hydrogen Production. Bulletin of Korean Chemical Society, 35, 1182-90.

[189] Gupta, B., Kumar, N., Panda, K., Kanan, V., Joshi, S., Visoly-Fisher, I., (2017). Role of oxygen functional groups in reduced graphene oxide for lubrication. Scientific Reports, 7, 1-14.

[190] Nguyen, A.K.Q., Huynh, T.T., Ho, V.T.T., (2016). Preparation and characterization of indium doped tin oxide (ITO) via a non-aqueous sol-gel. Molecular Crystals and Liquid Crystals, 635, 32-9.

[191] Ertis, I.F., Boz, I., (2017). Synthesis and characterization of metal-doped (Ni, Co, Ce, Sb) CdS catalysts and their use in methylene blue degradation under visible light irradiation. Modern Research in Catalysis, 6 (1).

[192] Iqbal, M., Wang, Y., Hu, H., He, M., Shah, A.H., Lin, L., et al., (2018). Cu₂O-tipped ZnO nanorods with enhanced photoelectrochemical performance for CO₂ photoreduction. Applied Surface Science, 443, 209-16.

[193] Liu, Y., Kang, Z., Si, H., Li, P., Cao, S., Liu, S., et al., (2017). Cactus-like hierarchical nanorod-nanosheet mixed dimensional photoanode for efficient and stable water splitting. Nano Energy, 35, 189-98.

[194] Momeni, M.M., Mahvari, M., Ghayeb, Y., (2019) Photoelectrochemical properties of iron-cobalt WTiO₂ nanotube photoanodes for water splitting and photocathodic protection of stainless steel. Journal of Electroanalytical Chemistry, 832, 7-23.

[195] Lee, J.M., Baek, J.H., Gill, T.M., Shi, X., Lee, S., Cho, I.S., et al., (2019) A Zn:BiVO₄/Mo:BiVO₄ homojunction as an efficient photoanode for photoelectrochemical water splitting. Journal of Materials Chemistry A, 7, 9019-24.

[196] Tayyebi, A., Soltani, T., Lee, B-K., Outokesh, M., Tayebi, M., (2017). Novel visible light photocatalytic and photoelectrochemical (PEC) activity of carbon-doped zinc oxide/reduced graphene oxide: supercritical methanol synthesis with enhanced photocorrosion suppression. Journal of Alloys and Compounds, 723, 1001-10.

[197] Chavhan, S., Senthilarasu, S., Lee, S-H., (2008). Annealing effect on the

structural and optical properties of a Cd_{1-x}Zn_xS thin film for photovoltaic applications. *Applied Surface Science*, 254, 4539-45.

[198] Quiñonez-Urias, D., Vera-Marquina, A., Berman-Mendoza, D., Leal-Cruz, A., García-Delgado, L., Zaldívar-Huerta, I., et al., (2014). Annealing effect on structural, morphological, and optical behaviors of CBD-CdS nanostructured films for solar cells. *Optical Material Express*, 4, 2280-9.

[199] Zeng, P., Zhang, Q., Peng, T., Zhang, X., (2011). One-pot synthesis of reduced graphene oxide-cadmium sulfide nanocomposite and its photocatalytic hydrogen production. *Physical Chemistry Chemical Physics*, 13, 21496-502.

[200] Chung, Y-D., Cho, D-H., Park, N-M., Lee, K-S., Kim, J., (2011). Effect of annealing on CdS/Cu (In, Ga) Se₂ thin-film solar cells. *Current Applied Physics*, 11, S65-S7.

[201] Belkhalifa, H., Ayed, H., Hafdallah, A., Aida, M., Ighil, RT., (2016). Characterization and studying of ZnO thin films deposited by spray pyrolysis: effect of annealing temperature. *Optik*, 127, 2336-40.

[202] Hatsuta, N., Takemori, D., Takashiri, M., (2016). Effect of thermal annealing on the structural and thermoelectric properties of electrodeposited antimony telluride thin films. *Journal of Alloys and Compounds*, 685, 147-52.

[203] Xie, G., Zhang, K., Fang, H., Guo, B., Wang, R., Yan, H., et al., (2013). A photoelectrochemical investigation on the synergetic effect between CdS and reduced graphene oxide for solar-energy conversion. *Asian Journal of Chemistry*, 8, 2395-400.

[204] Pareek, A., Paik, P., Borse, P.H., (2015). Role of transition metal-hydroxide (M-OH_x, M= Mn, Fe, Ni, Co) co-catalyst loading: efficiency and stability of CdS photoanode. *MRS Online Proceedings Library Archive*, 1776, 1-6.

[205] Pareek, A., Thotakuri, R., Dom, R., Kim, H.G., Borse, P.H., (2017). Nanostructure Zn-Cu co-doped CdS chalcogenide electrodes for opto-electric-power and H₂ generation. *International Journal of Hydrogen Energy*, 42, 125-32.

[206] Xu, F., Bai, D., Han, S., Wu, D., Gao, Z., Jiang, K., (2014). One-pot synthesis of graphene-Zn_xCd_{1-x}S QDs composites with improved photoelectrochemical performance for selective determination of Cu²⁺. *Sensors and Actuators B-Chem*, 203, 89-94.

[207] Boosagulla, D., Mandati, S., Allikayala, R., Sarada, B.V., (2018). Room

temperature pulse electrodeposition of CdS thin films for application in solar cells and photoelectrochemical cells. *ECS Journal of Solid State Science and Technology*, 7, P440.

[208] Zirak, M., Zhao, M., Moradlou, O., Samadi, M., Sarikhani, N., Wang, Q., et al, (2015). Controlled engineering of WS₂ nanosheets–CdS nanoparticle heterojunction with enhanced photoelectrochemical activity. *Solar Energy Materials and Solar Cells*, 141, 260-9.

[209] Shen, Q., Shi, X., Fan, M., Han, L., Wang, L., Fan, Q., (2015). Highly sensitive photoelectrochemical cysteine sensor based on reduced graphene oxide/CdS: Mn nanocomposites. *Journal of Electroanalytical Chemistry*, 759, 61-6.

[210] Verma, R., Tiwari, S.P., Kumari, R., Srivastava, R., (2018). Study of enhancement in the dielectric and electrical properties of WO₃-doped LiF nanocomposite. *Journal of Materials Science*, 53, 4199-208.

[211] Sagadevan, S., Chowdhury, Z.Z., Johan, M.R.B., Aziz, F.A., Roselin, L.S., Hsu, H-L., et al., (2019). Synthesis, characterization and electrochemical properties of cadmium sulfide–Reduced graphene oxide nanocomposites. *Results in Physics*, 12, 878-85.

[212] Ter Heijne, A., Schaetzle, O., Gimenez, S., Fabregat-Santiago, F., Bisquert, J., Strik, D.P., et al., (2011). Identifying charge and mass transfer resistances of an oxygen reducing biocathode. *Energy and Environmental Science*, 4, 5035-43.

[213] Sariket, D., Shyamal, S., Hajra, P., Mandal, H., Bera, A., Maity, A., et al, (2017). Temperature controlled fabrication of chemically synthesized cubic In₂O₃ crystallites for improved photoelectrochemical water oxidation. *Materials Chemistry and Physics*, 201, 7-17.

[214] Kalanur, S.S., (2019). Structural, optical, band edge and enhanced photoelectrochemical water splitting properties of tin-doped WO₃. *Catalysts*, 9, 456.

[215] Shen, C., Chua, C.S., Lim, Y.F., Liu, J., Wang, X., Liu, B., et al., (2016). A Molecular Relay-Modified CdS-Sensitized Photoelectrochemical Cell for Overall Water Splitting. *ChemElectroChem*, 3, 1471-7.

[216] Marchi, C., Panzeri, G., Pedrazzetti, L., Khalil, M., Lucotti, A., Parravicini, J., et al., (2021). One-step CZT electroplating from alkaline solution on flexible Mo foil for CZTS absorber. *Journal of Solid State Electrochemistry*, 25, 1807-13.

- [217] Che Isa, N.N., Mohd, Y., Mohd Zaki, M.H., Syed Mohamad, S.A., (2017) Electrodeposition and characterization of copper coating on stainless steel substrate from alkaline copper solution containing ethylenediaminetetraacetate (EDTA). *Journal of Mechanical Engineering (JMechE)*, 127-38.
- [218] Zhang, H., Yuan, J., Zhu, M., (2017). An electrochemical investigation of the EDTA influence on the cobalt-manganese electrodeposition in aqueous chloride electrolytes. *International Journal of Electrochemical Science*, 12, 8368-80.
- [219] Riveros, G., Lincot, D., Guillemoles, J., Henriquez, R., Schrebler, R., Cordova, R., et al., (2003). Redox and solution chemistry of the SeSO_3^{2-} -Zn-EDTA $^{2-}$ system and electrodeposition behavior of ZnSe from alkaline solutions. *Journal of Electroanalytical Chemistry*, 558, 9-17.
- [220] Shenouda, A.Y., El Sayed, M., (2015). Electrodeposition, characterization and photo electrochemical properties of CdSe and CdTe. *Ain Shams Engineering Journal*, 6, 341-6.
- [221] McCann, J., Kazacos, M.S., (1981). The Electrochemical deposition and formation of cadmium sulphide thin film electrodes in aqueous electrolytes. *Journal of Electroanalytical Chemistry and Interfacial Electrochemistry*, 119, 409-12.
- [222] Bhand, G.R., Chaure, N.B., (2017). Synthesis of CdTe, CdSe and CdTe/CdSe core/shell QDs from wet chemical colloidal method. *Materials Science in Semiconductor Processing*, 68, 279-87.
- [223] Hidayah, N., Liu, W-W., Lai, C-W., Noriman, N., Khe, C-S., Hashim, U., et al., (2017). Comparison on graphite, graphene oxide and reduced graphene oxide: Synthesis and characterization. *AIP Conference Proceedings: AIP Publishing LLC*.
- [224] Sharma, M., Sen, S., Gupta, J., Ghosh, M., Pitale, S., Gupta, V., et al., (2018). Tunable blue-green emission from ZnS (Ag) nanostructures grown by hydrothermal synthesis. *Journal of Materials Research*, 33, 3963-70.
- [225] Yu, J., Gong, C., Wu, Z., Wu, Y., Xiao, W., Su, Y., et al., (2015). Efficient visible light-induced photoelectrocatalytic hydrogen production using CdS sensitized TiO₂ nanorods on TiO₂ nanotube arrays. *Journal of Materials Chemistry A*, 3, 22218-26.
- [226] Wei, Z., Mao, W., Liu, J., Xiao, Y., Zhu, M., Tian, Y., (2020). CdS nanorods decorated with ultrathin MoS₂ nanosheets for efficient visible-light photocatalytic H₂ production. *Journal of Materials Science: Materials in Electronics*, 31, 4574-81.

- [227] Jiang, Q-S., Li, W., Wu, J., Cheng, W., Zhu, J., Yan, Z., et al., (2019). Electrodeposited cobalt and nickel selenides as high-performance electrocatalytic materials for dye-sensitized solar cells. *Journal of Materials Science: Materials in Electronics*, 30, 9429-37.
- [228] Nie, H., Fu, L., Zhu, J., Yang, W., Li, D., Zhou, L., (2018). Excellent tribological properties of lower reduced graphene oxide content copper composite by using a one-step reduction molecular-level mixing process. *Materials*, 11(600).
- [229] Moreira, V.R., Lebron, Y.A.R., da Silva, M.M., de Souza Santos, L.V., Jacob, R.S., de Vasconcelos, C.K.B., et al., (2020). Graphene oxide in the remediation of norfloxacin from aqueous matrix: simultaneous adsorption and degradation process. *Environmental Science and Pollution Research*, 27, 34513-28.
- [230] Lei, Y., He, Y., Fang, C., (2017). Composition-tunable ternary CdS_{1-x}Se_x/graphene composites with enhanced photocurrent response. *Journal of Materials Science: Materials in Electronics*, 28, 878-83.
- [231] Salem, A., Saion, E., Al-Hada, N.M., Shaari, A.H., Kamari, H.M., Soltani, N., et al., (2016). Formation of a colloidal CdSe and ZnSe quantum dots via a gamma radiolytic technique. *Applied Sciences*, 6(278).
- [232] Shanmugasundaram, A., Johar, M.A., Boppella, R., Kim, D-S., Jeong, Y-J., Kim, J.Y., et al., (2021). Stabilizing nanocrystalline Cu₂O with ZnO/rGO: Engineered photoelectrodes enables efficient water splitting. *Ceramics International*, 47, 7558-70.
- [233] Zhang, B., Ma, X., Ma, J., Zhou, Y., Liu, G., Ma, D., et al., (2020). Fabrication of rGO and g-C₃N₄ co-modified TiO₂ nanotube arrays photoelectrodes with enhanced photocatalytic performance. *Journal of Colloid and Interface Science*, 577, 75-85.
- [234] Ng, C., Yun, J-H., Tan, H.L., Wu, H., Amal, R., Ng, Y.H., (2018) A dual-electrolyte system for photoelectrochemical hydrogen generation using CuInS₂-In₂O₃-TiO₂ nanotube array thin film. *Science China Materials*, 61, 895-904.
- [235] Yan, D., Fu, X., Shang, Z., Liu, J., Luo, Ha., (2019). A BiVO₄ film photoanode with re-annealing treatment and 2D thin Ti₃C₂TX flakes decoration for enhanced photoelectrochemical water oxidation. *Chemical Engineering Journal*, 361, 853-61.
- [236] Hou, Y., Ahmed Syed, Z., Jiu, L., Bai, J., Wang, T., (2017). Porosity-enhanced solar powered hydrogen generation in GaN photoelectrodes. *Applied Physics Letters*, 111, 203901.

- [237] Zhang, X., Bian, X., Xu, H., Wu, W., (2021). Fabrication of WO₃/RGO/Ni:FeOOH heterostructure for synergistically enhancing photoelectrochemical water oxidation. *Applied Surface Science*, 542, 148579.
- [238] Li, B., Shao, X., Liu, T., Shao, L., Zhang, B., (2016). Construction of metal/WO₂.72/rGO ternary nanocomposites with optimized adsorption, photocatalytic and photoelectrochemical properties. *Applied Catalysis B: Environmental*, 198, 325-33.
- [239] Shi, Q., Song, X., Wang, H., Bian, Z., (2017). Enriched photoelectrochemical performance of phosphate doped BiVO₄ photoelectrode by coupling FeOOH and rGO. *Journal of The Electrochemical Society*, 165, H3018.
- [240] Zhang, Y-H., Cai, X-L., Guo, D-Y., Zhang, H-J., Zhou, N., Fang, S-M., et al., (2019). Oxygen vacancies in concave cubes Cu₂O-reduced graphene oxide heterojunction with enhanced photocatalytic H₂ production. *Journal of Materials Science: Materials in Electronics*, 30, 7182-93.
- [241] Zhu, H., Li, Q., (2013). Visible light-driven CdSe nanotube array photocatalyst. *Nanoscale Research Letters*, 8, 1-6.
- [242] Yadav, A.A., Masumdar, E., (2011). Photoelectrochemical performances of indium-doped CdS_{0.2}Se_{0.8} thin film electrodes prepared by spray pyrolysis. *Electrochimica Acta*, 56, 6406-10.
- [243] Zhang, W., Zhong, Q., Liu, X., Lu, Q., (2020). Inorganic Functionalization of CdS_xS_{1-x}/ZnS Core-Shell Quantum Dots and Their Photoelectric Properties. *Physica Status Solidi (a)*, 217, 2000010.
- [244] Lin, M., Wang, W., (2021). Passivation of ZnSe nanoparticles in sandwiched CdSe/ZnSe/ZnO nanotube array photoanode to substantially enhance solar photoelectrochemical water splitting for hydrogen evolution. *Colloids and Surfaces A: Physicochemical and Engineering Aspects*, 614, 126206.
- [245] Ye, Z., Hu, Z., Yang, L., Xiao, X., (2020). Stable p-type Cu: CdS_{1-x}Se_x/Pt Thin-Film Photocathodes with Fully Tunable Bandgap for Scavenger-Free Photoelectrochemical Water Splitting. *Solar RRL*, 4, 1900567.
- [246] Li, H., Wang, X., Zhang, L., Hou, B., (2015). Preparation and photocathodic protection performance of CdSe/reduced graphene oxide/TiO₂ composite. *Corrosion Science*, 94, 342-9.
- [247] de los Angeles Hernandez-Perez, M., Sanchez-Ramirez, E.A., Castillo-Plata, F.J.,

- Manzo-Robledo, A., Aguilar-Hernandez, J.R., Ezeta-Mejia, A., et al., (2020). Photoelectrochemical properties of chemically deposited cadmium sulphoselenide (CdS_{1-x}Sex/ITO) thin films. *Vacuum*, 175, 109277.
- [248] Pathak, P., Gupta, S., Grosulak, K., Imahori, H., Subramanian, V., (2015). Nature-inspired tree-like TiO₂ architecture: a 3D platform for the assembly of CdS and reduced graphene oxide for photoelectrochemical processes. *The Journal of Physical Chemistry C*, 119, 7543-53.
- [249] Bhat, S.S., Pawar, S.A., Potphode, D., Moon, C-K., Suh, J.M., Kim, C., et al., (2019). Substantially enhanced photoelectrochemical performance of TiO₂ nanorods/CdS nanocrystals heterojunction photoanode decorated with MoS₂ nanosheets. *Applied Catalysis B: Environmental*, 259, 118102.
- [250] Reddy, I.N., Reddy, C.V., Ravindranadh, K., Cho, M., Kim, D., Shim, J., (2020). A study of coral reef-like tetragonal Mn₃O₄ nanostructure photoelectrode for photoelectrochemical water splitting under visible irradiation. *Journal of Electroanalytical Chemistry*, 874, 114488.
- [251] Su, J., Liu, C., Liu, D., Li, M., Zhou, J., (2016). Enhanced Photoelectrochemical performance of the BiVO₄/Zn: BiVO₄ homojunction for water oxidation. *ChemCatChem*, 8, 3279-86.
- [252] Chen, S-M., Manavalan, S., Rajaji, U., Govindasamy, M., Chen, T-W., Ali, MA., et al., (2018). Determination of the antioxidant propyl gallate in meat by using a screen-printed electrode modified with CoSe₂ nanoparticles and reduced graphene oxide. *Microchimica Acta*, 185, 1-9.
- [253] Atacan, K., Güy, N., Boutra, B., Özacar, M., (2020). Enhancement of photoelectrochemical hydrogen production by using a novel ternary Ag₂CrO₄/GO/MnFe₂O₄ photocatalyst. *International Journal of Hydrogen Energy*, 45, 17453-67.
- [254] Su, J., Wang, J., Liu, C., Feng, B., Chen, Y., Guo, L., (2016). On the role of metal atom doping in hematite for improved photoelectrochemical properties: a comparison study. *RSC Advances*, 6, 101745-51.
- [255] Kumar, S., Ahirwar, S., Satpati, AK., (2019). Insight into the PEC and interfacial charge transfer kinetics at the Mo doped BiVO₄ photoanodes. *RSC Advances*, 9, 41368-82.

- [256] Anuar, K., Zainal, Z., Hussein, M., Saravanan, N., Haslina, I., (2002). Cathodic electrodeposition of Cu₂S thin film for solar energy conversion. *Solar Energy Materials and Solar Cells*, 73, 351-65.
- [257] Levinas, R., Tsyntsaru, N., Cesiulis, H., (2020). The characterisation of electrodeposited MoS₂ thin films on a foam-based electrode for hydrogen evolution. *Catalysts*, 10, 1182.
- [258] Yang, T., Huang, X., Zhou, H., Wu, G., Lai, T., (2016). Excitation mechanism of A_{1g} mode and origin of nonlinear temperature dependence of Raman shift of CVD-grown mono-and few-layer MoS₂ films. *Optics Express*, 24, 12281-92.
- [259] Tonndorf, P., Schmidt, R., Böttger, P., Zhang, X., Börner, J., Liebig, A., et al., (2013). Photoluminescence emission and Raman response of monolayer MoS₂, MoSe₂, and WSe₂. *Optics Express*, 21, 4908-16.
- [260] Rani, B.J., Ravi, G., Yuvakkumar, R., Velauthapillai, D., Saravanakumar, B., Al-Mohaimed, A.M., (2020). Investigation on copper based oxide, sulfide and selenide derivatives oxygen evolution reaction activity. *Applied Nanoscience*, 10, 4299-306.
- [261] Arellano-Tanori, O., Acosta-Enríquez, M., Ochoa-Landin, R., Iniguez-Palomares, R., Mendivil-Reynoso, T., Flores-Acosta, M., et al., (2014). Copper-selenide and copper-telluride composites powders sintetized by ionic exchange. *Chalcogenide Letters*, 11(13), 9.
- [262] Zhou, J., Yuan, L., Wang, J., Song, L., You, Y., Zhou, R., et al., (2020). Combinational modulations of NiSe₂ nanodendrites by phase engineering and iron-doping towards an efficient oxygen evolution reaction. *Journal of Materials Chemistry A*, 8, 8113-20.
- [263] Yan, Z., Du, L., Phillips, D.L., (2017). Multilayer core-shell MoS₂/CdS nanorods with very high photocatalytic activity for hydrogen production under visible-light excitation and investigation of the photocatalytic mechanism by femtosecond transient absorption spectroscopy. *RSC Advances*, 7, 55993-9.
- [264] Li, B., Jiang, L., Li, X., Ran, P., Zuo, P., Wang, A., et al., (2017). Preparation of monolayer MoS₂ quantum dots using temporally shaped femtosecond laser ablation of bulk MoS₂ targets in water. *Scientific Reports*, 7, 1-12.
- [265] Zou, Z., Wang, X., Huang, J., Wu, Z., Gao, F., (2019). An Fe-doped nickel selenide nanorod/nanosheet hierarchical array for efficient overall water splitting.

Journal of Materials Chemistry A, 7, 2233-41.

[266] Karthikeyan, R., Thangaraju, D., Prakash, N., Hayakawa, Y., (2015). Single-step synthesis and catalytic activity of structure-controlled nickel sulfide nanoparticles. *CrystEngComm*, 17, 5431-9.

[267] Jing, M., Long, F., Jing, L., Lv, X., Zhang, J., Wu, T., (2018). Dataset analysis on Cu₉S₅ material structure and its electrochemical behavior as anode for sodium-ion batteries. *Data in brief*, 20, 790-3.

[268] Su, L., Xiao, Y., Han, G., (2017). Synthesis of highly active cobalt molybdenum sulfide nanosheets by a one-step hydrothermal method for use in dye-sensitized solar cells. *Journal of Materials Science*, 52, 13541-51.

[269] Zhang, L., Sun, L., Huang, Y., Sun, Y., Hu, T., Xu, K., et al., (2017). Hydrothermal synthesis of N-doped RGO/MoSe₂ composites and enhanced electrocatalytic hydrogen evolution. *Journal of Materials Science*, 52, 13561-71.

[270] Li, Y., Yang, M., Tian, Z., Luo, N., Li, Y., Zhang, H., et al., (2019). Assembly of copper phthalocyanine on TiO₂ nanorod arrays as co-catalyst for enhanced photoelectrochemical water splitting. *Frontiers in Chemistry*, 7(334).

[271] Li, Y., Zhang, R., Li, J., Liu, J., Miao, Y., Guo, J., et al., (2021). TiO₂/CuPc/NiFe-LDH photoanode for efficient photoelectrochemical water splitting. *Chinese Chemical Letters*, 32, 1165-8.

[272] Shen, X., Zhao, L., Fan, W., Ren, J., Wang, Q., Wang, A., et al., (2021). Efficient photoelectrochemical water oxidation of cobalt phthalocyanine decorated BiVO₄ photoanode by improving kinetics. *Applied Surface Science*, 564, 150463.

[273] Xu, Y., Zhang, X., Chen, Z., Kempa, K., Wang, X., Shui, L., (2021). Chemical vapor deposition of amorphous molybdenum sulphide on black phosphorus for photoelectrochemical water splitting. *Journal of Materials Science & Technology*. 2021, 68, 1-7.

[274] Abdelmola, F.M., Ram, M.K., Takshi, A., Stafanakos, E., Kumar, A., Goswami, D.Y., (2017). Photoelectrochemical Cell Of Hybrid Regioregular Poly (3-Hexylthiophene-2, 5-Diyl) And Molybdenum Disulfide Film. *Surface Review and Letters*, 24, 1750026.

[275] Li, J., Jin, X., Li, R., Zhao, Y., Wang, X., Liu, X., et al., (2019). Copper oxide nanowires for efficient photoelectrochemical water splitting. *Applied Catalysis B*:

Environmental, 240, 1-8.

[276] Lee, C.W., Lin, F-W., Liao, P-H., Lee, M-L., Sheu, J-K., (2021). Stable photoelectrochemical water splitting using p-n GaN junction decorated with nickel oxides as photoanodes. *The Journal of Physical Chemistry C*, 125, 16776-83.

[277] Gondolini, A., Sangiorgi, N., Sangiorgi, A., Sanson, A., (2021). photoelectrochemical hydrogen production by screen-printed copper oxide electrodes. *Energies*, 14, 2942.

[278] Yang, Y., Xu, D., Wu, Q., Diao, P., (2016). Cu₂O/CuO bilayered composite as a high-efficiency photocathode for photoelectrochemical hydrogen evolution reaction. *Scientific Reports*. 6, 1-13.

[279] Qian, B., Yang, X., Li, X., Song, Z., (2020). Fabrication of 1D/2D pg-C₃N₄@RGO heterostructures with superior visible-light photoelectrochemical cathodic protection performance. *Journal of Solid State Electrochemistry*, 24, 1669-78.

CURRICULUM VITAE

Name-Surname: Özlem UĞUZ NELİ

EDUCATIONAL BACKGROUND

PhD: Marmara University, Institute of Pure and Applied Sciences, Chemical Engineering Programme (2017-2022). GPA: 4.00/4.00

MSc: Istanbul Technical University, Faculty of Chemical and Metallurgical Engineering, Chemical Engineering Programme (2014-2016). GPA: 3.88/4.00

BSc: Marmara University, Faculty of Engineering, Chemical Engineering Programme (2009-2013). GPA: 3.60/4.00

RECORDS

YDS: 92.5/100

ALES: 86.2/100

PUBLISHED ARTICLES

1. **Uğuz Özlem**, Koca Atif (2021). Hybrid photoelectrochemical-photocatalytic hydrogen evolution reaction with reduced graphene oxide-binary metal chalcogenide composites. *International Journal of Energy Research*. 45(13). 19303-19315.
2. Kaya Yeliz, Erçağ Ayşe, **Uğuz Özlem**, Koca Atif, Zorlu Yunus, Hacıoğlu Mayram, Tan Ayşe Seher Birteksöz (2021). New asymmetric bithiocarbohydrazones and their mixed ligand nickel(II) complexes: Synthesis, characterization, crystal structure, electrochemical-spectroelectrochemical property, antimicrobial and antioxidant activity. *Polyhedron*, 207.
3. **Uğuz Özlem**, Budak Özlem, Koca Atif (2021). Simultaneous electrodeposition of electrochemically reduced graphene oxide-binary metal chalcogenide composites to enhance photoelectrochemical performance. *International Journal of Hydrogen Energy*. 46(71). 35290-35301.
4. Budak Özlem, **Uğuz Özlem**, Koca Atif (2021). Simultaneous electrochemical deposition of nickel cobalt oxide-reduced graphene oxide composites for high

- performance asymmetric supercapacitors. *Journal of Energy Storage*. Available online: 12 November 2021.
5. Ayaz Rana Muhammad Zunain, Akyüz Duygu, **Uğuz Özlem**, Tanışık İrem, Sarıoğlu Cevat, Karaca Fatma, Özkaya Ali Rıza, Koca Atif (2020). Photoelectrochemical performance of thermally sulfurized $Cd_xZn_{1-x}S$ photoanode: Enhancement with reduced graphene oxide support. *Renewable Energy*. 162. 182-195.
 6. Tanışık İrem, **Uğuz Özlem**, Akyüz Duygu, Ayaz Rana Muhammad Zunain, Sarıoğlu Cevat, Karaca Fatma, Özkaya Ali Rıza, Koca Atif (2020). Solar-hydrogen production with reduced graphene oxide supported $Cd_xZn_{1-x}S$ photocatalysts. *International Journal of Hydrogen Energy*. 45(60). 34845-34856.
 7. **Uğuz Özlem**, Haykiri-Acma Hanzade, Yaman Serdar (2020). Combustion kinetics of lignite preheated under oxygen-enriched conditions. *Energy & Environment*. 31(5). 813-824.
 8. **Uğuz Özlem**, Haykiri-Acma Hanzade, Yaman Serdar (2020). Burning Resistance of Lignitic Coals Under Oxygen-Enriched Conditions. *Journal of Energy Resources Technology-Transactions of the ASME*. 142(8).
 9. Akyüz Duygu, Ayaz Rana Muhammad Zunain, Yılmaz Seda, **Uğuz Özlem**, Sarıoğlu Cevat, Karaca Fatma, Özkaya Ali Rıza, Koca Atif (2019). *International Journal of Hydrogen Energy*. 44(34). 18836-18847.

ATTENDED CONFERENCES

1. **Uğuz Neli Özlem**, Budak Özlem, Başey Aleya Nur, Koca Atif (2021). Studies on Photoelectrochemical Performance of Mo, Ni and Cu Decorated RGO- $CdS_{0.2}Se_{0.8}$ Photoelectrodes Fabricated by Electrodeposition Method. 72nd Annual ISE Meeting, Jeju, South Korea.
2. Budak Özlem, **Uğuz Neli Özlem**, Başey Aleya Nur, Koca Atif (2021). Photoelectrochemical Performance of RGO- $CdS_{0.2}Se_{0.8}$ Photoelectrodes Prepared by One-step Electrodeposition Method. 72nd Annual ISE Meeting, Jeju, South Korea.
3. Budak Özlem, **Uğuz Özlem**, Koca Atif (2020). Analyzing Various Parameters on Supercapacitor Performance. 2nd International Eurasian Conference on Science, Engineering and Technology. Gaziantep, Turkey.

4. **Uğuz Özlem**, Koca Atıf (2019). Photoelectrochemical Activity of Electrodeposited $Cd_xZn_{1-x}S$ Photoelectrodes Under Solar Light Irradiation. 3rd International Conference on Applications in Chemistry and Chemical Engineering. Skopje, North Macedonia.
5. **Uğuz Özlem**, Akyüz Duygu, Ayaz Rana Muhammad Zunain, Yılmaz Seda, Sarıoğlu Cevat, Karaca Fatma, Özkaya Ali Rıza, Koca Atıf (2019). Photoelectrochemical-Photocatalytic Dual Hydrogen Production of RGO- $Cd_{1-x}Zn_xS$. 4th International Hydrogen Technologies Congress. Edirne, Turkey.
6. Ayaz Rana Muhammad Zunain, Akyüz Duygu, **Uğuz Özlem**, Tanişik İrem, Sarıoğlu Cevat, Karaca Fatma, Özkaya Ali Rıza, Koca Atıf (2019). Enhanced Photoelectrochemical Activity of Reduced Graphene Oxide Decorated $Cd_xZn_{1-x}S$ Photocatalyst for Hydrogen Production. 4th International Hydrogen Technologies Congress. Edirne, Turkey.
7. **Uğuz Özlem**, Demirci Ali, Haykiri-Açma Hanzade, Yaman Serdar (2018). Applicability of Regression Analysis on the Oxygen Enriched Combustion of Adiyaman-Golbasi Lignite 2nd International Conference on Pure and Applied Mathematics. Van, Turkey.
8. **Uğuz Özlem**, Akyüz Duygu, Koca Atıf (2018). Electrochemical Sensing Applications of Metallophthalocyanines (MPcs). 69th Annual ISE Meeting. Bologna, Italy.
9. **Uğuz Özlem**, Haykiri-Açma Hanzade, Yaman Serdar (2018). Characterization Study of Kütahya-Tunçbilek Lignite During Oxygen Enriched Combustion. 14th International Combustion Symposium. Karabük, Turkey.
10. **Uğuz Özlem**, Akyüz Duygu, Ayaz Rana Muhammad Zunain, Tanişik İrem, Sarıoğlu Cevat, Karaca Fatma, Özkaya Ali Rıza, Koca Atıf (2018). Photoelectrochemical Hydrogen Production Using $Cd_{1-x}Zn_xS$ and Its Modifications with Graphene Derivatives. 3rd International Hydrogen Technologies Congress. Antalya, Turkey.
11. Ayaz Rana Muhammad Zunain, Akyüz Duygu, **Uğuz Özlem**, Tanişik İrem, Sarıoğlu Cevat, Karaca Fatma, Özkaya Ali Rıza, Koca Atıf (2018). Hydrogen Production from Water as Photoelectrochemical by Using Solar Light

- Irradiation. 3rd International Hydrogen Technologies Congress. Antalya, Turkey.
12. Akyüz Duygu, **Uğuz Özlem**, Tanişik İrem, Ayaz Rana Muhammad Zunain, Sarıoğlu Cevat, Karaca Fatma, Özkaya Ali Rıza, Koca Atıf (2018). The Effect of Co-catalyst and Novel Heterogeneous Active Photocatalysts for Hydrogen Evolution under Solar Energy. 3rd International Hydrogen Technologies Congress. Antalya, Turkey.
 13. Tanişik İrem, Akyüz Duygu, Ayaz Rana Muhammad Zunain, **Uğuz Özlem**, Sarıoğlu Cevat, Karaca Fatma, Özkaya Ali Rıza, Koca Atıf (2018). Active Photocatalysts Designed by Sulphurization Method for Hydrogen Production. 3rd International Hydrogen Technologies Congress. Antalya, Turkey.
 14. **Uğuz Özlem**, Haykiri-Açma Hanzade, Yaman Serdar (2017). Kinetic Study of Kütahya-Tunçbilek Lignite during Oxygen Enriched Conditions. 2nd International Conference on Advanced Engineering Technologies. Bayburt, Turkey.
 15. **Uğuz Özlem**, Haykiri-Açma Hanzade, Yaman Serdar (2017). Kinetics Study of Adıyaman-Gölbaşı Lignite during Oxygen Enriched Combustion. 6th International Conference on Renewable Fuels, Combustion and Fire. Nevşehir, Turkey.
 16. **Uğuz Özlem**, Haykiri-Açma Hanzade, Yaman Serdar (2016). Combustion of Tuncbilek Lignite in Oxygen Enriched Atmosphere. 8th Ege Energy Symposium and Exhibition. Afyon, Turkey.